Design Specifications for Wet-Bulb Aspirator Apparatus

by

Jacob P. Brenner

A thesis submitted in partial fulfillment of

the requirements for the degree of

Master of Science

(Mechanical Engineering)

at the

UNIVERSITY OF WISCONSIN-MADISON

2010

This thesis has been approved by

Dr. Gregory F. Nellis, Associate Professor	date
Dr. Douglas T. Reindl, Professor	date
Dr. John M. Pfotenhauer, Professor	date

Abstract

Aspirated psychrometers are commonly used for the measurement of the wet-bulb temperature. By knowing the wet-bulb temperature, dry-bulb temperature, and pressure, the thermodynamic state of a moist air stream can be determined. ASHRAE Standards 41.6-1994 (RA 2006) and 41.1-1986 (RA 1991) currently specify the detailed design guidelines and considerations required to construct an aspirated psychrometer that is capable of measuring the wet-bulb temperature to within ±0.1°C.

The aim of this project is to be able to specify the design guidelines and considerations required to construct an aspirated psychrometer capable of measuring the wet-bulb temperature to within ±0.05°C. This is done by means of an analytical model used to predict the error in the measurement of the wet-bulb temperature over a range of conditions. Also to validate the model an aspirated psychrometer is built in accordance with the model and tested over a range of experimental test conditions. The analytical model and the experimental test apparatus are described in detail in this document.

Acknowledgements

First and foremost I would like to thank my advisors, Professor Greg Nellis and Professor Doug Reindl for the hours spent reading the various portions of this document and for their technical support and guidance throughout this project. I would like to thank Professor John Pfotenhauer for his participation on my defense committee. I would also like to thank the American Society of Heating, Refrigeration, and Air-Conditioning Engineers (ASHRAE) for their financial support, and the members of the ASHRAE Project Monitoring Subcommittee overseeing this research for their continual feed-back throughout the project. Special thanks to Charles Wright and TSI Inc. for the donation of the velocity transducer to the project.

I also need to thank my family for their continuous support of me throughout college. I would especially like to thank my dad Joe, mom Joan, brothers Jason and Joe, sisters-in-law Holly and Leah, and brother Jamie. I truly would not have been able to make it through the past five and half years of college without your continual support and encouragement.

I would also like to thank Nick Edwards for his assistance relating to wicking height, as described in Chapter 5. Finally I would like to thank all of the Solar Energy Laboratory. All of you have made my time here enjoyable.

Executive Summary

A wet-bulb aspirator apparatus is one instrument that can be used to measure the wet-bulb temperature of a moist air stream. The wet-bulb temperature is an important psychrometric property and accurate measurements are essential for testing and rating of various types of HVAC&R equipment.

The goal of this research project is to develop and specify a technique that can be used to accurately measure the wet-bulb temperature with an aspirated psychrometer. Specifically, the research will provide the basis for improvements in ASHRAE Standard 41.6-1994 (RA 2006), *Standard Method for Measurement of Moist Air Properties*. The current ASHRAE Standard 41.6 defines the design guidelines to construct a wet-bulb aspirator apparatus capable of measuring the wet-bulb temperature to within ±0.10°C. One objective of this research is to outline design guidelines and considerations needed to improve the accuracy of wet-bulb temperature measurements to achieve an accuracy of ±0.05°C. This executive summary provides an overview of the theoretical and experimental work carried out to accomplish the project goal. A more detailed discussion of the work can be found in the final report.

Adiabatic Saturation, True Wet-Bulb, and Measured Wet-Bulb Temperature

To be able to accurately measure the wet-bulb temperature, it is important to first understand the definition of *wet-bulb temperature* and the closely-related quantity, *adiabatic saturation temperature*. The *adiabatic saturation temperature* is defined as the temperature obtained by

an air-water vapor mixture if it becomes saturated with water vapor in an adiabatic process (ASHRAE 41.1, 1991). The *true wet-bulb temperature* is determined by a balance between heat and mass transfer, as described in Nellis and Klein (2009).

To measure the wet-bulb temperature, a moist air stream is forced across a temperature sensor kept wetted by a moist cotton sock. As water from the sock evaporates, the sensor cools. The cooling of the sensor below the ambient dry-bulb temperature leads to convective heat gain from the air stream to the temperature sensor. The "true" wet-bulb temperature is the equilibrium temperature obtained when the energy loss by evaporation balances with the convective heat gain. An expression for the true wet-bulb temperature is given by:

$$T_{true,wb} = T_{db} - \frac{\overline{h}_D}{\overline{h}}\left(c_{v,wb} - c_{v,db}\right)\Delta h_{vap} \tag{0.1.1}$$

where T_{db} is the dry-bulb temperature, $\overline{h}_D$ is the average mass transfer coefficient, $\overline{h}$ is the average heat transfer coefficient, $c_{v,wb}$ and $c_{v,db}$ are the concentrations of water vapor at the wet-bulb temperature sensor and in the free stream air, respectively, and Δh_{vap} is the latent heat of vaporization for water.

Unfortunately, there are other forms of heat transfer to the temperature sensor, which cause the observed or "measured" wet-bulb temperature to differ from the "true" wet-bulb temperature. These "parasitic" forms of heat transfer to the temperature sensor principally include radiation and lead wire conduction. When the additional heat transfer associated

with the mechanisms of the parasitic is included in the energy balance, an expression for the measured (rather than the true) wet-bulb temperature is obtained:

$$T_{m,wb} = T_{db} - \frac{\overline{h}_D}{\overline{h}}\left(c_{v,wb} - c_{v,db}\right)\Delta h_{vap} + \delta_{wb,error} \tag{0.1.2}$$

$$\delta_{wb,error} = \frac{\dot{q}_{par}}{\overline{h}A_s} \tag{0.1.3}$$

where the only new terms are $\dot{q}_{par}$ which is the parasitic heat transfer, and A_s which is the surface area of the sensor.

Comparing Eq. (0.1.1) to Eq. (0.1.2) shows that the measured wet-bulb temperature differs from the true wet-bulb temperature by an amount that is equal to $\delta_{wb,error}$, given by Eq. (0.1.3). Examination of the error shows that there are three ways in which to minimize $\delta_{wb,error}$ and therefore improve the measurement of the wet-bulb temperature. The first, and most obvious way, is to reduce all forms of parasitic heat transfer to the temperature sensor. In reducing the parasitic heat transfer to the temperature sensor, the balance between the convective and evaporative heat exchange at the sensor is approached and the measured wet-bulb temperature becomes the true wet-bulb temperature. The other two approaches that can be pursued to reduce wet-bulb measurement error are by increasing the heat transfer coefficient and/or increasing the surface area of the sensor. Increasing either one of these values will increase the denominator in Eq. (0.1.3) and reduce the impact of a given level of parasitic heat transfer on the wet-bulb temperature measurement.

Modeling

Detailed analyses are carried out in order to determine the most accurate method to measure the wet-bulb temperature. The first step considered sensor orientation, relative to the moist air flow direction. The two orientations considered were axial and transverse. A transverse orientation is one in which the length dimension of the sensor is oriented perpendicular to the flow of air, as shown in Figure 1.

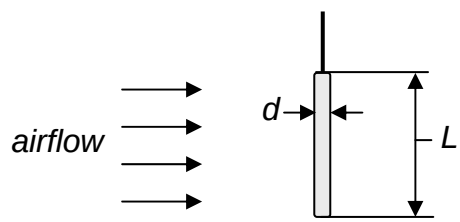

Figure 1: Temperature sensor positioned in the transverse orientation.

In the axial orientation, the length dimension of the temperature sensor is oriented parallel to the flow of air, as shown in Figure 2.

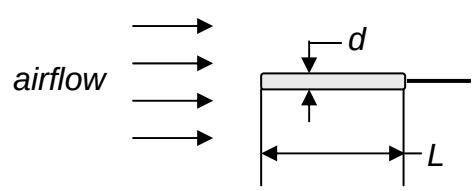

Figure 2: Temperature sensor positioned in the axial orientation.

The transverse orientation was determined to be preferential. The reason for this can be understood when the heat transfer coefficients associated with each sensor orientation are compared. The heat transfer coefficient for a sensor in the transverse orientation is almost twice that of a sensor in the axial configuration. As was shown in Eq. (0.1.3), an increase in the heat transfer coefficient reduces the error in the measurement of the wet-bulb

temperature. In other words for a defined error limit (e.g. ±0.05°C), more parasitic heat transfer can be tolerated with the transverse configuration than the axial orientation. Figure 3 shows the allowable parasitic heat transfer to the temperature sensor that achieves a +0.05°C wet-bulb error limit as a function of the air velocity for a sensor in both a transverse and axial configuration. Based on this result, the project proceeded with the temperature sensor positioned in the transverse orientation.

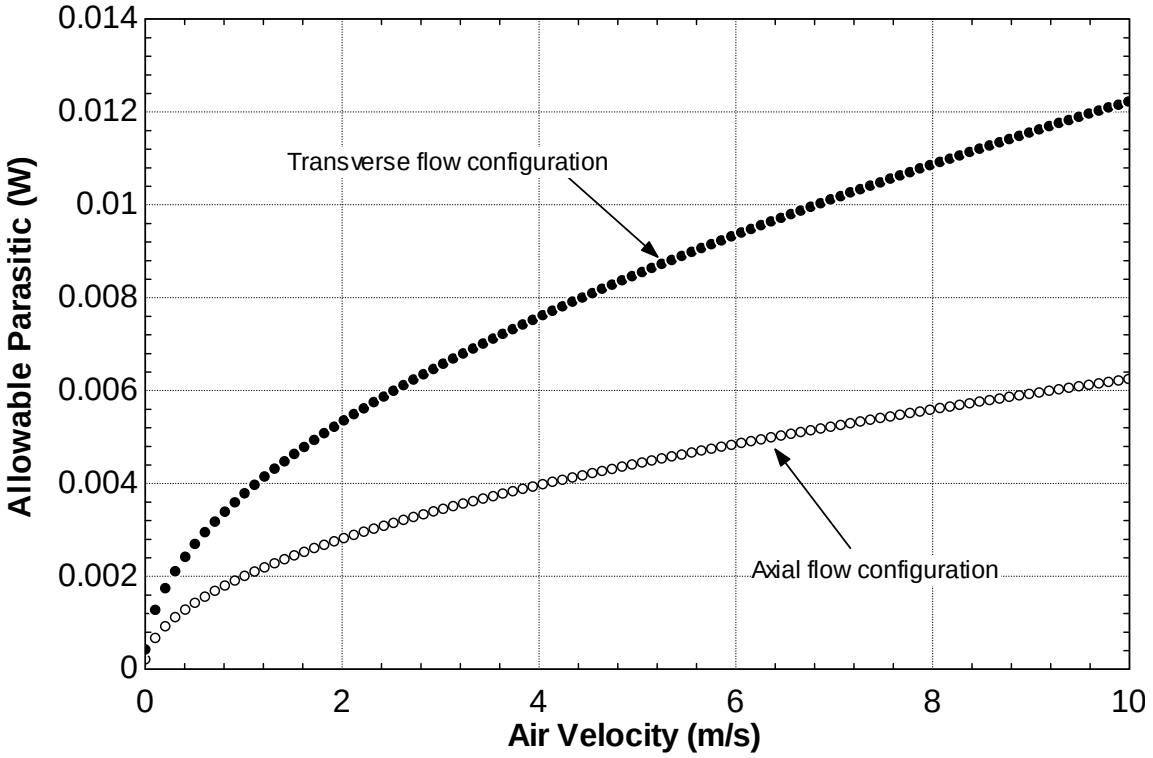

Figure 3: Allowable parasitic heat transfer to the temperature sensor as a function of air velocity for an error in the wet-bulb temperature measurement of 0.05°C.

The next step was to model each of the various forms of parasitic heat transfer to the wet-bulb temperature sensor. The first parasitic heat transfer to be modeled is radiation. Radiation to the temperature sensor is a concern because the wet-bulb temperature sensor is exposed to surroundings at an elevated temperature (the dry bulb temperature). The goal of

the radiation parasitic modeling was to optimize the design for a radiation shield and quantify the amount of radiation parasitic that could reasonably be expected.

After calculating the necessary view factors between the various surfaces participating in the radiation exchange and completing the radiation analysis, a radiation shield design that minimized the radiation heat gain to the wet-bulb temperature sensor was pursued. As expected, the radiation model underscored the importance of keeping the emissivity of the inside of the radiation shield as low as possible (e.g., 0.20 or less). The modeling showed that, even using a shield dimensionally optimized, it was not possible to reduce the radiation parasitic to the temperature sensor to a level that was sufficient to achieve the 0.05°C error target for measurement of the true wet-bulb. The radiation parasitic, with the optimized radiation shield geometry, was almost twice the acceptable limit for an air velocity of 4 m/s. From this analysis, it was clear that a "typical" or conventional radiation shield would not be sufficient to reduce the radiation parasitic to an acceptable level. Instead, a more sophisticated shield (e.g., one that is actively cooled) is required to reduce the parasitic heat gain to a level that would be able to achieve a wet-bulb measurement uncertainty less than 0.05°C. However, the impact to project cost was the prime issue for not pursuing further the actively cooled shields, and the design moved forward with a more "typical" radiation shield.

The parasitic associated with sensor sheath and lead wire conduction as well as elevated makeup water temperatures were also analyzed. The parasitic associated with conduction is due to the temperature sensor probe and lead wires being at or nearly at the dry-bulb temperature at the end opposite the wet-bulb sensor. Makeup water is the water used to wet

the cotton sock surrounding the wet-bulb temperature sensor. The makeup water is typically maintained in a reservoir which is at the dry-bulb temperature and subsequently fed to the wet-bulb temperature sensor by capillary action up the cotton wick covering the sensor. If the makeup water does not come to the wet-bulb temperature before reaching temperature sensor, there will be a parasitic gain to the wet-bulb temperature sensor associated with this flow of warm water.

A 6.35 mm (0.25 inch) diameter temperature sensor probe containing a four lead wire sensor is used in the project. The conduction analysis indicated that covering the entire temperature probe with a cotton sock and allowing water to wick as high up the sock as possible is a suitable way to guard against conduction parasitic. A wicking guard length of 8.9 cm (3.5 in) was found to be sufficient to completely guard the sensor against conduction parasitic over the entire range of psychrometric conditions tested. The wicking capability of the cotton material was not considered in this analysis.

The model of the makeup water parasitic considered the section of wick from the top of the water reservoir to the bottom of the temperature sensor. An analysis of this section of wick showed that 1.3 cm (0.5 in) of “free” wick must be exposed to the moist air stream to establish a sufficient thermal “guard” against makeup water parasitic and bring the makeup water from the dry-bulb temperature to the wet-bulb temperature for the entire range of experimental conditions.

The parasitic models showed that the primary source of parasitic to the temperature sensor is due to radiation. Both conduction and makeup water parasitic can be contributors but with the proper precautions, these parasitics can be minimized or even eliminated at all but the largest wet-bulb depressions (i.e., larger than 15°C). An empirical model of the wicking height was developed based on a separate set of experimental tests and used in conjunction with the conduction parasitic model. The wicking height model predicted wicking heights of less than the required 8.9 cm (3.5 in) at wet-bulb depressions greater than 15°C. This reduction in wicking height leads to small amounts of conduction parasitic at these large wet-bulb depressions.

Experimental Apparatus

The experimental aspirator apparatus was designed and constructed according to the model specifications. The purpose of the experimental apparatus was to confirm that the measurement results obtained experimentally matched those predicted analytically. A picture of the entire apparatus is shown in Figure 4.

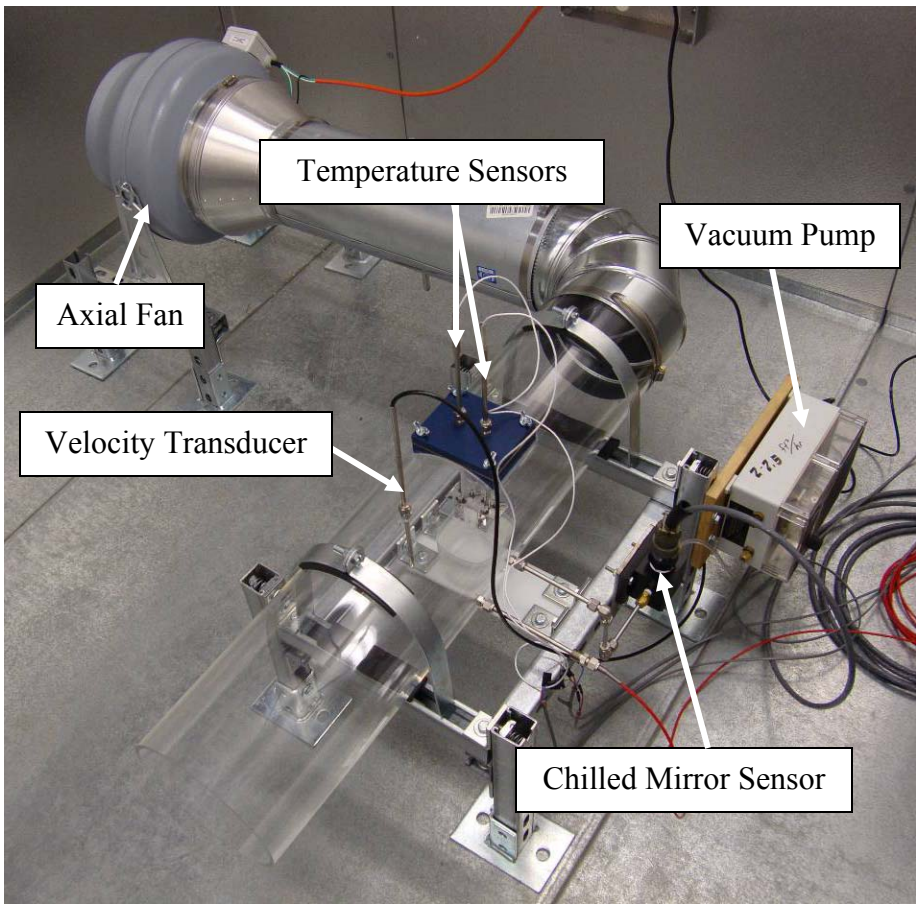

Figure 4: Experimental test apparatus for the measurement of wet-bulb temperature.

The apparatus pictured in Figure 4 is placed inside an environmental chamber where both the temperature and humidity can be varied. The test apparatus works by using an axial fan to draw air through a duct and over the temperature sensors. One of the temperature sensors was covered by a cotton sock. The end of the sock opposite the temperature sensor extends down, penetrates through the duct, and finally terminates in the water reservoir located just underneath the duct. Both the wet- and dry-bulb temperature sensors were placed inside of radiation shields, which were built to the specifications obtained based on optimization with the analytical model. The measurement taken by the wet-bulb temperature sensor is compared to the chilled mirror dew-point hygrometer; in this sense, the chilled mirror dew-

point hygrometer was used as the reference standard for testing the accuracy of the wet-bulb temperature measurement.

Experimental Measurements

Using the apparatus pictured in Figure 4, the wet-bulb temperature was measured (this is the "measured" wet-bulb temperature) over thirty test conditions and compared to the wet-bulb temperature obtained based on output of the chilled mirror dew-point hygrometer (this is the "true" wet-bulb temperature). The difference between the measured and true wet-bulb temperature is shown in Figure 5 as a function of wet-bulb depression for various values of the dew-point temperature.

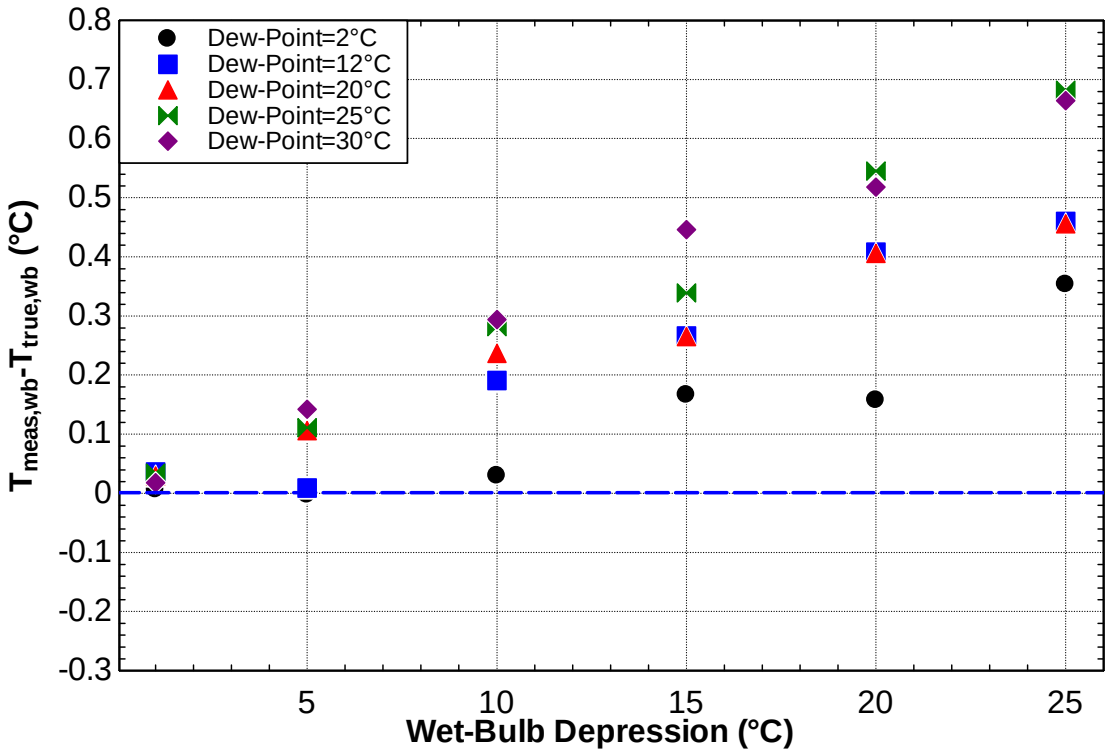

Figure 5: A plot of the difference between the measured wet-bulb temperature and the true wet-bulb temperature for each of the thirty conditions compiling the test matrix. Each symbol indicates a constant dew-point temperature.

Figure 5 shows that there is an increasing deviation between the measured wet-bulb temperature and the true wet-bulb temperature with increasing dew-point and wet-bulb depression. The measured wet-bulb temperature differs from the true wet-bulb temperature by as much as 0.7°C, which is much greater than the target accuracy goal of 0.05°C. The results of this set of tests were not surprising based on the model prediction of the error in the measurement of the wet-bulb temperature. In Figure 6, the model predicted wet-bulb temperature measurement error is overlaid onto the measurement error given by the experimental data; the upper and lower dashed lines correspond to the uncertainty in the model input parameters.

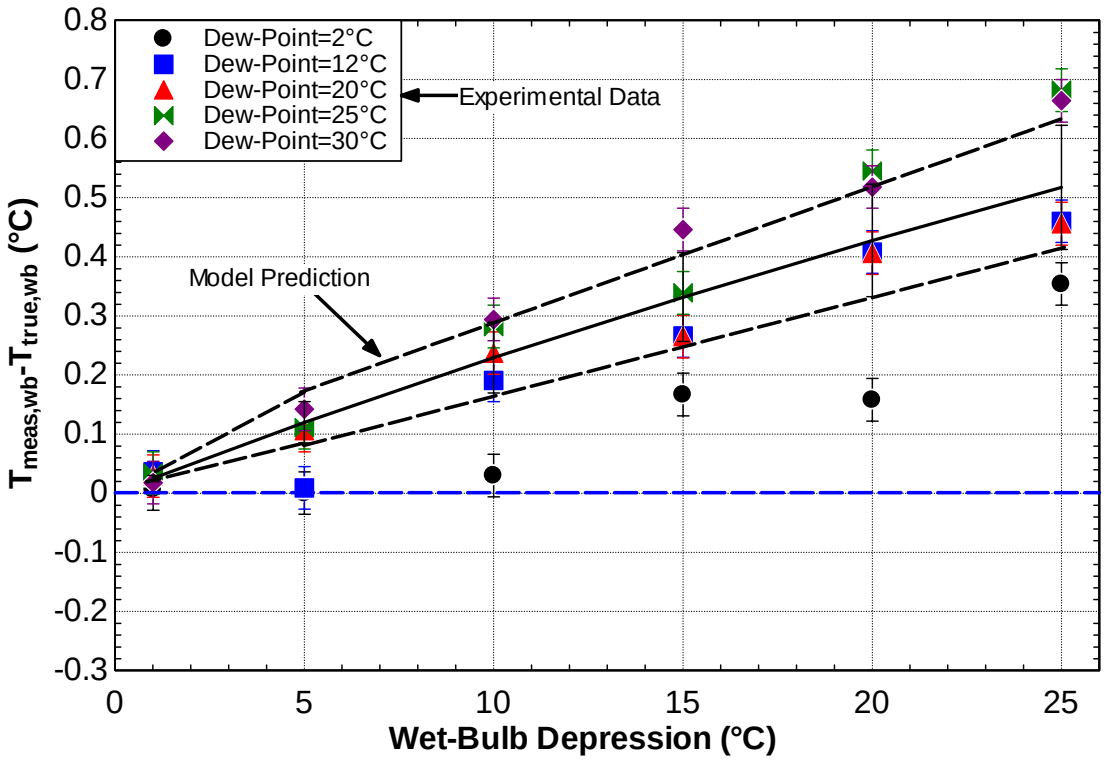

Figure 6: Model predicted error in the measurement of the true wet-bulb temperature. The error bars on each data marker indicate the uncertainty in the measurement result (±0.036°C). The model prediction range specified by the dashed lines accounts for the model uncertainty associated with uncertainty in the inputs.

The model prediction of the error in the measurement of the wet-bulb temperature was within approximately ±0.10°C of the experimental results for all test conditions except those occurring at a 2°C dew-point temperature. These data were deemed sufficient to validate the model and allowed the model to be used as a tool to determine general trends in measurement results with varying experimental parameters.

Figure 7 shows the difference between the measured wet-bulb temperature and the adiabatic saturation temperature over the entire range of test conditions.

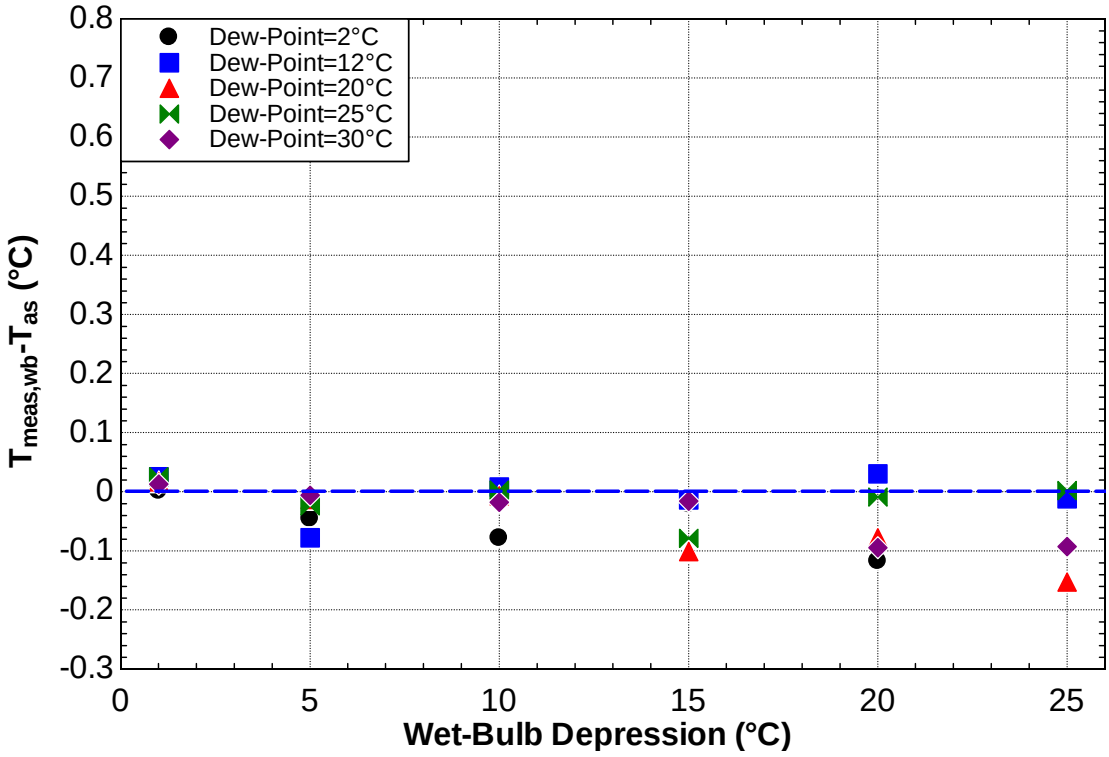

Figure 7: A plot of the difference between the measured wet-bulb temperature and the adiabatic saturation temperature for each of the thirty conditions compiling the test matrix. Each symbol indicates a constant dew-point temperature.

Figure 7 shows that the measured wet-bulb temperature provides a much better prediction of the adiabatic saturation temperature than of the true wet-bulb temperature. The measured wet-bulb temperature can be used to predict the adiabatic saturation temperature to within approximately ±0.05°C, with a slight negative bias, over the entire range of test conditions. Based on the model prediction, if either the air velocity is reduced from 4 m/s to 3.5 m/s or the radiation shield is removed, then the measured wet-bulb temperature will be able to predict the adiabatic saturation temperature to within approximately ±0.05°C over the entire range of test conditions.

The reason that the measured wet-bulb temperature is a good predictor of the adiabatic saturation temperature is because the adiabatic saturation temperature is larger than the true wet-bulb temperature by an amount that is almost exactly compensated for by the error associated with the parasitic heat transfer to the sensor. Wet-bulb temperature and adiabatic saturation temperature are often used interchangeably; however, these quantities are clearly not the same. As described previously, the wet-bulb temperature is achieved from the balance of convection and evaporation as a wet wick is aspirated. Adiabatic saturation temperature is the temperature obtained by moist air when it is adiabatically brought to saturation by the evaporation of liquid water. The advantage of using the measured wet-bulb temperature as a predictor of the adiabatic saturation temperature is that the parasitic heat transfer to the temperature sensing element does not need to be eliminated; it only needs to be controlled to a defined level.

Based on the theoretical and experimental work carried out in this research, it is not possible to directly measure the true wet-bulb temperature to within ±0.05°C using a conventional radiation shield. Radiation parasitic is the primary parasitic and resulted in the majority of the measurement error. The experimental data and analytical models developed did however indicate that with appropriate air velocity it is possible to control the parasitic so that the measured wet-bulb temperature is consistent with the adiabatic saturation temperature to within ±0.05°C.

Table of Contents

ABSTRACT ..... **I**

ACKNOWLEDGEMENTS ..... **III**

EXECUTIVE SUMMARY ..... **V**

TABLE OF CONTENTS ..... **XIX**

LIST OF FIGURES ..... **XXI**

LIST OF TABLES ..... **XXIX**

NOMENCLATURE ..... **XXXI**

CHAPTER 1 – INTRODUCTION **1**

1.1 MEASURING THE MOISTURE CONTENT OF AIR 1
1.1.1 Gravimetric Hygrometer *1*
1.1.2 Chilled Mirror Dew-Point Hygrometer *2*
1.1.3 Aspirated Psychrometer *3*
1.2 WET-BULB TEMPERATURE 4
1.2.1 True Wet-Bulb Temperature *4*
1.2.2 Measured Wet-Bulb Temperature *6*
1.3 RESEARCH OBJECTIVES 7

CHAPTER 2 – PARASITIC BUDGET **9**

2.1 TRANSVERSE FLOW CONFIGURATION 11
2.2 AXIAL FLOW CONFIGURATION 19
2.3 FLOW CONFIGURATION COMPARISON 20

CHAPTER 3 – MECHANISMS CONTRIBUTING TO PARASITIC HEAT TRANSFER **22**

3.1 RADIATION PARASITIC- TRANSVERSE CONFIGURATION 22
3.1.1 Radiation Shield Optimization *37*
3.1.2 Monte Carlo Method- Plate to Cylinder Radiation View Factor *49*
3.1.3 Monte Carlo Method- Plate to Plate with Cylinder between Radiation View Factor *69*
3.2 RADIATION PARASITIC- AXIAL CONFIGURATION 77
3.2.1 Radiation Shield Optimization *89*
3.3 CONDUCTION/ MAKEUP WATER PARASITIC 93
3.3.1 Upper Portion of Temperature Probe *95*
3.3.2 Lower Portion of Cotton Sock *110*
3.4 PARASITIC SUMMARY 116

CHAPTER 4 – EXPERIMENTAL TESTING **119**

4.1 EXPERIMENTAL EQUIPMENT & APPARATUS 119
4.1.1 Temperature Sensing Equipment *119*
4.1.2 Chilled Mirror Dew-Point Hygrometer *120*
4.1.3 Velocity Transducer *123*
4.1.4 Data Acquisition *123*
4.1.5 Pressure Measurement *124*
4.1.6 Axial Fan *124*
4.1.7 Environmental Chambers *126*
4.1.8 Experimental Apparatus *126*
4.2 EQUIPMENT UNCERTAINTY ANALYSIS 139

4.2.1 Temperature Measurement Uncertainty *139*
4.2.2 Dew-Point Temperature Measurement Uncertainty *143*
4.2.3 Atmospheric Pressure Measurement Uncertainty *147*
4.2.4 Adiabatic Saturation Temperature Measurement Uncertainty *149*
4.2.5 Velocity Measurement Uncertainty *152*
4.2.6 True Wet-Bulb Temperature Uncertainty *154*
4.3 TESTING PROCEDURE 156

CHAPTER 5 – WICKING HEIGHT **159**

5.1 WICKING HEIGHT MEASUREMENT APPARATUS 159
5.2 WICKING HEIGHT MEASUREMENT PROCEDURE 161
5.3 WICKING HEIGHT MEASUREMENT EXPERIMENTAL RESULTS 163
5.3.1 Effects of Free Stream Velocity and Relative Humidity on Wicking Height *164*
5 3.2 Effects of Evaporation Mass Flow Rate on Wicking Height *166*
5.4 WICKING HEIGHT MEASUREMENT UNCERTAINTY 168
5.4.1 Dry-Bulb Temperature Measurement Uncertainty *169*
5.4.2 Air Velocity Measurement Uncertainty *169*
5.4.3 Relative Humidity Measurement Uncertainty *169*
5.4.4 Wicking Height Measurement Uncertainty *170*
5.4.5 Evaporation Mass Flow Rate Uncertainty *170*
5.5 WICKING HEIGHT MEASUREMENT REPEATABILITY 171
5.6 IMPACT OF WICK ORIENTATION 172

CHAPTER 6 – RESULTS **180**

6.1 TEST MATRIX RESULTS (1) 180
6.2.1 Sock & Radiation Shield Replaced Daily *185*
6.2.2 Sock Replaced Daily, Radiation Shield Removed *187*
6.2.3 Sock & Radiation Shield Remain For All Tests *188*
6.2.4 Sock & Radiation Shield Replaced Daily, Parallel Sock Orientation *189*
6.2.5 Summary of Repeatability Test Results *191*
6.3 TEST MATRIX RESULTS (2) 194
6.4 MODEL PREDICTION 197
6.5 OTHER PARAMETERS IMPACTING WET-BULB TEMPERATURE MEASUREMENT 199
6.5.1 Duct Size *200*
6.5.2 Upstream Obstructions- Non-Uniform Velocity Distribution *205*
6.5.3 Sensor Diameter *208*

CHAPTER 7 – CONCLUSION **211**

REFERENCES **213**

APPENDIX **215**

THERMISTOR CALIBRATION CERTIFICATES 215
VELOCITY TRANSDUCER CALIBRATION CERTIFICATE 217
CHILLED MIRROR CALIBRATION CERTIFICATE 218

List of Figures

Figure 1-1: Heat transfer mechanisms occurring at the wet-bulb temperature sensing element. 5

Figure 1-2: Heat transfer mechanisms occurring at the wet-bulb temperature sensing element with the inclusion of miscellaneous parasitic gains. 6

Figure 2-1: Temperature sensor positioned in the transverse orientation. 10

Figure 2-2: Temperature sensor positioned in the axial orientation. 10

Figure 2-3: The allowable parasitic heat transfer to the wet-bulb temperature sensor oriented in a transverse configuration as a function of the air velocity over the sensor. As shown the three sets of data correspond to an error in the wet-bulb temperature measurement of 0.05°C, 0.1°C, and 0.2°C. 18

Figure 2-4: The allowable parasitic heat transfer to the wet-bulb temperature sensor oriented axially as a function of the air velocity over the sensor in an axial configuration. As shown the three sets of data correspond to an error in the wet-bulb temperature measurement of 0.05°C, 0.1°C, and 0.2°C. 20

Figure 2-5: Allowable parasitic heat transfer to the temperature sensor as a function of air velocity for an error in the wet-bulb temperature measurement of 0.05°C. 21

Figure 3-1: Isometric view of the radiation shield geometry modeled for the wet bulb temperature sensor in a transverse orientation. 23

Figure 3-2: Isometric view of the radiation shield and temperature sensor with the surfaces labeled. 28

Figure 3-3: The radiation parasitic to the wet-bulb as the upstream length of the shield is varied. The downstream shield extension is maintained at 40 mm (1.6 in). 39

Figure 3-4: The radiation parasitic to the wet-bulb as the downstream length of the shield is varied. The upstream shield extension is maintained at 11.7 mm. 40

Figure 3-5: Radiation parasitic as the emissivity of surface 2 (inside surface of shield) is varied. Both s_f and s_b remain at there optimal values, 6.57 mm (0.26 in) and 9.17 mm (0.36 in), respectively. 41

Figure 3-6: Radiation parasitic heat gain as a function of air velocity. The closed circles represent the parasitic heat transfer to the wet-bulb temperature sensor corresponding to errors in the wet-bulb temperature measurement of 0.05°C, 0.1°C, and 0.2°C. The open circles represent the parasitic heat transfer to the wet-bulb temperature sensor as a result of radiation. 43

Figure 3-7: Radiation parasitic heat gain as a function of the air velocity. The closed circles represent the parasitic heat transfer to the wet-bulb temperature sensor corresponding to errors in the wet-bulb temperature measurement of 0.05°C, 0.1°C, and 0.2°C. The open

circles represent the parasitic heat transfer to the wet-bulb temperature sensor as a result of radiation with and without screens at the inlet and exit. 45

Figure 3-8: Radiation parasitic heat gain as a function of the air velocity. The closed circles represent the parasitic heat transfer to the wet-bulb temperature sensor corresponding to errors in the wet-bulb temperature measurement of 0.05°C, 0.1°C, and 0.2°C. The open circles represent the parasitic heat transfer to the wet-bulb temperature sensor as a result of radiation with various shield configurations. The cooled shield is held at the wet-bulb temperature (19.4°C). 46

Figure 3-9: Radiation parasitic heat gain as a function of the length of the shield in the upstream and downstream direction. The closed circles represent the parasitic heat transfer to the wet-bulb temperature sensor corresponding to errors in the wet-bulb temperature measurement of 0.05°C, 0.1°C, and 0.2°C. The open circles represent the parasitic heat transfer to the wet-bulb temperature sensor as a result of radiation for a cooled shield with no screens. The air velocity is held constant at 4 m/s, and the length of the shield in both the upstream and downstream directions (s_f and s_b) are increased by equal amounts. The shield is at the wet-bulb temperature (19.4°C). 47

Figure 3-10: Radiation parasitic heat gain as a function of air velocity. The closed circles represent the parasitic heat transfer to the wet-bulb temperature sensor corresponding to errors in the wet-bulb temperature measurement of 0.05°C, 0.1°C, and 0.2°C. The open circles represent the parasitic heat transfer to the wet-bulb temperature sensor as a result of radiation for a cooled shield with no screens. The length of the shield in both the upstream and downstream directions (s_f and s_b) is kept at 20 mm (0.79 in) and the temperature of the shield is varied from the wet-bulb temperature to the dry-bulb temperature. 48

Figure 3-11: Radiation view factor of interest is from surface 1 to surface 2. Surface 1 is the inside surface of a rectangular flat plate. Surface 2 is the entire exterior of the circular cylinder. 49

Figure 3-12: Two surfaces exchanging radiation (Nellis and Klein, 2009). 50

Figure 3-13: Surface 1 is the under side of a flat plate with a width (*w*) and length (*h*). Surface 2 is a circular cylinder placed a distance (*s*) from the plate. The cylinder has a diameter (*d*) and length (*k*) and is centered under the plate in both the *x* and *y*-direction. 51

Figure 3-14: Unit vector displaying the direction of an emitted ray in terms of the polar and azimuthal angles. 54

Figure 3-15: Dotted lines represent the boundaries implemented in the MATLAB code. Once a ray endpoint is outside of the box created by the dotted lines it is no longer possible for it to strike surface 2. 59

Figure 3-16: View factor correlation available in EES (Klein, 2009). 62

Figure 3-17: Geometry implemented with the Monte Carlo method to verify results. 63

Figure 3-18: Fifty view factor estimates (points) as well as the average (line) using the Monte Carlo method at discrete *dL/d* values with the number of rays held at a constant value of $1x10^3$. 65

Figure 3-19: Fifty view factor estimates (points) as well as the average (line) using the Monte Carlo method at discrete *dL/d* values with the number of rays held at a constant value of $1x10^4$. 66

Figure 3-20: A plot showing 50 runs of the Monte Carlo method at *N* values of $1x10^3$, $1x10^4$, $1x10^5$, and $1x10^6$, with the *dL* held constant at *d/10* (1 mm). The "x" symbols represent the results produced in EES. 67

Figure 3-21: A comparison of the view factor calculated using EES and using the Monte Carlo method as a function of the distance between the plane and the cylinder. The Monte Carlo method implemented used an *N* value of $1x10^5$ and a *dL* value of *d/10*. 68

Figure 3-22: A comparison of the view factor calculated using EES and using the Monte Carlo method developed, as the width of the plane is varied. The Monte Carlo method implemented used an *N* value of $1x10^5$ and a *dL* value of *d/10*. 69

Figure 3-23: Isometric view of the geometry in which the view factor is computed. Surface 3 and surface 4 are the inside surfaces of flat plates facing each other with a circular cylinder centered between them. 70

Figure 3-24: Elevation and plan views of the geometry to be analyzed with surfaces labeled. 71

Figure 3-25: The geometry and mesh produced in ANSYS to verify the view factor calculation implemented in MATLAB. 76

Figure 3-26: Isometric view of the radiation shield geometry modeled for a temperature sensor in an axial flow configuration. 77

Figure 3-27: Radiation parasitic heat gain to an axial mounted temperature sensor as a function of air velocity. The closed circles represent the parasitic heat transfer to the axial wet-bulb temperature sensor corresponding to errors in the wet-bulb temperature measurement of 0.05°C, 0.1°C, and 0.2°C. The open circles represent the parasitic heat transfer to the axial wet-bulb temperature sensor as a result of radiation. The shield is kept at its optimal length, $L_{sh} \approx L$. 90

Figure 3-28: Radiation parasitic heat gain to the axially mounted temperature sensor as a function of air velocity. The closed circles represent the parasitic heat transfer to the axial wet-bulb temperature sensor corresponding to errors in the wet-bulb temperature measurement of 0.05°C, 0.1°C, and 0.2°C. The open circles represent the parasitic heat transfer to the axial wet-bulb temperature sensor as a result of radiation. The shield is kept at its optimal length, $L_{sh} \approx L$. 91

Figure 3-29: Radiation parasitic heat gain to an axial mounted temperature sensor as a function of the air velocity. The closed circles represent the parasitic heat transfer to the axial wet-bulb temperature sensor corresponding to errors in the wet-bulb temperature measurement of 0.05°C, 0.1°C, and 0.2°C. The open circles represent the parasitic heat transfer to the axial wet-bulb temperature sensor as a result of radiation with various shield configurations. The cooled shield is held at the wet-bulb temperature (19.4°C). 92

Figure 3-30: Schematic of the wicking setup modeled. A temperature sensor probe protrudes down from the top with the sensor located at the end of the probe. The wetting sock draws water from a reservoir via capillary action to the temperature sensor and up across the stem to thermally guard the sheath. 94

Figure 3-31: Top section of the temperature sensor probe modeled. 95

Figure 3-32: Cross-sectional view of the upper section of the temperature probe. 96

Figure 3-33: Thermal resistance network between a copper lead wire positioned at the center of the temperature probe and the exterior free stream air. The sheath and wet cotton sock are assumed to be at the same temperature (i.e. $T_{sh,w}$). 97

Figure 3-34: Energy transfer associated with a differential segment of the upper portion of the temperature probe. 101

Figure 3-35: Mass transfers associated with a differential segment of the upper portion of the temperature probe. 102

Figure 3-36: A plot of the temperature of the upper section of the probe at incremental distances from the top of the temperature probe in transverse orientation. The end distance corresponds to a position of $x = L$ in Figure 3-31 (L = 0.10 m or 4 in, in the above plot). .. 108

Figure 3-37: Heat transfer to the temperature sensor as a function of the distance in which the wick extends past the temperature sensor portion of the probe. The data is for an air velocity of 4 m/s at a wet-bulb temperature of 19.4°C and a dry-bulb temperature of 26.7°C. 109

Figure 3-38: Portion of the wick that draws water from the water reservoir up to the temperature sensor. The sock leaves the temperature sensor at a location of $x = 0$ and enters the water reservoir at a location of $x = L$. 110

Figure 3-39: Cross-sectional view of the wick geometries modeled in the analysis: (a) the wick remains in a cylindrical shape between the probe and the water reservoir, (b) the wick collapses on itself and is oriented perpendicular to the flow direction, and (c) the wick collapses on itself and is oriented parallel to the flow direction. The arrows represent the flow direction across the wicks as viewed from the top. 111

Figure 3-40: Plot of the heat transfer through the wet cotton sock at interval locations between the top of the makeup water reservoir and the bottom of the temperature sensor. The entire portion of the wick between the water reservoir and the bottom of the temperature sensor is exposed to the flow of the moist air stream. 114

Figure 3-41: Plot of the heat transfer through the wet cotton sock at interval locations between the makeup water reservoir and the temperature sensor. The plot contains the data corresponding to the sock connecting the water reservoir to the temperature sensor in three different geometric orientations. 116

Figure 4-1: Fluke Model 5640 thermistor probe..... 120

Figure 4-2: General Eastern Instruments OptiSonde Chilled Mirror Hygrometer. 121

Figure 4-3: General Eastern Instruments Model 1111H single stage dew-point temperature sensor. 122

Figure 4-4: Type 0111D pressure boss. 122

Figure 4-5: TSI Model 8455 velocity transducer. 123

Figure 4-6: Continental AXC300A Series Inline Duct Fan. 125

Figure 4-7: Variable autotransformer (ISE, Inc.). 125

Figure 4-8: Experimental test apparatus for the measurement of wet-bulb temperature. 127

Figure 4-9: Temperature measurement section of the experimental apparatus. 129

Figure 4-10: Isometric and side view of acrylic duct with the milled surface and the dimensions specified. 131

Figure 4-11: Isometric and front view of the flange mounted to the milled surface of the acrylic pipe. 132

Figure 4-12: Polyethylene mating flange attached to acrylic pipe. 133

Figure 4-13: Temperature sensor base plate. 134

Figure 4-14: Temperature sensor mounting assembly. 135

Figure 4-15: Wet- and dry-bulb temperature sensor probes with radiation shield. 136

Figure 4-16: Radiation shield used to reduce radiation parasitic to the temperature sensor probes used in the experimental apparatus. 137

Figure 4-17: EES output window for the uncertainty in the adiabatic saturation temperature. 150

Figure 4-18: The uncertainty in the adiabatic saturation temperature at each of the thirty test points compiling the test matrix. The uncertainty in the dry-bulb temperature, dew-point temperature, and pressure used to calculate the uncertainty in the adiabatic saturation temperature are 0.0225°C, 0.0408°C, and 0.026Psi, respectively. 151

Figure 4-19: EES output window for the uncertainty in the true wet-bulb temperature. 156

Figure 5-1: Experimental apparatus with modifications. 160

Figure 5-2: Wicking height measurement. 163

Figure 5-3: Wicking height as a function of air velocity for six different environmental set-points. Each environmental condition is labeled with the dry-bulb temperature, relative humidity and wet-bulb depression. 164

Figure 5-4: Wicking height as a function of evaporation mass flow rate for six different environmental set-points. Each environmental condition is labeled with the dry-bulb temperature and relative humidity. 166

Figure 5-5: Wicking height predicted by the model vs. measured wicking height with curves for ± 5% and ±10% error. 168

Figure 5-6: Schematic showing the portion of the cotton sock between the bottom of the temperature sensor and the top of the water reservoir. 173

Figure 5-7: Three different sock orientations. The sock on the left is oriented in a cylindrical shape. The sock in the middle is oriented with the flat portion of the wick parallel to the flow (air flow direction is into the page) and the one on the right is oriented with the flat portion perpendicular to the flow. 174

Figure 5-8: Predicted wicking height from the top of the water reservoir for the three different sock orientations. The data plotted is for a constant dew-point temperature of 2°C. Model predicted wicking heights deviate minimally with dew-point temperature (i.e., < 1 mm). 178

Figure 6-1: The difference between the measured wet-bulb temperature and the adiabatic saturation temperature for each of the thirty conditions in the test matrix. Each symbol indicates a constant dew-point temperature. 181

Figure 6-2: The difference between the measured wet-bulb temperature and the true wet-bulb temperature for each of the thirty conditions in the test matrix. Each symbol indicates a constant dew-point temperature. 182

Figure 6-3: The difference between the adiabatic saturation temperature and the true wet-bulb temperature as a function of wet-bulb temperature depression for various values of constant dew-point temperature. 184

Figure 6-4: Repeatability results for the two conditions corresponding to a 12°C dew-point temperature and a 10°C and 15°C wet-bulb depression. The radiation shield was in place for each of the tests and the cotton sock was replaced daily. Results specified by the same data marker were obtained from tests occurring on the same day. 186

Figure 6-5: Repeatability results for the two conditions corresponding to a 12°C dew-point temperature and a 10°C and 15°C wet-bulb depression. The radiation shield was completely removed for each of the tests and the cotton sock was replaced daily. Results specified by the same data marker were obtained from tests occurring on the same day. 187

Figure 6-6: Repeatability results for the two conditions corresponding to a 12°C dew-point temperature and a 10°C and 15°C wet-bulb depression. The radiation shield and the same cotton sock remained in place for the entire set of test runs. 188

Figure 6-7: Schematic showing the larger water reservoir connected to the smaller water reservoir that is used to wet the cotton sock. The large water reservoir with the larger surface area keeps the water level approximately constant throughout a test. 190

Figure 6-8: Repeatability results for the two conditions corresponding to a 12°C dew-point temperature and a 10°C and 15°C wet-bulb depression. The radiation shield was in place for all tests. All tests were done with the water level remaining constant throughout the test and the flat portion of the wick extending below the temperature sensor oriented parallel to the flow stream. Results specified by the same data marker were obtained from tests occurring with the same wick. 191

Figure 6-9: Radiation shield with the set screws removed on the wet-bulb temperature sensor side. 194

Figure 6-10: A plot of the difference between the measured wet-bulb temperature and the adiabatic saturation temperature for each of the thirty conditions in the test matrix. Each symbol indicates a constant dew-point temperature. 195

Figure 6-11: A plot of the difference between the measured wet-bulb temperature and the true wet-bulb temperature for each of the thirty conditions in the test matrix. Each symbol indicates a constant dew-point temperature. 196

Figure 6-12: Model predicted error in the measurement of the true wet-bulb temperature. The error bars on each data marker indicate the uncertainty in the measurement result (±0.036°C). The model prediction range specified by the dashed lines accounts for the model uncertainty associated with uncertainty in the inputs. 197

Figure 6-13: Guard used to isolate the guard portion of the sensor from the flow of air in order to simulate the removal of this portion of the sensor from a duct that is too small to accommodate the guard region. 201

Figure 6-14: Cotton wick terminated at the top of the radiation shield. 203

Figure 6-15: Experimental test setup with upstream bend added. 205

Figure 6-16: Velocity distribution in the duct with the elbow turned upright. 206

Figure 6-17: Velocity measurement locations. The locations are the following distances from the wall: location 1- 0.032*D, location 2-0.135*D, location 3-0.321*D, location 4-0.679*D, location 5-0.865*D, and location 6-0.968*D. D is the inner duct diameter, which in this case is 7.5 inches. 207

Figure 6-18: Model prediction of the error in the measurement of the true wet-bulb temperature for sensor diameters of 6.35, 4.8, and 3.2 mm in diameter and an air velocity of 4 m/s. 209

List of Tables

Table 4-1: Uncertainty in the temperature measurement using a current source with an uncertainty of ±0.05% at 10μA. 142

Table 4-2: Uncertainty in the temperature measurement using a current source with an uncertainty of ±0.01% at 10μA. 142

Table 4-3: Uncertainty in dew-point temperature measurement over entire dew-point temperature range of the chilled mirror hygrometer. 146

Table 4-4: Uncertainty in velocity measurement over the 0-10 m/s range. 154

Table 5-1: Uncertainty in the relative humidity measurement. 170

Table 5-2: The uncertainty in the mass flow rate prediction. As is shown, the uncertainty in the predicted evaporative mass flow rate increases with increasing air velocity and with decreasing relative humidity. 171

Table 5-3: Measured wicking heights at two specified conditions with the tests repeated four times for each test condition. 172

Table 6-1: Experimental test results. Limited aspiration refers to the apparatus shown in Figure 6-13. Fully aspirated is when the entire wick is exposed to the flow of air. 201

Table 6-2: Experimental test results. Aspirated sensor only data refers to the data taken with the sensor being wetted in the manner described by Figure 6-14. Fully aspirated is when the entire wick is exposed to the flow of air. 203

Nomenclature

A_{al}	cross-sectional area of alumina insulation (m^2)
A_c	cross-sectional area (m^2)
A_i	area of surface i (m^2)
A_{ld}	cross-sectional area of lead wire (m^2)
A_s	surface area (m^2)
A_{sh}	cross-sectional area of sheath (m^2)
A_w	cross-sectional area of water (m^2)
c_p	specific heat capacity (J/kg-K)
$c_{v,db}$	concentration of water vapor at the dry-bulb temperature (kg/m^3)
$c_{v,sat}$	concentration of saturated water vapor (kg/m^3)
$c_{v,wb}$	concentration of water vapor at the wet-bulb temperature (kg/m^3)
c_∞	concentration of water vapor in the free stream air (kg/m^3)
d	diameter (m)
dA	differential area segment (m^2)
$d_{in,sh}$	inner diameter of sheath (K/W)
$d_{out,ld}$	outer diameter of lead wires (K/W)
D_{sensor}	temperature sensor diameter (m)
d_{sh}	inner shield diameter (m)
$D_{w.a}$	diffusion coefficient of water vapor in air (m^2/s)
dx	differential in the x-direction (m)
dy	differential in the y-direction (m)
$E_{b,i}$	blackbody emissive power of surface i (W/m^2)
$F_{i,j}$	view factor from surface i to surface j (-)
h	height (m)
$\bar{h}$	average heat transfer coefficient (W/m^2-K)
$hits$	number of ray strikes (-)
$\bar{h}_D$	average mass transfer coefficient (m/s)
$\bar{h}_{D,cyl}$	average mass transfer coefficient over a cylinder (m/s)
$\bar{h}_{D,par}$	average mass transfer coef. over wick in parallel orientation (m/s)
h_g	enthalpy of water vapor (J/kg)
h_l	enthalpy of liquid water (J/kg)
I	current (A)
ict	number of rays generated (-)
I_{lower}	lower limit of output current range (A)
I_{out}	output current (A)
I_{upper}	upper limit of output current range (A)
J_i	radiosity of surface i (W/m^2)
k	thermal conductivity (W/m-K)
	length (m)
k_{al}	thermal conductivity of alumina (W/m-K)

kA_{top}	conductivity/cross-sectional area product of top portion (W-m/K)
kA_w	conductivity/cross-sectional area product of water (W-m/K)
k_{ld}	thermal conductivity of lead wire (W/m-K)
k_{sh}	thermal conductivity of sheath (W/m-K)
K_{temp}	temperature coefficient (ohm/K)
k_w	thermal conductivity of water (W/m-K)
L	length (m)
l	width (m)
L_{sh}	shield length (m)
L_{wick}	wicking height (m)
$L_{wick,bottom}$	wicking height on bottom portion of sensor (m)
$L_{wick,top,par}$	wicking height on top portion of sensor in parallel orientation (m)
$L_{wick,total,par}$	total wicking height with wick in parallel orientation (m)
$\dot{m}$	mass flow rate (kg/s)
$\dot{m}_{bottom,par}$	mass flow rate from bottom portion in parallel orientation (kg/s)
$\dot{m}_{evap}$	evaporative mass flow rate (kg/s)
$\dot{m}_l$	mass flow rate of liquid water (kg/s)
$\dot{m}_{top,par}$	mass flow rate from top portion in parallel orientation (kg/s)
$\dot{m}_{total,par}$	total mass flow rate from the wick (kg/s)
N	number of rays generated (-)
n	length (m)
P	probability distribution (-)
	pressure (Pa)
per	perimeter (m)
Pr	Prandtl number (-)
P_{lower}	lower limit on pressure range (Pa)
$P_{s,db}$	saturation pressure of water vapor at the dry-bulb temperature (Pa)
P_{upper}	upper limit on pressure range (Pa)
$P_{v,db}$	partial pressure of water vapor at the dry-bulb temperature (Pa)
$\dot{q}_{conv}$	rate of convective heat transfer (W)
$\dot{q}_{conv,i}$	rate of convective heat transfer to surface i (W)
$\dot{q}_{evap}$	rate of evaporative heat transfer (W)
$\dot{q}_i$	rate of heat transfer from surface i (W)
$\dot{q}_{par}$	rate of parasitic heat transfer (W)
$\dot{q}_{rad,i}$	rate of radiation heat transfer from surface i (W)
R	electrical resistance (ohm)
r	radial coordinate (m)
$\hat{r}$	radial unit vector (-)
Re	Reynolds number (-)
RH	relative humidity (-)
RR	ratio of thermal resistances (-)

$R_{cond,al}$	thermal resistance to conduction through alumina (K/W)
R_{conv}	thermal resistance to convection (K/W)
s	distance (m)
Sc	Schmidt number (-)
Sh	Sherwood number (-)
s_b	downstream shield extension (m)
s_f	upstream shield extension (m)
t	time (s)
th	thickness (m)
T_{as}	adiabatic saturation temperature (K)
T_{db}	dry-bulb temperature (K)
T_{dp}	dew-point temperature (K)
T_{film}	film temperature (K)
T_i	temperature of surface *i* (K)
T_{ld}	temperature of lead wires (K)
T_{lower}	lower limit of dew-point temperature range (K)
$T_{sh,w}$	temperature of sheath and wet cotton sock (K)
T_{upper}	upper limit of dew-point temperature range (K)
T_{wb}	wet-bulb temperature (K)
$T_{wb,m}$	measured wet-bulb temperature (K)
T_∞	free stream temperature (K)
u_∞	free stream air velocity (m/s)
V	voltage (V)
Vel	measured velocity (V)
Vel_{fs}	full scale velocity (V)
V_{fs}	full scale output voltage (V)
V_o	zero velocity output voltage (V)
V_{out}	sensor output voltage (V)
w	width (m)
x	length (m)
x_i	x-coordinate of point *i* (m)
y	length (m)
y_i	y-coordinate of point *i* (m)
z	length (m)

Greek Symbols

α	thermal diffusivity (m^2/s)
Δh_{vap}	latent heat of vaporization (J/kg)
ΔI	uncertainty in current output (A)
ΔP	uncertainty in pressure measurement (Pa)
ΔP_{cal}	uncertainty in calibrated pressure transmitter (Pa)
ΔP_I	uncertainty in pressure measurement due to current source (K)

ΔR_{DAQ}	uncertainty in electrical resistance measurement of DAQ (ohm)
ΔR_I	uncertainty in electrical resistance due to current source (ohm)
ΔT	uncertainty in temperature measurement (K)
ΔT_{cal}	uncertainty in calibrated temperature sensor (K)
ΔT_{DAQ}	uncertainty in temperature measurement due to the DAQ (K)
ΔT_{dp}	uncertainty in dew-point temperature measurement (K)
$\Delta T_{dp,cal}$	uncertainty in calibrated dew-point sensor (K)
$\Delta T_{dp,I}$	uncertainty in dew-point measurement due to current source (K)
ΔT_I	uncertainty in temperature measurement due to current source (K)
ΔV_{DAQ}	uncertainty in voltage measurement of DAQ (V)
ΔVel	uncertainty in velocity measurement (m/s)
ΔVel_{cal}	uncertainty in calibrated velocity sensor (m/s)
ΔVel_V	uncertainty in velocity due to voltage uncertainty (m/s)
ΔV_{out}	uncertainty in output voltage measurement (V)
$\delta T_{wb,m}$	error in the measurement of the true wet-bulb temperature (K)
δ_t	thermal boundary layer thickness (m)
$\delta_{t,sh}$	thermal boundary layer thickness extending from shield (m)
$\delta_{t,wb}$	thermal boundary layer thickness extending from sensor (m)
ε_i	emissivity of surface *i* (-)
ϕ	azimuthal angle (rad)
μ	viscosity (kg/m-s)
θ	angle (rad)
	polar angle (rad)
ρ	density (kg/m^3)
σ	Stefan-Boltzmann constant (5.67 x 10^{-8} W/m^2-K^4)
ν	kinematic viscosity (m^2/s)

Chapter 1 – Introduction

1.1 Measuring the Moisture Content of Air

Accurately measuring the moisture content of air is necessary in order to accurately determine the thermodynamic state of moist air. Moist air is a mixture of water vapor and dry air, thus it is not a pure substance. To determine the thermodynamic state of moist air, three independent properties are required. One property that is nearly always used to fix the state of moist air is total pressure. The two remaining properties could include combinations of dry bulb temperature, dew point temperature (or humidity ratio), wet bulb temperature, and relative humidity. Determining the dry bulb temperature of moist air is relatively straightforward but determining the moisture content of air is more difficult. Some ways in which to conduct these moisture measurements are through the use of devices such as a gravimetric hygrometer, a chilled mirror dew-point hygrometer, or an aspirated psychrometer. The primary objective of the research outlined in this report is to design, construct, and demonstrate an aspirated psychrometer device that can accurately measure wet-bulb temperature. The accurate measurement of the moisture content of air is important for many applications and in particular supports the Heating, Ventilation, Air-Conditioning, and Refrigeration (HVAC&R) industry.

1.1.1 Gravimetric Hygrometer

The gravimetric hygrometer is a primary standard for the measurement of water vapor in air (Wiederhold, 1997). A gravimetric hygrometer relies on the fundamental principles and the base units of measurement. At the National Institute of Standards and Testing (NIST) a

gravimetric hygrometer is used for the fundamental measurement of the concentration of water vapor in air. A gravimetric hygrometer works by separating water from the moist air stream by passing it through a desiccant. By accurately measuring the volume of dry air passed through the desiccant along with the mass of water absorbed, a fundamental measurement of the humidity can be made.

The gravimetric hygrometer has the advantage of being a very accurate and repeatable instrument. Unfortunately the gravimetric hygrometer is a large and cumbersome instrument that is very time consuming to use. Gravimetric hygrometers are expensive to build and can be expensive to operate because of the long sample times required for accurate results at low humidity levels. For these reasons the gravimetric hygrometer is not a practical option for most lab or field measurements.

1.1.2 Chilled Mirror Dew-Point Hygrometer

A chilled mirror hygrometer is an instrument used to measure the dew-point temperature of moist air. In this device, a mirror is carefully cooled until water vapor from the air begins to condense on its surface. Typically an electro-optic detection system is used to detect the formation of condensate on the chilled mirror surface. Once condensate is formed on the mirror surface, the temperature is controlled to maintain a certain thickness of condensation on the mirror at all times.

Like the gravimetric hygrometer, the chilled mirror hygrometer also relies on fundamental principles by directly measuring the dew-point temperature of moist air, and as a result is

very accurate. Chilled mirror hygrometers offer the advantage of being smaller and more compact than the gravimetric hygrometer and can be used for a wide array of applications. The drawbacks of the chilled mirror hygrometer include the importance of keeping the mirror surface clean, controlling the air flow across the sensor, and the high cost associated with the initial purchase.

1.1.3 Aspirated Psychrometer

An aspirated psychrometer measures the moisture content of air by simultaneously measuring both the wet- and dry-bulb temperature of an air stream. The psychrometer consists of two thermometers. The sensing element of one thermometer is dry (dry-bulb) whereas the sensing element of the other thermometer is wet (wet-bulb). In order to maintain liquid water at the surface of the wet-bulb sensor, a cotton wicking material continuously pulls makeup water from a water reservoir by capillary action. In the case of the aspirated psychrometer, the moist air stream is forced to flow over both the wet- and dry-bulb sensors (i.e., they are ventilated at a defined rate). With this information the moisture content of an air stream can be determined.

The benefit of an aspirated psychrometer is that the instrument can be constructed with relatively low expense and the device is simple to build in comparison with the other devices previously described. An aspirated psychrometer is also compact and portable whereas other instruments can be large and cumbersome making them difficult to apply to field measurements. As a result, an aspirated psychrometric measurement is the most cost effective technique for the experimental measurement of moisture content during the testing

of HVAC&R equipment. The biggest drawback of the aspirated psychrometer in comparison to an instrument such as a gravimetric hygrometer or a chilled mirror dew-point hygrometer is the reduced accuracy of the device. One objective of this research is to quantify the accuracy and repeatability of such a device over a range of moist air conditions.

1.2 Wet-Bulb Temperature

The wet-bulb temperature (T_{wb}) is often used interchangeably with the adiabatic saturation temperature (T_{as}), although they are defined differently. The "adiabatic saturation temperature" is the temperature obtained by the moist air when it is adiabatically brought to saturation by the evaporation of liquid water. The adiabatic saturation temperature is sometimes referred to as the "thermodynamic wet-bulb temperature" and it can be computed based solely on the thermodynamic properties of moist air and liquid water. The "wet-bulb temperature," on the other hand, is the steady-state temperature achieved by a wetted temperature sensor; this is the temperature at which the rate of energy gained by convection is exactly balanced by the rate of energy lost by evaporation. The wet-bulb and adiabatic saturation temperatures are quite similar for a wide range of conditions for an air-water mixture at atmospheric pressure.

1.2.1 True Wet-Bulb Temperature

The heat and mass transfer approach taken to determine the true wet-bulb temperature is outlined below, as described in Nellis and Klein (2009). The "true wet-bulb temperature" is the temperature reached by a wet-bulb sensor exposed to a stream of moist air in the absence of any external parasitic heat transfer not related to convection. As mentioned previously,

the true wet-bulb temperature found using this approach is the temperature at which the convective heat gain directly balances out the evaporative heat loss of the sensor.

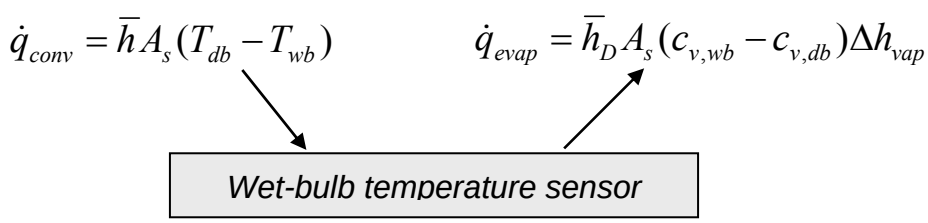

Figure 1-1: Heat transfer mechanisms occurring at the wet-bulb temperature sensing element.

An energy balance on the wet-bulb temperature sensor in Figure 1-1 gives:

$$\dot{q}_{conv} = \dot{q}_{evap} \tag{1.2.1}$$

where $\dot{q}_{conv}$ is the convective heat gain of the sensor and $\dot{q}_{evap}$ is the evaporative heat loss of the sensor. Substituting the mechanisms of heat transfer into Eq. (1.2.1):

$$\bar{h} A_s (T_{db} - T_{wb}) = \bar{h}_D A_s (c_{v,wb} - c_{v,db}) \Delta h_{vap} \tag{1.2.2}$$

where $\bar{h}$ is the heat transfer coefficient experienced on the outside of the sensor, A_s is the surface area of the sensor, T_{db} is the dry-bulb temperature, T_{wb} is the wet-bulb temperature, $\bar{h}_D$ is the mass transfer coefficient, $c_{v,wb}$ is the concentration of water vapor at the wet-bulb temperature, $c_{v,db}$ is the concentration of water vapor at the dry-bulb temperature, and Δh_{vap} is the latent heat of vaporization at the wet-bulb temperature. Solving for the wet-bulb temperature:

$$T_{wb} = T_{db} - \frac{\overline{h}_D}{\overline{h}}\left(c_{v,wb} - c_{v,db}\right)\Delta h_{vap} \tag{1.2.3}$$

As shown in Eq. (1.2.3), the wet-bulb temperature is determined from the dry-bulb temperature, the ratio of the mass to heat transfer coefficients, the concentration gradient driving the evaporation process, and the latent heat of vaporization of water from the wet-bulb sensor.

1.2.2 Measured Wet-Bulb Temperature

The measured wet-bulb temperature is determined in the same manner in which the true wet-bulb temperature is found. However, in any real measurement device there will be a parasitic heat transfer to the wet-bulb temperature sensor that will cause the measured wet-bulb temperature to deviate from the true wet-bulb temperature. Figure 1-2 indicates the actual mechanisms of heat transfer experienced by a wet-bulb temperature sensor.

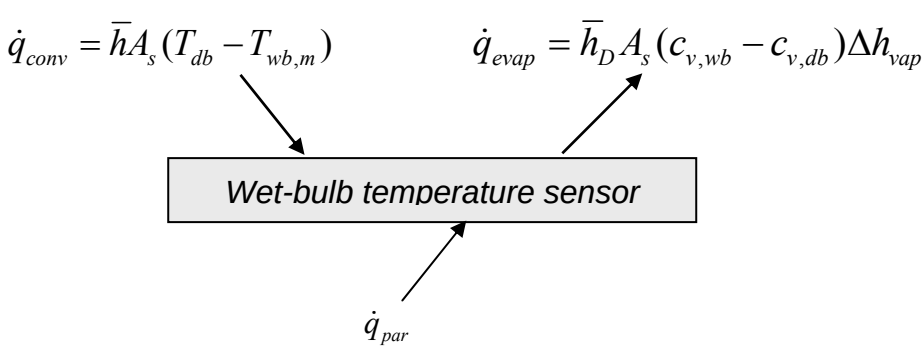

Figure 1-2: Heat transfer mechanisms occurring at the wet-bulb temperature sensing element with the inclusion of miscellaneous parasitic gains.

Similarly to Eq. (1.2.2), an energy balance on the wet-bulb temperature sensor gives:

$$\overline{h}A_s(T_{db} - T_{wb,m}) + \dot{q}_{par} = \overline{h}_D A_s(c_{v,wb} - c_{v,db})\Delta h_{vap} \tag{1.2.4}$$

The only difference between Eq. (1.2.2) and (1.2.4) is the additional term, $\dot{q}_{par}$ in Eq. (1.2.4), that is used to represent the parasitic heat transfers to the sensor. Solving Eq. (1.2.4) for the measured wet-bulb provides:

$$T_{wb,m} = T_{db} - \frac{\overline{h}_D}{\overline{h}}\left(c_{v,wb} - c_{v,db}\right)\Delta h_{vap} + \frac{\dot{q}_{par}}{\overline{h}A_s} \tag{1.2.5}$$

The measured wet-bulb temperature differs from the true wet-bulb temperature by an amount $\delta T_{wb,m}$, where:

$$\delta T_{wb,m} = \frac{\dot{q}_{par}}{\overline{h}A_s} \tag{1.2.6}$$

The focus of the research presented in this report deals with techniques to minimize or at least control $\delta T_{wb,m}$, allowing for the true wet-bulb temperature to be more closely determined by the measured wet-bulb temperature.

1.3 Research Objectives

As stated previously, the objective of the research is to reduce uncertainty in wet-bulb temperature measurements obtained from an aspirated psychrometer device. ASHRAE Standard 41.6-1994 (RA 2006) and ASHRAE Standard 41.1-1986 (RA 1991) discuss, in detail, the manner in which to construct an aspirated psychrometer that is capable of measuring the wet-bulb temperature to within ±0.1°C. This research aims to improve upon the techniques for measuring wet bulb using an aspirated psychrometer with the ultimate goal

of designing a psychrometer that is capable of measuring the wet-bulb temperature to within ±0.05°C.

In working to reduce the uncertainty in the measurement of the wet-bulb temperature, analytical models of the heat transfer mechanisms occurring at the wet-bulb temperature sensing element are developed. These analytical models are used to determine which parameters have the largest impact on the accuracy of the wet-bulb temperature measurement. The analytical models are then used to optimize the design in order to reduce the parasitic to an acceptable level. An experimental testing apparatus is constructed based on the optimized design in order to verify the accuracy of the models over a range of test conditions and quantify the actual accuracy of the device. The experimental test apparatus is also used to determine the impact of various other parameters on the measurement of the wet-bulb temperature (e.g. duct size, well water temperature, velocity non-uniformities, surroundings temperature, etc.). It is our hope that this process has clarified the true accuracy of the aspirated psychrometer and identified those parameters that have the largest impact on the accuracy of the device.

Chapter 2 – Parasitic Budget

To measure the wet-bulb temperature as accurately as possible, the parasitic heat transfer to the sensor must be minimized. The parasitic heat transfer, undoubtedly, cannot be eliminated but it will be important to consider and quantify the various mechanisms that contribute to parasitic heat transfer so steps can be taken to minimize them to the greatest extent possible. As the parasitic heat gain increases, a greater difference between the observed wet-bulb temperature and the true wet-bulb temperature will occur. With a goal of minimizing this difference (error) in wet-bulb temperature, a *parasitic budget*, is established. The *parasitic budget* represents the maximum amount of parasitic heat transfer to the sensor that can be tolerated while limiting the error in the wet-bulb temperature measurement to a specified level.

Referring back to Eq. (1.2.6), there appears to be two direct approaches that can be applied to minimize the wet-bulb temperature measurement error: by increasing the heat transfer coefficient to the temperature sensor and by increasing the area of the sensor. Somewhat confounding is that an increase in either of these parameters, may result in an increase in the parasitic heat gain to the sensor. As the area of the sensor is increased, the parasitic heat transfer to the sensor as a result of radiation increases; the accuracy improvement resulting from the increased area is then offset by the increase in the parasitic. Similarly if the velocity of the air used to aspirate the psychrometer is increased to increase the heat transfer coefficient, the sensor is more susceptible to dry out, leading to an increase in the parasitic

heat gain by conduction through the sensor sheath and lead wires. The heat transfer coefficient can be altered in ways other than by increasing the velocity across the sensor.

One way the heat transfer coefficient can be enhanced is by establishing a favorable orientation of the temperature sensor, relative to the air flow across the sensor. ASHRAE Standard 41.6 (2006) outlines a procedure for measuring the wet-bulb temperature using a temperature sensor oriented in either the axial or transverse direction. The transverse orientation is shown in Figure 2-1.

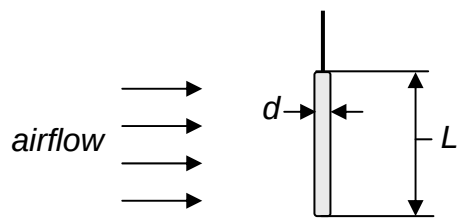

Figure 2-1: Temperature sensor positioned in the transverse orientation.

As shown in the figure, the transverse orientation refers to a sensor which is oriented with the length of the sensor perpendicular to the air flow. The axial orientation is one in which the sensor is aligned parallel with the air flow as shown in Figure 2-2.

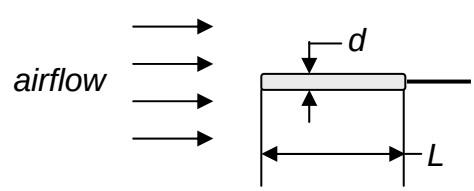

Figure 2-2: Temperature sensor positioned in the axial orientation.

This chapter documents procedures for calculating the parasitic budget for a temperature sensor in both a transverse and an axial orientation. The two orientations are compared and recommendations for minimizing measurement error are provided.

2.1 Transverse Flow Configuration

In this section, a detailed description of the calculation of the parasitic budget for a temperature sensor oriented in the transverse flow configuration is provided. The initial target uncertainty in the wet-bulb temperature is ±0.05°C. The temperature sensor modeled here is of standard size with a length (L) of 30.5 mm (1.2 in) and a diameter (d) of 6.35 mm (0.25 in). The nominal psychrometric condition considered in this preliminary analysis is a dry-bulb temperature (T_{db}) of 26.7°C and a wet-bulb temperature (T_{wb}) of 19.4°C. The free stream air velocity (u_∞) is 4 m/s and the pressure (P) is at standard atmospheric. These parameters are entered into Engineering Equation Solver (EES) (Klein 2010) as shown below.

```
$TabStops 0.2 0.4 0.6 0.8 3.5 in
$UnitSystem SI MASS RAD K PA J

"Inputs"
T_db_c=26.7[C]                                  "dry-bulb temp C"
T_db=converttemp(C,K,T_db_c)                    "dry-bulb temp K"
T_wb=converttemp(C,K,19.4[C])                   "wet-bulb temp"
d=0.25[inch]*convert(inch,m)                    "sensor diameter"
L=1.2[inch]*convert(inch,m)                     "sensor length"
u_inf=4[m/s]                                    "free stream air velocity"
P=101325[Pa]                                    "atmospheric pressure"
```

The relative humidity (RH) corresponding to T_{db} of 26.7°C and T_{wb} of 19.4°C is also specified. To determine the state of the moist air stream, the dry-bulb temperature, relative

humidity, and absolute pressure are specified. The moist air property relationship used in EES is based on a correlation developed by Hyland and Wexler (1983).

```
RH=0.515572785 [-]                                    "relative humidity"
```

The properties of the free stream air are now determined using the internal property routines in EES. The three properties used to specify the state of the moist air stream flowing over the temperature sensor are the film temperature (T_{film}), the air pressure, and the relative humidity of the stream.

$$T_{film} = \frac{T_{wb} + T_{db}}{2} \tag{2.1.1}$$

From this information the density (ρ), conductivity (k), viscosity (μ), and specific heat capacity (c_p) are determined.

```
T_film=(T_wb+T_db)/2                                  "film temperature"
rho=density(AirH2O,T=T_film,P=P,R=RH)                 "density"
k=conductivity(AirH2O,T=T_film,P=P,R=RH)              "conductivity"
mu=viscosity(AirH2O,T=T_film,P=P,R=RH)                "viscosity"
c_p=CP(AirH2O,T=T_film,P=P,R=RH)                      "specific heat capacity"
```

The internal function **D_12_gas** in EES is used to find the diffusion coefficient ($D_{w,a}$) of water vapor in air, at the film temperature and atmospheric pressure. The correlation for the diffusion coefficient is based on the Chapmann-Enskog relationship presented in Poling et al. (2000).

```
D_w_a=D_12_gas('H2O','Air',T_film,P)                  "diffusion coefficient"
```

The latent heat of vaporization (Δh_{vap}) of water is evaluated at the wet-bulb temperature and is calculated by:

$$\Delta h_{vap} = h_{T=T_{WB},x=1} - h_{T=T_{WB},x=0} \tag{2.1.2}$$

```
Dh_vap=enthalpy(Water,x=1,T=T_wb)-enthalpy(Water,x=0,T=T_wb) "latent heat of vaporization"
```

The kinematic viscosity (ν) and the thermal diffusivity (α) of the free stream air are calculated by:

$$\nu = \frac{\mu}{\rho} \tag{2.1.3}$$

$$\alpha = \frac{k}{\rho c_p} \tag{2.1.4}$$

```
nu=mu/rho                                   "kinematic viscosity"
alpha=k/(rho*c_p)                           "thermal diffusivity"
```

With this information the Prandtl (Pr), Schmidt (Sc), and Reynolds (Re) numbers are computed.

$$\mathrm{Pr} = \frac{\nu}{\alpha} \tag{2.1.5}$$

$$\mathrm{Sc} = \frac{\nu}{D_{w,a}} \tag{2.1.6}$$

$$\mathrm{Re} = \frac{u_\infty d \rho}{\mu} \tag{2.1.7}$$

```
Pr=nu/alpha                                    "Prandtl number"
Sc=nu/D_w_a                                    "Schmidt number"
Re=u_inf*d*rho/mu                              "Reynolds number"
```

The Reynolds and Prandtl numbers are used to find the Nusselt number using the internal function **External_Flow_Cylinder_ND** in EES. This function is based on the Churchill and Bernstein (1977) correlation to determine the Nusselt number. From the Nusselt number, the average heat transfer coefficient ($\bar{h}$) on the outside of the cylindrical temperature sensor is calculated.

$$\bar{h} = \frac{Nusselt\ k}{d} \tag{2.1.8}$$

With the average heat transfer coefficient, the rate of convective heat gain to the wet-bulb temperature sensor can be found by:

$$\dot{q}_{conv} = h\pi dL(T_{db} - T_{wb}) \tag{2.1.9}$$

```
Call External_Flow_Cylinder_ND(Re,Pr:Nusselt,C_d1)   "Nusselt number"
h=Nusselt*k/d                                        "heat transfer coefficient"
q_dot_conv=h*pi*d*L*(T_db-T_wb)                      "convective heat transfer"
```

The next step is to determine the rate of evaporative heat transfer from the wet-bulb sensor. The first step is to calculate the Sherwood number (Sh). Sometimes referred to as the "Nusselt number for mass transfer," the Sherwood number represents the ratio of convective to diffusive mass transport. The Sherwood number for the wet bulb temperature sensor is found from the Reynolds and Schmidt numbers, again using a correlation developed by

Churchill and Bernstein (1977). The Sherwood number and the diffusion coefficient are used to calculate the mass transfer coefficient ($\bar{h}_D$).

$$\bar{h}_D = \frac{\mathrm{Sh}\, D_{w,a}}{d} \tag{2.1.10}$$

```
Call External_Flow_Cylinder_ND(Re,Sc:Sh,C_d2)          "Sherwood number"
h_D=Sh*D_w_a/d                                         "mass transfer coefficient"
```

Before the rate of heat loss due to evaporation is calculated, the mass transfer of vapor from the wet-bulb sensor is determined. The mass transfer of moisture occurring from the wet bulb sensor is the result of a concentration gradient of water on the wetted sock covering the temperature sensor to the free stream of air moving across the sensor. To find the concentration of water vapor in the free stream air, the partial pressure of water vapor in the free stream air is determined. This is done by knowing:

$$P_{v,db} = RH\ P_{s,db} \tag{2.1.11}$$

where $P_{v,db}$ is the partial pressure of water vapor in the free stream air, and $P_{s,db}$ is the pressure of water vapor in a saturated air stream at the dry-bulb temperature. The RH is already known and the saturation water vapor pressure at T_{db} is computed using the internal property routines in EES.

```
P_v_db=RH*pressure(Water,T=T_db,x=1)                   "vapor pressure- free stream"
```

The concentration of water vapor in the free stream is the density of water at the partial pressure previously computed and the dry-bulb temperature. The concentration of water

vapor at the wet-bulb is simply the density of saturated water vapor (i.e. quality of 1) at the wet-bulb temperature.

```
c_v_db=density(Water,P=p_v_db,T=T_db)          "concentration- free stream"
c_v_wb=density(Water,T=T_wb,x=1)               "concentration- wet-bulb"
```

Assuming the concentration of water vapor over the wet bulb temperature sensor surface is constant, the mass transfer of water ($\dot{m}_{evap}$) from the surface of the wetted temperature sensor to the free stream air can then be determined by:

$$\dot{m}_{evap} = \pi \; d \; L \; \overline{h}_D \; (c_{v,wb} - c_{v,db}) \tag{2.1.12}$$

The heat transfer from the wet-bulb associated with this evaporation ($\dot{q}_{evap}$) is:

$$\dot{q}_{evap} = \dot{m}_{evap} \Delta h_{vap} \tag{2.1.13}$$

```
m_dot_evap=pi*d*L*h_D*(c_v_wb-c_v_db)          "mass transfer"
q_dot_evap=m_dot_evap*Dh_vap                   "evaporative heat transfer"
```

At this point, the wet-bulb temperature is removed from the EES code and $\dot{q}_{evap}$ is set equal to $\dot{q}_{conv}$. When this is done and the code is run and T_{wb} is equal to 19.4°C, which ensures that all of the inputs are entered correctly.

To model the actual wet bulb temperature sensor, consideration of additional mechanisms of heat transfer is necessary. The sum of additional sources of heat transfer is referred to as the parasitic heat transfer ($\dot{q}_{par}$) and consists of a group of parasitic heat transfers to the wet-bulb

that includes: radiation, conduction through temperature sensor leads, along with other possible mechanisms. With the parasitic heat transfer to the wet-bulb sensor, the energy balance becomes:

$$\dot{q}_{evap} = \dot{q}_{conv} + \dot{q}_{par} \tag{2.1.14}$$

The objective is to determine the limit in parasitic heat transfer to the wet-bulb temperature sensor allowed to limit the error in the wet-bulb temperature measurement to within 0.05°C. To do this the difference between the wet-bulb temperature calculated, and the true wet-bulb temperature (i.e. 19.4°C) is set to 0.05°C. When this is done the parasitic heat gain of the temperature sensor corresponding to an error in the wet-bulb temperature measurement of 0.05°C is found.

```
q_dot_evap=q_dot_conv+q_dot_par          "energy balance"
DELTA_wb=0.05[C]                         "set error in wet-bulb temp"
T_wb_C=converttemp(K,C,T_wb)             "wet-bulb temp in C"
DELTA_wb=T_wb_C-19.4[C]                  "error in wet-bulb temp"
```

With the parameters as specified, the limit in parasitic heat transfer for this psychrometric condition is $\dot{q}_{par} = 7.54 \text{ mW}$. This means is that, for the given temperature sensor exposed to air at a velocity of 4 m/s, the parasitic heat transfer to the wet-bulb must be kept below 7.54 mW to be able to measure the wet-bulb temperature within 0.05°C at the nominal test condition of 26.7°C/19.4°C.

With a larger budget for parasitic heat transfer, it is easier for the temperature sensor to measure the wet-bulb temperature within the desired accuracy of 0.05°C. One way to

increase the parasitic budget is to increase the velocity of air across the sensor. Figure 2-3 shows the allowable parasitic heat gain to the wet-bulb temperature sensor over a range of air velocities with measured the wet-bulb temperature error as a parameter.

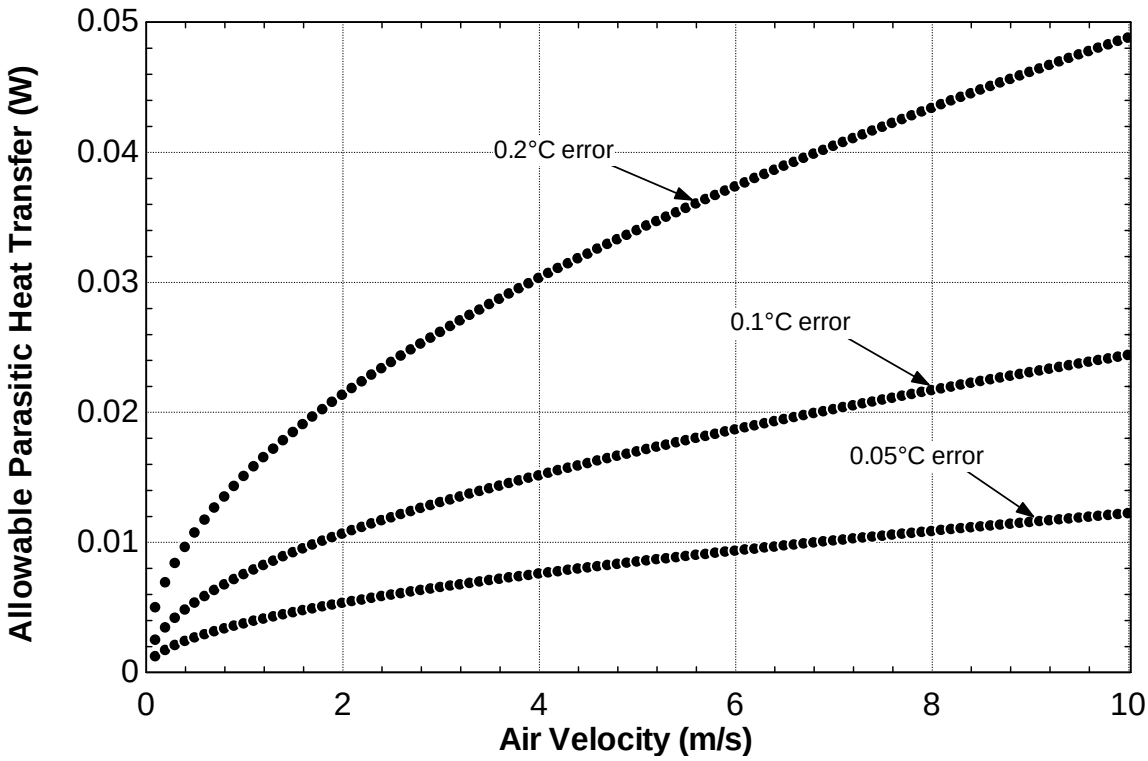

Figure 2-3: The allowable parasitic heat transfer to the wet-bulb temperature sensor oriented in a transverse configuration as a function of the air velocity over the sensor. As shown the three sets of data correspond to an error in the wet-bulb temperature measurement of 0.05°C, 0.1°C, and 0.2°C.

From Figure 2-3 it is clear that high air velocities provide a larger budget for parasitic heat transfer to the wet-bulb sensor. At an air velocity of 10 m/s, the wet-bulb sensor can tolerate a parasitic heat gain of 12.18 mW and still limit the error in wet-bulb temperature measurement to 0.05°C. However, there is an upper limit on the air velocity which is not shown in Figure 2-3. If the air velocity is too high, the water surrounding the wet-bulb temperature sensor in the wetted sock will evaporate too quickly and the temperature sensor

used to observe the wet-bulb temperature will begin to dry and no longer be capable of measuring the wet-bulb temperature.

2.2 Axial Flow Configuration

The allowable parasitic heat transfer to the wet-bulb temperature sensor is dependent on the sensor orientiation. That is, the allowable parasitic will be different for a sensor in a transverse configuration compared to one oriented in an axial configuration. The parasitic budget is calculated in exactly the same manner for both orientations with one exception. The exception is that the heat and mass transfer coefficients along the temperature sensor are approximated using the EES procedure **External_Flow_Plate_ND** for the axial orientation rather than the **External_Flow_Cylinder_ND** procedure, as was used for the transverse orientation. The **External_Flow_Plate_ND** function uses the Churchill and Ozoe (1973) correlation to determine the Nusselt and Schmidt numbers for flow over a flat plate. A detailed description of the calculation of the allowable parasitic budget for a temperature sensor in a transverse flow configuration is in found in the previous section.

Similar to the transverse configuration the allowable parasitic heat transfer to the wet-bulb temperature sensor increases with increasing air velocity. Figure 2-4 illustrates the parasitic heat transfer to the wet-bulb temperature sensor oriented axially and the corresponding wet bulb temperature sensor errors of 0.05°C, 0.1°C, and 0.2°C for air velocities ranging from 0 to 10 m/s.

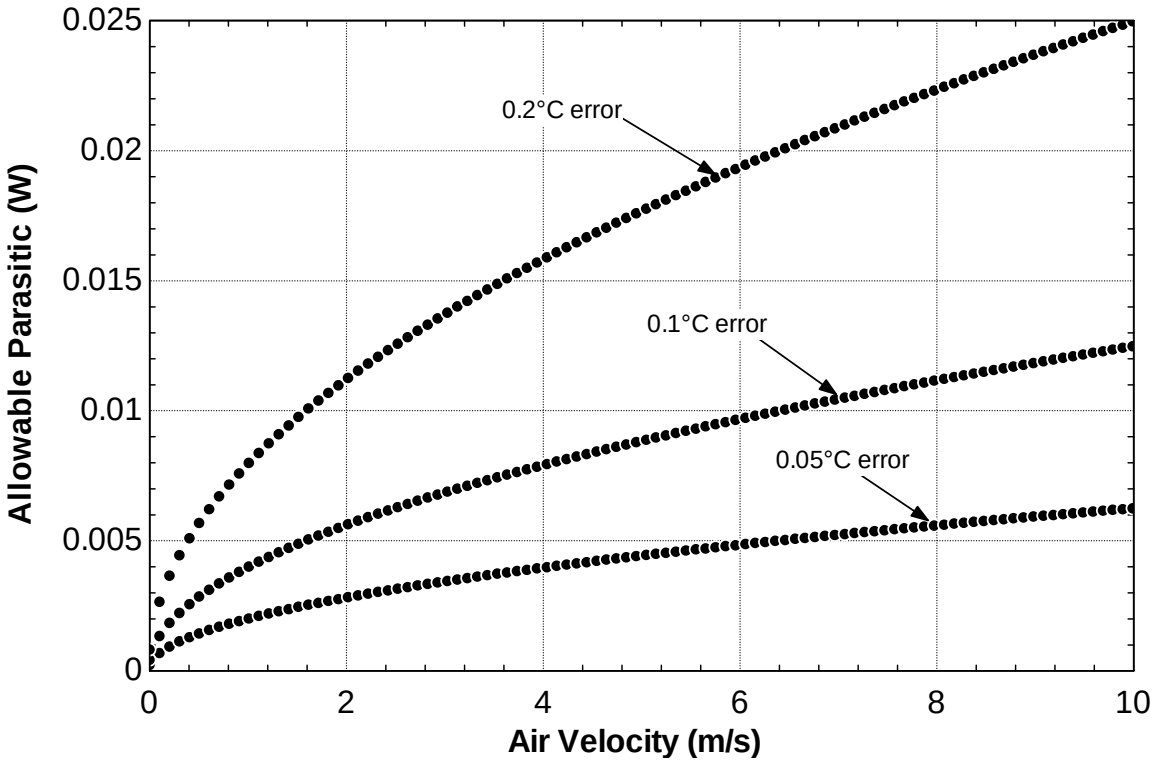

Figure 2-4: The allowable parasitic heat transfer to the wet-bulb temperature sensor oriented axially as a function of the air velocity over the sensor in an axial configuration. As shown the three sets of data correspond to an error in the wet-bulb temperature measurement of 0.05°C, 0.1°C, and 0.2°C.

At an air velocity of 4 m/s, the allowable parasitic heat transfer corresponding to an error in the wet-bulb temperature of 0.05°C is only 3.94 mW. The allowable parasitic can be increased from 3.94 mW to 6.24 mW by increasing the air velocity from 4 m/s to 10 m/s.

2.3 Flow Configuration Comparison

The parasitic budget calculations described previously in this chapter indicate the clear advantage of positioning the temperature probe in the transverse configuration. The allowable parasitic heat gain to the temperature sensor for a probe positioned in the transverse configuration is nearly two times that of a sensor in the axial flow orientation.

This is represented graphically in Figure 2-5 below for an error limit in the wet-bulb temperature measurement of 0.05°C.

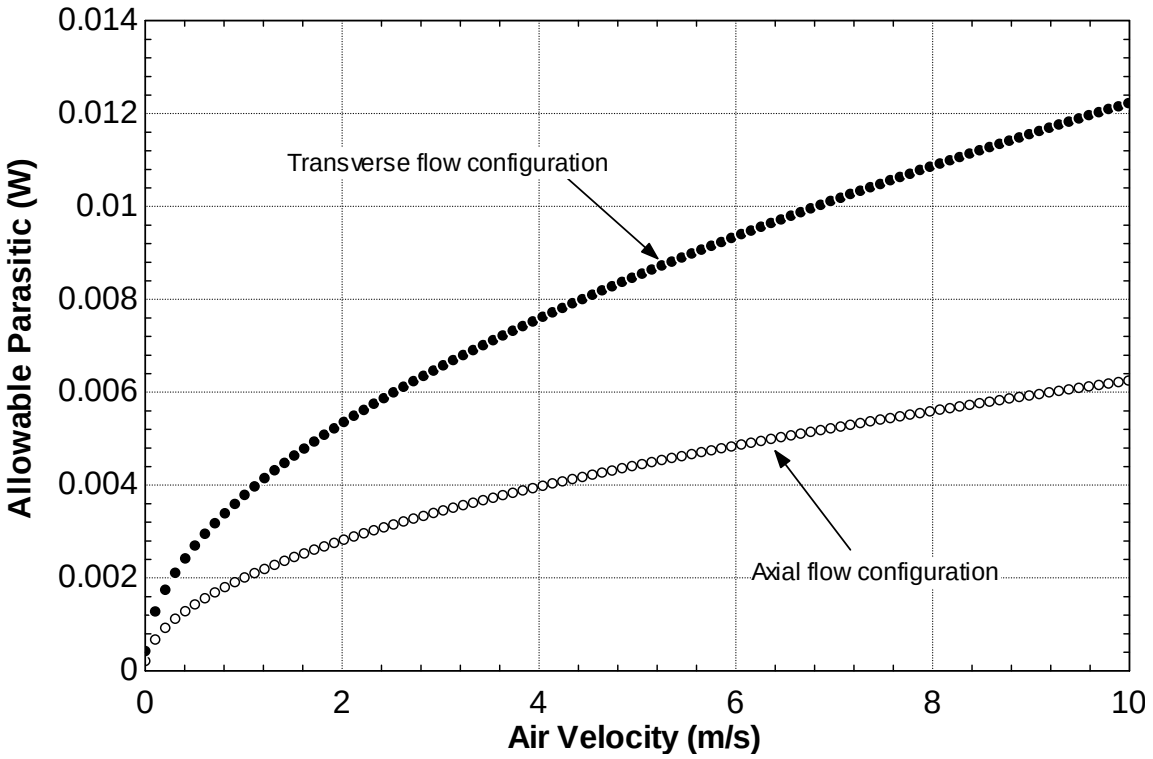

Figure 2-5: Allowable parasitic heat transfer to the temperature sensor as a function of air velocity for an error in the wet-bulb temperature measurement of 0.05°C.

The transverse flow configuration has a much higher parasitic budget than the axial flow configuration due to the higher heat transfer coefficient experienced by the sensor in the transverse configuration. Referring back to Eq. (1.2.6) it is clear why the higher heat transfer coefficient results in an increased parasitic budget.

Chapter 3 – Mechanisms Contributing to Parasitic Heat Transfer

The calculations outlined in Chapter 2 focused on determining the amount of parasitic heat transfer that the wet-bulb temperature sensor could tolerate while still maintaining an error in the wet-bulb temperature measurement of 0.05°C or less. This chapter will work to quantify the expected amount of parasitic heat transfer to the wet-bulb temperature sensor from a variety of sources including radiation, conduction through temperature sensor leads, and parasitic associated with the makeup water.

3.1 Radiation Parasitic- Transverse Configuration

Radiation heat transfer from the surrounding environment to the wet bulb temperature sensor will occur. To limit the parasitic effects associated with radiation, a radiation shield can be applied. The radiation parasitic model for a temperature sensor in a transverse orientation aims to quantify the amount of radiation parasitic the wet-bulb temperature sensor will receive. The geometry associated with the application of a radiation shield to the temperature sensor is shown in Figure 3-1.

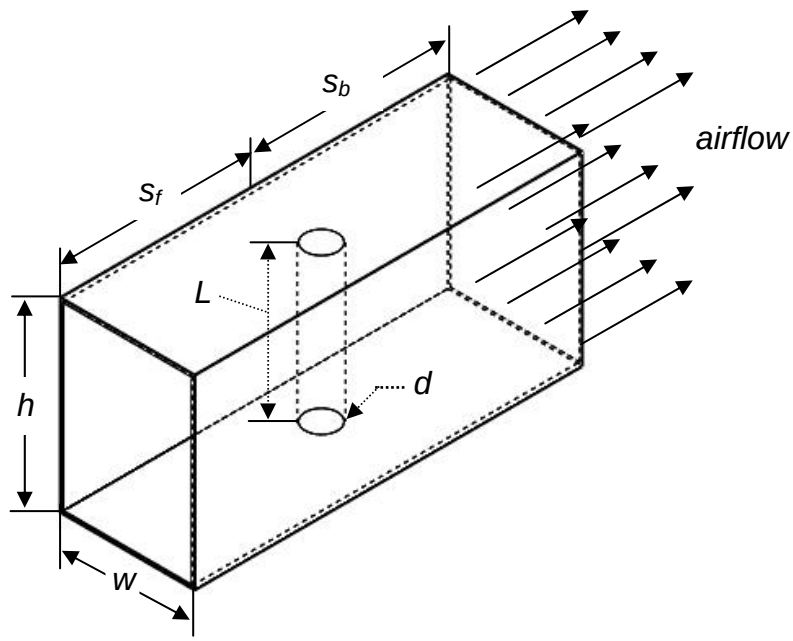

Figure 3-1: Isometric view of the radiation shield geometry modeled for the wet bulb temperature sensor in a transverse orientation.

The inside width of the shield is w and the height is h. The shield extends a distance s_f upstream of the temperature sensor and a distance s_b downstream of the centerline of the wet bulb temperature sensor. The wet bulb temperature sensor is modeled as a cylinder centered within the shield in both the width and height direction. The sensor has a diameter d and a length L.

The radiation parasitic is evaluated at a nominal test condition, test condition 1 (i.e. T_{wb} = 19.4°C, T_{db} = 26.7°C). These along with the other inputs are entered into EES as follows:

```
$TabStops 0.2 0.4 0.6 0.8 3.5 in
$UnitSystem SI MASS RAD K PA J


"Inputs"
T_db_c=26.7[C]                                  "dry-bulb temp C"
T_wb_c=19.4[C]                                  "wet-bulb temp C"
T_db=converttemp(C,K,T_db_c)                    "dry-bulb temp K"
```

```
T_wb=converttemp(C,K,T_wb_c)                    "wet-bulb temp K"
d=0.25[inch]*convert(inch,m)                    "sensor diameter"
L=1.2[inch]*convert(inch,m)                     "sensor length"
u_inf=4[m/s]                                    "air flow velocity"
```

The size of the temperature sensor used in the model is of common size (6.35 mm diameter) and consistent with the size sensor used in establishing the parasitic budget. The air velocity (u_∞) is what the current ASHRAE Standard 41.6 (2006) requires for a wet-bulb temperature sensor positioned in a transverse flow configuration, $u_\infty = 4$ m/s.

The width (w) for the radiation shield is established by considering the growth of the thermal boundary layer that extends from each side of the radiation shield. The thermal boundary layer needs to envelope the temperature sensor. An approximation for the distance in which a thermal boundary layer extends from a surface is given by Eq. (3.1.1) (Nellis and Klein, 2009):

$$\delta_t \approx 2\sqrt{\alpha t} \tag{3.1.1}$$

In Eq. (3.1.1) α is the thermal diffusivity and t is the time relative to the step change in surface conditions. The thermal diffusivity is calculated from the thermal conductivity (k), density (ρ), and specific heat capacity (c_p) of the free stream air.

$$\alpha = \frac{k}{\rho\, c_p} \tag{3.1.2}$$

These properties are found using the internal property routine in EES for a moist air stream with a film temperature (T_{film}) equal to the dry-bulb temperature, pressure (P) equal to standard atmospheric, and a relative humidity (RH) corresponding to that of test condition 1.

```
T_film=T_db                                          "film temp"
P=101325[Pa]                                         "atmospheric pressure"
RH=0.515572785[-]                                    "relative humidity"
k=conductivity(AirH2O,T=T_film,P=P,R=RH)             "conductivity"
rho=density(AirH2O,T=T_film,P=P,R=RH)                "density"
c_p=CP(AirH2O,T=T_film,P=P,R=RH)                     "specific heat capacity"
alpha=k/(rho*c_p)                                    "thermal diffusivity"
```

The time, relative to the step change in surface conditions (i.e. t in Eq. (3.1.1)), can be found by knowing the distance traveled by the thermal wave (x) and the free stream velocity of the fluid flow (u_∞).

$$t = \frac{x}{u_\infty} \tag{3.1.3}$$

In the EES model, x is replaced with s_f, the distance from the front of the shield to the temperature sensor. After a distance of s_f, the boundary layer has grown from the radiation shield to intersect the wet-bulb sensor. An intersection of the boundary layers downstream of the temperature sensor has no impact on the accuracy of the measurement.

```
t=s_f/u_inf                                          "time"
delta_T=2*sqrt(alpha*t)                              "thermal boundary layer thickness"
```

From δ_t, an appropriate limit for the width (w) of the shield is determined. The width (w) is set equal to the diameter of the temperature sensor (d) plus twice the thickness of the boundary layer (δ_t) at a distance of s_f. This corresponds to a shield width in which the

boundary layer extending from each side of the shield, parallel to the sensor, contacts the edge of the sensor at a distance of s_f from the front of the shield. Since the temperature sensor will have a very small boundary layer extending from it, this will only give an approximation of the width of the radiation shield. The actual limit on the width of the shield will be slightly larger.

$$w = 2\delta_t + d \tag{3.1.4}$$

```
w=2*delta_T+d                                    "width of shield"
```

A similar approach is taken to determine the minimum height (h) of the radiation shield. Twice the thermal boundary layer thickness (δ_t) is added to the length of the temperature sensor (L) to give an approximate limit on the minimum allowable height for the radiation shield.

$$h = 2\delta_t + L \tag{3.1.5}$$

```
h=2*delta_T+L                                    "height of shield"
```

It is important to keep the width (w) and the height (h) to a minimum to ensure that the temperature sensor radiates primarily to the low emissivity radiation shield and as little as possible to the high emissivity surroundings (i.e. the open ends of the shield). The previously described limits are the <u>minimum</u> dimensions for both the width (w) and height (h) of the radiation shield. The distance the shield extends upstream (s_f) and the distance in which the shield extends downstream (s_b) can be varied, however. For the initial calculation these

parameters are both set to an arbitrary value of 40 mm (1.6 in). The thickness of the shield (*th*) is also specified at a value of 0.5 mm (0.02 in).

```
s_f=40[mm]*convert(mm,m)                    "length of shield upstream"
s_b=40[mm]*convert(mm,m)                    "length of shield downstream"
th=0.5[mm]*convert(mm,m)                    "thickness of shield"
```

After specifying the parameters associated with the radiation shield, the surfaces participating in the radiation, along with their associated emissivity and area must be specified. The surface that is referred to as *surface 1* represents the entire external surface of the wet-bulb sensor. This consists of the cylindrical outer sheath of the sensor along with the two ends of the temperature sensor. The outside of the sensor will be covered with a white cotton sock that has an emissivity of 0.80 (Cole-Parmer). The 0.80 emissivity is based on a value given for white cotton, but is still a best guess estimate of the actual emissivity of a wet cotton sock.

```
"surface 1- temperature sensor"
A[1]=2*0.25*pi*d^2+pi*d*k                   "surface area"
epsilon[1]=0.8[-]                           "emissivity of cotton cloth"
```

Surface 2 is the entire interior surface of the radiation shield; this includes the top and bottom, as well as the two sides of the shield. For modeling purposes, the emissivity of *surface 2* is set to a value of 0.20, a value attainable with a range of materials including polished aluminum (Omega, 1998).

```
"surface 2- inside of the radiation shield"
A[2]=2*w*(s_f+s_b)+2*h*(s_f+s_b)            "surface area"
epsilon[2]=0.2[-]                           "emissivity"
```

The outside of the shield is *surface 3*. Similar to the inside of the shield this includes the top and bottom along with the two outer sides of the shield. The emissivity of this surface is also set to a value of 0.20.

```
"surface 3- outside of the radiation shield"
A[3]=2*(w+2*th)*(s_f+s_b)+2*(h+2*th)*(s_f+s_b)          "surface area"
epsilon[3]=0.2[-]                                        "emissivity"
```

Surfaces 1-3 are shown in Figure 3-2 below.

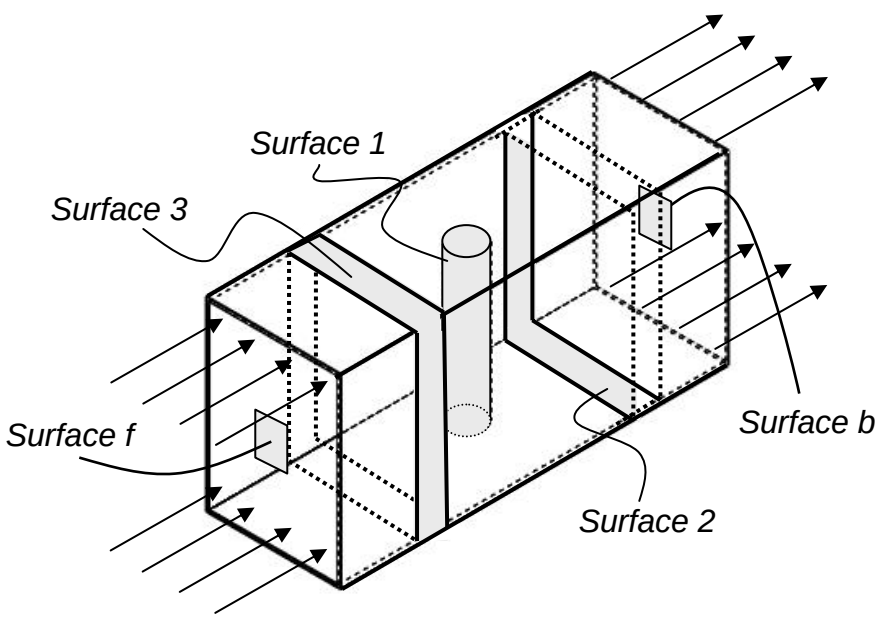

Figure 3-2: Isometric view of the radiation shield and temperature sensor with the surfaces labeled.

The final surface participating in the radiation exchange is *surface 4*. *Surface 4* is not shown in Figure 3-2, but it is composed of the surroundings outside of the shield. Without being able to quantify a specific size of the surroundings, *surface 4* is given an arbitrarily large area. The emissivity of the surroundings is assumed to be 0.95.

```
"surface 4- surroundings"
A[4]=1[m^2]                                    "arbitrarily large surface area"
epsilon[4]=0.95[-]                             "emissivity of surroundings"
```

Although *surfaces 1-4* are the only surfaces participating in the thermal radiation, two more surfaces are defined to simplify the computation of the necessary radiation view factors. The two additional surfaces specified are *surface f* and *surface b* corresponding to the upstream open face and downstream open face, respectively. Refer to Figure 3-2 to get a clearer understanding of *surface f* and *surface b*. Both of these surfaces are a part of the surroundings as such, they can be thought of as virtually closing the sensor's radiation shield.

```
A_f=h*w                                        "front open end"
A_b=h*w                                        "back open end"
```

With the surfaces defined the view factors are determined. The first view factors calculated correspond to the front open surface (*surface f*). *Surface f* is a flat surface with dimensions *w* x *h*. From inspection it is clear that the front surface will not see itself, thus $F_{f,f}$ is zero.

The view factor from the front surface to the back surface ($F_{f,b}$) is a view factor from a flat plate to a flat plate with a cylinder placed between. A Monte Carlo method for computing this radiation view factor is described in detail in Section 3.1.3 of this report. This view factor is implemented in EES as a function,**F3D_32.**

The next radiation view factor calculated is from the front surface (*surface f*) to the cylinder (*surface 1*). The view factor between these two surfaces, geometrically, is a view factor between a flat plate and a circular cylinder. The Monte Carlo method used to find this view

factor is described in Section 3.1.2 of this report. This view factor is also implemented as a function in EES as **F3D_31**.

The final surface seen by *surface f* is *surface 2* (i.e. the inside of the shield). Applying the enclosure rule:

$$F_{f,2} = 1 - F_{f,f} - F_{f,b} - F_{f,1} \tag{3.1.6}$$

```
"view factors"
F_f_f=0                                          "front to front"
F_f_b=F3D_32(w,h,d,k,s_f,s_b,100000)             "front to back"
F_f_1=F3D_31(w,h,d,k,s_f,100000)                 "front to surface 1"
F_f_2=1-F_f_b-F_f_1-F_f_f                        "front to surface 2"
```

With all of the view factors from *surface f* determined, the view factors from *surface b* is now determined. The view factors from *surface b* are computed in the exact same manner as those from *surface f* making certain to use the appropriate parameters. The view factors from *surface b* may be different than those from *surface f* because the shield may extend farther in the downstream direction than it does in the upstream direction (i.e. $s_b \neq s_f$). For this reason these two surfaces are treated as separate surfaces.

```
F_b_b=0                                          "back to back"
F_b_f=F3D_32(w,h,d,k,s_b,s_f,100000)             "back to front"
F_b_1=F3D_31(w,h,d,k,s_b,100000)                 "back to surface 1"
F_b_2=1-F_b_b-F_b_f-F_b_1                        "back to surface 2"
```

With all of the view factors computed for both the front and back surface, reciprocity is used to calculate the view factors from *surfaces 1* and *2* to *surfaces f* and *b*.

$$F_{1,\mathrm{f}} = \frac{A_\mathrm{f} F_{\mathrm{f},1}}{A_1} \tag{3.1.7}$$

$$F_{1,\mathrm{b}} = \frac{A_\mathrm{b} F_{\mathrm{b},1}}{A_1} \tag{3.1.8}$$

$$F_{2,\mathrm{f}} = \frac{A_\mathrm{f} F_{\mathrm{f},2}}{A_2} \tag{3.1.9}$$

$$F_{2,\mathrm{b}} = \frac{A_\mathrm{b} F_{\mathrm{b},2}}{A_2} \tag{3.1.10}$$

```
F_1_f=A_f*F_f_1/A[1]                    "surface 1 to front"
F_1_b=A_b*F_b_1/A[1]                    "surface 1 to back"
F_2_f=A_f*F_f_2/A[2]                    "surface 2 to front"
F_2_b=A_b*F_b_2/A[2]                    "surface 2 to back"
```

The view factors from *surface 1* (i.e. the temperature sensor) are now computed. With *surface 1* being a circular cylinder it can undoubtedly not see itself. Thus, the view factor $F_{1,1}$ is zero. The view factor $F_{1,3}$ is also determined by inspection to be zero, since the temperature sensor cannot see the outside surface of the radiation shield.

The two remaining view factors are $F_{1,2}$ and $F_{1,4}$. The view factor from the temperature sensor to the surroundings ($F_{1,4}$) is the sum of the view factors from *surface 1* to *surface f* and from *surface 1* to *surface b*.

$$F_{1,4} = F_{1,\mathrm{f}} + F_{1,\mathrm{b}} \tag{3.1.11}$$

This is because all of the radiation seen by the temperature sensor (*surface 1*) from the surroundings (*surface 4*) occurs through the front and back open surfaces. By knowing $F_{1,4}$ three of the four view factors are known and $F_{1,2}$ is determined by the enclosure rule.

$$F_{1,2} = 1 - F_{1,1} - F_{1,3} - F_{1,4} \tag{3.1.12}$$

```
F[1,1]=0                                    "surface 1 to surface 1"
F[1,2]=1-F[1,1]-F[1,3]-F[1,4]               "surface 1 to surface 2"
F[1,3]=0                                    "surface 1 to surface 3"
F[1,4]=F_1_f+F_1_b                          "surface 1 to surface 4"
```

Moving on to *surface 2*, the view factor $F_{2,1}$ is immediately known by reciprocity:

$$F_{2,1} = \frac{A_1 F_{1,2}}{A_2} \tag{3.1.13}$$

Similarly to *surface 1* the view factor from *surface 2* to the surroundings ($F_{2,4}$) is:

$$F_{2,4} = F_{2,\mathrm{f}} + F_{2,\mathrm{b}} \tag{3.1.14}$$

Again all of the radiation "seen" by the inside surface of the shield (*surface 2*) from the surroundings (*surface 4*) is through the front and back open sections of the radiation shield.

$F_{2,3}$ is determined by inspection to be zero- the inside of the radiation shield cannot see the outside surface of the radiation shield. By knowing three of the four view factors the remaining view factor is calculated with the use of the enclosure rule.

$$F_{2,2} = 1 - F_{2,1} - F_{2,3} - F_{2,4} \tag{3.1.15}$$

```
F[2,1]=A[1]*F[1,2]/A[2]                    "surface 2 to surface 1"
F[2,2]=1-F[2,1]-F[2,3]-F[2,4]              "surface 2 to surface 2"
F[2,3]=0                                   "surface 2 to surface 3"
F[2,4]=F_2_f+F_2_b                         "surface 2 to surface 4"
```

All of the view factors from *surface 3* can be determined by inspection. $F_{3,1}$ is the view factor from the outside of the radiation shield to the temperature sensor. It is equal to zero because the outside of the radiation shield cannot see the temperature sensor. $F_{3,2}$ is also zero because the outside of the radiation shield cannot see the inside of the shield. $F_{3,3}$ is zero since the outside of the shield is unable to see itself. Finally, by the enclosure rule or simply by inspection, $F_{3,4}$ is one.

```
F[3,1]=0                                   "surface 3 to surface 1"
F[3,2]=0                                   "surface 3 to surface 2"
F[3,3]=0                                   "surface 3 to surface 3"
F[3,4]=1                                   "surface 3 to surface 4"
```

By knowing all of the view factors from *surfaces 1-3* the view factors from *surface 4* can be determined. By reciprocity:

$$F_{4,1} = \frac{A_1 F_{1,4}}{A_4} \tag{3.1.16}$$

$$F_{4,2} = \frac{A_2 F_{2,4}}{A_4} \tag{3.1.17}$$

$$F_{4,3} = \frac{A_3 F_{3,4}}{A_4} \tag{3.1.18}$$

From the enclosure rule:

$$F_{4,4} = 1 - F_{4,1} - F_{4,2} - F_{4,3} \tag{3.1.19}$$

```
F[4,1]=A[1]*F[1,4]/A[4]                                  "surface 4 to surface 1"
F[4,2]=A[2]*F[2,4]/A[4]                                  "surface 4 to surface 2"
F[4,3]=A[3]*F[3,4]/A[4]                                  "surface 4 to surface 3"
F[4,4]=1-F[4,1]-F[4,2]-F[4,3]                            "surface 4 to surface 4"
```

With all of the view factors and areas known for each surface, a systematic approach is taken to solve the diffuse, gray surface radiation problem at hand. The net rate of radiation exchange from surface *i* to itself and the other three surfaces is found by (Nellis and Klein, 2009):

$$\dot{q}_i = \frac{\varepsilon_i A_i (E_{b,i} - J_i)}{(1-\varepsilon_i)} \text{ for } i = 1...4 \tag{3.1.20}$$

where ε_i is the emissivity of surface *i*, A_i is the area of surface *i*, $E_{b,i}$ is the blackbody emissive power of surface *i*, and J_i is the radiosity of surface *i*. An energy balance for each radiosity node is also needed.

$$\dot{q}_i = A_i \sum_{j=1}^{4} F_{i,j} (J_i - J_j) \text{ for } i = 1...4 \tag{3.1.21}$$

To implement these energy balances in EES a duplicate loop is used:

```
"energy balances"
duplicate i=1,4
    q_dot_rad[i]=epsilon[i]*A[i]*(E_b[i]-J[i])/(1-epsilon[i])        "surface heat transfer rates"
    q_dot_rad[i]=A[i]*sum(F[i,j]*(J[i]-J[j]),j=1,4)                  "radiosity energy balances"
end
```

To solve the problem the appropriate boundary condition must be determined. Since there are four surfaces four boundary condition are needed. The two obvious boundary conditions are the temperatures of *surface 1* and *surface 4*. *Surface 1* is the wet-bulb temperature

sensor, thus its temperature is the wet-bulb temperature. *Surface 4* consists of the surroundings which are at the dry-bulb temperature.

$$T_1 = T_{wb} \tag{3.1.22}$$

$$T_4 = T_{db} \tag{3.1.23}$$

By knowing the temperatures of *surface 1* and *surface 4* the blackbody emissive powers are:

$$E_{b,1} = \sigma T_1^4 \tag{3.1.24}$$

$$E_{b,4} = \sigma T_4^4 \tag{3.1.25}$$

where σ is Stefan-Boltzmann's constant (5.67×10^{-8} W m^{-2} K^{-4}).

```
"boundary conditions"
T[1]=T_wb                                   "temp sensor temperature"
T[4]=T_db                                   "surroundings temperature"
E_b[1]=sigma#*T[1]^4                        "blackbody emissive power"
E_b[4]=sigma#*T[4]^4                        "blackbody emissive power"
```

A third boundary condition is determined from the assumption that the temperature of the inside surface of the shield (*surface 2*) is equal to the temperature of the outside surface of the shield (*surface 3*). This assumption is made because the shield is made from a very thin sheet of metal with minimal conductive resistance.

$$T_2 = T_3 \tag{3.1.26}$$

For the final boundary condition, an energy balance on the radiation shield is performed. The heat transfers due to both convection and radiation must balance each other. To

determine the average heat transfer coefficient experienced on the outside and inside of the shield the internal EES function **External_Flow_Plate** is used. This function uses the Churchill and Ozoe (1973) correlation to determine the Nusselt number.

```
T[2]=T[3]                                                          "temperatures are equal"

Call External_Flow_Plate('AirH2O', T_inf, T_s,  P, u_inf, Length: tau, h_conv, C_f, Nusselt, Re)
T_inf=T_db                                                         "free stream air temperature"
T_s=(T[2]+T[3])/2                                                  "plate surface temp"
length=s_f+s_b                                                     "length of plate"
```

The convective heat transfer <u>to</u> both the inside and outside of the radiation shield can be determined by:

$$\dot{q}_{conv,2} = \bar{h}\ A_2\ (T_{db} - T_2) \tag{3.1.27}$$

$$\dot{q}_{conv,3} = \bar{h}\ A_3\ (T_{db} - T_3) \tag{3.1.28}$$

The heat transfer <u>from</u> the shield due to radiation is already determined by Eq. (3.1.20) and (3.1.21). From this information an energy balance on the radiation shield is written.

$$\dot{q}_{conv,2} + \dot{q}_{conv,3} = \dot{q}_{rad,2} + \dot{q}_{rad,3} \tag{3.1.29}$$

Solving for the remaining blackbody emissive powers:

$$E_{b,2} = \sigma T_2^4 \tag{3.1.30}$$

$$E_{b,3} = \sigma T_3^4 \tag{3.1.31}$$

With this information, the problem is fully specified and the parasitic heat gain experienced by the wet-bulb temperature sensor due to radiation is found.

```
q_dot_conv[2]=h_bar*A[2]*(T_db-T[2])                          "convective heat xfer- surface 2"
q_dot_conv[3]=h_bar*A[3]*(T_db-T[3])                          "convective heat xfer- surface 3"

q_dot_conv[2]+q_dot_conv[3]=q_dot_rad[2]+q_dot_rad[3]         "energy balance on shield"

E_b[2]=sigma#*T[2]^4                                          "blackbody emissive power"
E_b[3]=sigma#*T[3]^4                                          "blackbody emissive power"
```

The quantity of interest is the net rate of radiation heat transfer to the wet-bulb temperature sensor, which is the negative of $\dot{q}_{rad,1}$.

$$\dot{q}_{rad,wb} = -\dot{q}_{rad,1} \tag{3.1.32}$$

```
q_rad_wb=-q_dot_rad[1]                                        "heat transfer to sensor"
```

With the parameters as specified above, $\dot{q}_{rad,wb} = 18.62 \text{ mW}$.

3.1.1 Radiation Shield Optimization

Section 3.1 outlined the procedure taken to estimate the parasitic heat gain of the wet-bulb as a result of radiation. This section focuses on optimizing the design of the radiation shield. Various parameters are altered to determine what has the largest impact on the effectiveness of the radiation shield.

As is shown in Figure 3-1 there are only four dimensions of the radiation shield that can be varied: the height (h), width (w), upstream extension (s_f), and downstream extension (s_b). The size of the temperature sensor remains constant at d equal to 6.35 mm (0.25 in) and L equal to 30.5 mm (1.2 in). Initially the emissivity of the shield is 0.2 (both inside and out),

the emissivity of the wet-bulb temperature sensor is 0.8, and the emissivity of the surroundings is 0.95.

As described in Section 3.1, w and h are made as small as possible while making certain that the thermal boundary layer extending from the shield does not affect the wet-bulb sensor. When this is done, there are only two remaining parameters to vary, s_f and s_b. As s_f is extended, w and h must increase. This is because the thermal boundary layer extending from the shield has more time to develop, thus extending farther. Initially, the parameters are at the same values as in Section 3.1. The distance in which the shield extends both upstream and downstream (s_f and s_b) is 40 mm (1.6 in) and the air velocity is maintained at 4 m/s. The values of h and w corresponding to these parameters are 32.3 mm (1.3 in) and 8.21 mm (0.32 in), respectively and the wet-bulb experiences a parasitic heat gain of 18.62 mW as a result of radiation.

Figure 3-3 shows the radiation parasitic to the wet-bulb sensor while the upstream extension of the radiation shield is varied.

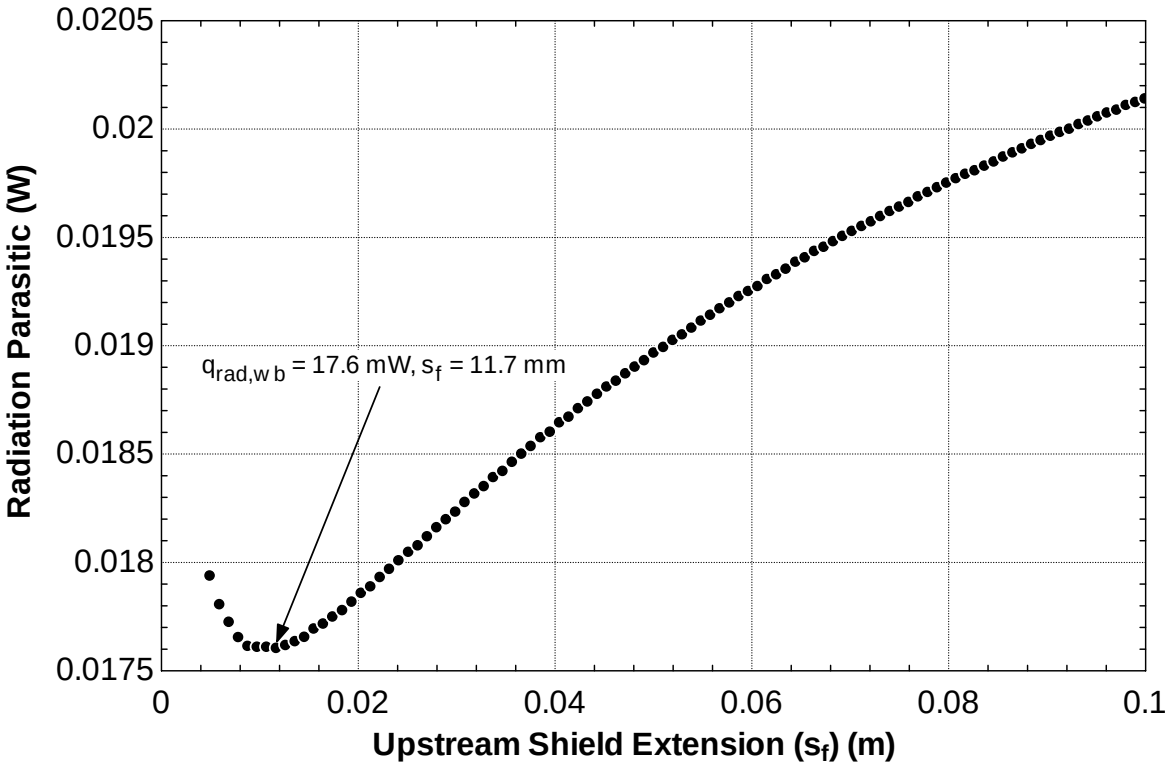

Figure 3-3: The radiation parasitic to the wet-bulb as the upstream length of the shield is varied. The downstream shield extension is maintained at 40 mm (1.6 in).

A shield extending 11.7 mm (0.46 in) in the upstream direction corresponds to a radiation parasitic of 17.6 mW. With s_f equal to 11.7 mm (0.46 in), h and w are equal to 31.5 mm (1.2 in) and 7.36 mm (0.29 in), respectively.

In Figure 3-4, s_f is held constant at a value of 11.7 mm (0.46 in) and s_b is varied.

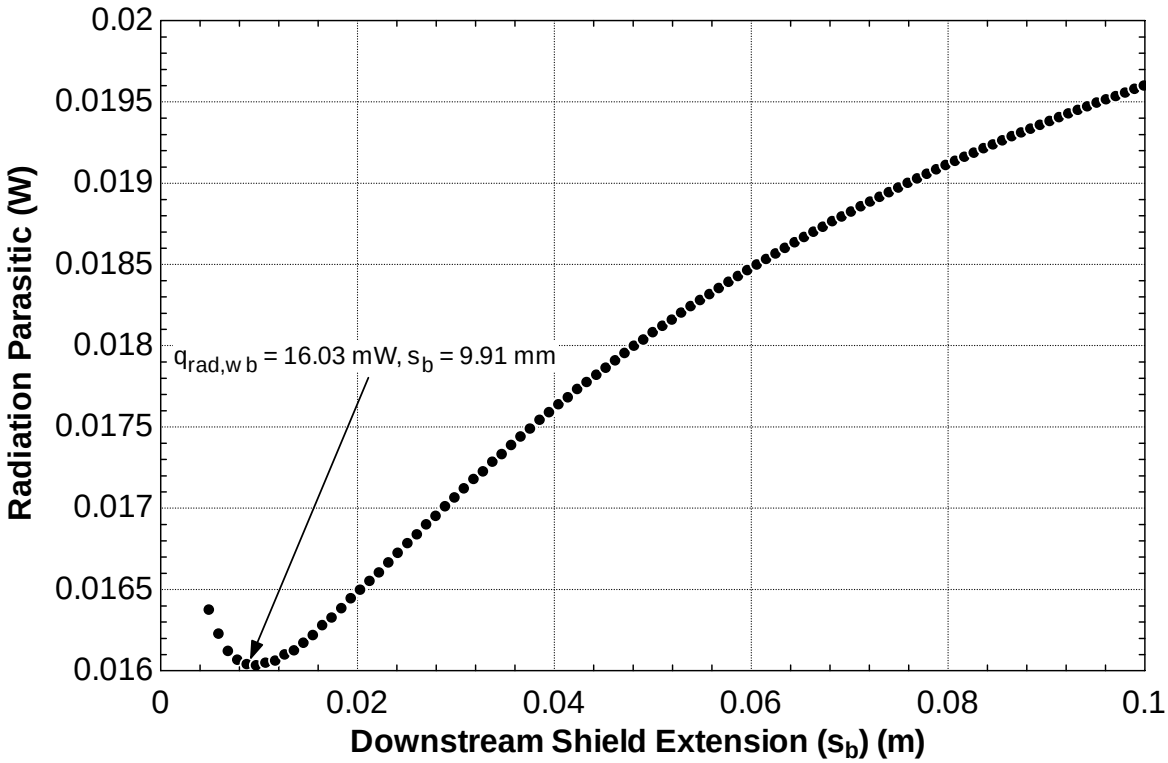

Figure 3-4: The radiation parasitic to the wet-bulb as the downstream length of the shield is varied. The upstream shield extension is maintained at 11.7 mm.

The optimal value of s_b is 9.91 mm (0.39 in) when the upstream shield extension is held constant at a value of 11.7 mm (0.46 in). By decreasing the value of s_b from 40 mm (1.6 in) to 9.91 mm (0.39 in), the radiation parasitic is reduced from 17.6 mW to 16.03 mW.

Next the optimization features of EES were used to allow both s_f and s_b to vary while the radiation parasitic to the wet-bulb is minimized. The optimization function within EES produced a minimum value in the radiation parasitic of 15.85 mW with corresponding values of s_f and s_b at 6.57 mm (0.26 in) and 9.17 mm (0.36 in), respectively. After using the model to determine the optimal geometrical parameters, other properties of the shield are tested.

Section 9 of ASHRAE Standard 41.6 (2006) calls for radiation shields for a wet-bulb sensor in a transverse configuration to be "in the form of parallel plates, polished on the outside and blackened on the inside." It is unknown why the standard called for the surfaces of the radiation shield to be "blackened on the inside" since that configuration would increase the radiative heat gain to the wet bulb sensor. The radiation shield should be reflective (polished) on the inside to reduce the emissivity and minimize the radiation parasitic to the wet bulb sensor. Figure 3-5 confirms this fact as it shows the radiation parasitic to the wet-bulb as a function of the emissivity of the inside of the radiation shield.

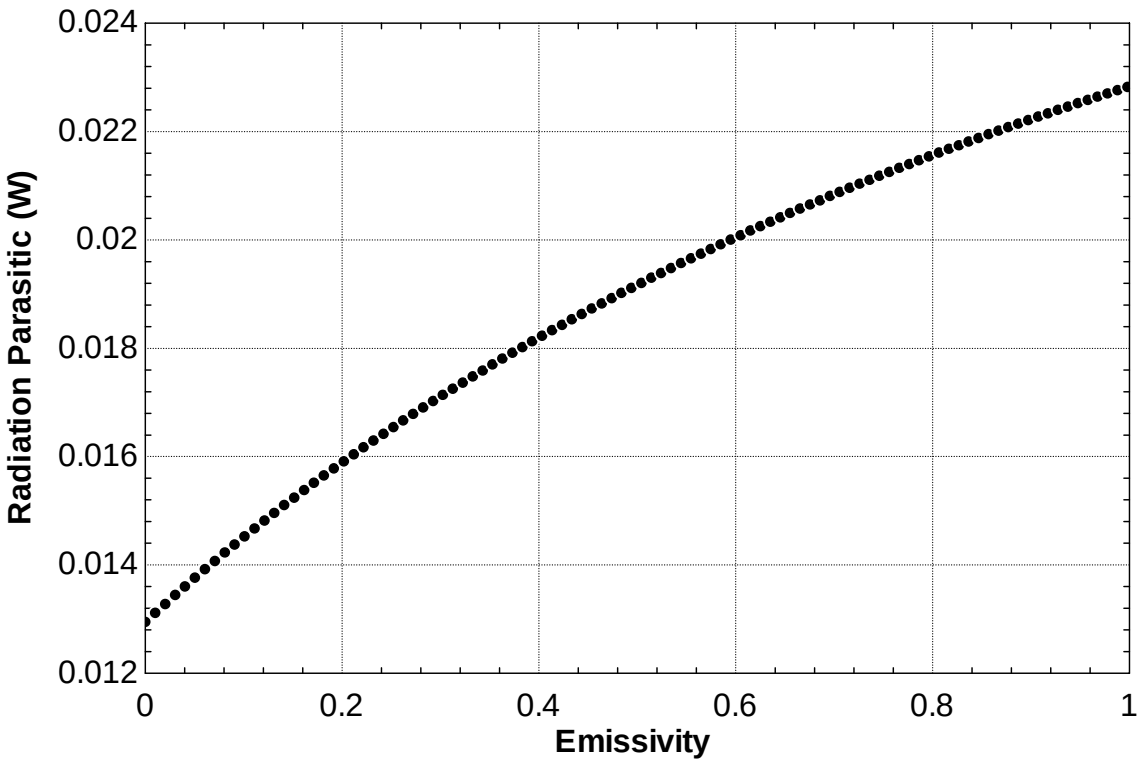

Figure 3-5: Radiation parasitic as the emissivity of surface 2 (inside surface of shield) is varied. Both s_f and s_b remain at there optimal values, 6.57 mm (0.26 in) and 9.17 mm (0.36 in), respectively.

From Figure 3-5 it is clear that the inside surface of the radiation shield should be as low of an emissivity as possible. To keep the present analysis reasonable, an achievable emissivity of 0.2 is used, consistent with polished aluminum (Omega, 1998).

A similar plot of the emissivity of the outside of the radiation shield shows that the emissivity of the outside of the shield has little impact on the effectiveness of the shield. The reason is because the convection on the outside of the radiation shield is the dominate heat transfer mechanism experienced by the shield and the shield quickly comes to the dry-bulb temperature. With the shield at the dry-bulb temperature, there is no radiation occurring between the outside of the shield and the surroundings which are also at the dry-bulb temperature.

With the optimal s_f and s_b parameters determined and knowing that the emissivity should be held as low as possible, the radiation parasitic to the wet-bulb temperature sensor is plotted as a function of the air velocity as shown in Figure 3-6.

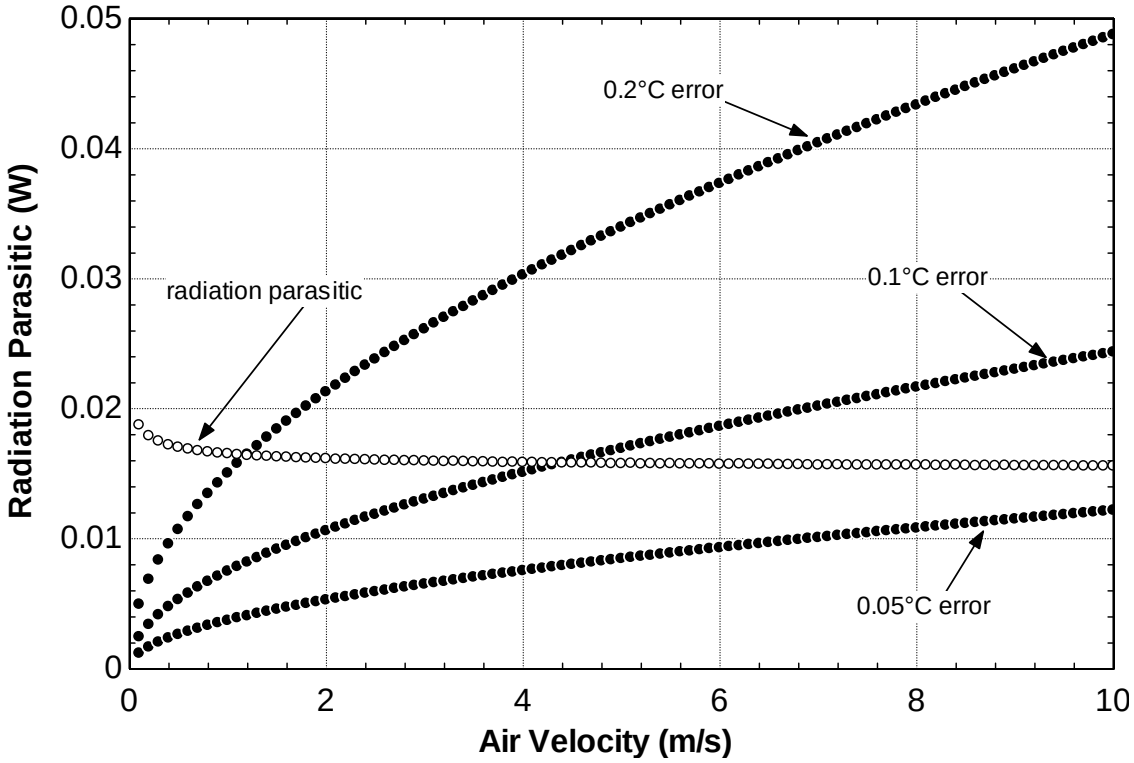

Figure 3-6: Radiation parasitic heat gain as a function of air velocity. The closed circles represent the parasitic heat transfer to the wet-bulb temperature sensor corresponding to errors in the wet-bulb temperature measurement of 0.05°C, 0.1°C, and 0.2°C. The open circles represent the parasitic heat transfer to the wet-bulb temperature sensor as a result of radiation.

The radiation parasitic is reduced slightly as the velocity is increased because the thermal boundary layer extending from the shield is reduced and the shield can be brought in closer to the sensor. Unfortunately, the optimized radiation shield is not sufficient to reduce the radiation parasitic to a level below that required to limit the error in the wet-bulb temperature measurement to 0.05°C. Furthermore, secondary calculations in Section 3.3 suggest that other parasitic heat transfer mechanisms (e.g., conduction and sensible energy associated with the makeup water) are comparatively smaller parasitics that are more easily controlled. Therefore, controlling radiation is the key challenge to making accurate wet-bulb

measurements which motivates the exploration of more sophisticated methods for shielding the sensor from radiation parasitic.

One option to limit the radiation parasitic heat gain is the addition of low emissivity screens or louvers to the upstream and downstream open ends of the radiation shield. The purpose of these appurtenances is to prevent the sensor form seeing the "black" high temperature surroundings through the inlet and exit planes of the shields. This is simulated by reducing the surface area of the front and back open faces and increasing the surface area of the shield. A definite improvement is observed when the area of the front and back openings are reduced by a factor of two; this is possible with the use of a relatively simple shield. The improvement is shown in Figure 3-7; the use of a radiation shield at the front and back openings reduces the parasitic by about 3 mW and allows the radiation to approximately match the budget at an air velocity of 10 m/s. However, given the presence of other parasitics, this level of radiation gain is still too large to limit the error to 0.05°C.

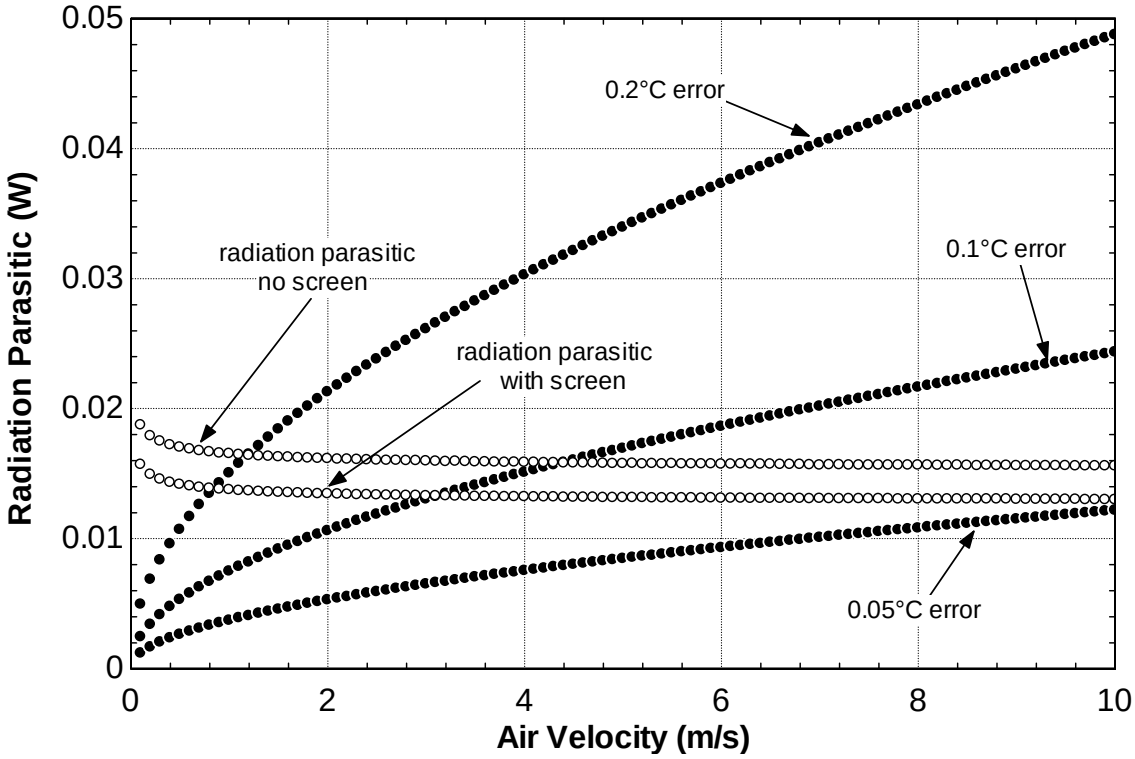

Figure 3-7: Radiation parasitic heat gain as a function of the air velocity. The closed circles represent the parasitic heat transfer to the wet-bulb temperature sensor corresponding to errors in the wet-bulb temperature measurement of 0.05°C, 0.1°C, and 0.2°C. The open circles represent the parasitic heat transfer to the wet-bulb temperature sensor as a result of radiation with and without screens at the inlet and exit.

The next option explored is the idea of actively cooling the radiation shield. If the radiation shield is cooled to near the wet-bulb temperature, then the radiation parasitic can be reduced dramatically. In Figure 3-8 it is observed that cooling the shield does have a significant impact on the radiation parasitic to the wet-bulb temperature sensor.

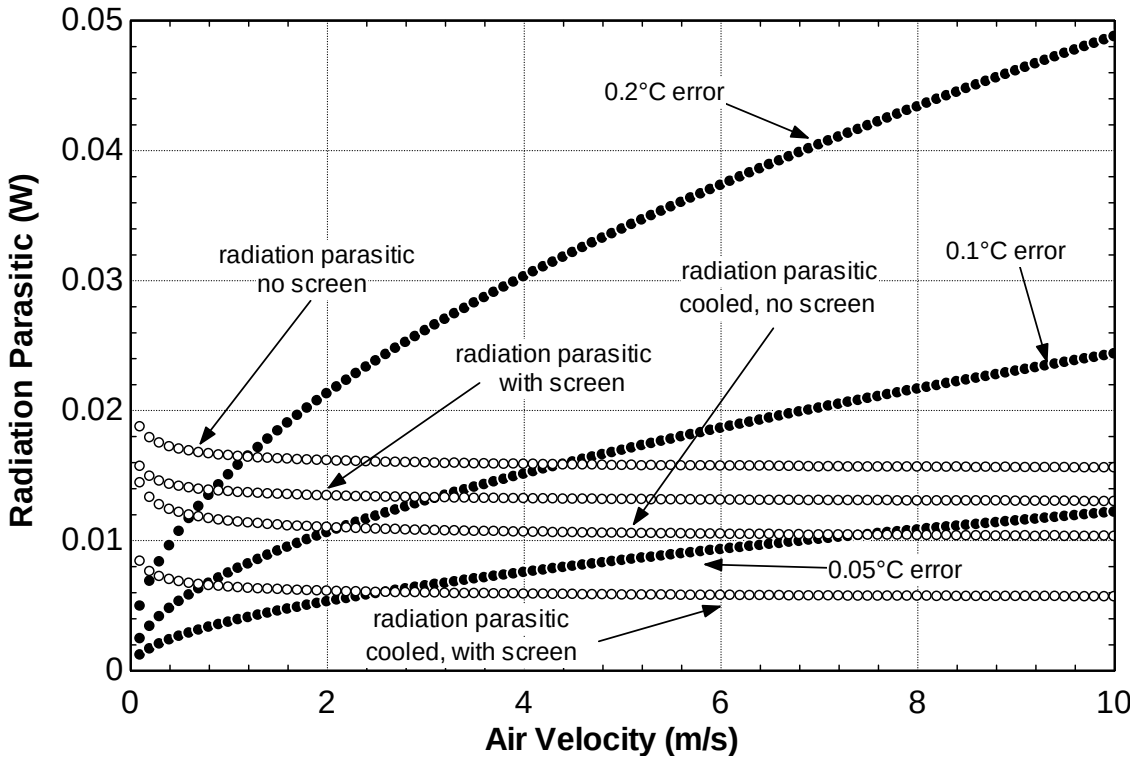

Figure 3-8: Radiation parasitic heat gain as a function of the air velocity. The closed circles represent the parasitic heat transfer to the wet-bulb temperature sensor corresponding to errors in the wet-bulb temperature measurement of 0.05°C, 0.1°C, and 0.2°C. The open circles represent the parasitic heat transfer to the wet-bulb temperature sensor as a result of radiation with various shield configurations. The cooled shield is held at the wet-bulb temperature (19.4°C).

Figure 3-8 shows that if the shield is cooled to the wet-bulb temperature and screens are added to the front and back of the shield then the radiation parasitic can be reduced to a level that is well within the parasitic energy budget to achieve the 0.05°C wet-bulb temperature measurement error. For all points in Figure 3-8, the radiation shield remains at the size that was found to be optimal for an uncooled shield (s_f = 6.57 mm (0.26 in), s_b = 9.17 mm (0.36 in)). However, the optimal size of a cooled shield is much longer. Figure 3-9 shows the radiation parasitic for a cooled shield (without screens) as a function of the length of the cooled shield, as well as the parasitic budgets for various values of the error.

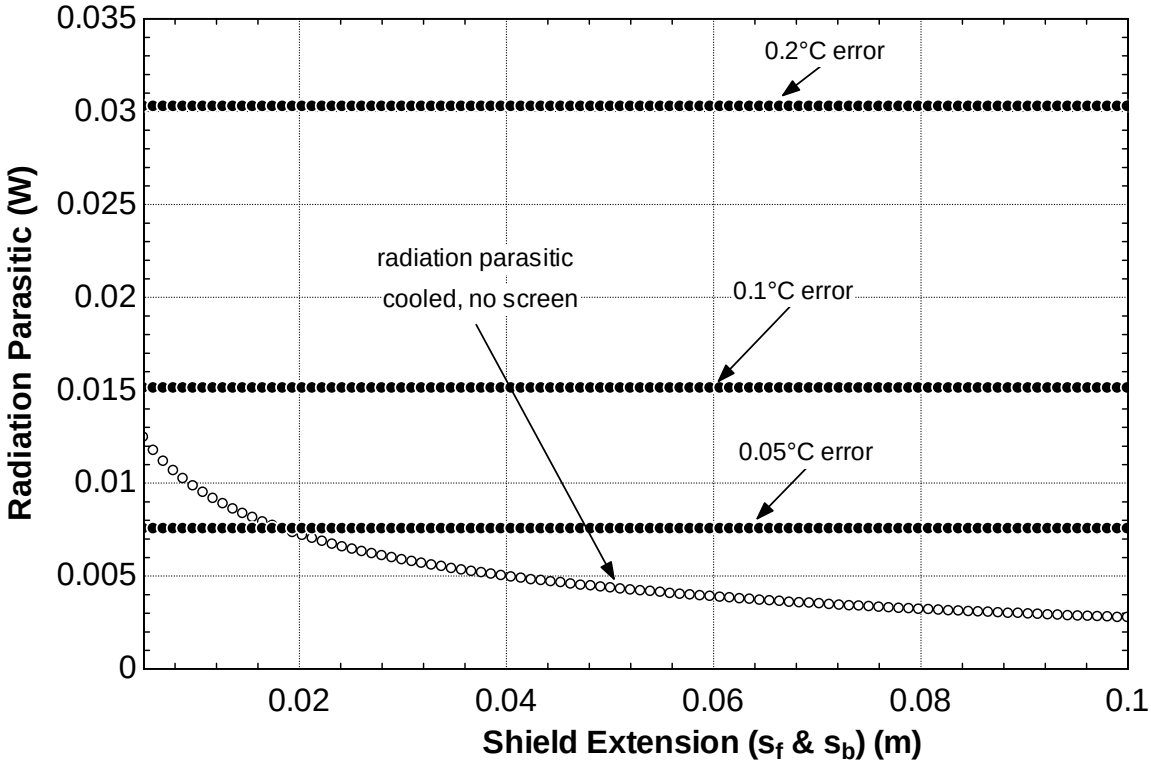

Figure 3-9: Radiation parasitic heat gain as a function of the length of the shield in the upstream and downstream direction. The closed circles represent the parasitic heat transfer to the wet-bulb temperature sensor corresponding to errors in the wet-bulb temperature measurement of 0.05°C, 0.1°C, and 0.2°C. The open circles represent the parasitic heat transfer to the wet-bulb temperature sensor as a result of radiation for a cooled shield with no screens. The air velocity is held constant at 4 m/s, and the length of the shield in both the upstream and downstream directions (s_f and s_b) are increased by equal amounts. The shield is at the wet-bulb temperature (19.4°C).

The radiation parasitic continues to decrease as the shield is extended away from the temperature sensor. At an s_f and s_b value of about 20 mm (0.79 in) the radiation parasitic to the wet-bulb is just below the allowable parasitic budget for a 0.05°C error. The air velocity in Figure 3-9 is held constant at 4 m/s, but as shown in the previous figures, an increased air velocity increases the budget for allowable parasitic to the wet-bulb temperature sensor. The shield considered in Figure 3-9 does not include screens on either of the open ends. Adding screens does help to reduce the parasitic but it may be easier to simply extend the shield rather than adding screens.

Figure 3-10 illustrates the radiation parasitic as a function of air velocity for a cooled shield in which the temperature of the shield is varied.

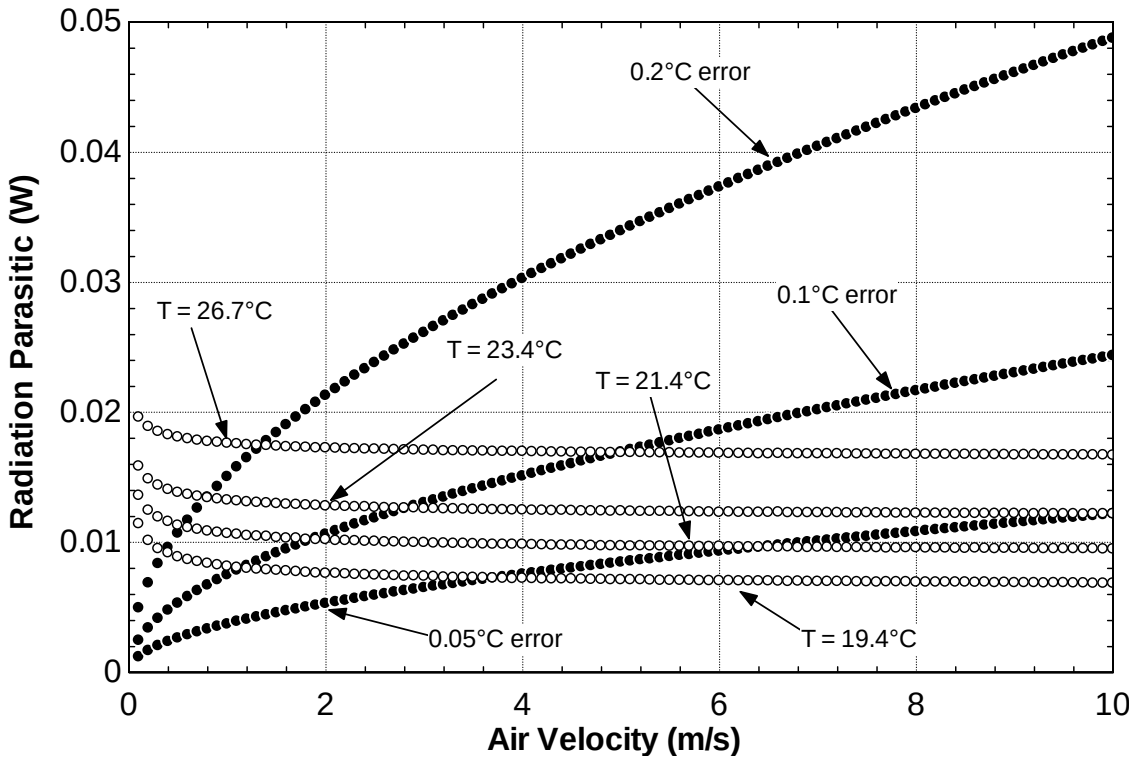

Figure 3-10: Radiation parasitic heat gain as a function of air velocity. The closed circles represent the parasitic heat transfer to the wet-bulb temperature sensor corresponding to errors in the wet-bulb temperature measurement of 0.05°C, 0.1°C, and 0.2°C. The open circles represent the parasitic heat transfer to the wet-bulb temperature sensor as a result of radiation for a cooled shield with no screens. The length of the shield in both the upstream and downstream directions (s_f and s_b) is kept at 20 mm (0.79 in) and the temperature of the shield is varied from the wet-bulb temperature to the dry-bulb temperature.

It is clear from Figure 3-10 that cooling the shield from the dry-bulb temperature to the wet-bulb temperature significantly reduces the radiation parasitic to the wet-bulb. Even with the shield only two degrees above the wet-bulb temperature there is an increase in the radiation parasitic of about 3 mW, relative to the value that is achieved if the shield is kept at the wet-bulb temperature. In Figure 3-10 the total length of the shield is held constant at 40 mm as

the shield is cooled. For a radiation shield cooled to the wet-bulb temperature there is no real optimal length because the parasitic continues to decrease as the shield length increases. As the radiation shield is cooled less, however, the optimal length of the shield continually decreases. The implementation of actively cooled radiation shields is readily achievable through the use of thermoelectrics. In this configuration, the cold side of a thermoelectric cooler would serve as the interior of the radiation shield. The input energy to the cold-side of the thermoelectric cooler would be modulated to match the observed wet-bulb temperature. The team elected to forego this approach due to cost constraints.

3.1.2 Monte Carlo Method- Plate to Cylinder Radiation View Factor

As mentioned previously, the radiation view factor between a plate (*surface 1*) and a cylinder (*surface 2*) is necessary for the calculation of the radiation parasitic to the wet-bulb temperature sensor. The view factor of interest is represented in Figure 3-11.

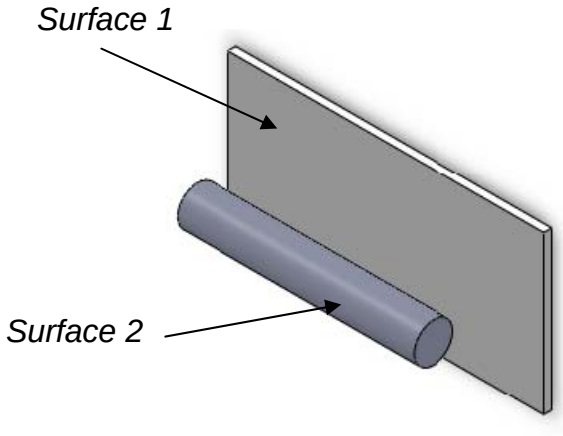

Figure 3-11: Radiation view factor of interest is from surface 1 to surface 2. Surface 1 is the inside surface of a rectangular flat plate. Surface 2 is the entire exterior of the circular cylinder.

An extensive search showed that no analytical solution for this configuration is available. Therefore, the view factor is calculated using a Monte Carlo technique as outlined in this section of the report.

In general, the view factor between two surfaces *i* and *j* can be computed according to (Nellis and Klein, 2009):

$$A_i F_{i,j} = A_j F_{j,i} = \int^{A_j} \int^{A_i} \frac{\cos\theta_i \theta_j}{\pi r^2} dA_i dA_j \tag{3.1.33}$$

where r is the distance between differential area segment dA_i and dA_j. The angle θ_i is the angle formed between the normal to dA_i and a vector connecting differential areas dA_i and dA_j. Likewise, θ_j is the angle formed between the normal to dA_j and a vector connecting differential areas dA_j and dA_i. Figure 3-12 below shows these parameters more clearly.

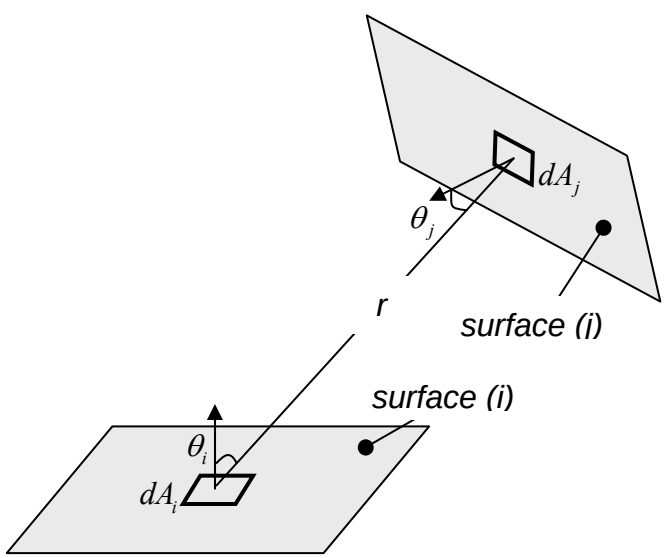

Figure 3-12: Two surfaces exchanging radiation (Nellis and Klein, 2009).

The direct computation of the view factor requires the evaluation of a complicated double integral. Therefore, the Monte Carlo method is used as a numerical alternative to determine the radiation view factor.

The Monte Carlo method propagates rays from random locations on surface 1 at random angles; the probability distribution used to select the angle is based on the assumption that the surface is a diffuse emitter. Some of the rays that propagate from surface 1 strike surface 2. As the number of rays generated is increased, an increasingly accurate representation of the view factor is obtained by taking the ratio of the number of rays originating from surface 1 that strike surface 2 to the total number of rays that leave surface 1. For a more comprehensive explanation of the Monte Carlo method refer to Siegel and Howell (2002).

The view factor, $F_{1,2}$, is from surface 1 (finite plane) to surface 2 (finite horizontal cylinder) as shown in Figure 3-13.

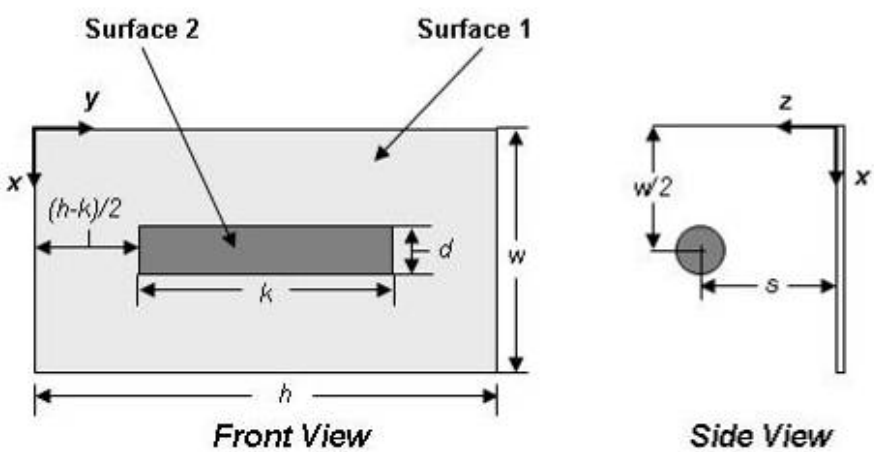

Figure 3-13: Surface 1 is the under side of a flat plate with a width (*w*) and length (*h*). Surface 2 is a circular cylinder placed a distance (*s*) from the plate. The cylinder has a diameter (*d*) and length (*k*) and is centered under the plate in both the ***x*** and ***y***-direction.

In using the Monte Carlo method to determine radiation view factors the following steps must be repeated numerous times:

1. Select a ray origin on surface 1
2. Select a random direction in which to orient the ray
3. Determine if the ray leaving surface 1 strikes surface 2

A function is programmed in MATLAB to carry out these steps. The function takes the geometrical parameters (see Figure 3-13) as inputs and outputs the view factor from surface 1 to surface 2:

```
function[F]=F_12(N,w,h,d,k,s)

%Inputs
%N  number of rays to generate
%w  width of the flat plate (x-direction)
%h  length of flat plate (y-direction)
%d  diameter of the cylinder
%k  length of the cylinder (y-direction)
%s  distance between center of cylinder and plate

%Outputs
%F         view factor
```

Counters are initialized in order to track the number of rays generated (*ict*) and the number of times a ray strikes surface 2 (*hits*):

```
      ict=0;  %counter of the number of rays
      hits=0; %counter for the number of hits
```

A while loop is setup that terminates when the counter reaches the user-specified number of rays (*N*):

```
      while (ict<N)      %terminate loop when N rays have been generated
            ict=ict+1;  %increment the ray counter
```

Now starting locations for the rays generated on surface 1 must be specified. This is done using a random number generator in MATLAB (the function *rand*) that randomly (uniform distribution) generates a number between 0 and 1. The *x*-location is randomly positioned along the entire width (*w*) of the plate and the *y*-location along the entire length (*h*) of the plate.

```
            x=rand*w;   %randomly select a ray origin (x-location)
            y=rand*h;   %randomly select a ray origin (y-location)
```

Once the ray origin is defined, the angle at which the ray is emitted from surface 1 must be defined. The view factor calculated here uses the assumption that the surface behaves as a diffuse emitter; that is, radiation is emitted uniformly in all directions. The easiest way to describe a ray emitted from a surface is using spherical coordinates with the polar and azimuthal angles, θ and ϕ, respectively. A graphical representation of a unit vector in the spherical coordinate system is presented in Figure 3-14.

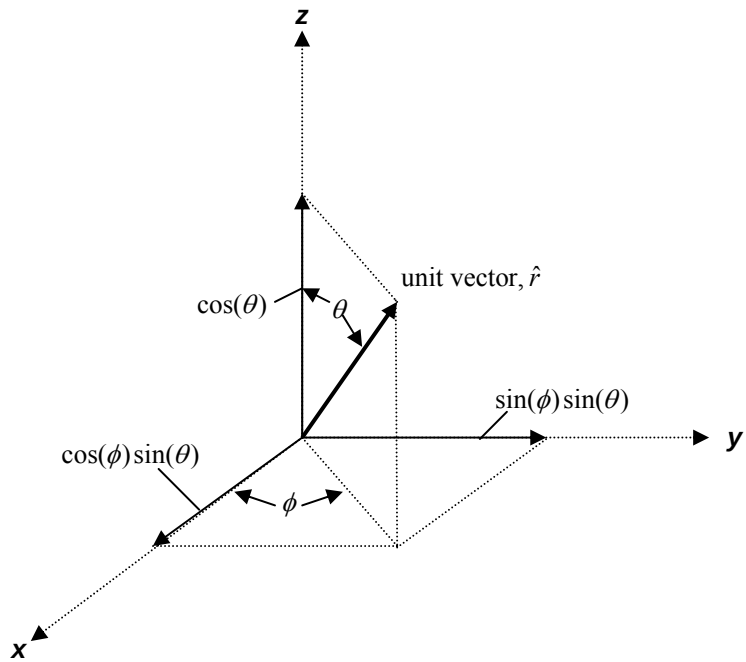

Figure 3-14: Unit vector displaying the direction of an emitted ray in terms of the polar and azimuthal angles.

Eq. (3.1.34) represents a unit vector $\hat{r}$ in the direction of the emitted ray in terms of its polar and azimuthal angles.

$$\hat{r} = [\cos(\phi)\sin(\theta)]\hat{i} + [\sin(\phi)\sin(\theta)]\hat{j} + [\cos(\theta)]\hat{k} \tag{3.1.34}$$

Both the polar and azimuthal angles must be chosen at random from a probability distribution that is representative of a diffuse emitter (normal distribution). The cumulative probability, P_θ, of emission from a diffusely-emitting surface at polar angles between 0 and θ for all azimuthal angles is (Nellis and Klein, 2009):

$$P_\theta = \sin^2(\theta) \tag{3.1.35}$$

The cumulative probability, P_ϕ, of emission from a diffusely-emitting surface at azimuthal angles between 0 and ϕ for all polar angles given by Nellis and Klein (2009) is:

$$P_\phi = \frac{\phi}{2\pi} \tag{3.1.36}$$

The cumulative probability function P_θ has a value that ranges from 0 to 1 as θ increases from 0 to π/2. Similarly the cumulative probability function P_ϕ has a value that ranges from 0 to 1 as ϕ increases from 0 to 2π. By solving Eq. (3.1.35) and (3.1.36) for θ and ϕ respectively, randomly selected polar and azimuthal angles can be chosen by allowing a random number generator to produce values for P_θ and P_ϕ between 0 and 1.

$$\theta = \sin^{-1}\left(\sqrt{P_\theta}\right) \tag{3.1.37}$$

$$\phi = 2\pi P_\phi \tag{3.1.38}$$

This process is implemented in MATLAB again using the function *rand* which randomly generates a number between 0 and 1 with a uniform distribution.

```
Ptheta=rand; %uniformly distr. random number between 0 and 1
theta=asin(sqrt(Ptheta)); %randomly chosen polar angle
Pphi=rand; %uniformly distr. random number between 0 and 1
phi=Pphi*2*pi; %randomly chosen azimuthal angle
```

The next step in the process is to determine whether or not the ray leaving surface 1 actually strikes surface 2. The position of the ray as it leaves the surface and grows in length, L, can be determined by multiplying the ray unit vector, Eq. (3.1.34), by L and adding to it the ray

starting location (x,y). With this information, the location of the ray can be specified by (x_i, y_i, z_i):

$$x_i = x + L\cos(\phi)\sin(\theta) \tag{3.1.39}$$

$$y_i = y + L\sin(\phi)\sin(\theta) \tag{3.1.40}$$

$$z_i = L\cos(\theta) \tag{3.1.41}$$

Another *while loop* is implemented in MATLAB with the purpose of slowly increasing the length of the ray by an increment, *dL,* and checking after each increase whether the ray location has intersected with the volume occupied by the cylinder (i.e., whether the ray has hit surface 2). The length by which the ray grows during each step (dL) is initially set to a value of $d/10$, where d is the diameter of the cylinder associated with surface 2. (Note that the sensitivity of the results to the size of the length step is examined in later in this section of the report.) The initial starting length L is s-$d/2$, examination of Figure 3-13 shows that this is the shortest possible ray that is able to strike surface 2. After the addition of each incremental length step, the ray location is evaluated (x_i, y_i, z_i).

```
dL=d/10;        %length increment
L=((s-d/2)-dL); %initial length of the ray
done=0;
while(done==0)
      L=L+dL; %increment ray length by dL
      x_i=x+L*cos(phi)*sin(theta); %ending x-location
      y_i=y+L*sin(phi)*sin(theta); %ending y-location
            z_i=L*cos(theta); %ending z-location
```

The *while loop* continues to run until one of two conditions are met: (1) it is determined that the ray has hit surface 2, or (2) it is determined that the ray has reached a location in space where it is no longer possible for the ray to ever strike surface 2, and therefore has missed.

The first step in determining if the ray has hit surface 2 is to determine if its y-location (y_i) lies within the range of y-values that is occupied by surface 2 (i.e., is the ray axially within the extent of the cylinder). The range of y-values in which it is possible for the ray to strike surface 2 is:

$$\frac{h-k}{2} \leq y_i \leq \frac{h-k}{2} + k \tag{3.1.42}$$

Where h is the length of the plate and k is the length of the cylinder. As shown in Figure 3-13, the cylinder is centered with the plate in the y-direction.

This process is implemented in MATLAB with the following *if* statement:

```
if ((y_i>=((h-k)/2))&&(y_i<=(((h-k)/2)+k)))
```

If the y-coordinate of the ray endpoint does lie within the range of y-values that encompass surface 2, then the function proceeds to another nested *if* statement that determines whether or not the x- and z-locations of the ray endpoint lie within the area encompassed by surface 2 in the x-z plane (i.e., is the ray within the circular area projected by the cylinder). The x- and z-locations that lie on the circular area composing surface 2 in the x-z plane satisfy the following equation:

$$\sqrt{(x_i - 0.5\,w)^2 + (z_i - s)^2} \leq 0.5\,d \tag{3.1.43}$$

When both *if* statements are true, then it can be established that the ray has hit surface 2 and the *hit* counter is incremented by one. A hit of surface 2 also prompts the program to exit the inner while loop and move to the outer while loop where a new ray is generated and tracked. Both of these steps are implemented with the following MATLAB code that sets the *hit* indicator to 1 (indicating a hit) and the done indicator to 1 (indicating that the inner while loop is done):

```
                        if (sqrt((x_i-0.5*w)^2+(z_i-s)^2)<=0.5*d)
                              hit=1;
                              done=1;
                        end
                  end
```

When either of the previous two if conditions are not satisfied, a second *if* statement is used to determine whether the endpoint of the ray is at a location where it can no longer strike surface 2. Figure 3-15 shows the volume of space within which the program will continue to run and track the ray.

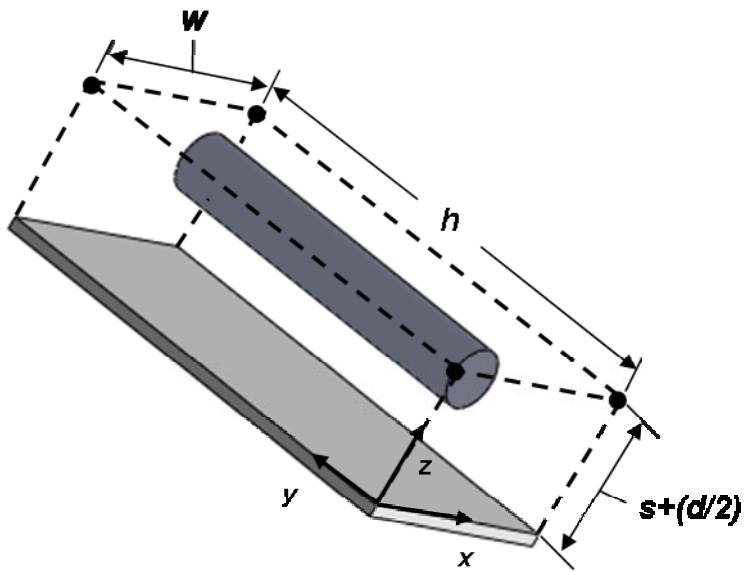

Figure 3-15: Dotted lines represent the boundaries implemented in the MATLAB code. Once a ray endpoint is outside of the box created by the dotted lines it is no longer possible for it to strike surface 2.

Once either x_i, y_i, or z_i lie outside of the volume shown in Figure 3-15, it is no longer possible for the ray to ever strike surface 2. When this is true, the *hit* indicator is set to 0 (indicating a miss) and the done indicator is set to 1 (indicating that the inner *while* loop should be terminated). The program moves to the outer *while* loop where a new ray is generated and tracked.

```
            if((y_i<0)||(y_i>h)||(x_i<0)||(x_i>w)||(z_i<0)||
                  (z_i>s+d/2))
                  hit=0;
                  done=1;
            end
      end
```

When the ray has not struck surface 2, or entered an area in which it can no longer strike surface 2, the inner while loop increments the length and the steps are repeated.

The hit indicator is used to increment the number of hits.

```
            if (hit==1)
                  hits=hits+1;    %if ray hits then increment hit counter
            end
      end
```

When the number of rays (*ict*) has reached the user specified number of rays (*N*) then the outer *while loop* is terminated. At this point, the view factor is determined by dividing the number of hits by the total number of rays generated.

$$F_{1,2} = \frac{hits}{ict} \tag{3.1.44}$$

```
      F=hits/ict; %view factor
end
```

The function described above assumes that the cylinder is centered in front of the plate, as shown in Figure 3-13, and placed a distance $s > d/2$ away from the plate. Another limit is that the cylinder cannot extend beyond the ends of the plate.

The next step is to verify that the Monte Carlo method developed produces accurate results. The MATLAB code using the Monte Carlo method to determine the specified radiation view factor is listed in its entirety below:

```
function[F]=F_12(N,w,h,d,k,s)

%Inputs
%N  number of rays to generate
%w  width of the flat plate (x-direction)
%h  length of flat plate (y-direction)
%d  diameter of the cylinder
%k  length of the cylinder (y-direction)
```

```
%s  distance between center of cylinder and plate

%Outputs
%F         view factor

    ict=0;  %counter of the number of rays
    hits=0; %counter for the number of hits

    while (ict<N)   %terminate loop when N rays have been generated
        ict=ict+1;  %increment the ray counter

        x=rand*w;   %randomly select a ray origin (x-location)
        y=rand*h;   %randomly select a ray origin (y-location)
        Ptheta=rand; %uniformly distributed random number between 0 and 1
        theta=asin(sqrt(Ptheta)); %randomly chosen polar angle
        Pphi=rand; %uniformly distributed random number between 0 and 1
        phi=Pphi*2*pi; %randomly chosen azimuthal angle

        dL=d/10;    %length increment
        L=((s-d/2)-dL); %initial length of the ray
        done=0;
        while(done==0)
            L=L+dL; %increment ray length by dL
            x_i=x+L*cos(phi)*sin(theta); %x-location of the end of the ray
            y_i=y+L*sin(phi)*sin(theta); %y-location of the end of the ray
            z_i=L*cos(theta); %z-location of the end of the ray

                if ((y_i>=((h-k)/2))&&(y_i<=(((h-k)/2)+k)))
                    if (sqrt((x_i-0.5*w)^2+(z_i-s)^2)<=0.5*d)
                        hit=1;
                        done=1;
                    end
                end

            if ((y_i<0)||(y_i>h)||(x_i<0)||(x_i>w)||(z_i<0)||(z_i>s+d/2))
                hit=0;
                done=1;
            end
        end

        if (hit==1)
            hits=hits+1; %if ray hits then increment hit counter
        end
    end
    F=hits/ict; %view factor
end
```

To verify the accuracy of the Monte Carlo program, the model is implemented in a limiting condition where a view factor correlation is available. A correlation is available for the view

factor between a flat plate and a cylinder when the two objects are of equal length, as shown in Figure 3-16. This correlation has been programmed in EES. The EES software correlation is based on the findings of Wiebelt and Ruo (1963), and Howell (1982).

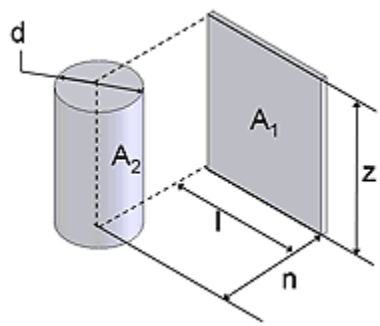

Figure 3-16: View factor correlation available in EES (Klein, 2009).

In Figure 3-16, *l* is the width of the plate, *n* is the distance from the plate to the center of the cylinder, *z* is the height of the plate, and *d* is the diameter of the cylinder. Figure 3-17 shows the equivalent geometry that is modeled using the Monte Carlo method.

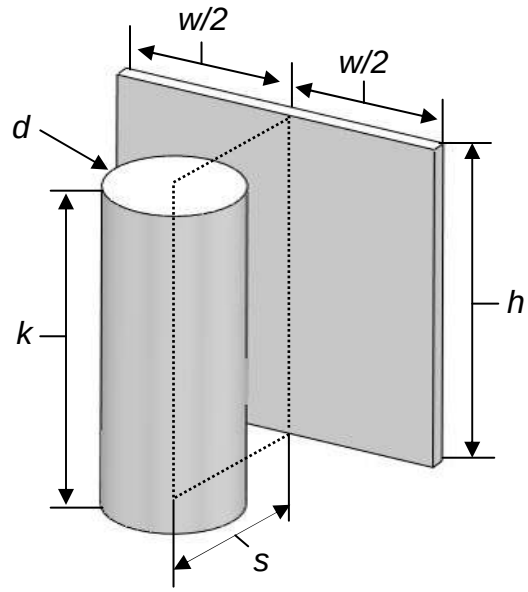

Figure 3-17: Geometry implemented with the Monte Carlo method to verify results.

In Figure 3-17, *w* is the width of the plate, *s* is the distance from the plate to the center of the cylinder, *h* is the height of the plate, *k* is the height of the cylinder, and *d* is the diameter of the cylinder. To verify the model against the correlation available in EES the height of the cylinder *k* is set equal to the height of the plate *h.*

Due to the symmetry of the problem shown in Figure 3-17, the view factors between the plate and the cylinder are equal in both Figure 3-16 and Figure 3-17. If the Monte Carlo method is implemented for both geometries, Figure 3-17 has twice the number of rays being emitted from the plate (assuming an equal ray density), but also has twice as many rays striking the circular cylinder. Therefore, the view factors are equal because the ratio of the number of rays emitted to the number of strikes is equal.

When using the Monte Carlo method, it is important to determine an appropriate number of rays that must be generated to yield accurate view factor estimates. For the particular Monte Carlo method developed in this text, it is also important to determine the length increment, *dL*, required to produce accurate results. Increasing the number of rays generated and decreasing the length scale will tend to increase the computational time necessary to solve the problem while improving accuracy. For this reason, it is important to determine the smallest number of rays and the longest ray increment that will produce accurate results. The first set of simulations is run to determine the impact of decreasing the incremental length scale, *dL*, on the accuracy of the results produced.

The initial model has a geometry in which w = 50 mm (2.0 in), h = 100 mm (3.9 in), d = 10 mm (0.39 in), k = 100 mm (3.9 in), and s = 10 mm (0.39 in), with the parameters corresponding to those labeled in Figure 3-17. This corresponds to values of l = 25 mm (0.98 in), n = 10 mm (0.39 in), z = 100 mm (3.9 in), and d = 10 mm (0.39 in) as labeled in Figure 3-16. The solution is computed in EES:

```
$UnitSystem SI MASS RAD PA K J
$TabStops 0.2 0.4 0.6 0.8 3.5 in

F=F3D_15(l,n,z,d)                                   "view factor, plane to cylinder"

"parameters"
l=25[mm]*convert(mm,m)                              "width of plane"
n=10[mm]*convert(mm,m)                              "plane to cylinder distance"
z=100[mm]*convert(mm,m)                             "plane and cylinder height"
d=10[mm]*convert(mm,m)                              "cylinder diameter"
```

This solution leads to a view factor of $F_{1,2}$ = 0.2221.

The model is initially run in MATLAB by setting the number of rays equal to $1x10^3$ and varying the incremental length to diameter ratio (*dL/d)* from $1x10^{-1}$ to $1x10^{-4}$. Figure 3-18 shows the variation in the view factor produced by the Monte Carlo method as the incremental length to diameter ratio is varied.

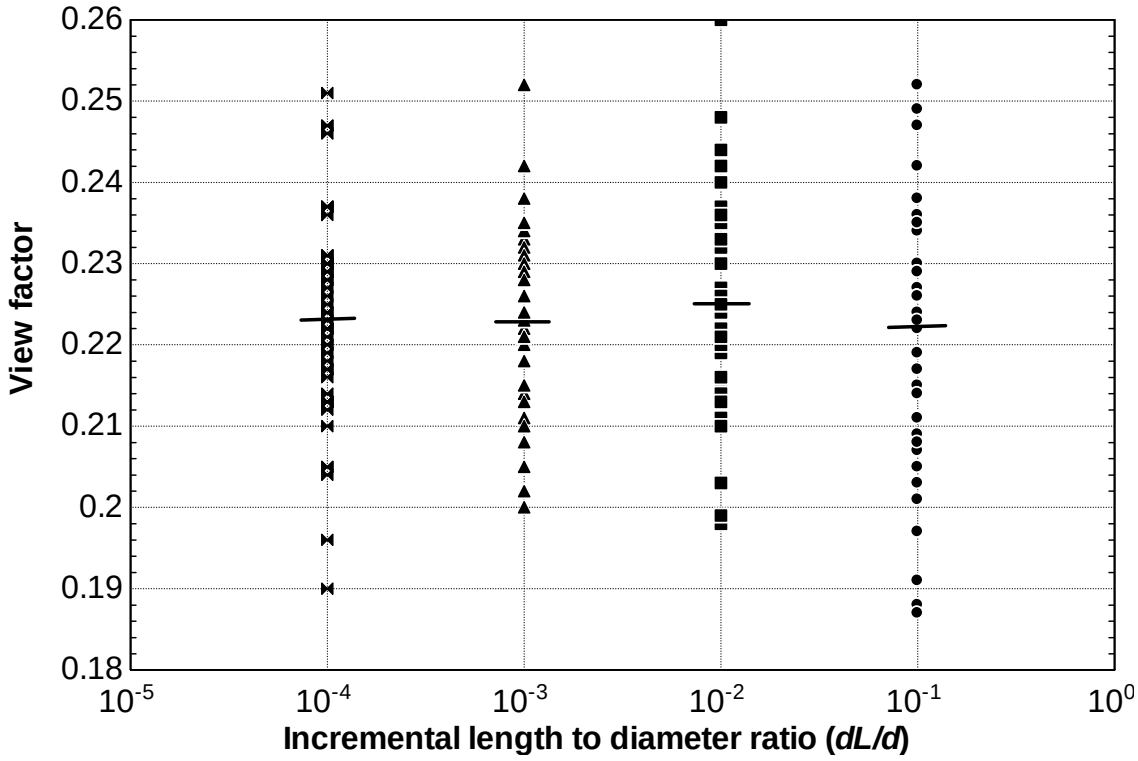

Figure 3-18: Fifty view factor estimates (points) as well as the average (line) using the Monte Carlo method at discrete *dL/d* values with the number of rays held at a constant value of $1x10^3$.

No appreciable reduction in the view factor variation is associated with a decreased value of *dL/d.* All of the results appear to be centered on the view factor calculated using EES (0.2221). The same plot is shown in Figure 3-19 using an *N* value of $1x10^4$ instead of $1x10^3$.

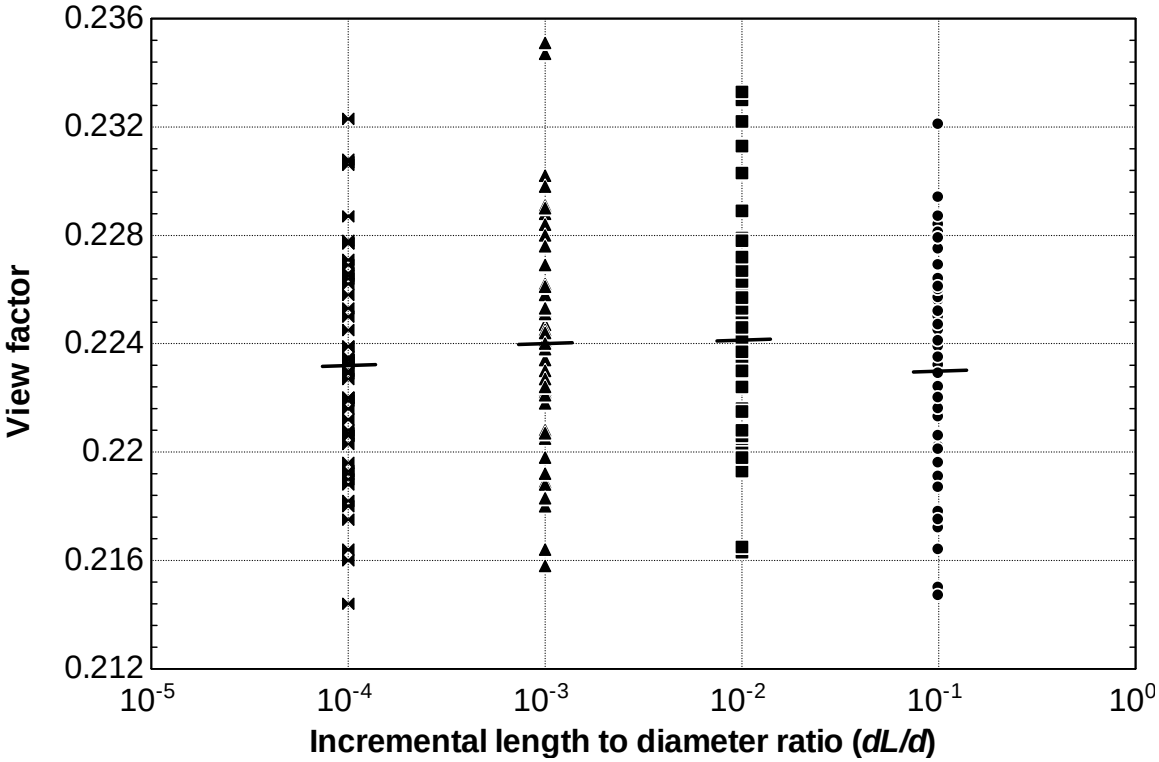

Figure 3-19: Fifty view factor estimates (points) as well as the average (line) using the Monte Carlo method at discrete *dL/d* values with the number of rays held at a constant value of $1x10^4$.

Figure 3-19 also shows that the variability of the results remains relatively constant with *dL* provided that *dL* is less than *d*/10. The variability of the results is reduced significantly relative to Figure 3-18, but this is due to the increase in the number rays.

In order to determine the number of rays required by the Monte Carlo method, the model is implemented using *N* values ranging from $1x10^3$ to $1x10^6$ with *dL* held constant at *d*/10. These results are shown in Figure 3-20.

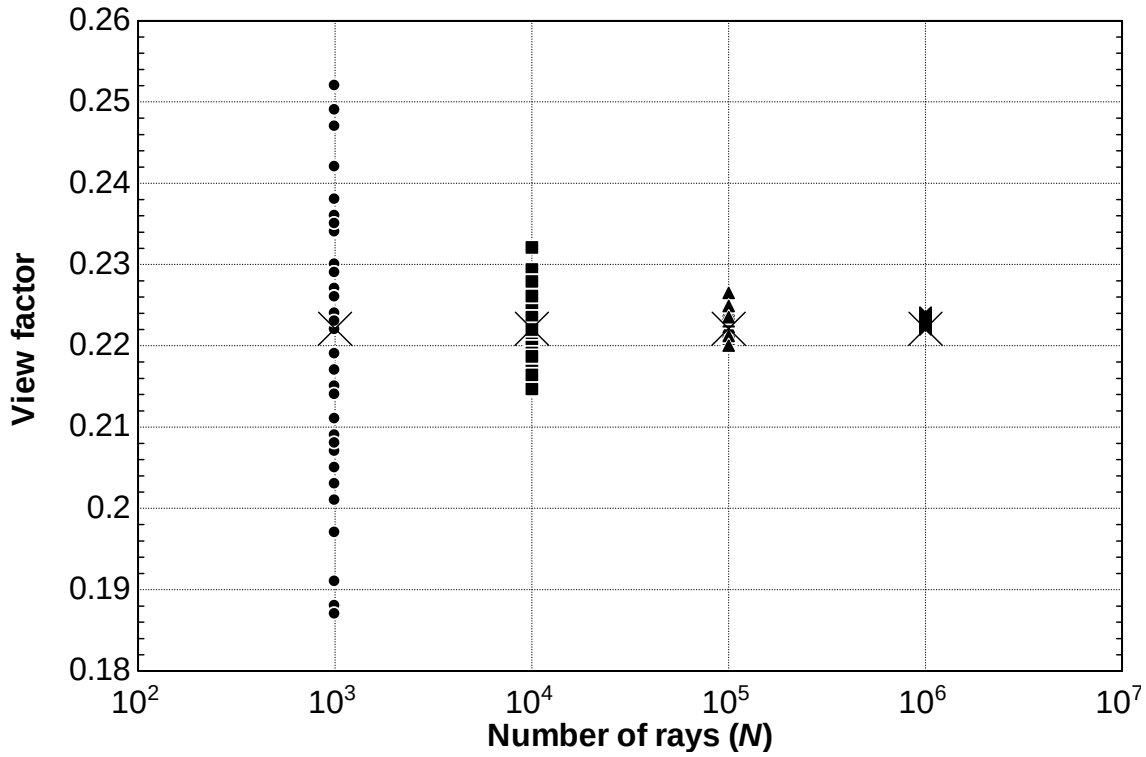

Figure 3-20: A plot showing 50 runs of the Monte Carlo method at *N* values of $1x10^3$, $1x10^4$, $1x10^5$, and $1x10^6$, with the *dL* held constant at *d/10* (1 mm). The "x" symbols represent the results produced in EES.

Figure 3-20 shows that increasing the value of *N* significantly reduces the variability in the results produced by the Monte Carlo method. The 50 runs at an *N* value of $1x10^5$ provide an average view factor of 0.2230 with a standard deviation of 0.0013. This corresponds to an error between the average view factor and the actual view factor of 0.40%. When the value of *N* is increased from $1x10^5$ to $1x10^6$, the average view factor is 0.2229 with a standard deviation of 0.0005. This corresponds to an error in the average view factor of 0.36%. These results suggest that an *N* value of $1x10^5$ or larger is sufficient to provide results that have an accuracy of less than 1%.

Figure 3-21 illustrates the view factor provided by EES and using the Monte Carlo technique as a function of the distance between the plane and the cylinder

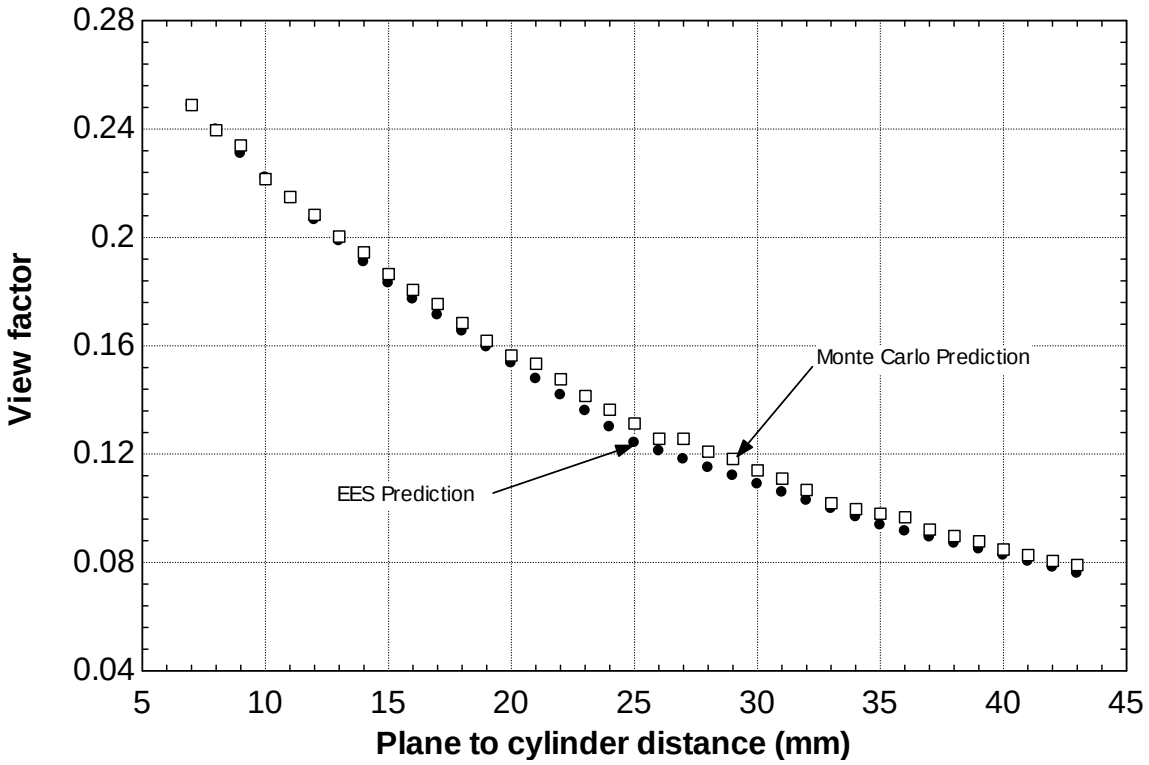

Figure 3-21: A comparison of the view factor calculated using EES and using the Monte Carlo method as a function of the distance between the plane and the cylinder. The Monte Carlo method implemented used an *N* value of $1x10^5$ and a *dL* value of *d/10*.

Figure 3-21 shows that the view factor produced using EES and the view factor produced using the Monte Carlo method agree. In Figure 3-22 the width of the plane is varied while the other parameters are held constant. The numeric value of the plane width corresponds to the dimension *l* in Figure 3-16 and *w*/2 in Figure 3-17. Figure 3-22 also demonstrates the agreement between the view factor predicted using EES and the Monte Carlo method with the width of the plate being varied while the other parameters are held constant.

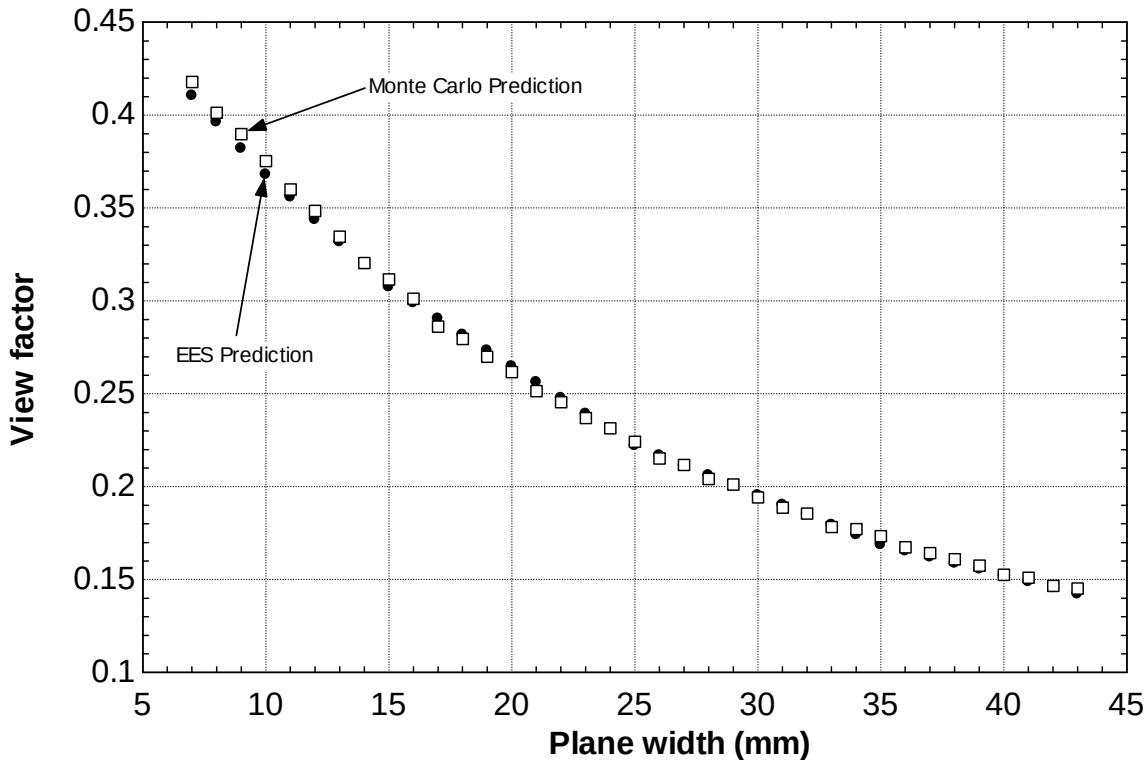

Figure 3-22: A comparison of the view factor calculated using EES and using the Monte Carlo method developed, as the width of the plane is varied. The Monte Carlo method implemented used an *N* value of $1x10^5$ and a *dL* value of *d/10*.

3.1.3 Monte Carlo Method- Plate to Plate with Cylinder between Radiation View Factor

The other view factor required for the model of the radiation shielding of temperature sensor in a transverse flow configuration is the view factor between two plates with a circular cylinder centered between them. The geometry is shown in Figure 3-23.

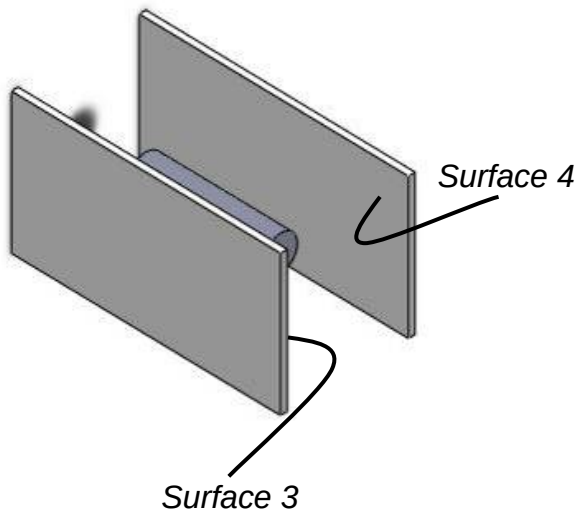

Figure 3-23: Isometric view of the geometry in which the view factor is computed. Surface 3 and surface 4 are the inside surfaces of flat plates facing each other with a circular cylinder centered between them.

To avoid confusion with the view factor calculation described in Section 3.1.2 the surfaces have been named surface 3 and surface 4. Again the Monte Carlo method is needed to compute the radiation view factor from surface 3 to surface 4 ($F_{3,4}$), as a review of relevant literature produced no such correlation. Figure 3-24 shows a detailed drawing of the geometry with the relevant variables and parameters labeled.

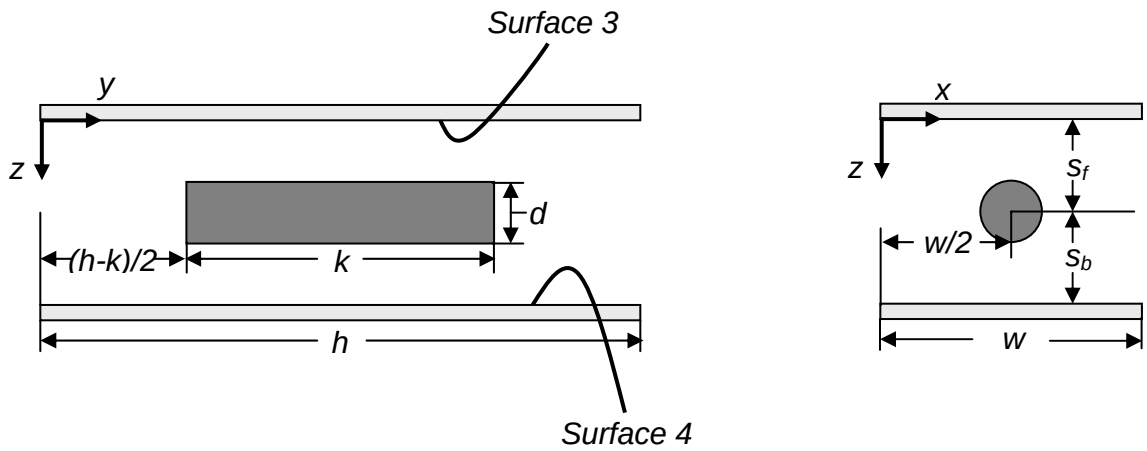

Figure 3-24: Elevation and plan views of the geometry to be analyzed with surfaces labeled.

To be clear, the two plates are of equal length (h) and width (w). The thickness is irrelevant because the view factor found is between the inside surface of each plate. The temperature sensor (cylinder) is centered with the plates in the x-direction, but is not necessarily centered in the z-direction. The center of the cylinder is located a distance of s_f from surface 3 in the z-direction and a distance of s_b from surface 4, also in the z-direction. The cylinder is centered with the two plates in the y-direction.

The function **F_34** uses the Monte Carlo method and is input into MATLAB in much the same way as **F_12**, as described in the previous section. The function takes the geometrical parameters as inputs and produces the view factor between two surfaces as the output.

```
function[F]=F_34(N,w,h,d,k,s_f,s_b)

%Inputs
%N  number of rays to generate
%w  width of the flat plate (x-direction)
%h  length of flat plate (y-direction)
%d  diameter of the cylinder
%k  length of the cylinder (y-direction)
%s_f surface 3 to cyl. center (z-direction)
```

```
%s_b surface 4 to cyl. center (z-direction)

%Outputs
%F         view factor
```

Counters are initiated and tracked in a *while loop* to monitor both the number of rays generated and the number of hits (i.e. a ray leaving surface 3 and striking surface 4).

```
    ict=0;  %counter of the number of rays
    hits=0; %counter for the number of hits

    while (ict<N)   %terminate loop when N rays have been generated
        ict=ict+1;  %increment the ray counter
```

In the same manner as before ray origins encompassing the entire emitting surface (surface 3) are created. For each ray origin a set of randomly chosen polar and azimuthal angles are also created.

```
        x=rand*w;   %randomly select a ray origin (x-location)
        y=rand*h;   %randomly select a ray origin (y-location)
        Ptheta=rand; %uniformly distributed random number between 0 and 1
        theta=asin(sqrt(Ptheta)); %randomly chosen polar angle
        Pphi=rand; %uniformly distributed random number between 0 and 1
        phi=Pphi*2*pi; %randomly chosen azimuthal angle
```

Rays are generated having an initial length L and are slowly incremented by dL. The end location of each ray is tracked by its coordinates x_i, y_i, z_i. This process is repeated using a *while loop*. This *while loop* will continue to increment the ray length L by a distance dL tracking its location until certain conditions are satisfied.

```
            dL=d/10;    %length increment
            L=((s_f-d/2)-dL);   %initial length of the ray
            done=0;
            while(done==0)
            L=L+dL; %increment ray length by dL
                  x_i=x+L*cos(phi)*sin(theta); %x-location, end of ray
                  y_i=y+L*sin(phi)*sin(theta); %y-location, end of ray
```

```
z_i=L*cos(theta); %z-location, end of ray
```

Within the *while loop* an *if* statement, implemented in the same manner as **F_12**, checks to see if the ray has struck the interior circular cylinder. When this statement is true (i.e. the ray has struck the cylinder) the *while loop* is exited and a new ray is generated. A ray striking the cylinder can no longer strike surface 4 and therefore *hit* = 0 and the ray is no longer tracked.

```
        if ((y_i>=((h-k)/2))&&(y_i<=(((h-k)/2)+k)))
            if (sqrt((x_i-0.5*w)^2+(z_i-s_f)^2)<=0.5*d)
                hit=0;
                done=1;
            end
        end
```

If the conditions are not satisfied for the first *if* statement the program moves onto a second *if* statement; this statement tests to see if the ray has reached a location where it is no longer possible to strike the interior circular cylinder. (See $\boldsymbol{F_{12}}$ view factor calculation from Section 3.1.2.) When this *if* statement is satisfied (i.e. the ray has moved outside of the box defined in Figure 3-15) the conditions for exiting the interior *while loop* are again met (*done* = 2). It is still not determined whether or not this ray will strike surface 4 so *hit* = 0.

```
        if(y_i<0)||(y_i>h)||(x_i<0)||(x_i>w)||(z_i<0)||
          (z_i>s_f+d/2))
            hit=0;
            done=2;
        end
    end
```

If it is determined that ray missed the cylinder, a new ray is not immediately generated. The ray position continues to be tracked to determine if it will hit surface 4, now that it has not hit

the interior circular cylinder. As stated previously, when a ray misses the cylinder *done* = 2. This condition closes the first interior *while loop*, but opens a second. The second interior *while loop* finds the *x*- and *y*-location of the ray when it has reached a *z*-location of $(s_f + s_b)$. This *z*-location corresponds to the *z*-location of surface 4. From this information the length of all rays striking surface 4 can be found.

$$z_i = s_f + s_b \tag{3.1.45}$$

$$z_i = L\cos(\theta) \tag{3.1.46}$$

$$L = \frac{s_f + s_b}{\cos(\theta)} \tag{3.1.47}$$

By knowing the length of all rays as they reach the *z*-location of surface 4, the x_i and y_i locations can be found.

$$x_i = x + \frac{s_f + s_b}{\cos(\theta)} \cos(\phi)\sin(\theta) \tag{3.1.48}$$

$$y_i = y + \frac{s_f + s_b}{\cos(\theta)} \sin(\phi)\sin(\theta) \tag{3.1.49}$$

An *if* statement is used to test if (x_i,y_i) lies on surface 4. When this is true the ray has struck surface 4 and a successful hit is generated, *hit* = 1. When (x_i,y_i) lies outside of surface 4 the ray has missed and *hit* = 0. In both instances *done* = 3 and the loop is exited.

```
while(done==2)
      L=(s_f+s_b)/cos(theta);
      x_i=x+L*cos(phi)*sin(theta);
      y_i=y+L*sin(phi)*sin(theta);

            if ((y_i>=0)&&(y_i<=h)&&(x_i>=0)&&(x_i<=w))
```

```
                                        hit=1;
                                        done=3;
                                else
                                        hit=0;
                                        done=3;
                                end
                        end
```

At this point the hit counter is incremented if *hit* = 1 and a new ray is generated. The process is repeated until the counter (*ict*) has reached the user specified number of rays (*N*).

```
                        if (hit==1)
                            hits=hits+1; %if ray hits then increment counter
                        end
        end
```

The view factor is calculated by dividing the total number of hits (*hits*) by the total number of rays emitted (*ict*).

```
                F=hits/ict; %view factor
end
```

Since there are no analytical solutions to a view factor between two equally sized plates with a cylinder between, the Monte Carlo method developed is verified using the view factor calculator in ANSYS. The geometry and the associated mesh for one of the tests done in ANSYS are shown in Figure 3-25.

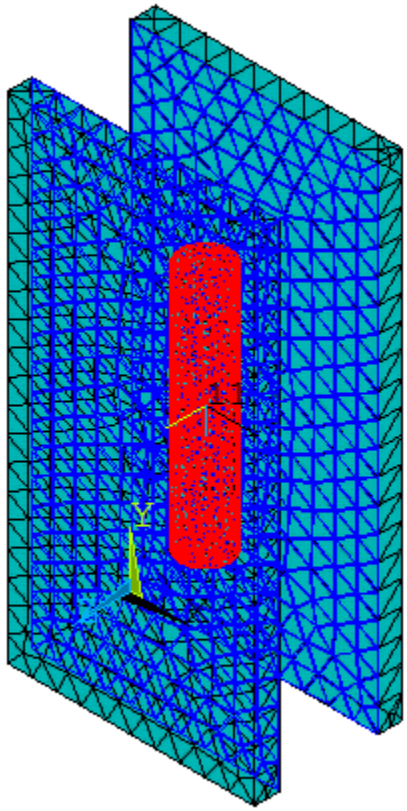

Figure 3-25: The geometry and mesh produced in ANSYS to verify the view factor calculation implemented in MATLAB.

In the particular geometry shown in Figure 3-25 w is 50 mm (2.0 in), h is 100 mm (3.9 in), d is 10 mm (0.39 in), k is 50 mm (2.0 in), and s_f and s_b are both 10 mm (0.39 in). For this geometry, the MATLAB code above produces a view factor ($F_{3,4}$) of 0.4614 and the solution in ANSYS is 0.4604. With this type of agreement over a range of geometries it is clear that the MATLAB code used to implement the Monte Carlo method is producing accurate results.

3.2 Radiation Parasitic- Axial Configuration

This section of the report provides a detailed description of the model used to determine the parasitic radiation heat transfer to the wet-bulb temperature sensor in an axial configuration. The wet-bulb temperature sensor is placed in an axial flow configuration with a cylindrical radiation shield surrounding it. The geometry of the radiation shield and sensor is shown in Figure 3-26 below.

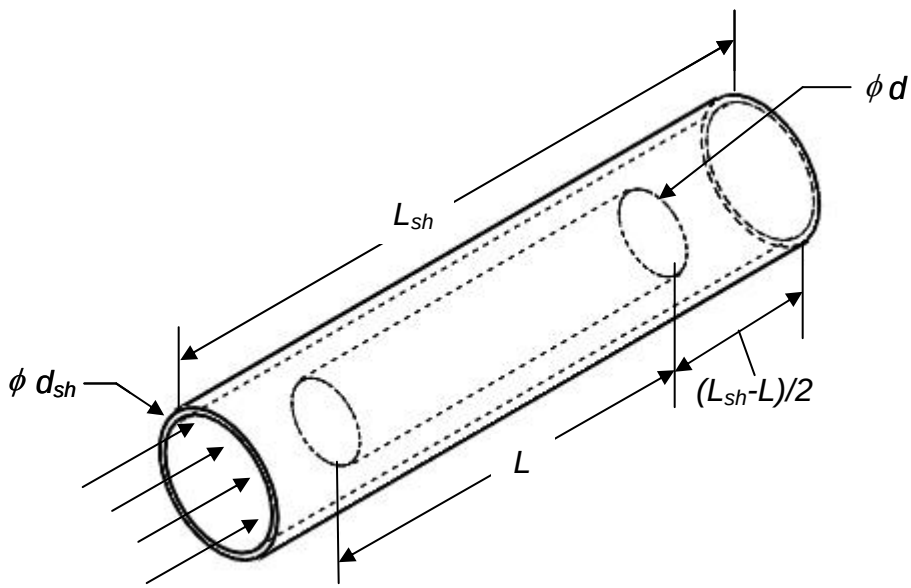

Figure 3-26: Isometric view of the radiation shield geometry modeled for a temperature sensor in an axial flow configuration.

The shield has a length of L_{sh}, an inside diameter of d_{sh}, and a thickness of *th*. The temperature sensor is of length *L* and diameter *d*. With the available view factors the sensor must be placed in the center of the shield to ensure accurate results. With this the distance between the end of the sensor and the end of the shield is $(L_{sh}-L)/2$ as shown in Figure 3-26.

The radiation model is computed at a standard test condition, test condition 1 (i.e. T_{wb} = 19.4°C, T_{db} = 26.7°C). These, along with the other inputs, are entered into EES as follows:

```
$TabStops 0.2 0.4 0.6 0.8 3.5 in
$UnitSystem SI MASS RAD K PA J

T_db_C=26.7[C]                                  "dry-bulb temp C"
T_wb_C=19.4[C]                                  "wet-bulb temp C"
T_db=converttemp(C,K,T_db_C)                    "dry-bulb temp K"
T_wb=converttemp(C,K,T_wb_C)                    "wet-bulb temp K"
d=0.25[inch]*convert(inch,m)                    "sensor diameter"
L=1.2[inch]*convert(inch,m)                     "sensor length"
u_inf=2[m/s]                                    "air flow velocity"
```

The temperature sensor geometry is consistent with a size commonly used in practice and is the same size as used in all other calculations produced in this report. The current ASHRAE Standard 41.6 requires the wet-bulb temperature sensor to be positioned in an axial flow configuration with the air velocity (u_∞) at 2 m/s.

For the purpose of describing the manner in which the radiation shield is modeled, the length of the shield (L_{sh}) is set to an arbitrary value slightly longer than the length of the temperature sensor, L_{sh} = 40 mm (1.6 in); however, this value is later optimized. The shield thickness (th) is set to a value of 0.5 mm (0.02 in) for the calculation.

```
L_sh=40[mm]*convert(mm,m)                       "shield length"
th=0.5[mm]*convert(mm,m)                        "shield thickness"
```

The diameter of the shield (d_{sh}) is not arbitrary, rather, the diameter of the shield is set so that it is sufficiently far from the sensor that the thermal boundary layers extending from the sensor and from the shield do not interact, which would impact the measurement of the wet-

bulb temperature. An approximation for the distance that a thermal boundary layer extends from a surface, δ_t, is given by Eq. (3.2.1) (Nellis and Klein, 2009):

$$\delta_t \approx 2\sqrt{\alpha t} \tag{3.2.1}$$

where α is the thermal diffusivity and t is the time relative to the step change in surface conditions. The thermal diffusivity is calculated from the thermal conductivity (k), density (ρ), and specific heat capacity (c_p) of the free stream air.

$$\alpha = \frac{k}{\rho\, c_p} \tag{3.2.2}$$

These properties are determined using the internal property routine in EES for a moist air stream at the film temperature (T_{film}), standard atmospheric pressure (P), and with a relative humidity (RH) corresponding to that of test condition 1.

$$T_{film} = \frac{T_{wb} + T_{db}}{2} \tag{3.2.3}$$

```
T_film=(T_db+T_wb)/2                                  "film temperature"
P=101325[Pa]                                          "atmospheric pressure"
RH=0.515408099 [-]                                    "relative humidity"
k=conductivity(AIRH2O,T=T_film,P=P,R=RH)              "thermal conductivity"
rho =density(AIRH2O,T=T_film,P=P,R=RH)                "density"
c_p =CP(AIRH2O,T=T_film,P=P,R=RH)                     "specific heat capacity"
alpha=k/(rho*c_p)                                     "thermal diffusivity"
```

The time relative to the step change in surface condition (i.e. t in Eq. (3.2.1)) is found by knowing the distance traveled by the fluid (x) and the free stream velocity of the fluid flow (u_∞).

$$t = \frac{x}{u_\infty} \tag{3.2.4}$$

For a temperature sensor in the axial configuration, the boundary layer extending from both the shield and the sensor itself are considered. To determine t for the boundary layer extending from the shield ($\delta_{t,sh}$), x is replaced with $\frac{(L_{sh} - L)}{2} + L$. This corresponds to a distance from the front of the shield to the end of the sensor and is the most downstream location where the thickness of the boundary layer is important. Beyond the wet-bulb temperature sensor, it no longer matters if the boundary layer from the shield intersects the boundary layer from the temperature sensor. To determine the maximum thickness of the boundary layer extending form the temperature sensor ($\delta_{t,wb}$) x, in Eq. (3.2.4), is replaced with L, the length of the temperature sensor.

$$\delta_{t,sh} = 2\sqrt{\alpha \frac{\frac{(L_{sh} - L)}{2} + L}{u_\infty}} \tag{3.2.5}$$

$$\delta_{t,wb} = 2\sqrt{\alpha \frac{L}{u_\infty}} \tag{3.2.6}$$

```
delta_t_sh=2*sqrt(alpha*(((L_sh-L)/2)+L)/u_inf)        "boundary layer from shield"
delta_t_wb=2*sqrt(alpha*L/u_inf)                       "boundary layer from sensor"
```

By knowing the thickness of the thermal boundary layer extending from both the radiation shield and the wet-bulb temperature sensor, a minimum shield diameter (d_{sh}) is specified.

$$d_{sh} \geq d + 2\delta_{t,sh} + 2\delta_{t,wb} \tag{3.2.7}$$

Because the diameter of the shield is specified using Eq. (3.2.7) it is possible to vary the length of the shield while ensuring that the diameter of the shield is kept to a minimum. The smallest shield diameter will always result in the least radiation parasitic as it minimizes the amount that the surroundings radiate to the sensor.

With the dimensions of the temperature sensor and radiation shield determined, the surfaces participating in the radiation exchange are completely defined. *Surface 1* is the outside surface of the cylindrical temperature sensor, excluding the ends. The emissivity of the sensor (ε_1) is set to a value of 0.80 which corresponds to the emissivity of cotton cloth (Cole-Parmer).

```
"surface 1- temperature sensor"
A[1]=pi*d*L                                    "surface area"
epsilon[1]=0.8[-]                              "emissivity"
```

Surface 2 consists of the inside surface of the radiation shield. The emissivity of the inside surfaces of the radiation shield are set to a value of 0.20 based on a value that is attainable with a range of materials, including polished aluminum (Omega, 1998).

```
"surface 2- inside of the radiation shield"
A[2]=pi*d_sh*L_sh                              "surface area"
epsilon[2]=0.2[-]                              "emissivity"
```

The outside surface of the cylindrical radiation shield is *surface 3*. The model suggests that the emissivity of *surface 3* has no impact on the radiation parasitic (due to convection to the shield warming it to the dry bulb temperature). However, the emissivity of the outside of the shield is set equal to the emissivity of the inside of the shield at a value of 0.20.

```
"surface 3- outside of the radiation shield"
A[3]=pi*(d_sh+2*th)*(L_sh)                    "surface area"
epsilon[3]=0.2[-]                             "emissivity"
```

The final surface participating in the radiation exchange is *surface 4*. *Surface 4* consists of the surroundings outside of the shield. The surroundings radiate to the sensor through the two open ends of the radiation shield. Since the surface area of the surroundings cannot be quantified, the area of surface 4 is set to an arbitrarily large value. The surroundings are essentially "black" and are given an emissivity (ε_4) value of 0.95.

```
"surface 4- surroundings"
A[4]=1[m^2]                                   "arbitrarily large surface area"
epsilon[4]=0.95[-]                            "emissivity"
```

To aid in the calculation of view factors one additional surface is specified. The final surface specified is *surface s*. *Surface s* consists of two imaginary circular surfaces located at the front and back (open) ends of the radiation shield.

```
"surface s- ends of shield"
A_s=2*0.25*pi*d_sh^2                          "surface area"
```

With the surfaces participating in the radiation exchange completely defined, the view factors between *surfaces 1-4* are defined. Starting with *surface 1*, the view factor from *surface 1* to itself ($F_{1,1}$ - the sensor to itself) is determined by inspection to be 0. The view factor from *surface 1* to *surface 3* ($F_{1,3}$ - the sensor to the outer surface of the shield) is also determined by inspection to be 0. The two remaining view factors from *surface 1* are $F_{1,2}$ and $F_{1,4}$. $F_{1,2}$ is the view factor from the outside surface of a small interior cylinder to the inside surface of a larger outer cylinder. This view factor is built into EES as the function **F3D_26** which uses

a correlation from Rae (1975). With $F_{1,2}$ determined, three of the four view factors from *surface 1* are known and the last view factor ($F_{1,4}$) can be found using the enclosure rule.

$$F_{1,4} = 1 - F_{1,1} - F_{1,2} - F_{1,3} \tag{3.2.8}$$

```
F[1,1]=0                                                    "surface 1 to surface 1"
F[1,2]=F3D_26(((L_sh-L)/2),L,((L_sh-L)/2),d/2,d_sh/2)       "surface 1 to surface 2"
F[1,3]=0                                                    "surface 1 to surface 3"
F[1,4]=1-F[1,1]-F[1,2]-F[1,3]                               "surface 1 to surface 4"
```

To determine all of the view factors associated with *surface 2*, it is necessary to compute the view factor from *surface 2* to *surface s*. With this in mind, the first view factor found is from *surface 1* to *surface s* ($F_{1,s}$). $F_{1,s}$ is equal to $F_{1,4}$, since the only place in which the sensor sees the surroundings is through *surface s*. Through reciprocity the view factor from *surface s* to *surface 1* is found.

$$F_{s,1} = \frac{A_1 F_{1,s}}{A_s} \tag{3.2.9}$$

The next view factor found is from *surface s* to itself ($F_{s,s}$). The view factor between two circular surfaces with a cylinder centered between them is determined using a correlation from Shukla and Ghosh (1985). With $F_{s,s}$ determined, the view factor $F_{s,2}$ can be computed using the enclosure rule and $F_{2,s}$ can be determined by reciprocity.

$$F_{s,2} = 1 - F_{s,1} - F_{s,s} \tag{3.2.10}$$

$$F_{2,s} = \frac{A_s F_{s,2}}{A_2} \tag{3.2.11}$$

```
F_1_s=F[1,4]                                                "surface 1 to open ends"
```

```
F_s_1=A[1]*F_1_s/A_s                                                    "open ends to surface 1"
F_s_2=1-F_s_1-F_s_s                                                     "open ends to surface 2"

F_s_s=(1-(R_3*LL-R_1)^2/(R_1*(LL-1))^2)*(1-LL/R_1*(((LL/(2*R_1))^2+1)^0.5-LL/(2*R_1)))
R_1=(d_sh/2)/((L_sh-L)/2)                                               "parameter of equation"
R_3=(d/2)/((L_sh-L)/2)                                                  "parameter of equation"
LL=L_sh/((L_sh-L)/2)                                                    "parameter of equation"

F_2_s=A_s*F_s_2/A[2]                                                    "surface 2 to open ends"
```

The view factor from *surface 2* to *surface 1* ($F_{2,1}$) can be determined from $F_{1,2}$ through reciprocity. $F_{2,3}$ by inspection is 0, the inside surface of the shield cannot see the outside surface of the shield. $F_{2,4}$ is equal to $F_{2,s}$ because all of the radiation exchange between *surface 2* and the surroundings occurs through *surface s*. With three of the four view factors from *surface 2* known, the enclosure rule is used to determine $F_{2,2}$.

$$F_{2,1} = \frac{A_1 F_{1,2}}{A_2} \tag{3.2.12}$$

$$F_{2,2} = 1 - F_{2,1} - F_{2,3} - F_{2,4} \tag{3.2.13}$$

```
F[2,1]=A[1]*F[1,2]/A[2]                                                 "surface 2 to surface 1"
F[2,2]=1-F[2,1]-F[2,3]-F[2,4]                                           "surface 2 to surface 2"
F[2,3]=0                                                                "surface 2 to surface 3"
F[2,4]=F_2_s                                                            "surface 2 to surface 4"
```

All of the view factors from *surface 3* are determined by inspection. The outside surface of the radiation shield cannot see the temperature sensor, the inside surface of the radiation shield, or itself, therefore $F_{3,1} = F_{3,2} = F_{3,3} = 0$. The only surface seen by *surface 3* is the surroundings (i.e. $F_{3,4} = 1$).

```
F[3,1]=0                                                                "surface 3 to surface 1"
F[3,2]=0                                                                "surface 3 to surface 2"
F[3,3]=0                                                                "surface 3 to surface 3"
F[3,4]=1                                                                "surface 3 to surface 4"
```

With the view factors for *surfaces 1-3* determined all of the view factors from *surface 4* are determined by reciprocity and the enclosure rule.

$$F_{4,1} = \frac{A_1 F_{1,4}}{A_4} \tag{3.2.14}$$

$$F_{4,2} = \frac{A_2 F_{2,4}}{A_4} \tag{3.2.15}$$

$$F_{4,3} = \frac{A_3 F_{3,4}}{A_4} \tag{3.2.16}$$

$$F_{4,4} = 1 - F_{4,1} - F_{4,2} - F_{4,3} \tag{3.2.17}$$

```
F[4,1]=A[1]*F[1,4]/A[4]                    "surface 4 to surface 1"
F[4,2]=A[2]*F[2,4]/A[4]                    "surface 4 to surface 2"
F[4,3]=A[3]*F[3,4]/A[4]                    "surface 4 to surface 3"
F[4,4]=1-F[4,1]-F[4,2]-F[4,3]              "surface 4 to surface 4"
```

With each surface and its corresponding view factors determined, a systematic approach is used to solve the diffuse, gray surface radiation problem. The net rate of radiation exchange from any surface *i* is found by (Nellis and Klein, 2009):

$$\dot{q}_i = \frac{\varepsilon_i A_i (E_{b,i} - J_i)}{(1 - \varepsilon_i)} \text{ for } i = 1 \ldots 4 \tag{3.2.18}$$

where ε_i is the emissivity of surface *i*, A_i is the area of *surface i*, $E_{b,i}$ is the blackbody emissive power of *surface i*, and J_i is the radiosity of *surface i*. An energy balance for each radiosity node leads to:

$$\dot{q}_i = A_i \sum_{j=1}^{4} F_{i,j}(J_i - J_j) \text{ for } i = 1...4 \tag{3.2.19}$$

To implement these energy balances in EES, a duplicate loop is used:

```
"energy balances"
duplicate i=1,4
    q_dot_rad[i]=epsilon[i]*A[i]*(E_b[i]-J[i])/(1-epsilon[i])        "surface heat transfer rates"
    q_dot_rad[i]=A[i]*sum(F[i,j]*(J[i]-J[j]),j=1,4)                  "radiosity energy balances"
end
```

To close the equation set, an appropriate boundary condition must be determined for each surface. *Surface 1* is the wet-bulb temperature sensor, thus its temperature is the wet-bulb temperature. *Surface 4* consists of the surroundings which are at the dry-bulb temperature.

$$T_1 = T_{wb} \tag{3.2.20}$$

$$T_4 = T_{db} \tag{3.2.21}$$

By knowing the temperatures of *surface 1* and *surface 4* the blackbody emissive powers are:

$$E_{b,1} = \sigma T_1^4 \tag{3.2.22}$$

$$E_{b,4} = \sigma T_4^4 \tag{3.2.23}$$

where σ is Stefan-Boltzmann's constant (5.67×10^{-8} W m^{-2} K^{-4}).

```
"boundary conditions"
T[1]=T_wb                                   "temp sensor temperature"
T[4]=T_db                                   "surroundings temperature"
E_b[1]=sigma#*T[1]^4                        "black body emissive power"
E_b[4]=sigma#*T[4]^4                        "black body emissive power"
```

A third boundary condition is determined from the assumption that the temperature of the inside surface of the shield (*surface 2*) is equal to the temperature of the outside surface of the shield (*surface 3*). This assumption is appropriate because the shield is made from a very thin sheet of metal with minimal conductive resistance.

$$T_2 = T_3 \tag{3.2.24}$$

For the final boundary condition an energy balance on the radiation shield is performed. The heat transfers due to both convection and radiation must balance each other. To determine the average heat transfer coefficient experienced on the inside of the shield (*surface 2*) the internal EES function **PipeFlow** is used. This function uses the correlations discussed in Section 5.2.4 of Nellis and Klein (2009). The average heat transfer coefficient experienced on the outside of the radiation shield (*surface 3*) is found using the **External_Flow_Plate** function in EES, which uses the Churchill and Ozoe (1973) correlation to determine the Nusselt number.

```
T[2]=T[3]                                                    "temperatures are equal"

"heat transfer coefficient- surface 2"
call PipeFlow('AirH2O',T_db,P,m_dot,d_sh,L_sh,RelRough:h_conv_2T, h_conv_2H ,DELTAP,
Nusselt_2T, f_2, Re_2)
RelRough=1e-6[-]                                             "roughness approximation"
m_dot=0.25*pi*d_sh^2*u_inf*rho_2                             "mass flow rate"
rho_2=Density(Air,T=T_db,P=P)                                "density"

"heat transfer coefficient- surface 3"
Call External_Flow_Plate('AirH2O',T_db,T[3],P,u_inf,L_sh:tau,h_conv_3,C_f_3,Nusselt_3,Re_3)
```

With the heat transfer coefficient on the inside and outside of the radiation shield known, the convective heat transfer <u>to</u> the inside and outside of the radiation shield, respectively, is:

$$\dot{q}_{conv,2} = h_{conv,2T} A_2 (T_{db} - T_2) \tag{3.2.25}$$

$$\dot{q}_{conv,3} = h_{conv,3} A_3 (T_{db} - T_3) \tag{3.2.26}$$

The heat transfer <u>from</u> the shield due to radiation is already determined by Eq. (3.2.18) and (3.2.19). From this information an energy balance on the radiation shield is written.

$$\dot{q}_{conv,2} + \dot{q}_{conv,3} = \dot{q}_{rad,2} + \dot{q}_{rad,3} \tag{3.2.27}$$

Solving for the remaining blackbody emissive powers:

$$E_{b,2} = \sigma T_2^4 \tag{3.2.28}$$

$$E_{b,3} = \sigma T_3^4 \tag{3.2.29}$$

With this information, the problem is fully defined and the parasitic heat gain experienced by the wet-bulb temperature sensor due to radiation can be found.

```
q_dot_conv[2]=A[2]*h_conv_2T*(T_db-T[2])          "convective heat xfer- surface 2"
q_dot_conv[3]=A[3]*h_conv_3*(T_db-T[3])           "convective heat xfer- surface 3"

q_dot_conv[3]+q_dot_conv[2]=q_dot_rad[2]+q_dot_rad[3]   "energy balance"

E_b[2]=sigma#*T[2]^4                              "black body emissive power"
E_b[3]=sigma#*T[3]^4                              "black body emissive power"
```

The quantity of interest is the net rate of radiation heat transfer to the wet-bulb temperature sensor, which is the negative of $\dot{q}_{rad,1}$.

$$\dot{q}_{rad,wb} = -\dot{q}_{rad,1} \tag{3.2.30}$$

```
q_rad_wetbulb=-q_dot_rad[1]                       "heat transfer to the sensor"
```

With the parameters as specified above, the net radiation parasitic is $\dot{q}_{rad,wb} = 10.96\ \text{mW}$. The next section deals with the optimization of the shield geometry.

3.2.1 Radiation Shield Optimization

This section of the report focuses on the optimization of the radiation shield to reduce the radiation parasitic to the wet-bulb to as small of value as possible. From Figure 3-26 it is clear that the only parameter free to vary is the length of the shield (L_{sh}). As described in Section 3.2 the diameter of the shield is specified by the length of the shield due to the boundary layers extending from the sensor and the shield.

The model of the radiation shield, as described in Section 3.2, is optimized in EES. The internal optimization tool in EES finds that the minimum amount of radiation heat transfer to the wet-bulb temperature sensor occurs when the shield is approximately the same length as the temperature sensor. The reason for this is because *surface 1* (i.e. the temperature sensor) is the outside surface of the temperature sensor, excluding the ends of the sensors. Excluding the ends greatly simplifies the calculation of the view factors. When the surface area is approximated in this manner, the view factor between the temperature sensor and the inside surface of the radiation shield is nearly one when the shield is of the same length as the sensor and increasing the length of the shield does little to increase the view factor. The model fails to capture the radiation exchange from the surroundings to the ends of the temperature sensor. When the ends of the temperature sensor are taken into account, an additional parasitic of ≈1 mW is expected.

Figure 3-27 is a plot of the radiation parasitic to the wet-bulb sensor at the optimal shield geometry as determined by the EES model described in Section 3.2.

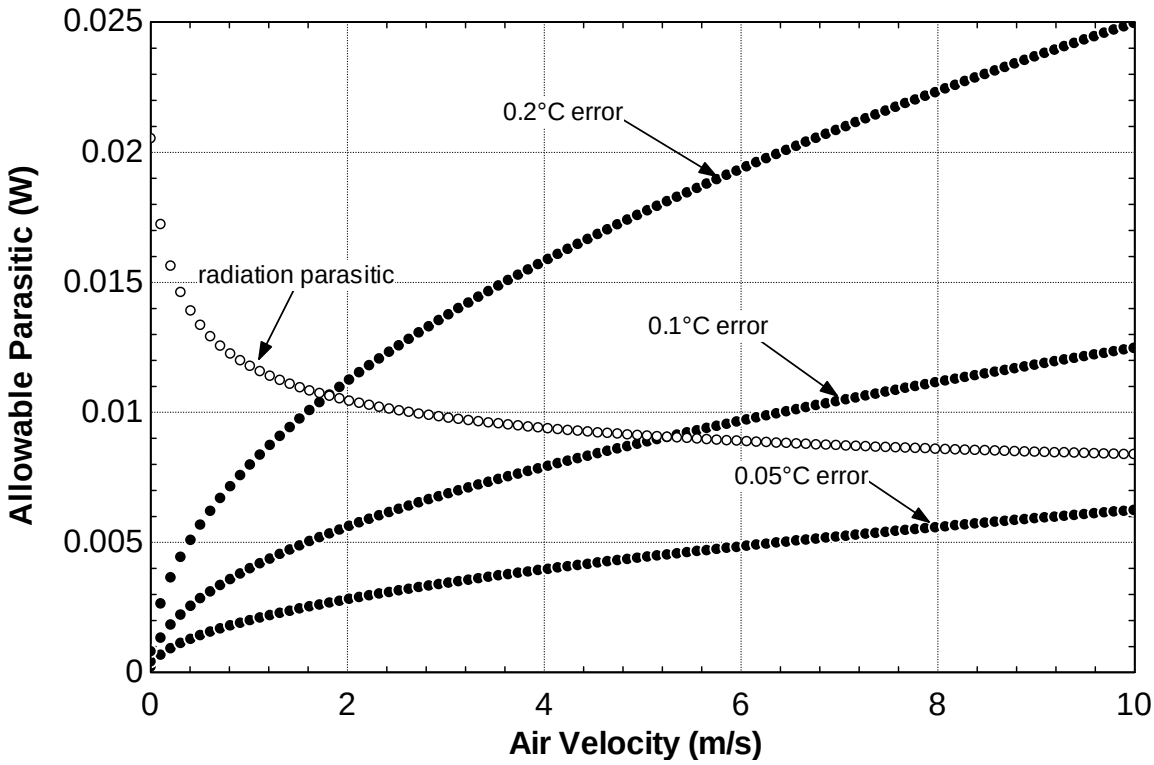

Figure 3-27: Radiation parasitic heat gain to an axial mounted temperature sensor as a function of air velocity. The closed circles represent the parasitic heat transfer to the axial wet-bulb temperature sensor corresponding to errors in the wet-bulb temperature measurement of 0.05°C, 0.1°C, and 0.2°C. The open circles represent the parasitic heat transfer to the axial wet-bulb temperature sensor as a result of radiation. The shield is kept at its optimal length, $L_{sh} \approx L$.

Similarly to the transverse configuration, as the air velocity across the axial mounted temperature sensor is increased, the parasitic heat gain to the sensor is reduced. The is due to the fact that as the air velocity increases the boundary layers extending from the shield and the temperature sensor are not as large and therefore the shield can be brought in closer to the

sensor. The model shows that at an air velocity of 10 m/s the radiation parasitic is still more than 2 mW above what is acceptable for an error in the wet-bulb temperature of 0.05°C.

The impact of adding low emissivity screens or louvers to the upstream and downstream open ends of the radiation shield is illustrated in Figure 3-28.

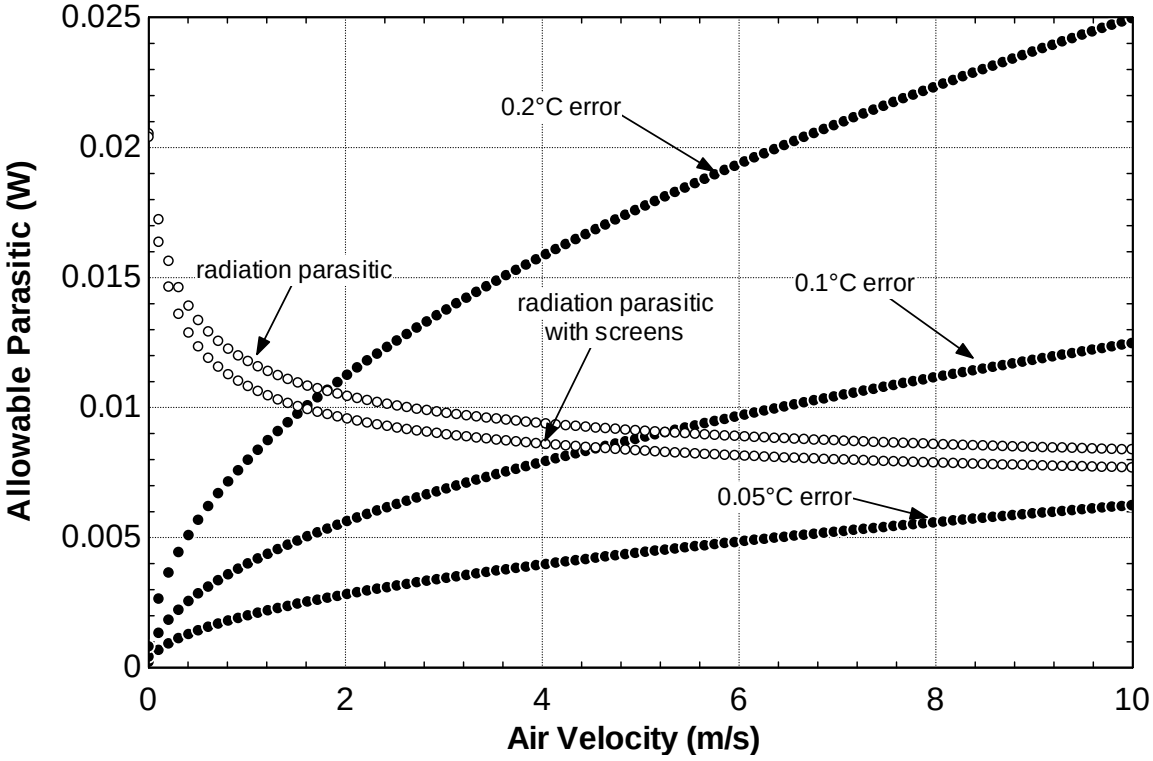

Figure 3-28: Radiation parasitic heat gain to the axially mounted temperature sensor as a function of air velocity. The closed circles represent the parasitic heat transfer to the axial wet-bulb temperature sensor corresponding to errors in the wet-bulb temperature measurement of 0.05°C, 0.1°C, and 0.2°C. The open circles represent the parasitic heat transfer to the axial wet-bulb temperature sensor as a result of radiation. The shield is kept at its optimal length, $L_{sh} \approx L$.

The models of the radiation shield with the high emissivity screens is approximated by reducing the surface area of the front and back open ends of the shield by a factor of two and increasing the surface area of the radiation shield by an equal amount. The addition of

screens reduces the radiation parasitic to the wet-bulb by less than 1 mW. The screens have only a small impact because in the model there is only a small amount of radiation exchange occurring between the surroundings and the sensor.

Again the parasitic heat transfer to the wet-bulb is above the allowable quantity. Figure 3-29 illustrates the impact of cooling the radiation shield to the wet-bulb temperature.

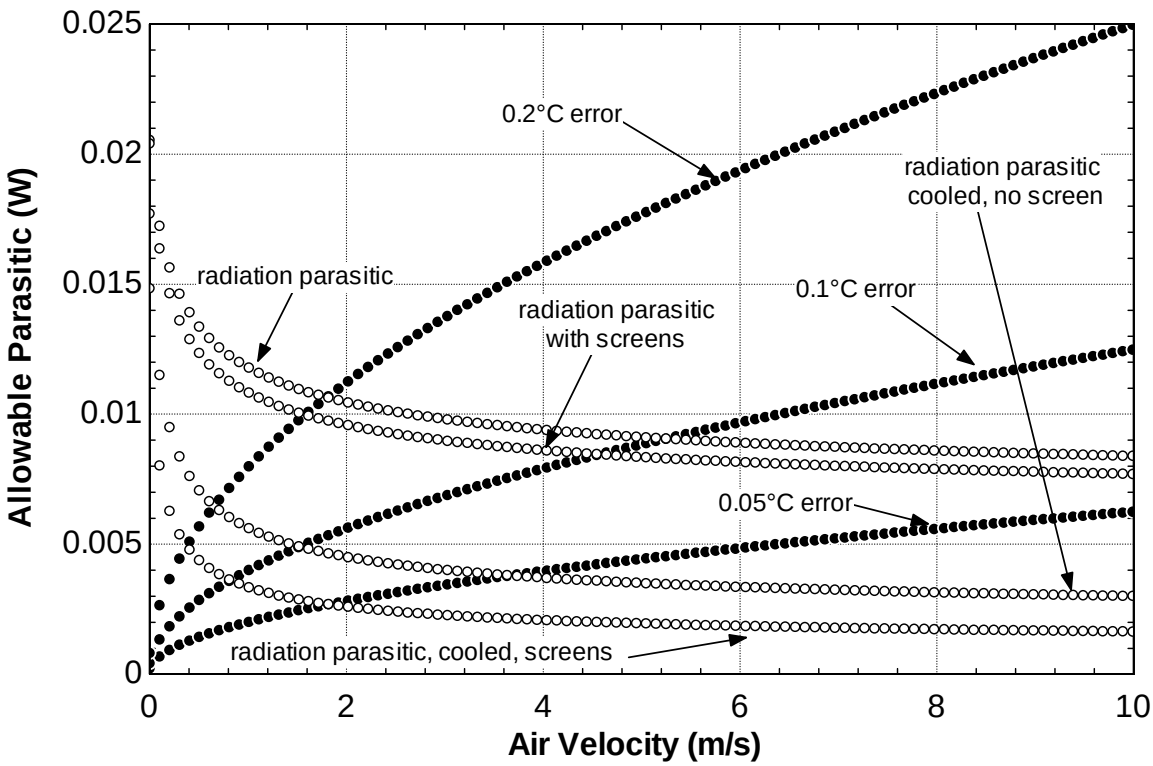

Figure 3-29: Radiation parasitic heat gain to an axial mounted temperature sensor as a function of the air velocity. The closed circles represent the parasitic heat transfer to the axial wet-bulb temperature sensor corresponding to errors in the wet-bulb temperature measurement of 0.05°C, 0.1°C, and 0.2°C. The open circles represent the parasitic heat transfer to the axial wet-bulb temperature sensor as a result of radiation with various shield configurations. The cooled shield is held at the wet-bulb temperature (19.4°C).

From Figure 3-29 it is clear that cooling the radiation shield significantly reduces the amount of parasitic heat transfer to the wet-bulb temperature sensor. Similarly to the transverse flow

configuration a cooled radiation shield can reduce the parasitic below the 0.05°C error "budget".

3.3 Conduction/ Makeup Water Parasitic

This section considers the combined parasitic effects of the makeup water flow, conduction through the sheath and temperature sensor leads, evaporation from the wet cotton sock, and convection along the sensor sheath. Figure 3-30 is a schematic of the sensor wetting apparatus.

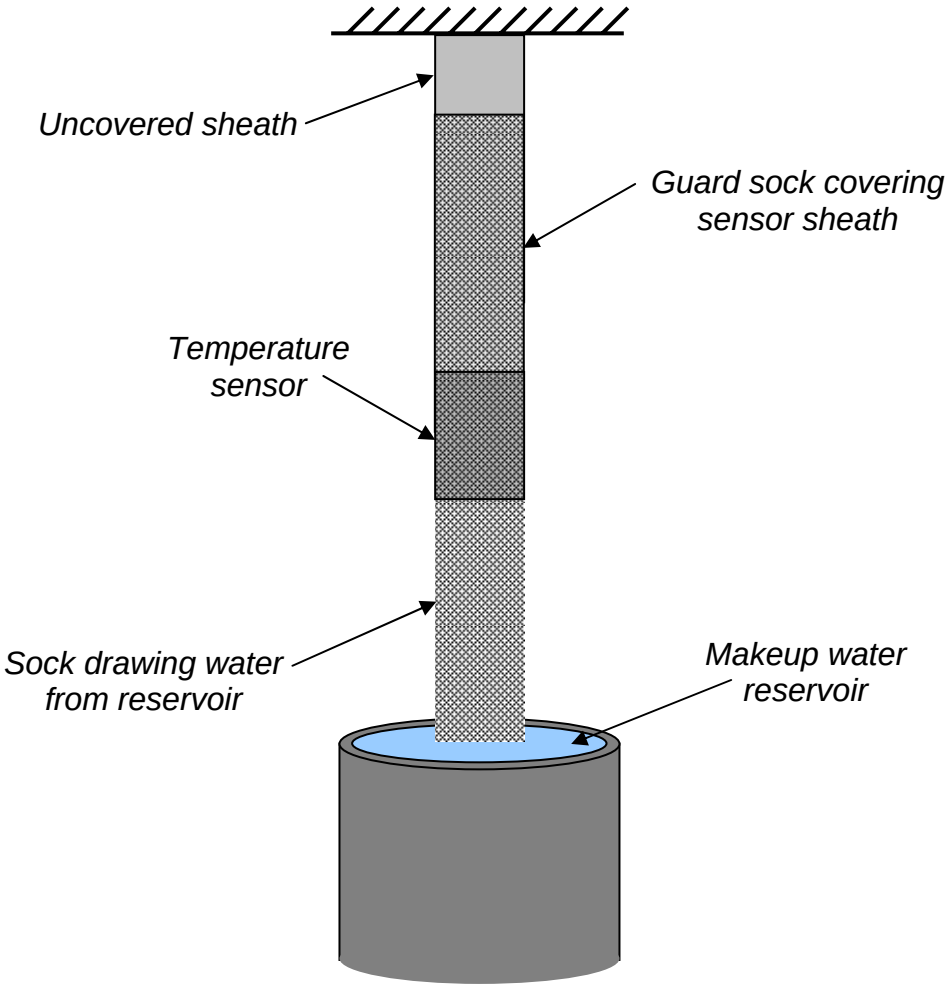

Figure 3-30: Schematic of the wicking setup modeled. A temperature sensor probe protrudes down from the top with the sensor located at the end of the probe. The wetting sock draws water from a reservoir via capillary action to the temperature sensor and up across the stem to thermally guard the sheath.

The first step in the modeling process is the derivation of the appropriate energy and mass balances. The schematic shown in Figure 3-30 is separated into three sections for modeling purposes: (1) the upper portion of the temperature probe, (2) the section of the temperature probe housing the temperature sensor, and (3) the lower portion of the wet cotton sock which extends into the water reservoir.

3.3.1 Upper Portion of Temperature Probe

In this analysis the section of the probe considered is the portion extending from the end of the wet sock opposite the temperature sensor ($x = 0$) to the start of the temperature sensor ($x = L$). This is shown more clearly in Figure 3-31.

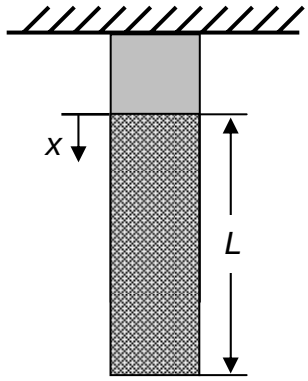

Figure 3-31: Top section of the temperature sensor probe modeled.

The position of $x = 0$, as shown in Figure 3-31 is at the location where the cotton sock extending onto the temperature probe terminates; this position is assumed to be at the dry-bulb temperature. At $x = L$ the section of the temperature probe which houses the temperature sensor begins. This is the location in which the temperature of the probe must be at the wet-bulb temperature to ensure accurate results.

There are four copper lead wires that are located in the center of the temperature probe and they are separated from the sheath by alumina insulation tubing and powder, as shown in Figure 3-32.

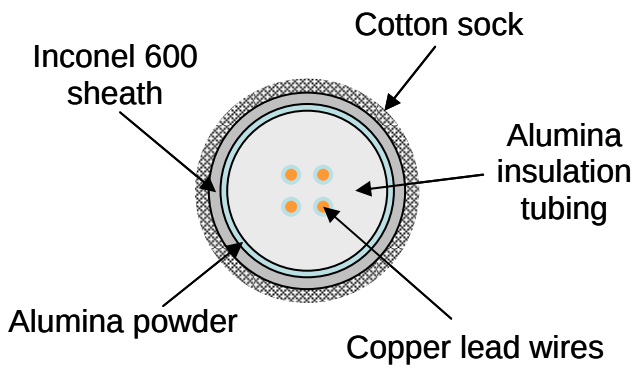

Figure 3-32: Cross-sectional view of the upper section of the temperature probe.

A conservative estimate of the thermal conductivity of alumina insulation tubing is 15 W/m-K (Auerkari, 1996). The relatively high thermal conductivity suggests that the copper lead wires are well coupled, thermally, to the sheath. To be certain, however, that the temperature of the lead wires will be nearly equal to the temperature of the sheath and wick at each x-position an additional calculation is done. This calculation will establish whether it is possible to lump the sheath, wet cotton sock, and lead wires together at a single temperature or if the copper lead wires will have to be considered independently of the sheath and wet cotton sock. This calculation is done by treating the sheath and the wet cotton sock as being at the same temperature and determining the ratio of the thermal resistance between the sheath/sock and the copper wires to the thermal resistance between the sheath/sock and the surroundings. Figure 3-33 shows a simple resistance network between the copper lead wires and the free stream air on the exterior of the temperature probe.

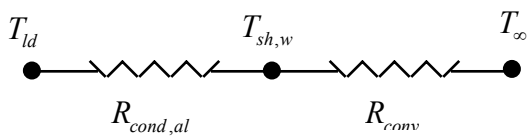

Figure 3-33: Thermal resistance network between a copper lead wire positioned at the center of the temperature probe and the exterior free stream air. The sheath and wet cotton sock are assumed to be at the same temperature (i.e. $T_{sh,w}$).

The thermal resistances shown in Figure 3-33 are calculated using Eq. (3.3.1) and (3.3.2) below. $R_{cond,al}$ is the resistance due to conduction through the alumina insulation/powder, and R_{conv} is the convective resistance from the sheath/sock to the outside air.

$$R_{cond,al} = \frac{\ln\left(\dfrac{d_{in,sh}}{d_{out,ld}}\right)}{2\,\pi\,L\,k_{al}} \tag{3.3.1}$$

$$R_{conv} = \left(\frac{1}{\bar{h}\;L\;per}\right) \tag{3.3.2}$$

In Eq. (3.3.1) $d_{in,sh}$ and $d_{out,ld}$ are the inner diameter of the sheath and the outer diameter of the lead wire, respectively, L is the length of probe/wire considered, and k_{al} is the thermal conductivity of the alumina insulation. In Eq. (3.3.2) $\bar{h}$ is the average heat transfer coefficient experience on the outside of the sheath, L is the again the length of the probe/wire considered, and *per* is a measure of the perimeter of the sheath.

The appropriate parameters are entered in EES (Note the heat transfer coefficient, $\bar{h}$, used in the calculation is consistent with a free stream air velocity of 4 m/s across the exterior of the sheath):

```
$TabStops 0.2 0.4 0.6 0.8 3.5 in
$UnitSystem SI MASS RAD K PA J

T_db=converttemp(C,K,26.7)                          "dry-bulb temperature"
T_wb=converttemp(C,K,19.4)                          "wet-bulb temperature"
T_film=(T_db+T_wb)/2                                "film temperature"
P=101325[Pa]                                        "atmospheric pressure"
RH=0.515572785 [-]                                  "relative humidity"

L=2[in]*convert(in,m)                               "arbitrary length segment"
d_out_ld=0.51054[mm]*convert(mm,m)                  "diameter of leads"

d_out_sh=0.25[in]*convert(in,m)                     "outer diameter of sheath"
d_in_sh=d_out_sh-2*th                               "inner diameter of sheath"
th=0.01[in]*convert(in,m)                           "thickness of sheath"

k_al=15[W/m-K]                                      "thermal conductivity- alumina"

h_bar=83.35[W/m^2-K]                                "heat transfer coefficient"
per=d_out_sh*pi                                     "perimeter of the sheath"

R_cond_al=ln(d_in_sh/d_out_ld)/(2*pi*L*k_al)        "conductive resistance of the air"

R_conv=1/(h_bar*L*per)                              "convective resistance"
```

The value of interest is the ratio of the conductive resistance to the convective resistance. This resistance ratio (*RR*) calculation is shown in Eq. (3.3.3) below.

$$RR = \frac{R_{cond,al}}{R_{conv}} \tag{3.3.3}$$

A large value of *RR* corresponds to a large resistance between the sheath and lead wires that cannot be neglected. On the other hand, if *RR* is very small (e.g., < 0.1) then the resistance

between the sheath and the lead wires can be neglected and the lead wires will be at the same temperature as the sheath/sock.

```
RR=R_cond_al/R_conv                                    "ratio of resistances"
```

With the parameters as specified $RR = 0.04$. The small value of RR suggests that the copper wires do come to the sheath temperature and therefore it is not necessary to evaluate the copper lead wires independently of sheath and wet cotton sock.

With this information an appropriate energy balance is derived for the upper portion of the temperature probe. The three methods of heat transfer through a differential segment of the upper section of the temperature probe that are considered are axial conduction, convection and evaporation to the free stream air, and the energy associated with the makeup water.

The rate equation used to describe the axial conduction through upper section of the probe is Fourier's law:

$$\dot{q} = -kA_c \frac{d}{dx} T(x) \tag{3.3.4}$$

where $T(x)$ is the temperature at position x. When conduction through only one material is considered, k is the conductivity and A_c is the cross-sectional area of the material through which conduction is occurring. The RR previously calculated suggests that the entire cross-section of the upper section of the probe is at a uniform temperature. This means that there are effectively four pathways for energy to transfer via axial conduction (i.e. lead wires,

alumina insulation, sheath, and wet cotton sock) and an effective conductivity/cross-sectional area product is necessary (kA_{top}). To combine the effects of the four conduction pathways the effective conductivity/cross-sectional area product (kA_{top}) is computed by:

$$kA_{top} = k_{ld} A_{ld} + k_{al} A_{al} + k_{sh} A_{sh} + k_w A_w \tag{3.3.5}$$

where k_{ld}, k_{al}, k_{sh}, and k_w are the conductivities of the copper lead wire, the alumina insulation, the inconel sheath, and the wet cotton sock respectively and A_{ld}, A_{al}, A_{sh}, and A_w are the associated cross-sectional areas. The conductivity of the water is used to approximate the conductivity of the wet cotton sock.

The convective heat transfer from a differential segment of the temperature probe is:

$$\dot{q} = \bar{h}\ per\ (T(x) - T_\infty)\ dx \tag{3.3.6}$$

where $\bar{h}$ is the average heat transfer coefficient experienced along the temperature probe, *per* is the perimeter of the temperature probe, $T(x)$ is the temperature at position x, T_∞ is the free stream air temperature, and dx is the differential length segment.

The evaporative heat transfer from a differential segment of the temperature probe is:

$$\dot{q}(x) = \bar{h}_D\ per\ (c_{v,sat}(T(x)) - c_\infty)\ h_g(T(x))\ dx \tag{3.3.7}$$

where $\bar{h}_D$ is the average mass transfer coefficient experienced along the temperature probe, *per* is again the perimeter of the temperature probe, $c_{v,sat}$ $(T(x))$ is the concentration of

saturated water vapor corresponding to the temperature ($T(x)$) at the given location, c_∞ is the concentration of water vapor in the free stream air, $h_g(T(x))$ is the enthalpy of water vapor corresponding to the temperature ($T(x)$) at the given location, and dx is the differential length segment. The concentration gradient drives the mass transfer of water from the wet-bulb to the free stream air and as a result energy is transferred from the temperature probe.

The energy associated with the makeup water is:

$$\dot{q}(x) = \dot{m}_l(x)\ h_l(T(x)) \tag{3.3.8}$$

In Eq. (3.3.8) $\dot{m}_l(x)$ is the mass flow rate of liquid water wicking along the sock and $h_l(T(x))$ is the enthalpy of the liquid water at a given x location.

The energy transfers both into and out of a differential segment of the upper portion of the temperature probe, as discussed previously, are shown in Figure 3-34.

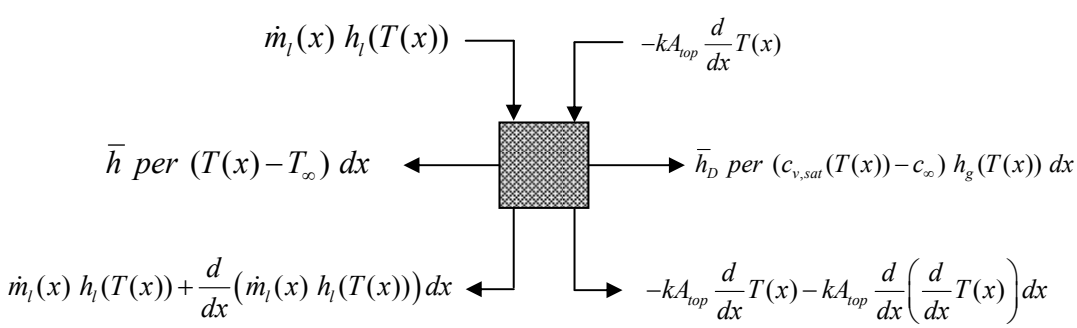

Figure 3-34: Energy transfer associated with a differential segment of the upper portion of the temperature probe.

Writing an energy balance on the differential segment shown in Figure 3-34 yields Eq. (3.3.9):

$$\begin{aligned}
&\dot{m}_l(x)\ h_l(T(x)) - kA_{top}\frac{d}{dx}T(x) = \dot{m}_l(x)\ h_l(T(x))... \\
&+\frac{d}{dx}\left(\dot{m}_l(x)\ h_l(T(x))\right)dx - kA_{top}\frac{d}{dx}T(x) - kA_{top}\frac{d}{dx}\left(\frac{d}{dx}T(x)\right)dx... \\
&+\bar{h}\ per\ (T(x)-T_\infty)\ dx + \bar{h}_D\ per\ (c_{v,sat}(T(x))-c_\infty)\ h_g(T(x))\ dx
\end{aligned} \tag{3.3.9}$$

The mass balance associate with the same differential segment of the upper section of the probe is derived. The mass transfer from the temperature probe due to evaporation is:

$$\dot{m} = \bar{h}_D\ per\ (c_{v,sat}(T(x)) - c_\infty)\ dx \tag{3.3.10}$$

The appropriate mass transfers to and from a differential segment of the upper section of the probe is shown in Figure 3-35.

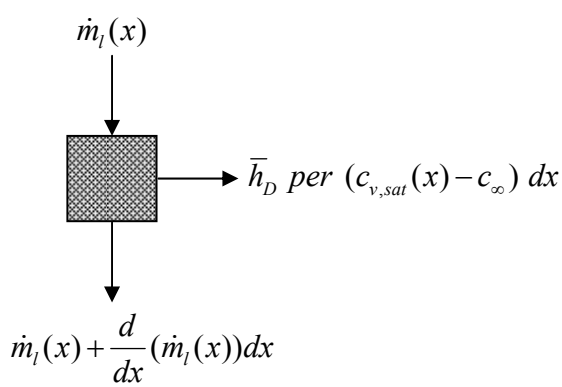

Figure 3-35: Mass transfers associated with a differential segment of the upper portion of the temperature probe.

A mass balance on the differential portion of the temperature probe shown in Figure 3-35 is written in Eq. (3.3.11) below:

$$\dot{m}_l(x) = \dot{m}_l(x) + \frac{d}{dx}\left(\dot{m}_l(x)\right)dx + \bar{h}_D \; per \; (c_{v,sat}(T(x)) - c_\infty) \; dx \tag{3.3.11}$$

Both the mass and energy balance equation (i.e. Eq. (3.3.9) and (3.3.11)) for the upper portion of the temperature probe are simplified and written below as Eq. (3.3.12) and (3.3.13) , respectively.

$$\begin{aligned} 0 &= h_l(T(x))\frac{d}{dx}\dot{m}_l(x) + \dot{m}_l(x)\frac{d}{dx}h_l(T(x)) - kA_{top} \; \frac{d}{dx}\left(\frac{d}{dx}T(x)\right)... \\ &+\bar{h} \; per \; (T(x) - T_\infty) + \bar{h}_D \; per \; (c_{v,sat}(T(x)) - c_\infty) \; h_g(T(x)) \end{aligned} \tag{3.3.12}$$

$$\frac{d}{dx}\dot{m}_l(x) = -\bar{h}_D \; per \; (c_{v,sat}(T(x)) - c_\infty) \tag{3.3.13}$$

For further simplification of the energy balance, the change in the mass flow rate as a function of location (x), which is defined in Eq. (3.3.13), is substituted into Eq. (3.3.12). This substitution leads to:

$$\begin{aligned} 0 &= -\bar{h}_D \; per \; (c_{v,sat}(T(x)) - c_\infty) \; h_l(T(x)) + \dot{m}_l(x)\frac{d}{dx}h_l(T(x))... \\ &-kA_{top} \; \frac{d}{dx}\left(\frac{d}{dx}T(x)\right) + \bar{h} \; per \; (T(x) - T_\infty) + \bar{h}_D \; per \; (c_{v,sat}(T(x)) - c_\infty) \; h_g(T(x)) \end{aligned} \tag{3.3.14}$$

Simplifying Eq. (3.3.14):

$$\begin{aligned} 0 &= \dot{m}_l(x)\frac{d}{dx}h_l(T(x)) - kA_{top}\frac{d}{dx}\left(\frac{d}{dx}T(x)\right) + \bar{h} \; per \; (T(x) - T_\infty)... \\ &+\bar{h}_D \; per \; (c_{v,sat}(T(x)) - c_\infty) \; \Delta h_{fg}(T(x)) \end{aligned} \tag{3.3.15}$$

where:

$$\Delta h_{fg}(T(x)) = h_g(T(x)) - h_l(T(x)) \tag{3.3.16}$$

In Eq. (3.3.15) $\frac{d}{dx} h_l(T(x))$ is closely approximated by $c_p \frac{d}{dx} T(x)$ where c_p is the specific heat capacity of water, which is assumed constant over the temperature range of interest, and $T(x)$ is the temperature of the sheath/sock at the x location of interest. Applying these assumptions, Eq. (3.3.15) becomes:

$$\begin{aligned} 0 = \dot{m}_l(x)\ c_p \frac{d}{dx} T(x) - kA_{top} \frac{d}{dx}\left(\frac{d}{dx} T(x)\right) + \bar{h}\ per\ (T(x) - T_\infty)... \\ + \bar{h}_D\ per\ (c_{v,sat}(T(x)) - c_\infty)\ \Delta h_{fg}(T(x)) \end{aligned} \tag{3.3.17}$$

With the mass and energy balances for the upper section of the temperature probe written in Eq. (3.3.13) and (3.3.17), three state variables of interest are apparent: mass flow rate of liquid, probe temperature, and the gradient in the temperature of the probe. The state equations (i.e., the rates of change of the state variables) are derived in order to solve the set of differential equations. From the differential segment of the upper portion of the probe:

$$\frac{d}{dx} \dot{m}_l(x) = -\bar{h}_D\ per\ (c_{v,sat}(T(x)) - c_\infty) \tag{3.3.18}$$

$$\frac{d}{dx}\big(T(x)\big) = \frac{d}{dx}\big(T(x)\big) \tag{3.3.19}$$

$$\begin{aligned} \frac{d}{dx}\left(\frac{d}{dx} T(x)\right) = \frac{\dot{m}_l(x)\ c_p}{kA_{top}} \frac{d}{dx} T(x) + \frac{\bar{h}\ per}{kA_{top}}\big(T(x) - T_\infty\big)... \\ + \frac{\bar{h}_D\ per}{kA_{top}}\ (c_{v,sat}(T(x)) - c_\infty)\ \Delta h_{fg}(T(x)) \end{aligned} \tag{3.3.20}$$

To solve the given set of differential equations, a fully implicit numerical integration scheme is implemented in EES.

The parameters necessary to solve the system of differential equations along with boundary conditions are specified in EES. Note the model is implemented at nominal test condition 1 (T_{db} = 26.7°C/ T_{wb} = 19.4°C) and with an air velocity of 4 m/s:

```
$TabStops 0.2 0.4 0.6 0.8 3.5 in
$UnitSystem SI MASS RAD K PA J

"Free stream air conditions"
T_db=converttemp(C,K,26.7)                          "dry-bulb temperature"
T_wb=converttemp(C,K,19.4)                          "wet-bulb temperature"
P=Po#                                               "atmospheric pressure"
RH=0.515572785 [-]                                  "relative humidity"
u_inf=4[m/s]                                        "free-stream air velocity"

"Sensor Dimensions"
d=0.25[in]*convert(in,m)                            "diameter"
k=1.2[in]*convert(in,m)                             "length"
per=pi*d                                            "perimeter"

"Material properties and dimensions"
L_in=4[in]                                          "length of probe in inches"
L=L_in*convert(in,m)                                "length of probe to analyze"

d_out_sh=0.25[in]*convert(in,m)                     "outer diameter of sheath"
d_in_sh=d_out_sh-2*th                               "inner diameter of sheath"
th=0.01[in]*convert(in,m)                           "thickness of sheath"

d_out_ld=0.51054[mm]*convert(mm,m)                  "diameter of bare leads"

d_out_w=d_out_sh+2*th_w                             "outer wick diameter"
d_in_w=d_out_sh                                     "inner wick diameter"
th_w=0.5[mm]*convert(mm,m)                          "thickness of wick"

A_ld=4*0.25*pi*d_out_ld^2                           "cross-sectional area"
k_ld=k_('Copper',T=T_film)                          "thermal conductivity of copper"

A_al=0.25*pi*d_in_sh^2-A_ld                         "cross-sectional area"
k_al=15[W/m-K]                                      "thermal conductivity of alumina"

A_sh=0.25*pi*(d_out_sh^2-d_in_sh^2)                 "cross-sectional area"
k_sh=14.8[W/m-K]                                    "thermal conductivity of sheath"
```

```
A_w=0.25*pi*(d_out_w^2-d_in_w^2)                    "cross-sectional area"
k_w=Conductivity(Water,T=T_film,P=P)                "thermal conductivity of water"

"Axial conduction- kA products"
kA_top=k_ld*A_ld+k_al*A_al+k_sh*A_sh+k_w*A_w        "kA product"

"Heat and mass transfer coefficients"
T_film=(T_wb+T_db)/2                                "film temperature"
rho=density(AIRH2O,T=T_film,P=P,R=RH)               "density"
k_air=conductivity(AIRH2O,T=T_film,P=P,R=RH)        "conductivity"
mu=viscosity(AIRH2O,T=T_film,P=P,R=RH)              "viscosity"
c=CP(AIRH2O,T=T_film,P=P,R=RH)                      "specific heat capacity"

D_w_a=D_12_gas('H2O','AIR',T_film,P)                "diffusion coefficient"

nu=mu/rho                                           "kinematic viscosity"
alpha=k_air/(rho*c)                                 "thermal diffusivity"

Pr=nu/alpha                                         "Prandtl number"
Sc=nu/D_w_a                                         "Schmidt number"
Re=u_inf*d*rho/mu                                   "Reynolds number"
Le=alpha/D_w_a                                      "Lewis number"

Call External_Flow_Cylinder_ND(Re,Pr:Nusselt,C_d1)  "Nusselt number"
h=Nusselt*k_air/d                                   "heat transfer coefficient"

Call External_Flow_Cylinder_ND(Re,Sc:Sh,C_d2)       "Sherwood number"
h_D=Sh*D_w_a/d                                      "mass transfer coefficient"

P_v_inf=RH*pressure(Water,T=T_db,x=1)               "vapor pressure of free stream air"
c_v_inf=density(Water,P=P_v_inf,T=T_db)             "concentration-free stream"

cp=SpecHeat(Water,T=T_film,P=P)                     "specific heat of water"
```

An in-depth description of the calculation of the moist air properties of the free stream air and the calculation of both the heat and mass transfer coefficient across the temperature sensor can be found in Section 2.1. With these parameters now specified in EES, the next step is to set up a duplicate loop to carry out the numerical integration necessary to solve system of differential equations. The duplicate loop creates M steps in which each step is of length Δx, where:

$$\Delta x = \frac{L}{M-1} \tag{3.3.21}$$

```
"Integral Parameters"
M=75[-]                                                    "number of length steps"
DELTAx=L/(M-1)                                             "length of time step"
duplicate j=1,M
    x[j]=(j-1)*L/(M-1)                                     "length assoc. with each time step"
    x_in[j]=x[j]*convert(m,in)
end
```

The boundary condition for mass flow rate at the upper end of the wick (i.e., at x = 0 mm Figure 3-31) is 0 kg/s because there is no place for the liquid to go once it reaches the end of the wick material. The temperature of the probe at the upper end of the wick (x=0) is set to be at the dry-bulb temperature. At the location in which the temperature sensor portion of the probe begins (i.e. $x = L$), the temperature of the probe is assumed to be at the wet-bulb temperature.

```
"Boundary Conditions"
m_dot_l[1]=0[kg/s]                                         "initial mass flow rate of liquid"
T[1]=T_db                                                  "initial probe temperature"
T[M]=T_wb                                                  "probe end temperature"
```

After the boundary conditions are specified, the local latent heat of vaporization and concentration of saturated water vapor are calculated at each x location.

```
duplicate j=1,(M-1)

    DELTAh_fg[j+1]=Enthalpy(Water,T=T[j+1],x=1)-Enthalpy(Water,T=T[j+1],x=0)
    c_v_sat[j+1]=density(Water,T=T[j+1],x=1)
```

This information is enough to complete the numerical integration necessary to solve the differential equations specified in Eq. (3.3.18) to (3.3.20).

```
    m_dot_l[j+1]=m_dot_l[j]-h_D*per*(c_v_sat[j+1]-c_v_inf)*DELTAx
    dT\dx[j+1]=dT\dx[j]+(m_dot_l[j+1]*cp/kA_top*dT\dx[j+1]+h*per/kA_top*(T[j+1]-
     ...T_db)+h_D*per/kA_top*(c_v_sat[j+1]-c_v_inf)*DELTAh_fg[j+1])*DELTAx
```

```
    T[j+1]=T[j]+dT\dx[j+1]*DELTAx
end
```

The temperature of the upper section of the probe is plotted against the distance from the beginning of the wick (i.e. $x = 0$ in Figure 3-31) for a wet bulb depression of 7.3°C.

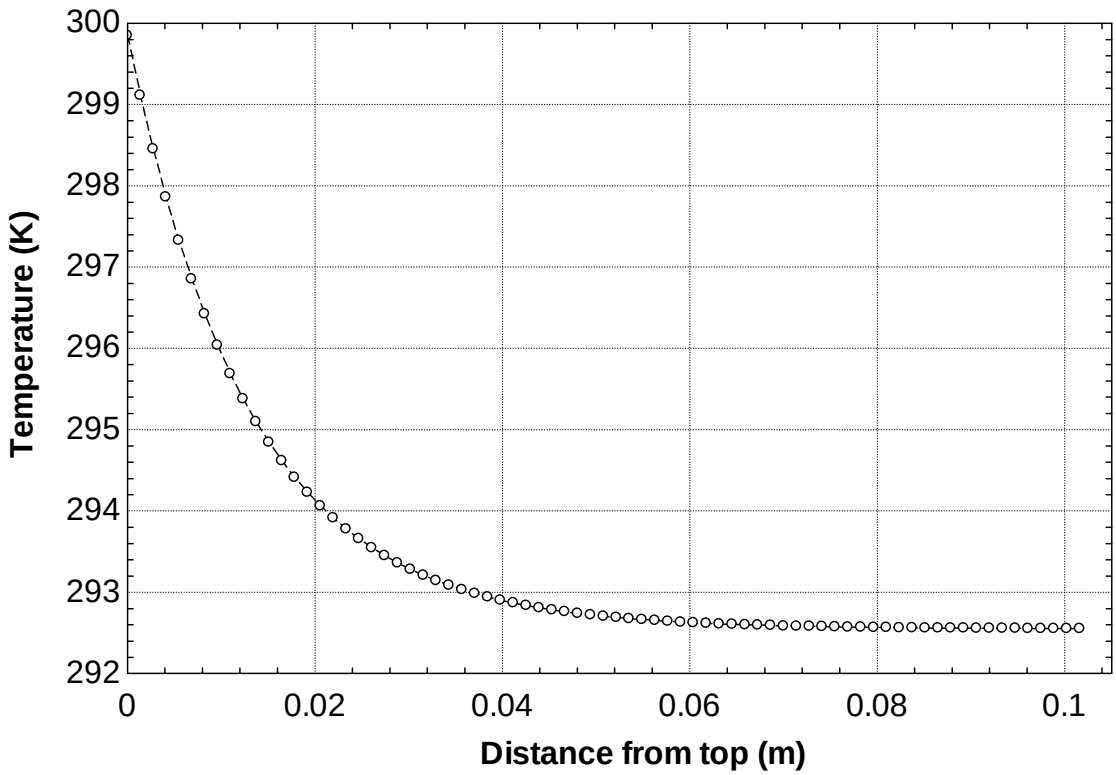

Figure 3-36: A plot of the temperature of the upper section of the probe at incremental distances from the top of the temperature probe in transverse orientation. The end distance corresponds to a position of $x = L$ in Figure 3-31 ($L = 0.10$ m or 4 in, in the above plot).

The temperature profile displayed in Figure 3-36 shows that, at a distance of 0.10 m (4 in) from the top of the probe, the temperature of the probe closely approaches the wet-bulb temperature. With the probe approaching the wet-bulb temperature, the corresponding parasitic heat gain axially through the temperature sensor approaches zero.

Figure 3-37 represents the amount of parasitic heat transfer to the temperature sensor for given values of wick extension above the sensor.

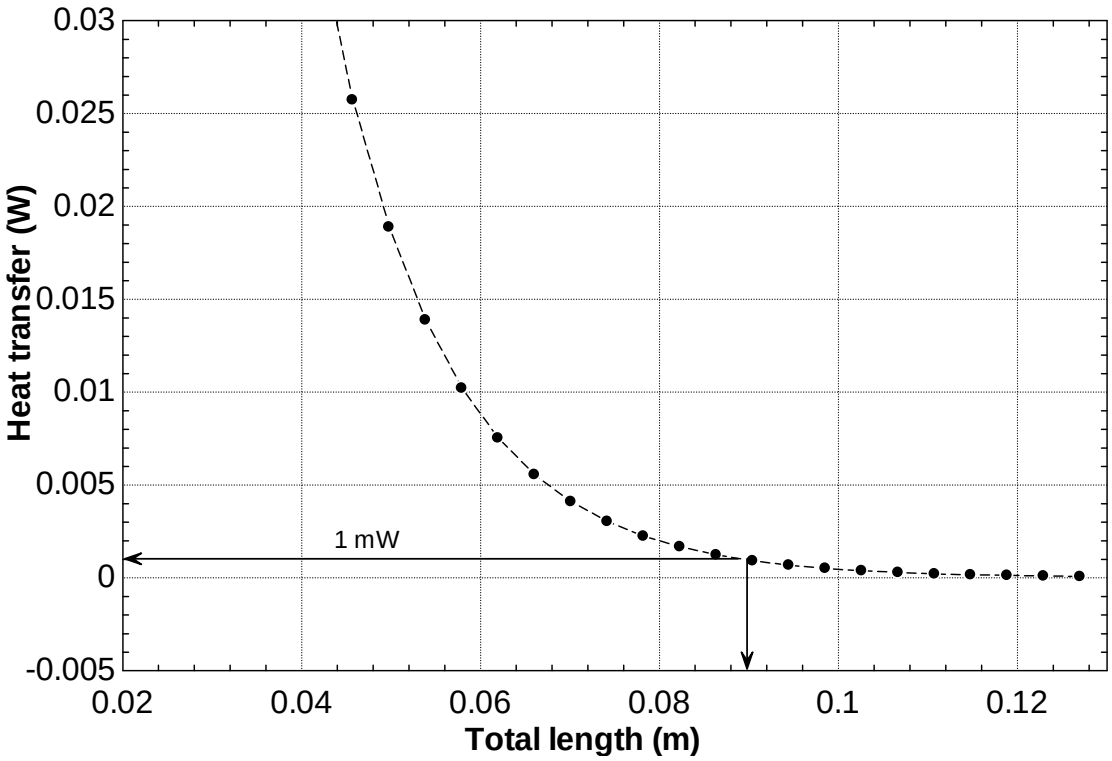

Figure 3-37: Heat transfer to the temperature sensor as a function of the distance in which the wick extends past the temperature sensor portion of the probe. The data is for an air velocity of 4 m/s at a wet-bulb temperature of 19.4°C and a dry-bulb temperature of 26.7°C.

The arrowed lines in Figure 3-37 represent the amount in which the sock must extend beyond the tip of the temperature probe to reduce the parasitic heat transfer to the temperature sensor to a value of 1mW or less. If the parasitic heat transfer to the sensor from the probe is to be reduced to 1 mW the wick must extend a distance of at least 0.09 m (3.6 in) on to the probe beyond the temperature sensor.

In Chapter 5 an empirical model is developed which allows for the prediction of the wicking height at any psychrometric condition. This empirical model is used in conjunction with the conduction/makeup water parasitic model discussed here to more accurately predict the parasitic heat transfer to the temperature sensor over an entire range of conditions.

3.3.2 Lower Portion of Cotton Sock

Section 3.3.1 quantifies the parasitic heat transfer to the temperature sensor form the upper portion of the temperature probe. The parasitic calculated in Section 3.3.1 includes the parasitic due to the makeup water, and the combined effects of conduction through the lead wires, alumina insulation, and wet cotton sock surrounding the temperature probe. In this section the parasitic associated with the lower portion of the sock is calculated. Figure 3-38 shows the section of the sock that is considered.

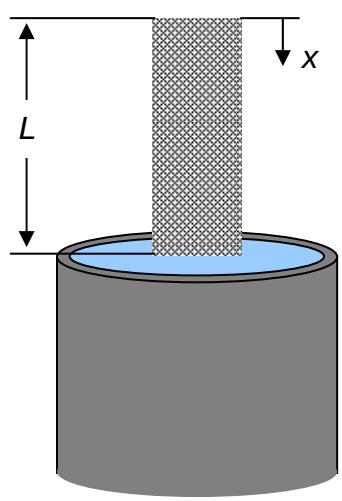

Figure 3-38: Portion of the wick that draws water from the water reservoir up to the temperature sensor. The sock leaves the temperature sensor at a location of $x = 0$ and enters the water reservoir at a location of $x = L$.

The parasitic calculation is done for a wet cotton sock having three different geometries. A cross-sectional view of the three different geometries is shown in Figure 3-39.

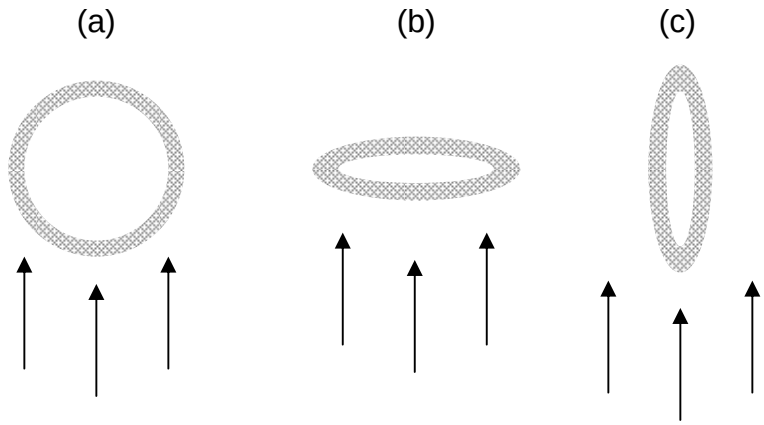

Figure 3-39: Cross-sectional view of the wick geometries modeled in the analysis: (a) the wick remains in a cylindrical shape between the probe and the water reservoir, (b) the wick collapses on itself and is oriented perpendicular to the flow direction, and (c) the wick collapses on itself and is oriented parallel to the flow direction. The arrows represent the flow direction across the wicks as viewed from the top.

Similar to Section 3.3.1, it is necessary to complete both an energy and mass balance on a differential section of the lower portion of the cotton sock. There are a few slight differences in the way in which the energy and mass balances are carried out for the lower portion of the cotton sock compared to the upper region which includes the sock as well as the lead wires and sheath. In the lower portion of the device, axial conduction only occurs through the sock since there is nothing in the interior of the sock. From the energy and mass balances the three state variables are:

$$\frac{d}{dx}\left(\frac{d}{dx}T(x)\right)=\frac{\dot{m}_l(x)\,c_p}{kA_w}\frac{d}{dx}T(x)+\frac{\overline{h}\;per}{kA_w}(T(x)-T_\infty)\ldots$$
$$+\frac{\overline{h}_D\;per}{kA_w}\;(c_{v,sat}(T(x))-c_\infty)\;\Delta h_{fg}(T(x)) \tag{3.3.22}$$

$$\frac{d}{dx}\big(T(x)\big)=\frac{d}{dx}\big(T(x)\big) \tag{3.3.23}$$

$$\frac{d}{dx}\dot{m}_l(x) = -\bar{h}_D \; per \; (c_{v,sat}(T(x)) - c_\infty) \tag{3.3.24}$$

The heat and mass transfer coefficients experienced on the outside of the cylindrical wick (Figure 3-39(a)) are calculated in the same manner as before and under the assumption that the wet cotton sock remains in a cylindrical shape. The only new term is in Eq. (3.3.22) where:

$$kA_w = k_w A_w \tag{3.3.25}$$

In Eq. (3.3.25) k_w is the conductivity of water and A_w is the cross-sectional area of the wet cotton sock. The necessary parameters are specified in EES and to remain consistent with Section 3.3.1 the ambient air conditions remain at standard test condition 1 and the air velocity is set to 4 m/s.

```
$TabStops 0.2 0.4 0.6 0.8 3.5 in
$UnitSystem SI MASS RAD K PA J

"Free stream air conditions"
T_db=converttemp(C,K,26.7)                          "dry-bulb temperature"
T_wb=converttemp(C,K,19.4)                          "wet-bulb temperature"
P=Po#                                               "atmospheric pressure"
RH=0.515572785 [-]                                  "relative humidity"
u_inf=4[m/s]                                        "free-stream air velocity"

"Sensor Dimensions"
d=0.25[in]*convert(in,m)                            "diameter"
k=1.2[in]*convert(in,m)                             "length"
per=pi*d                                            "perimeter"

"Material properties and dimensions"
L=1[in]*convert(in,m)                               "length of probe to analyze"

d_out_sh=0.25[in]*convert(in,m)                     "outer diameter of sheath"
d_in_sh=d_out_sh-2*th                               "inner diameter of sheath"
th=0.01[in]*convert(in,m)                           "thickness of sheath"

d_out_w=d_out_sh+2*th_w                             "outer wick diameter"
d_in_w=d_out_sh                                     "inner wick diameter"
```

```
th_w=0.5[mm]*convert(mm,m)                          "thickness of wick"

A_w=0.25*pi*(d_out_w^2-d_in_w^2)                    "cross-sectional area"
k_w=Conductivity(Water,T=T_film,P=P)                "thermal conductivity of water"

"Axial conduction- kA products"
kA_w=k_w*A_w                                        "kA product of sock"

"Heat and mass transfer coefficients"
T_film=(T_wb+T_db)/2                                "film temperature"
rho=density(AIRH2O,T=T_film,P=P,R=RH)               "density"
k_2=conductivity(AIRH2O,T=T_film,P=P,R=RH)          "conductivity"
mu=viscosity(AIRH2O,T=T_film,P=P,R=RH)              "viscosity"
c=CP(AIRH2O,T=T_film,P=P,R=RH)                      "specific heat capacity"

D_w_a=D_12_gas('H2O','AIR',T_film,P)                "diffusion coefficient"

nu=mu/rho                                           "kinematic viscosity"
alpha=k_2/(rho*c)                                   "thermal diffusivity"

Pr=nu/alpha                                         "Prandtl number"
Sc=nu/D_w_a                                         "Schmidt number"
Re=u_inf*d*rho/mu                                   "Reynolds number"
Le=alpha/D_w_a                                      "Lewis number"

Call External_Flow_Cylinder_ND(Re,Pr:Nusselt,C_d1)  "Nusselt number"
h=Nusselt*k_2/d                                     "heat transfer coefficient"

Call External_Flow_Cylinder_ND(Re,Sc:Sh,C_d2)       "Sherwood number"
h_D=Sh*D_w_a/d                                      "mass transfer coefficient"

P_v_inf=RH*pressure(Water,T=T_db,x=1)               "vapor pressure of free stream air"
C_v_inf=density(Water,P=P_v_inf,T=T_db)             "concentration-free stream"

cp=SpecHeat(Water,T=T_film,P=P)                     "specific heat of water"
```

The system of equations is solved in the exact same manner as in Section 3.3.1 with the only exception being the boundary conditions specified. The temperature of the sock at the temperature sensor (i.e. x = 0 mm Figure 3-38) is set equal to the wet-bulb temperature and the temperature of the sock once it reaches the makeup water reservoir (i.e. $x = L$) is set equal to the dry-bulb temperature. This assumes that the water in the reservoir is at the dry-bulb temperature. The final boundary condition specified is the mass flow rate of water at x = 0. The mass flow rate at x = 0 is the sum of the mass flow due to evaporation from both the

upper portion of the temperature probe and from temperature sensor section of the probe. With the boundary conditions specified the numerical integration is carried out in EES.

Figure 3-40 represents the amount of heat transfer through the wick at interval locations between makeup water reservoir and the temperature sensor.

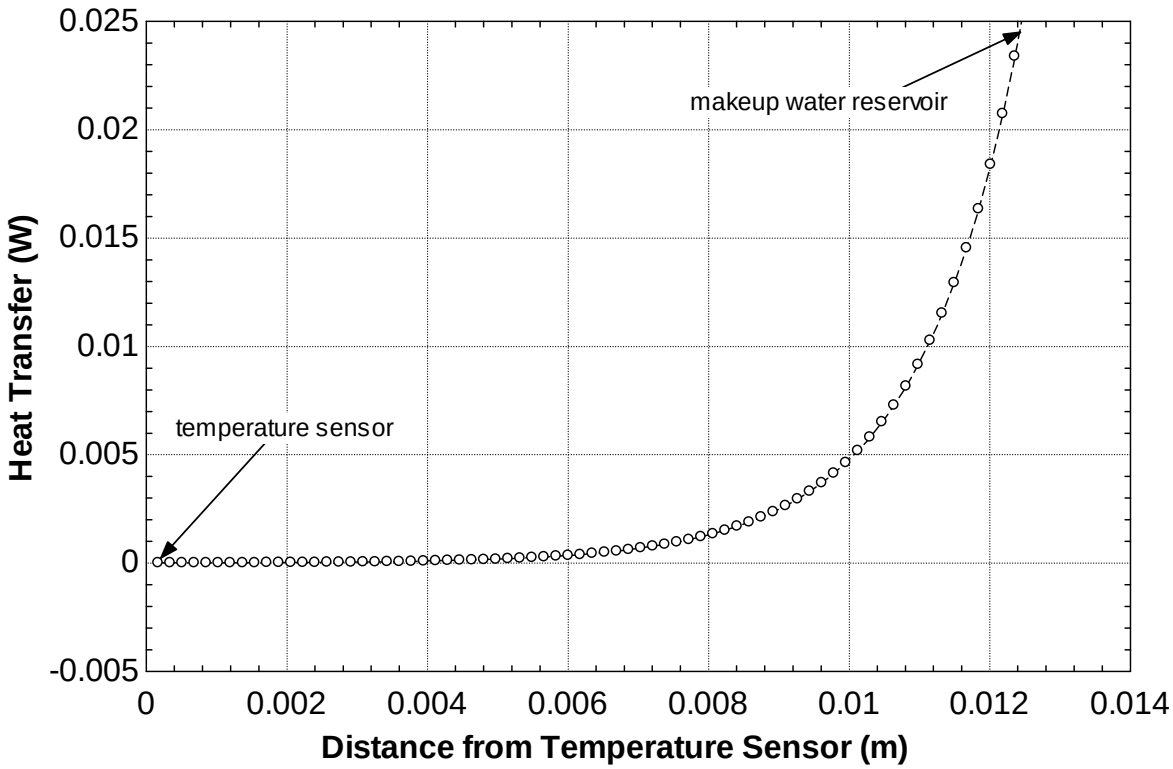

Figure 3-40: Plot of the heat transfer through the wet cotton sock at interval locations between the top of the makeup water reservoir and the bottom of the temperature sensor. The entire portion of the wick between the water reservoir and the bottom of the temperature sensor is exposed to the flow of the moist air stream.

From the plot it is clear that the temperature of the wick quickly reaches the wet-bulb temperature and as a result there is a negligible amount of parasitic heat transfer to the temperature sensor. A distance of about 13 mm (0.5 in) is a sufficient length for eliminating the parasitic associated with the makeup water being at the dry-bulb temperature.

The calculation of the parasitic heat transfer associated with the makeup water for a collapsed wet cotton sock positioned both parallel and perpendicular to the flow direction is exactly the same as the calculation for a wet cotton sock that remains cylindrically shaped, with one exception. The correlation used for the heat and mass transfer coefficients in Eq. (3.3.22) (3.3.24) is modified to reflect the different external flow condition. For the collapsed wet cotton sock turned parallel to the air flow direction, the **External_Flow_Plate_ND** correlation is used in EES, as determined by Churchill & Ozoe (1973). This correlation is used to calculate the Nusselt and Schmidt numbers which are used to find the heat and mass transfer coefficients experienced along the wick. In analyzing the collapsed wet cotton sock turned perpendicular to the air flow, a correlation from Jakob (1949) and White (2003) is used to determine the heat and mass transfer coefficients experienced by a flat plate oriented perpendicular to the flow stream. The correlation in EES is **External_Flow_VerticalPlate_ND**.

The results of these analyses are overlaid on Figure 3-40 and shown in Figure 3-41.

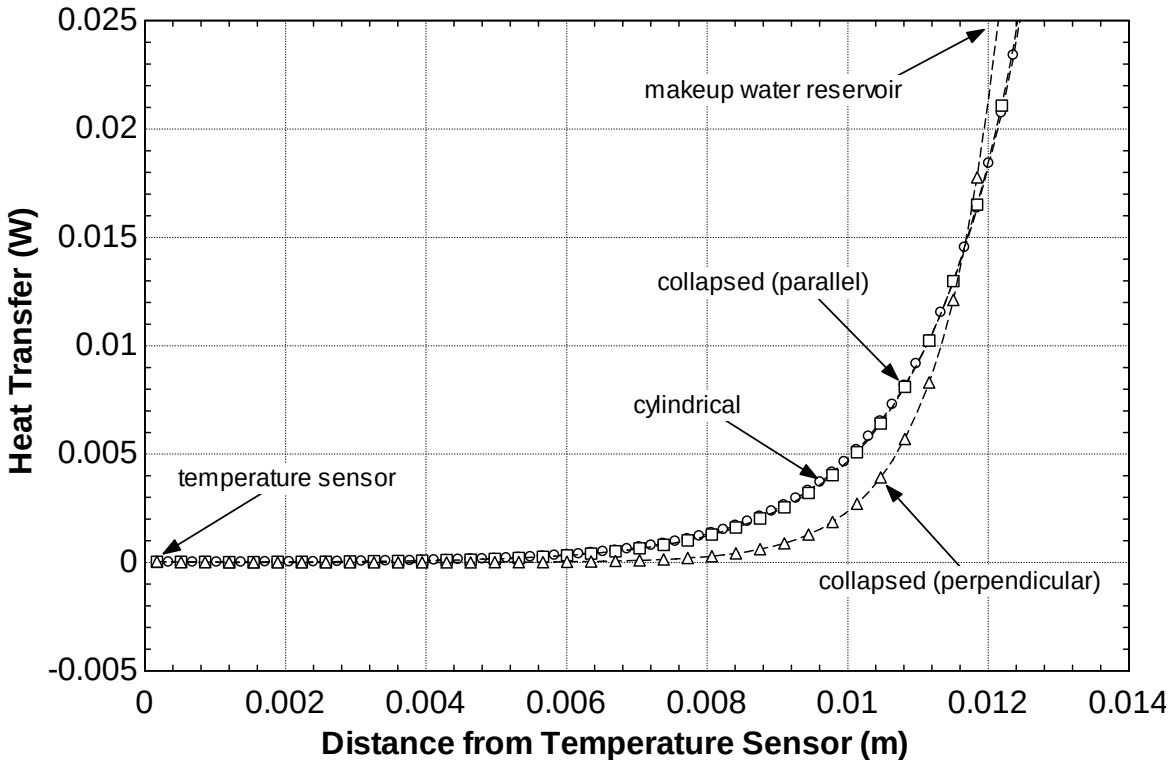

Figure 3-41: Plot of the heat transfer through the wet cotton sock at interval locations between the makeup water reservoir and the temperature sensor. The plot contains the data corresponding to the sock connecting the water reservoir to the temperature sensor in three different geometric orientations.

From Figure 3-41, it is clear that the geometric orientation of the cotton sock between the makeup water reservoir and the temperature sensor has little impact on the amount of heat transfer through the sock. The cotton sock collapsed on itself and oriented parallel to the flow produces almost the same results as the cotton sock remaining in a cylindrical shape. The collapsed sock oriented perpendicular to the flow, however, does produces slightly better results as the temperature of the sock approaches the wet-bulb temperature more quickly.

3.4 Parasitic Summary

In Sections 3.1 and 3.2 calculations are performed to determine the amount of radiation parasitic expected by a temperature sensor oriented in a transverse and axial configuration,

respectively. **The models described in both of these sections suggest that even with standard radiation shields in place, the radiation parasitic cannot be reduced to an acceptable level for the measurement of the wet-bulb temperature to within ±0.05°C.** If more elaborative designs of the radiation shields are considered (e.g. shield cooling and shield entrance and exit screens) the models do indicate that the radiation parasitic can be reduced below the allowable parasitic budget.

The standard radiation shields do not appear to work better for the transverse configuration compared to the axial configuration, or visa versa. With the radiation shield reducing the parasitic to the temperature sensor by proportionately equal amounts for both the transverse and axial configuration, the decision is made to terminate the analysis of the axially configured temperature sensor at this point. The transverse configuration is the favorable configuration because of its inherently larger parasitic budget over the range of velocities under consideration.

In Section 3.3 calculations are performed to determine the amount of parasitic heat transfer to the temperature sensor that could be expected as a result of conduction through the sheath and lead wires. Also considered in these calculations is the amount of parasitic that can be expected as a result of the makeup water temperature being at a value other than the wet-bulb temperature. These analyses indicate that a wet cotton sock extending a distance of 4 inches onto the temperature sensor probe, beyond the sensor itself, is enough to approximately guard the temperature sensor from conduction parasitic. On the makeup water side of the temperature sensor much less sock is needed. The models indicate that 1.3 cm (0.5 in) of wet

cotton sock exposed to moving air stream is enough to eliminate all parasitic associated with makeup water.

Chapter 4 – Experimental Testing

4.1 Experimental Equipment & Apparatus

The design of the aspirated wet-bulb temperature measurement apparatus is based largely on the analytical models that have been described in the previous chapters. The construction of the wet-bulb temperature measurement apparatus utilizes the optimization results to minimize all forms of parasitic heat transfer to the wet-bulb temperature sensor. The modeled parasitics include radiation, axial conduction along the temperature sensor sheath and lead wires, and energy transfer associated with the makeup water. The findings from the analytical models were used to guide the design process and the equipment used to construct the experimental apparatus was selected in a manner that aimed to achieve the project objectives.

4.1.1 Temperature Sensing Equipment

The goal of the project is to measure the wet-bulb temperature to an accuracy of ±0.05°C, and as a result it is necessary to select temperature sensing equipment that can provide a measurement with this degree of accuracy. The temperature sensors selected for use as both dry-bulb and wet-bulb temperature measurement are Model 5640 Thermistor Probes from Fluke Corporation, Hart Scientific Division. The probes have a nominal resistance of 4.4 kΩ at 25°C. The manufacturer's stated uncertainty in the temperature measurement for the probes is ±0.002°C over a temperature range of 0°C-60°C. Physically, the temperature probes are 6.35 mm (0.25 in) in diameter and 23 cm (9 in) in length with a four wire output connection, as shown in Figure 4-1.

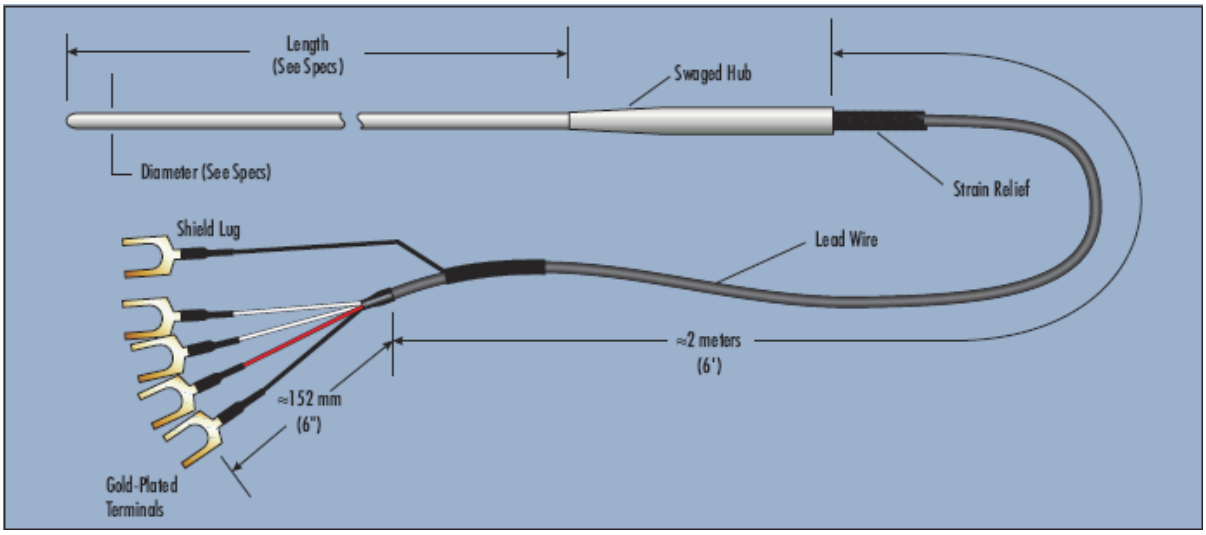

Figure 4-1: Fluke Model 5640 thermistor probe.

A thermistor is a temperature measurement device where the resistance varies with temperature in a deterministic and consistent manner. Since the datalogger is capable of measuring a voltage signal, it is necessary to supply the sensors with a known input current. The input current source used is a LakeShore Model 218 Temperature Monitor. The LakeShore Model 218 provides a current of 10 μA with an uncertainty of ±0.01% of the output.

4.1.2 Chilled Mirror Dew-Point Hygrometer

It is necessary to compare the wet-bulb temperature measured by the thermistor to a wet-bulb temperature measurement produced by an instrument with a known uncertainty. The instrument used as the basis for comparison is a chilled mirror dew-point hygrometer. Although the chilled mirror dew-point hygrometer does not measure the wet-bulb

temperature directly, the wet-bulb temperature can be determined from the dew-point temperature, pressure, and dry-bulb temperature.

The chilled mirror dew-point hygrometer used for this experiment is a General Eastern Instruments OptiSonde Chilled Mirror Hygrometer combined with a Model 1111H Single Stage Sensor having a rhodium mirror and a mylar vapor barrier. The GE OptiSonde Chilled Mirror Hygrometer has a two channel, 4-20 mA output and is pictured in Figure 4-2.

Figure 4-2: General Eastern Instruments OptiSonde Chilled Mirror Hygrometer.

The Model 1111H is an open-type sensor having a 2.54 cm (1 in) NPT connection that allows it to be connected to a standard pipe fitting or mounted in a type 0111D pressure boss. Figure 4-3 shows the Model 1111H sensor, which is capable of measuring a 45°C dew-point temperature depression at a dry bulb temperature of 25°C and a pressure 760 mmHg (1 atm).

Figure 4-3: General Eastern Instruments Model 1111H single stage dew-point temperature sensor.

For the experiment, the model 1111H sensor is threaded into a type 0111D pressure boss, which is shown in Figure 4-4.

Figure 4-4: Type 0111D pressure boss.

The 6.35 mm (0.25 in) compression fittings on the otherwise sealed pressure boss allow for a controlled air stream to be drawn across the chilled mirror sensor. A vacuum pump and air flow meter are attached downstream of the pressure boss to draw a known and consistent flow of air from the test section across the chilled mirror sensor. The vacuum pump and flow meter assembly are a General Eastern Instruments Model SSM-1 Sampling Module.

4.1.3 Velocity Transducer

A hot wire anemometer is used to measure the air velocity at the location of the temperature sensors. The sensor used is a TSI Model 8455 velocity transducer with a cylindrical shape measuring 6.35 mm (0.25 in) diameter and 30.5 cm (12 in) long. The transducer has a 0-5 V output over a 0-10 m/s measured air velocity. The velocity transducer is shown in Figure 4-5.

Figure 4-5: TSI Model 8455 velocity transducer.

4.1.4 Data Acquisition

The outputs from the previously defined sensors are recorded using a Campbell Scientific CR23X Micrologger. The CR23X is able to measure the voltage with an uncertainty of ±200 μV over the 0-200 mV range; this measurement range is consistent with the output voltage range of the temperature sensors. There is a higher uncertainty, ±5000 μV, associated with measuring voltages on the 0-5 V range; this range is consistent with the output voltage range of the velocity transducer and the chilled mirror hygrometer. To reduce the voltage uncertainties of the data logger each of the channels is calibrated. Each channel is calibrated

by supplying it with a range of known voltages and comparing the voltage measurement of the Campbell Scientific with the known voltage values. With this information a calibration curve is fit for each channel. A Keithley 2700 Multimeter is used to measure the known input voltage to a higher degree of accuracy than is capable by the Campbell Scientific Micrologger. Through this calibration process the uncertainty in the voltage measurement made by the Campbell Scientific CR23X Micrologger is reduced to ±10 μV over the 0-200 mV range and ±200 μV over the 0-5 V range.

Both the chilled mirror hygrometer and the barometric pressure transmitter output a 4-20 mA current which needs to be converted into a voltage allowing it to be read by the data logger. To convert the current to a voltage Monarch Instrument MA250R precision resistors are used. The precision resistors have a nominal resistance value of 250 Ω.

4.1.5 Pressure Measurement

To determine the adiabatic saturation temperature, it is necessary to dynamically measure the atmospheric pressure during testing. A Druck PTX 1225 barometric pressure transmitter is used to directly measure the atmospheric pressure during the time of testing. The Druck transmitter has a 594 to 879 mmHg (11.5 to 17 psia) pressure range with an accuracy of ±0.15% of the full scale reading. The output of the transmitter is a 4-20 mA current.

4.1.6 Axial Fan

An axial fan is used to draw air through a cylindrical duct and across the temperature sensors. The Continental AXC300A Series Inline Duct Fan, shown in Figure 4-6, was selected in

order to produce an air velocity in the range from 0-10 m/s through the duct test section. Both the inlet and outlet of the fan are 30.5 cm (12 in) in diameter and its rated capacity is 0.41 m^3/s (865 ft^3/min).

Figure 4-6: Continental AXC300A Series Inline Duct Fan.

To vary the speed over the range of air velocities required for testing, the fan is connected to a Variable Autotransformer shown in Figure 4-7.

Figure 4-7: Variable autotransformer (ISE, Inc.)

The autotransformer is an ISE, Inc. Model: 3PN1020B-XDVM with a 120 volt ac input and a 0-280 volt ac output.

4.1.7 Environmental Chambers

The completely constructed test apparatus is placed inside of a temperature and humidity-controlled environmental chamber. The purpose of the environmental chamber is to create the psychrometric conditions over a predefined range of temperature and humidity levels. Tescor, Inc. designed and built the environmental chamber, which is capable of providing dry bulb temperatures in the range of -10°C to 60°C over a dew-point temperature range of 5°C to 30°C.

4.1.8 Experimental Apparatus

The completed experimental apparatus is shown in Figure 4-8 below with key components labeled.

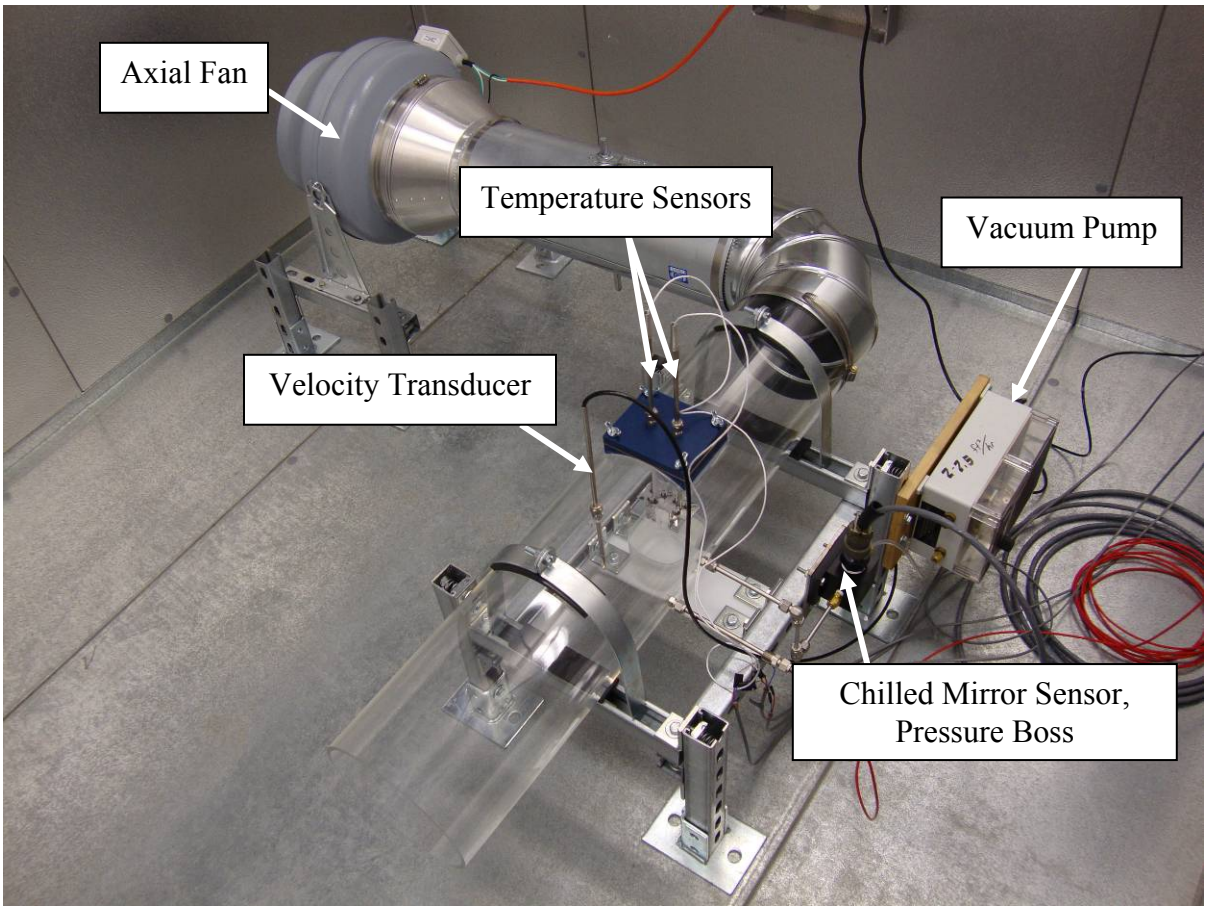

Figure 4-8: Experimental test apparatus for the measurement of wet-bulb temperature.

Air in the environmental chamber is drawn through the test section and across the temperature sensors by the axial fan and expelled directly back into the environmental chamber. This arrangement of the experimental apparatus was selected because the fan is located downstream of the temperature sensors and it draws air across the sensors rather than blowing air over the temperature sensors. This is done to ensure that the condition of the air from the chamber is not altered in any way, as would be the case if the air were to pass through the fan before passing over the temperature sensors.

Attached to the upstream end of the fan is a 30.5 cm (12 in) to 20.3 cm (8 in) diameter aluminum reducer, which is connected to a 20.3 cm (8 in) diameter by 61 cm (2 ft) long galvanized steel snap-lock round duct. The reducer is attached to the fan and the snap-lock duct using zinc plated worm-drive hose clamps. Continuing upstream of the snap-lock duct is a 20.3 cm (8 in) diameter galvanized steel 90 degree elbow. The purpose of the elbow is to ensure that the temperature sensors do not experience a radiation heat transfer with the fan. Because the fan operates a temperature higher than the dry-bulb temperature within the chamber, the radiation parasitic to the wet-bulb temperature sensor would increase if the sensor is able to 'see' the fan. The upstream end of the 90 degree elbow is attached to a 20.3 cm (8 in) O.D. (19.1 cm (7.5 in) I.D.) clear acrylic duct. The duct diameter of 20.3 cm (8 in) was selected, in part, for convenience. Both dry bulb and wet-bulb temperature measurements are made within this section of the experimental apparatus. Figure 4-9 provides a closer look at this section of the apparatus.

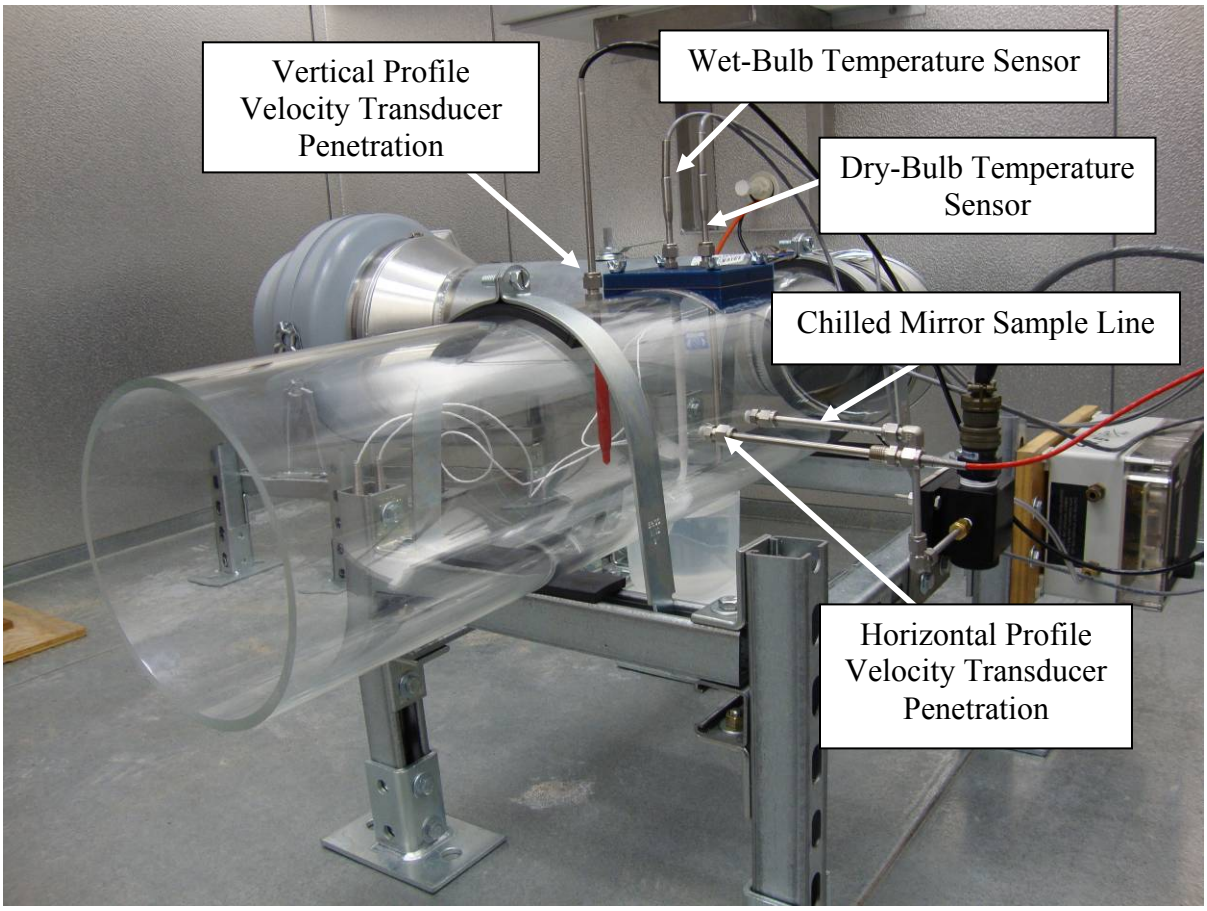

Figure 4-9: Temperature measurement section of the experimental apparatus.

The sensors are installed in a 20.3 cm (8 in) O.D. transparent acrylic duct. This duct is larger than would be expected in a typical application; however, a large duct provides greater flexibility for evaluating test parameters. For example, the height at which the cotton sock is able to draw water onto the temperature sensor probe and the distance between the water reservoir and temperature sensor. The analytical models and other calculations performed indicate that an 8 inch duct diameter is not a requirement for the accurate measurement of wet-bulb temperature.

Looking at Figure 4-9 and moving from the far upstream end of the acrylic duct towards the downstream end it is clear that the first penetrations of the duct are entry penetrations for the velocity transducer. There are two penetrations, both of which are located 16 inches from the duct entrance. One penetration is on the very top of the duct and protrudes vertically down through the center of the duct cross-section. The other penetration is on the side of the duct and protrudes horizontally across, again through the center of the duct cross-section. At each of these penetration locations a 3.2 mm (0.125 in) NPT hole is tapped into the acrylic duct. Threaded into the 3.2 mm (0.125 in) NPT holes are stainless steel Swagelok compression fittings (SS-400-1-2BT). The fittings are bored through fittings that are made to connect to 6.35 mm (0.25 in) O.D. tubing. Bored through fittings are used to allow the 6.35 mm (0.25 in) O.D. velocity transducer to slide completely through the fitting. Also, the stainless steel ferrules inside of the compression fittings are replaced with PTFE ferrules (T-400-SET). The use of PTFE ferrules allows the penetration depth of the velocity transducer to be adjusted while ensuring that the probe is not damaged in the process.

The next penetration of the acrylic duct, moving from the upstream end to the downstream end, is for the air sample line to the chilled mirror dew-point hygrometer sensor. This penetration is located 7.6 cm (3 in) downstream from the velocity transducer penetrations and is aligned with the horizontal axis cutting through the center of the duct cross-section. The penetration is again a 3.2 mm (0.125 in) NPT hole. Threaded into the hole is a stainless steel Swagelok compression fitting (SS-400-1-2). The compression fitting attaches to a 6.35 mm (0.25 in) stainless steel tube, which is plumbed to the inlet compression fitting of the pressure boss. The fittings used to plumb the stainless steel tubing to the pressure boss are 6.35 mm

(0.25 in) stainless steel Swagelok compression elbows (SS-400-9). Threaded into the top of the pressure boss is the chilled mirror dew-point hygrometer sensor, which measures the dew-point temperature of the sample air stream. To draw air through the pressure boss, a 6.35 mm (0.25 in) clear plastic tube is used to connect the outlet of the pressure boss to the inlet of the sample module. The sample module is a vacuum pump and flow meter combination which allows for the proper adjustment of the flow of air over the chilled mirror sensor.

The final penetration shown in Figure 4-9 is for the temperature sensors. The temperature sensors are located 56 cm (22 in) from the upstream end of the acrylic duct and mounted in a manner as illustrated in Figure 4-9. The first step taken to construct the mounting bracket for the temperature sensor is to mill a flat surface onto the top of the acrylic duct. Figure 4-10 provides a CAD representation of the milled surface in the acrylic duct

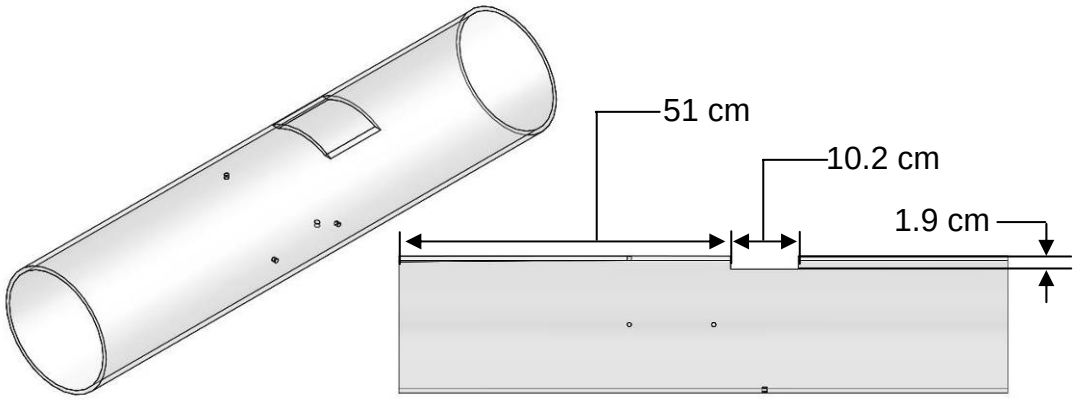

Figure 4-10: Isometric and side view of acrylic duct with the milled surface and the dimensions specified.

As shown in Figure 4-10, the milled surface begins 51 cm (20 in) from the upstream end of the acrylic duct and extends 4 inches downstream. The surface is milled a depth of 1.9 cm

(0.75 in) relative to the top of the acrylic duct. Mounted to the milled surface is a 1.9 cm (0.75 in) thick piece of abrasive resistant polyethylene with the center section removed, as shown in Figure 4-11.

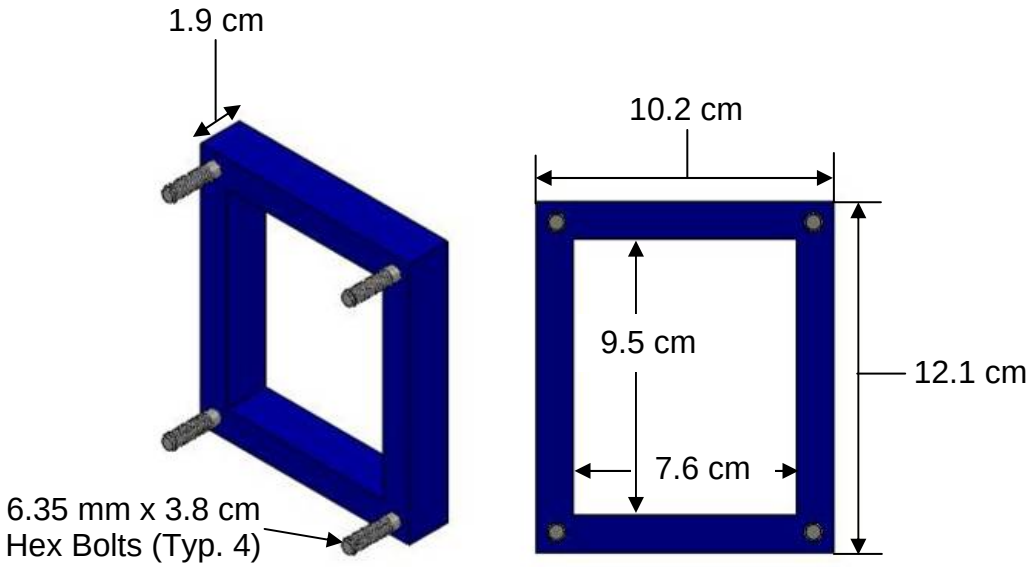

Figure 4-11: Isometric and front view of the flange mounted to the milled surface of the acrylic pipe.

The purpose of the polyethylene is to act as a mounting flange for the temperature sensor base plate. The polyethylene flange, shown in Figure 4-11, has 6.35 mm x 3.8 cm (0.25 in x 1.5 in) hex bolts counter sunk into each corner. The back-side of the flange is attached to the milled mating surface of the clear acrylic pipe using clear silicone caulk. To more clearly illustrate this, a CAD model showing the flange attached to the acrylic pipe is shown in Figure 4-12.

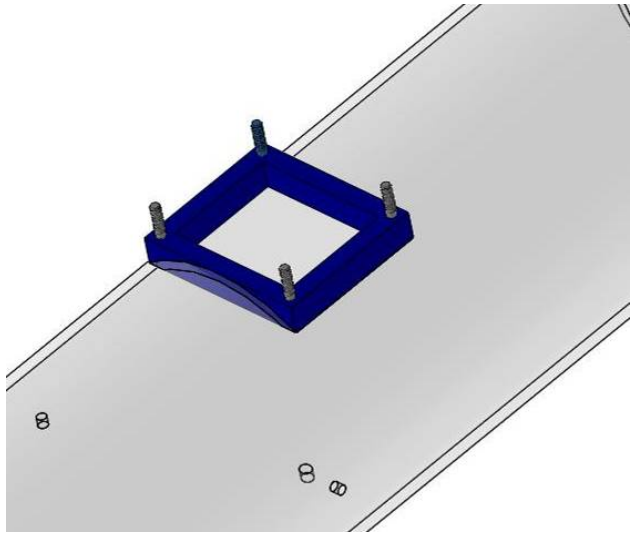

Figure 4-12: Polyethylene mating flange attached to acrylic pipe.

After the flange is attached to the acrylic pipe, the temperature sensor base plate is attached. The temperature sensor base plate is made from a piece of 1.3 cm (0.5 in) thick abrasive-resistant polyethylene. Four 6.35 mm (0.25 in) diameter clearance holes are drilled in each corner of the temperature sensor base plate to match the 6.35 mm (0.25 in) bolts extending from flange. Located in the center of the base and spaced 3.8 cm (1.5 in) apart are two 3.2 mm (0.125 in) NPT holes. Threaded into these holes are stainless steel Swagelok compression fittings (SS-400-1-2BT). These compression fittings are modified in a manner that is similar to the fittings used for the velocity transducer; the fittings are bored through and the stainless steel ferrules are replaced with PTFE ferrules. These fittings allow the distance with which the sensors extend into the duct to be easily adjusted without damaging the temperature probes. The temperature sensor base plate (without the temperature sensors) is shown in Figure 4-13.

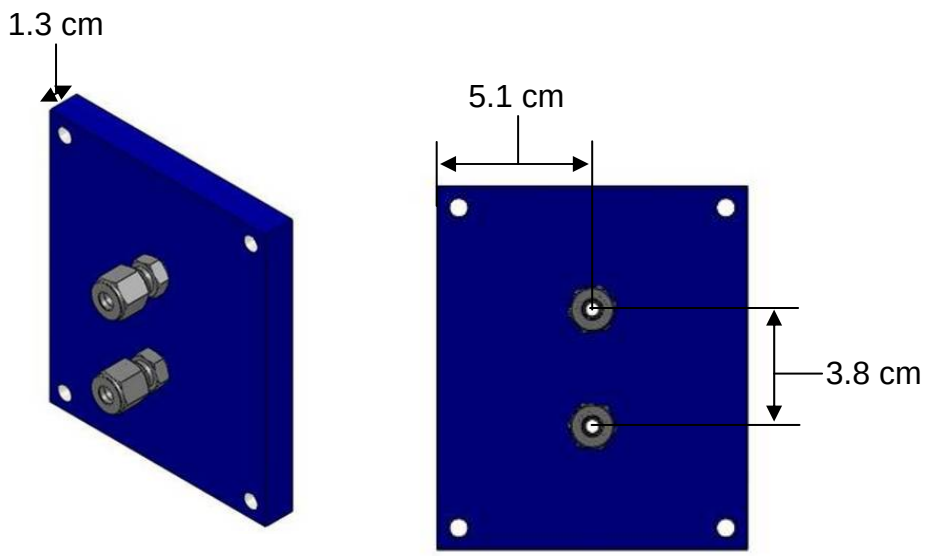

Figure 4-13: Temperature sensor base plate.

The temperature sensor base plate shown in Figure 4-13 is mated with the flange that is permanently attached to the acrylic duct. A gasket is placed between the two mating surfaces to ensure a sufficient seal when the temperature sensor base plate is bolted to the flange. Figure 4-14 shows an exploded view of the temperature sensor base plate being attached to the mating flange.

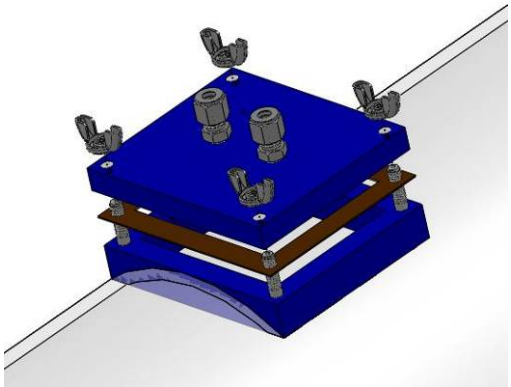

Figure 4-14: Temperature sensor mounting assembly.

As shown in Figure 4-14, wing nuts are used to attach the temperature sensor base plate to the mating flange and compress the gasket.

The two temperature sensor probes are inserted into the bored through compression fittings on the temperature sensor base plate. The compression fittings are tightened when the temperature probes are approximately 1.3 cm (0.5 in) from the bottom of the acrylic pipe. According to the analytical models, a 1.3 cm (0.5 in) length of wick between the reservoir and the temperature probe is enough to essentially eliminate the parasitic heat transfer associated with the makeup water being at the dry-bulb temperature. Once the temperature probes are inserted to a proper depth, the base plate is unbolted and the cotton sock is pulled over the wet-bulb temperature sensor. The cotton sock used to cover the wet-bulb temperature probe and wick water from the reservoir is 6.35 mm (0.25 in) wet-bulb lab wick manufactured by the Pepperell Braiding Company. After the cotton sock is pulled over the temperature probe, the radiation shield for both the dry- and wet-bulb is attached. The

temperature sensors with the cotton sock and radiation shield attached are shown in Figure 4-15.

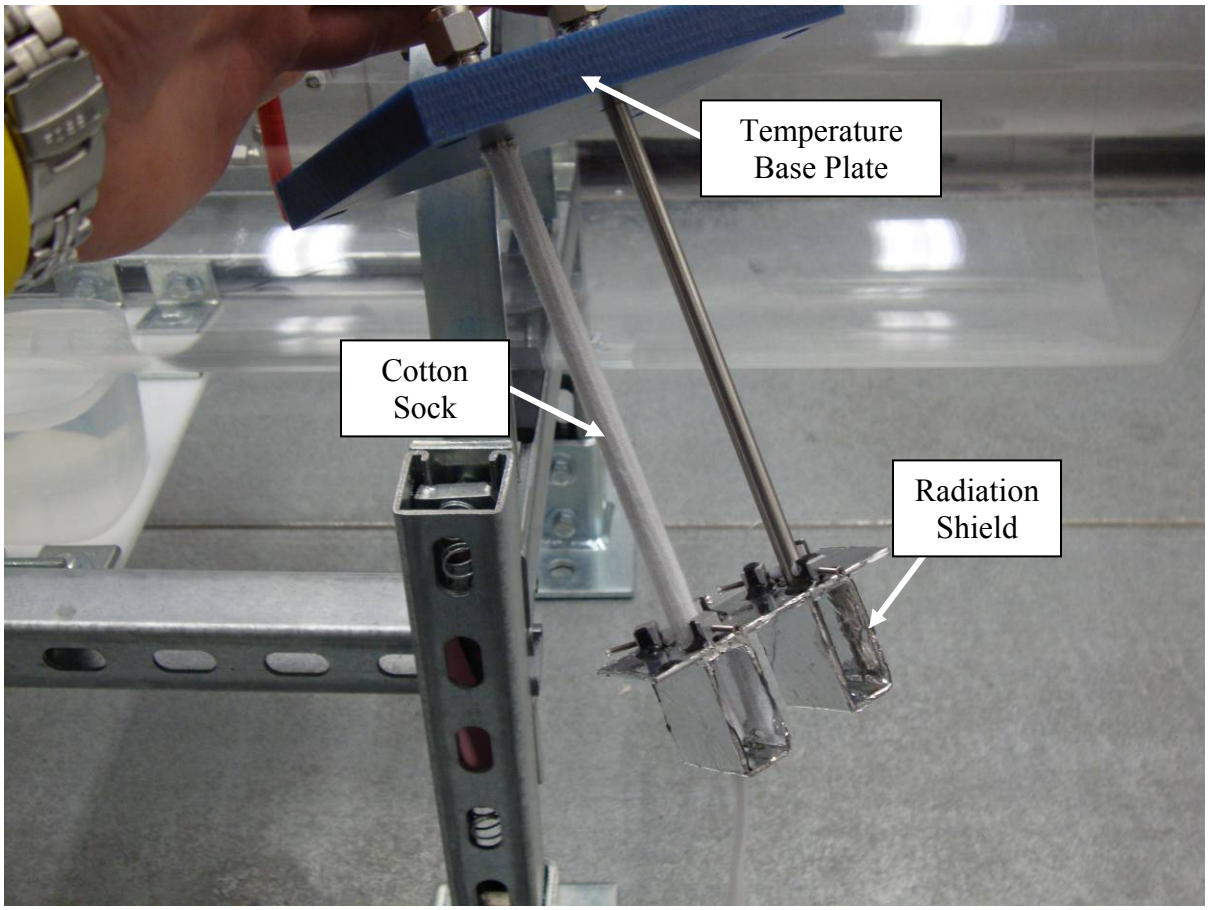

Figure 4-15: Wet- and dry-bulb temperature sensor probes with radiation shield.

The radiation shield is made from 1.6 mm (0.0625 in) thick alloy 1100 aluminum. The dimensions of the radiation shield are specified in Figure 4-16.

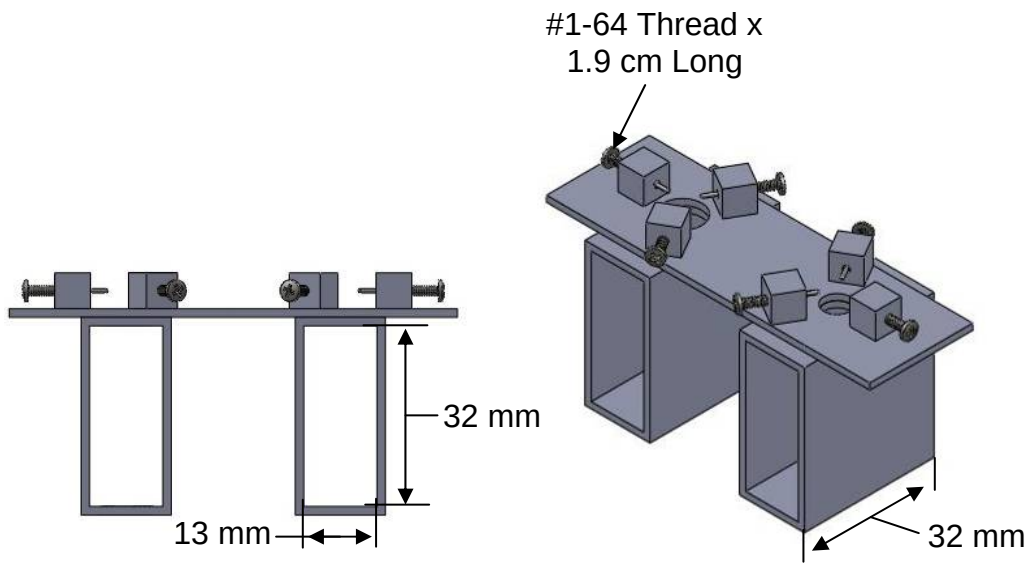

Figure 4-16: Radiation shield used to reduce radiation parasitic to the temperature sensor probes used in the experimental apparatus.

The inside shield width is 13 mm (0.5 in). The temperature sensor probes have a diameter of 6.35 mm (1/4 inch). This leaves approximately 3 mm (1/8 inch) of open space between the dry-bulb temperature sensor probe and the wall of the shield on each side of the probe. There is a slightly smaller space between the wet-bulb temperature sensor probe and the wall of the shield (approximately 2 mm) due to the presence of the cotton sock over the probe.

The shield has an inside height of 32 mm (1.3 in) and the length of the shield parallel to the flow direction is 32 mm (1.3 in). The hole through the top of the shield used to accommodate the temperature sensor is 1.1 cm (0.4375 in) in diameter and located in the center of the top plate. Therefore, the shield extends 16 mm (0.63 in) in both the upstream and downstream direction from the center of the thru-hole. As shown in Figure 4-16, small #1-64 thread x 1.9 cm (0.75 in) long screws are used to attach the shield to both the dry- and

wet-bulb temperature sensor probes. To eliminate conduction from the screw tips to the temperature probes, Teflon® tips are glued onto each screw tip.

The shiny covering shown on the radiation shield in Figure 4-15 is aluminized Mylar. The purpose of the Mylar is to reduce the emissivity of the inside surface of the radiation shield. A spray adhesive is used to securely attach the aluminized Mylar to the aluminum shield. As is shown in Figure 4-15, the shield constructed for the experimental apparatus has a Mylar covering on both the interior and exterior of the shield. The analytical models suggest that the achieving a low emissivity on the internal surface of the shield is much more important than the external surface.

Although not shown in Figure 4-8, a 6.35 mm (0.25 in) NPT hole is tapped into the clear acrylic test section. The hole is tapped into the top of the acrylic duct and located 10 cm (4 in) downstream of the wet- and dry-bulb temperature sensors. Threaded into the tapped hole is a 6.35 mm (0.25 in) PVC nipple. The nipple is threaded on both ends and is used to connect the pressure transmitter to the test section.

The final penetration in the test section is a 0.95 cm (0.375 in) hole drilled through the bottom of the clear acrylic duct in line with the wet-bulb temperature sensor. The hole is needed to link the cotton sock surrounding the wet-bulb temperature probe to the water reservoir on the underside of the pipe. It is important to keep the water reservoir as close as possible to the underside of the pipe to reduce the distance in which water must wick to reach the wet-bulb temperature sensor.

The stand used to hold the experimental apparatus is constructed out of 4.1 cm x 4.1 cm (1.625 in x 1.625 in), zinc-plated, steel slotted strut channel. To fasten the acrylic pipe to the strut channel, 20.3 cm (8 in) zinc-plated, steel strut mount pipe clamps are used. The pipe clamps are made for 21.9 cm (8.625 in) O.D. pipe however, so 0.79 cm (0.3125 in) thick fluoroelastomer rubber is placed on both the bottom and top sides of the pipe to ensure a tight fit.

4.2 Equipment Uncertainty Analysis

This section of the report quantifies the uncertainty associated with each piece of measurement equipment and the resulting uncertainty associated with the measurement of wet-bulb temperature.

4.2.1 Temperature Measurement Uncertainty

When measuring temperature with a thermistor, there are three sources of uncertainty: the uncertainty associated with the data acquisition system's measurement of voltage, the uncertainty in the current source used to power the sensor, and the calibrated uncertainty of the sensor itself. Assuming that these three uncertainties are unbiased and uncorrelated, they can be combined in order to determine the overall uncertainty in the temperature measurement according to:

$$\Delta T = \sqrt{\Delta T_{DAQ}^2 + \Delta T_I^2 + \Delta T_{cal}^2} \tag{4.2.1}$$

where ΔT_{DAQ} is the uncertainty in the data acquisition system's voltage measurement, ΔT_I is the uncertainty in the current source, ΔT_{cal} is the calibrated uncertainty of the sensor, and ΔT is the total uncertainty in the temperature measurement.

The uncertainty in the temperature measurement that results from the data acquisition system is a result of the uncertainty in the measured voltage. The associated uncertainty in the measured resistance of the thermistor is:

$$\Delta R_{DAQ} = \frac{\Delta V_{DAQ}}{I} \tag{4.2.2}$$

where ΔR_{DAQ} is the uncertainty in the resistance measurement, ΔV_{DAQ} is the uncertainty in the voltage measured by the data acquisition system, and I is the current used to power the sensor. The temperature coefficient of the thermistors (i.e., the derivative of the resistance with respect to temperature) is used to relate the uncertainty in the resistance measurement to an uncertainty in measured temperature.

$$\Delta T_{DAQ} = \frac{\Delta R_{DAQ}}{K_{temp}(T)} \tag{4.2.3}$$

where $K_{temp}(T)$ is the temperature coefficient of the given thermistor; note that the temperature coefficient is a function of temperature because the resistance of a thermistor is not a linear function of temperature.

The uncertainty in the current source plays a large role in the uncertainty of the temperature measurement. The uncertainty in the resistance that results from the uncertainty in current is:

$$\Delta R_I = \frac{\Delta I}{I} R(T) \tag{4.2.4}$$

where ΔI is the given uncertainty in the current source, *R(T)* is the resistance of the thermistor, and ΔR_I is the uncertainty in the resistance measurement that results from the uncertainty in the current source. The uncertainty in the resistance measurement as a result of the current source is related to an uncertainty in the temperature measurement by the temperature coefficient.

$$\Delta T_I = \frac{\Delta R_I}{K_{temp}(T)} \tag{4.2.5}$$

The final error contributing to an uncertainty in the temperature measurement is the calibrated uncertainty of the sensor itself (ΔT_{cal}). This is the manufacturer's specified uncertainty in the device.

The results listed in Table 4-1 correspond to a Model 5640 Thermistor from Fluke. The sensor has a nominal resistance of 4.4 kΩ at 25°C, with a calibrated uncertainty of 2 mk over a 0-60°C range. The data acquisition system used for these calculations is a Campbell Scientific CR23X Micrologger with a calibrated voltage uncertainty of 10 μV over a ±200 mV range, and the current source used for the calculations is a LakeShore Model 101 Current Source with a ±0.05% uncertainty at 10 μA. The resulting uncertainty in temperature is

shown in Table 4-1 at the seven calibration points where the temperatures and corresponding resistances are known. The temperature coefficient (K_{temp}) is approximated at each temperature from a fit of the resistance as a function of temperature.

T (°C)	R (Ω)	K_{temp} (Ω/°C)	I (μA)	V (mV)	ΔT_{DAQ} (mK)	ΔT_I (mK)	ΔT_{cal} (mK)	**ΔT (mK)**
-.002	11832	425	10	118.3	2.35	13.9	2	**14.3**
9.99	7562	340	10	75.6	2.94	11.1	2	**11.7**
19.99	4959	210	10	49.6	4.76	11.8	2	**12.9**
29.98	3333	130	10	33.3	7.69	12.8	2	**15.1**
39.98	2289	85	10	22.9	11.8	13.5	2	**18.0**
49.98	1605	55	10	16.1	18.2	14.6	2	**23.4**
59.96	1147	45	10	11.5	22.2	12.8	2	**25.7**

Table 4-1: Uncertainty in the temperature measurement using a current source with an uncertainty of ±0.05% at 10μA.

The results in Table 4-2 are the uncertainty results obtained using the same equipment except that the current source is a LakeShore Model 218 Temperature Monitor which has an uncertainty in the current of ±0.01% at 10μA (which is better than the LakeShore Model 101 Current Source used in Table 4-1.)

T (°C)	R (Ω)	K_{temp} (Ω/°C)	I (μA)	V (mV)	ΔT_{DAQ} (mK)	ΔT_I (mK)	ΔT_{cal} (mK)	**ΔT (mK)**
-.002	11832	425	10	118.3	2.35	2.78	2	**4.16**
9.99	7562	340	10	75.6	2.94	2.22	2	**4.20**
19.99	4959	210	10	49.6	4.76	2.36	2	**5.68**
29.98	3333	130	10	33.3	7.69	2.56	2	**8.35**
39.98	2289	85	10	22.9	11.8	2.69	2	**12.2**
49.98	1605	55	10	16.1	18.2	2.92	2	**18.5**
59.96	1147	45	10	11.5	22.2	2.55	2	**22.5**

Table 4-2: Uncertainty in the temperature measurement using a current source with an uncertainty of ±0.01% at 10μA.

Note that the use of the more accurate current source improves the measurement, particularly at low temperature where the resistance of the sensor is high.

4.2.2 Dew-Point Temperature Measurement Uncertainty

The dew-point temperature is measured using a chilled mirror dew-point hygrometer. The dew-point hygrometer outputs a 4-20 mA current that is proportional to the dew-point temperature. The output current is linearly related to the dew-point temperature reading, as shown in Eq. (4.2.6).

$$T_{dp} = \frac{\left(I_{out} - I_{lower}\right)\left(T_{upper} - T_{lower}\right)}{\left(I_{upper} - I_{lower}\right)} + T_{lower} \tag{4.2.6}$$

where I_{out} is the chilled mirror output current, T_{upper} and T_{lower} are the upper and lower limits on the dew-point temperature range, respectively, I_{upper} and I_{lower} are the upper and lower limits of the output current (i.e. 20 mA and 4 mA), respectively, and T_{dp} is the dew-point temperature.

The uncertainty in the dew-point temperature measurement is due to both the uncertainty in the measurement of the output current as well as the calibrated uncertainty of the chilled mirror dew-point hygrometer. These two uncertainties can be combined using a square root of the sum of squares method if it is assumed that the two uncertainties are both unbiased and uncorrelated.

$$\Delta T_{dp} = \sqrt{\Delta T_{dp,I}^2 + \Delta T_{dp,cal}^2} \tag{4.2.7}$$

where $\Delta T_{dp,I}$ is the uncertainty in the dew-point temperature due to the uncertainty in the measured current output, $\Delta T_{dp,cal}$ is the uncertainty in the dew-point temperature as a result of the calibrated uncertainty in the chilled mirror dew-point hygrometer, and ΔT_{dp} is the total uncertainty in the dew-point temperature.

The current output of the chilled mirror dew-point hygrometer is not measured directly by the data acquisition system; rather, the data acquisition system measures a voltage. The output current is converted to a voltage using a known resistance.

$$I_{out} = \frac{V}{R} \tag{4.2.8}$$

where V is the measured voltage, R is the known resistance, and I_{out} is the current output from the dew-point hygrometer. The uncertainty in the measured current is:

$$\Delta I_{out} = \sqrt{\left(\frac{\partial I_{out}}{\partial V}\Delta V\right)^2 + \left(\frac{\partial I_{out}}{\partial R}\Delta R\right)^2} \tag{4.2.9}$$

where $\frac{\partial I_{out}}{\partial V}$ is the partial derivative of the output current with respect to the voltage, ΔV is the uncertainty in the voltage measurement, $\frac{\partial I_{out}}{\partial R}$ is the partial derivative of the output current with respect to the resistance, ΔR is the uncertainty in the resistance, and ΔI_{out} is the uncertainty in the measured current. Using Eq. (4.2.8) to provide the partial derivatives leads to:

$$\frac{\partial I_{out}}{\partial V} = \frac{1}{R} \tag{4.2.10}$$

$$\frac{\partial I_{out}}{\partial R} = -\frac{V}{R^2} \tag{4.2.11}$$

Substituting these results into Eq. (4.2.9):

$$\Delta I_{out} = \sqrt{\left(\frac{\Delta V}{R}\right)^2 + \left(\frac{V \Delta R}{R^2}\right)^2} \tag{4.2.12}$$

The uncertainty in the current contributes to an uncertainty in the dew-point temperature measurement according to:

$$\Delta T_{dp,I} = \frac{\partial T_{dp}}{\partial I_{out}} \Delta I_{out} \tag{4.2.13}$$

where $\frac{\partial T_{dp}}{\partial I_{out}}$ is the partial derivative of the dew-point temperature with respect to the output current. Using Eq. (4.2.6) to evaluate the partial derivative:

$$\frac{\partial T_{dp}}{\partial I_{out}} = \frac{\left(T_{upper} - T_{lower}\right)}{\left(I_{upper} - I_{lower}\right)} \tag{4.2.14}$$

Substituting Eq. (4.2.14) and (4.2.12) into Eq. (4.2.13) yields:

$$\Delta T_{dp,I} = \frac{\left(T_{upper} - T_{lower}\right)}{\left(I_{upper} - I_{lower}\right)} \sqrt{\left(\frac{\Delta V}{R}\right)^2 + \left(\frac{V \Delta R}{R^2}\right)^2} \tag{4.2.15}$$

The remaining uncertainty in the dew-point temperature is a result of the calibrated uncertainty in the chilled mirror dew-point hygrometer provided by the manufacturer.

An OptiSonde General Eastern Chilled Mirror Hygrometer with a Model 1111H Single Stage Chilled Mirror is used to make the dew-point temperature measurement. The calibrated uncertainty of the device is 0.04°C over the operating range of interest. To measure the current output, a 250 Ω precision resistor is used with the Campbell Scientific 23X Micrologger. A Keithley 2700 Multimeter has been used to precisely measure the resistance of the 250 Ω precision resistor using a four wire resistance measurement technique. The multimeter is capable of measuring the resistance to within an uncertainty of ±0.031Ω. The calibrated uncertainty in the voltage measured by the Campbell Scientific Micrologger over the 1-5 V range is 200 μV. The output temperature range for the chilled mirror hygrometer is set to -10°C to 40°C. With this information, the equations presented in the previous section are used to estimate the uncertainty in the dew-point temperature measurement. These results are summarized in Table 4-3.

T_{dp} (°C)	I_{out} (mA)	$\Delta T_{dp,I}$ (mK)	$\Delta T_{dp,cal}$ (mK)	$\boldsymbol{\Delta T_{dp}}$ **(mK)**
-10	4	2.94	40.0	**40.1**
2.5	8	3.98	40.0	**40.2**
15	12	5.28	40.0	**40.3**
27.5	16	6.69	40.0	**40.6**
40	20	8.14	40.0	**40.8**

Table 4-3: Uncertainty in dew-point temperature measurement over entire dew-point temperature range of the chilled mirror hygrometer.

Note that the uncertainty in the measurement of the dew-point temperature is dominated by the calibrated uncertainty in the sensor itself over the entire temperature range.

4.2.3 Atmospheric Pressure Measurement Uncertainty

The atmospheric pressure measurement is made using a pressure transmitter which outputs a 4-20 mA current proportional to the measured pressure. The measured pressure is determined from the output current according to:

$$P = \frac{(I_{out} - I_{lower})(P_{upper} - P_{lower})}{(I_{upper} - I_{lower})} + P_{lower} \tag{4.2.16}$$

where I_{out} is the output current of the pressure transmitter, P_{upper} and P_{lower} are the upper and lower limits on the pressure range of the transmitter, respectively, I_{upper} and I_{lower} are the upper and lower limits of the output current (i.e. 20 mA and 4 mA), respectively, and P is the pressure measured by the sensor.

The uncertainty in the pressure measurement is due to both the uncertainty in the measurement of the output current as well as the calibrated uncertainty of the pressure transmitter. These two uncertainties can be combined using a square root of the sum of squares method.

$$\Delta P = \sqrt{\Delta P_I^2 + \Delta P_{cal}^2} \tag{4.2.17}$$

where ΔP_I is the uncertainty in the pressure due to the uncertainty in the measured current output, ΔP_{cal} is the uncertainty in the pressure as a result of the calibrated uncertainty in the pressure transmitter, and ΔP is the total uncertainty in the measured pressure.

The uncertainty in the pressure due to the uncertainty in the current source is found in a manner which is analogous to the uncertainty in the dew-point temperature due to the uncertainty in the current source.

$$\Delta P = \frac{(P_{upper} - P_{lower})}{(I_{upper} - I_{lower})} \sqrt{\left(\frac{\Delta V}{R}\right)^2 + \left(\frac{V \Delta R}{R^2}\right)^2} \tag{4.2.18}$$

where again, V is the measured voltage (i.e. after the current is converted to a voltage), ΔV is the uncertainty in the voltage measurement, R is the nominal resistance value of the shunt resistor used to convert the current to a voltage, and ΔR is uncertainty in the resistance value of the shunt resistor. The remaining uncertainty in the pressure measurement is a result of the calibrated uncertainty in the pressure transmitter, as provided by the manufacturer.

A Druck PTX 1225 pressure transmitter is used to measure the atmospheric pressure. The calibrated uncertainty of the device is ±0.15% (of full scale) and the transmitter measurement range is from 594 to 879 mmHg (11.5 to 17 psia). To measure the current output, a 250Ω precision resistor is used with the Campbell Scientific 23X Micrologger. A Keithley 2700 Multimeter has been used to precisely measure the resistance of the 250 Ω precision resistor using a four wire resistance measurement technique. The multimeter is capable of measuring

the resistance to within an uncertainty of ±0.031Ω. The calibrated uncertainty in the voltage measured by the Campbell Scientific Micrologger over the 1-5 V range is 200 μV. With this information, the equations presented in the previous section are used to estimate the uncertainty in the atmospheric pressure measurement. The uncertainty in the pressure measurement under conditions typically experienced during testing is 1.3 mmHg (0.026 psia). This uncertainty value is due entirely to the calibrated uncertainty in the pressure transmitter and none of it is as a result of the uncertainty in the ability to measure the output current.

4.2.4 Adiabatic Saturation Temperature Measurement Uncertainty

To determine the adiabatic saturation temperature from the dew-point temperature, a general purpose equation solver, EES, is used. EES has built-in psychrometric properties and is capable of performing other functions such as uncertainty analysis. Fixing the psychrometric state requires three independent inputs. The three inputs used here include: the total pressure, dry-bulb temperature, and the dew-point temperature. With these inputs, EES iteratively determines the adiabatic saturation temperature corresponding to the measured experimental conditions.

As mentioned previously, one measurement required to determine the adiabatic saturation temperature is the total pressure. The total pressure is measured using a Druck PTX 1225 pressure transmitter. The uncertainty in this total pressure measurement is estimated to be 1.3 mmHg (0.026 psi), as discussed in the pressure measurement uncertainty section. The uncertainty in the dry-bulb temperature measurement is 22.5 mK, as estimated previously.

This uncertainty value is consistent with the use of a Fluke Model 5640 Precision Thermistor powered by a LakeShore Model 218 current source (the same equipment used to make the wet-bulb temperature measurement). Finally, the uncertainty in the dew-point temperature is 40.8 mK, as discussed in the dew-point temperature measurement uncertainty section. These parameters are entered into EES as follows:

```
$UnitSystem SI J C PA
$TabStops 0.2 0.4 0.6 3.5 in

T_dp=15.7[C]                                        "dew-point temp"
T_db=26.7[C]                                        "dry-bulb temp"
P=14.2[Psi]*convert(Psi,Pa)                         "total pressure"

DELTAP=0.026[Psi]*convert(Psi,Pa)                   "uncertainty in pressure"
DELTAT_db=0.0225[C]                                 "uncertainty in dry-bulb temp"
DELTAT_dp=0.0408[C]                                 "uncertainty in dew-point temp"

T_as=WetBulb(AirH2O,P=P,T=T_db,D=T_dp)              "adiabatic saturation temperature"
```

The uncertainty propagation function in EES is used to quantify the uncertainty in the adiabatic saturation temperature as a result of the uncertainty in the pressure, dry-bulb temperature, and the dew-point temperature. Figure 4-17 below shows the uncertainty propagation output window provided by EES.

Unit Settings: SI C Pa J mass deg

Variable±Uncertainty	Partial derivative	% of uncertainty
T_{as} = 19.36±0.02436 [C]		
P = 97906±179.3 [Pa]	$\partial T_{as}/\partial P$ = 0.00002378	3.07 %
T_{db} = 26.7±0.0225 [C]	$\partial T_{as}/\partial T_{db}$ = 0.3108	8.25 %
T_{dp} = 15.7±0.0408 [C]	$\partial T_{as}/\partial T_{dp}$ = 0.5622	88.69 %

No unit problems were detected.

Figure 4-17: EES output window for the uncertainty in the adiabatic saturation temperature.

Figure 4-17 shows that the uncertainty in the adiabatic saturation temperature for the conditions specified is approximately 24.4 mK. The figure also shows that the uncertainty in the adiabatic saturation temperature is primarily due to the dew-point temperature (88.7%). The uncertainty in the dry-bulb temperature and the pressure are low enough that they have very little impact on the adiabatic saturation temperature, 8.3% and 3.1%, respectively. The uncertainty in the adiabatic saturation temperature is also calculated with the specified uncertainties over the entire test matrix. The results are summarized in Figure 4-18.

		Wet-Bulb Temperature Depression					
		1ºC	**5ºC**	**10ºC**	**15ºC**	**20ºC**	**25ºC**
Dew-Point Temperature	**2ºC**	$T_{dry\text{-}bulb}$=4.21(ºC) $T_{wet\text{-}bulb}$=3.21(ºC) **ΔT_{as}=21.3mK**	$T_{dry\text{-}bulb}$=12.3(ºC) $T_{wet\text{-}bulb}$=7.3(ºC) **ΔT_{as}=19.1mK**	$T_{dry\text{-}bulb}$=21.3(ºC) $T_{wet\text{-}bulb}$=11.3(ºC) **ΔT_{as}=17.6mK**	$T_{dry\text{-}bulb}$=29.6(ºC) $T_{wet\text{-}bulb}$=14.6(ºC) **ΔT_{as}=16.9mK**	$T_{dry\text{-}bulb}$=37.3(ºC) $T_{wet\text{-}bulb}$=17.3(ºC) **ΔT_{as}=16.7mK**	$T_{dry\text{-}bulb}$=44.7(ºC) $T_{wet\text{-}bulb}$=19.7(ºC) **ΔT_{as}=16.8mK**
	12ºC	$T_{dry\text{-}bulb}$=13.7(ºC) $T_{wet\text{-}bulb}$=12.7(ºC) **ΔT_{as}=25.3mK**	$T_{dry\text{-}bulb}$=20.1(ºC) $T_{wet\text{-}bulb}$=15.1(ºC) **ΔT_{as}=23.4mK**	$T_{dry\text{-}bulb}$=27.8(ºC) $T_{wet\text{-}bulb}$=17.8(ºC) **ΔT_{as}=21.6mK**	$T_{dry\text{-}bulb}$=35.1(ºC) $T_{wet\text{-}bulb}$=20.1(ºC) **ΔT_{as}=20.5mK**	$T_{dry\text{-}bulb}$=42.2(ºC) $T_{wet\text{-}bulb}$=22.2(ºC) **ΔT_{as}=19.7mK**	$T_{dry\text{-}bulb}$=49.0(ºC) $T_{wet\text{-}bulb}$=24.0(ºC) **ΔT_{as}=19.3mK**
	20ºC	$T_{dry\text{-}bulb}$=21.4(ºC) $T_{wet\text{-}bulb}$=20.4(ºC) **ΔT_{as}=28.8mK**	$T_{dry\text{-}bulb}$=27.1(ºC) $T_{wet\text{-}bulb}$=22.1(ºC) **ΔT_{as}=27.1mK**	$T_{dry\text{-}bulb}$=33.9(ºC) $T_{wet\text{-}bulb}$=23.9(ºC) **ΔT_{as}=25.4mK**	$T_{dry\text{-}bulb}$=40.6(ºC) $T_{wet\text{-}bulb}$=25.6(ºC) **ΔT_{as}=24.2mK**	$T_{dry\text{-}bulb}$=47.2(ºC) $T_{wet\text{-}bulb}$=27.2(ºC) **ΔT_{as}=23.2mK**	$T_{dry\text{-}bulb}$=53.6(ºC) $T_{wet\text{-}bulb}$=28.6(ºC) **ΔT_{as}=22.5mK**
	25ºC	$T_{dry\text{-}bulb}$=26.3(ºC) $T_{wet\text{-}bulb}$=25.3(ºC) **ΔT_{as}=30.7mK**	$T_{dry\text{-}bulb}$=31.6(ºC) $T_{wet\text{-}bulb}$=26.6(ºC) **ΔT_{as}=29.3mK**	$T_{dry\text{-}bulb}$=38.1(ºC) $T_{wet\text{-}bulb}$=28.1(ºC) **ΔT_{as}=27.7mK**	$T_{dry\text{-}bulb}$=44.5(ºC) $T_{wet\text{-}bulb}$=29.5(ºC) **ΔT_{as}=26.5mK**	$T_{dry\text{-}bulb}$=50.8(ºC) $T_{wet\text{-}bulb}$=30.8(ºC) **ΔT_{as}=25.5mK**	$T_{dry\text{-}bulb}$=56.9(ºC) $T_{wet\text{-}bulb}$=31.9(ºC) **ΔT_{as}=24.7mK**
	30ºC	$T_{dry\text{-}bulb}$=31.3(ºC) $T_{wet\text{-}bulb}$=30.3(ºC) **ΔT_{as}=32.4mK**	$T_{dry\text{-}bulb}$=36.3(ºC) $T_{wet\text{-}bulb}$=31.3(ºC) **ΔT_{as}=31.2mK**	$T_{dry\text{-}bulb}$=42.4(ºC) $T_{wet\text{-}bulb}$=32.4(ºC) **ΔT_{as}=29.9mK**	$T_{dry\text{-}bulb}$=48.5(ºC) $T_{wet\text{-}bulb}$=33.5(ºC) **ΔT_{as}=28.7mK**	$T_{dry\text{-}bulb}$=54.6(ºC) $T_{wet\text{-}bulb}$=34.6(ºC) **ΔT_{as}=27.7mK**	$T_{dry\text{-}bulb}$=60.6(ºC) $T_{wet\text{-}bulb}$=35.6(ºC) **ΔT_{as}=26.9mK**

Figure 4-18: The uncertainty in the adiabatic saturation temperature at each of the thirty test points compiling the test matrix. The uncertainty in the dry-bulb temperature, dew-point temperature, and pressure used to calculate the uncertainty in the adiabatic saturation temperature are 0.0225°C, 0.0408°C, and 0.026Psi, respectively.

The uncertainty in the wet-bulb temperature ranges from 0.0167°C to 0.0324°C for the various conditions specified in the test matrix, as illustrated in Figure 4-18.

4.2.5 Velocity Measurement Uncertainty

When measuring the air velocity with a hot wire type velocity sensor, there are two sources of measurement uncertainty: the uncertainty associated with the data acquisition system's ability to measure voltage and the calibrated uncertainty of the sensor. Assuming the individual uncertainties are unbiased and uncorrelated, the 95% confidence interval of the velocity uncertainty is determined by using the square root of the sum of squares of the two contributing uncertainties.

$$\Delta Vel = \sqrt{\Delta Vel_V^2 + \Delta Vel_{cal}^2} \tag{4.2.19}$$

where ΔVel_V is the uncertainty in the velocity due to the uncertainty in the voltage measurement, ΔVel_{cal} is the calibrated uncertainty of the velocity sensor, and ΔVel is the total uncertainty in the velocity measurement.

To determine the impact of the voltage uncertainty on the velocity it is necessary to understand how the voltage is related to the velocity. The voltage output of the velocity sensor is converted into a velocity by:

$$Vel = \frac{\left(V_{out} - V_o\right)}{\left(V_{fs} - V_o\right)} Vel_{fs} \tag{4.2.20}$$

where V_{out} is the sensor output voltage, V_o is the output voltage of the sensor when the velocity is zero, V_{fs} is the full scale output voltage, Vel_{fs} is the full scale velocity, and Vel is the velocity measured by the sensor. The uncertainty in the velocity due to the uncertainty in the voltage measurement is:

$$\Delta Vel_V = \frac{\partial Vel}{\partial V_{out}} \Delta V_{out} \tag{4.2.21}$$

where ΔV_{out} is the uncertainty in the measurement of the output voltage. Solving for the partial derivative of velocity with respect to voltage using Eq. (4.2.20):

$$\frac{\partial Vel}{\partial V_{out}} = \frac{Vel_{fs}}{V_{fs} - V_o} \tag{4.2.22}$$

Substituting Eq. (4.2.22) into Eq. (4.2.21) yields:

$$\Delta Vel_V = \frac{Vel_{fs}}{V_{fs} - V_o} \Delta V_{out} \tag{4.2.23}$$

The remaining uncertainty in the velocity measurement is due to the calibrated uncertainty of the velocity sensor (ΔV_{cal}), which is specified by the manufacturer.

The Campbell Scientific CR23X Micrologger is again used to measure the voltage output of the device. The velocity sensor is a TSI Model 8455 with a 0-5 V output voltage over a 0-10 m/s air velocity range. The uncertainty in the device is ±2.0% of the reading plus ±0.5% of the full scale selected range (i.e., 10 m/s). Also when the velocity sensor is used outside of the 18-28°C range there is an additional uncertainty of 0.2% of the velocity reading per °C in the temperature deviation. The calibrated data logger can measure the 0-5 V output voltage with an uncertainty of 200 μV. Table 4-4 summarizes the uncertainty in the velocity measurement.

Vel (m/s)	V_{out} (Volt)	ΔVel_V (m/s)	ΔVel_{cal} (m/s)	**ΔVel (m/s)**
2	1.0	0.0004	0.22	**0.22**
4	2.0	0.0004	0.39	**0.39**
6	3.0	0.0004	0.56	**0.56**
8	4.0	0.0004	0.73	**0.73**
10	5.0	0.0004	0.90	**0.90**

Table 4-4: Uncertainty in velocity measurement over the 0-10 m/s range.

The uncertainty values specified in Table 4-4 are representative of the test condition in which the dry-bulb temperature is 60.6°C, leading to worst case velocity uncertainties. The results indicate that the calibrated uncertainty of the temperature sensor is the dominant uncertainty in the velocity measurement and that a 0.39 m/s uncertainty in velocity can be expected at an air velocity of 4 m/s.

4.2.6 True Wet-Bulb Temperature Uncertainty

The true wet-bulb is measured in the manner described in Section 1.2.1. This calculation is entered into EES using a procedure that is very similar to Section 2.1, which describes the calculation for the parasitic heat transfer to a sensor in a transverse flow configuration. The only exception is that in the calculation outlined in Section 2.1 the relative humidity is used as the third property necessary to specify the state of the moist air. When using the model to determine the wet-bulb temperature the relative humidity is not known, however, meaning that the dew-point temperature must be used instead. The dew-point temperature is directly measured from chilled mirror dew-point hygrometer. With this the three properties necessary to specify the state of the moist air are known: dry-bulb temperature, pressure, and dew-point temperature. To determine the true wet-bulb temperature, the parasitic heat

transfer to the sensor is set equal to zero and the system of equations described in Section 2.1 are solved.

The uncertainties used for each of the measured quantities are consistent with the uncertainties calculated in the preceding sections, with the exception of the uncertainty in the velocity measurement. Specifically, the uncertainty in the pressure is ±1.3 mmHg (±0.026 psi), the uncertainty in the dry-bulb temperature is ±0.0225°C, and the uncertainty in the dew-point temperature is ±0.0408°C. The uncertainty in the velocity is increased from ±0.39 m/s to ±0.5 m/s. The reason for this is because even though the velocity can be measured to within ±0.39 m/s it can only be controlled to within ±0.5 m/s. The diameter of the sensor and the length of the sensor are also inputs that have an inherent uncertainty associated with them, but the uncertainty analysis indicates that the uncertainty in each of these parameters has no impact on the uncertainty in the predicted true wet-bulb temperature. As a result the uncertainty in each of these measurements is not considered. All of the uncertainties used are upper bounds for the uncertainty values as calculated in the preceding sections. The idea is that by using these uncertainties an upper bound on the uncertainty in the predicted true wet-bulb temperature is determined.

Figure 4-19 shows the uncertainty propagation output window from EES at one of the nominal test conditions.

Unit Settings: SI C Pa J mass deg

Variable±Uncertainty	Partial derivative	% of uncertainty
$T_{wb,act}$ = 19.22±0.02444 [C]		
P = 98659±179.3 [Pa]	$\partial T_{wb,act}/\partial P$ = 0.00002512	3.40 %
T_{db} = 26.7±0.0225 [C]	$\partial T_{wb,act}/\partial T_{db}$ = 0.2977	7.51 %
T_{dp} = 15.7±0.0408 [C]	$\partial T_{wb,act}/\partial T_{dp}$ = 0.5655	89.09 %
Velocity = 4±0.5 [m/s]	$\partial T_{wb,act}/\partial$ Velocity = -0.00005118	0.00 %

No unit problems were detected.

Figure 4-19: EES output window for the uncertainty in the true wet-bulb temperature.

As shown in Figure 4-19, the uncertainty in the true wet-bulb temperature at the nominal test condition (26.7°C DB/ 19.4°C WB) is ±0.0244°C. The uncertainty propagation window indicates that the largest source of uncertainty in the true wet-bulb temperature is due to the uncertainty in the dew-point temperature, followed distantly by the dry-bulb temperature, and the pressure. Also indicated by the output window is that the uncertainty in the velocity has no impact on the uncertainty in the true wet-bulb temperature. The uncertainty in the true wet-bulb temperature is computed over the entire test matrix and the results obtained are very similar to the uncertainty values of the adiabatic saturation temperature, which are shown in Figure 4-18. The uncertainty in the true wet-bulb temperature ranges from ±0.03°C to ±0.02°C.

4.3 Testing Procedure

The following procedure is used to measure the wet-bulb temperature with the experimental apparatus. The first step is to replace the wet-bulb temperature sensor with the velocity transducer. The velocity transducer is placed in the location within the duct and the radiation shield where the wet-bulb temperature will be measured during normal operation. The

velocity at the sensor location is adjusted to achieve the desired velocity for the test by adjusting the Variable Autotransformer used to control the axial fan.

Once the appropriate air velocity has been obtained, the velocity transducer is removed and the wet-bulb temperature sensor is installed in its location. The cotton sock covering the wet-bulb temperature sensor is replaced daily to avoid contamination by particulates in the air stream. In addition to being replaced daily, each cotton sock is boiled in distilled water for a period of ten minutes to avoid particulate contamination. The cotton sock is allowed to dry before the installation. After the new cotton sock is installed, the radiation shield is replaced and the temperature sensor base plate is fastened to the mounting flange. Once the temperature sensors are secured at the appropriate location (i.e., 1.3 cm (0.5 in) from the bottom of the pipe), the water reservoir is filled with distilled water.

The next step is to turn on the environmental chamber and activate the required instrumentation. The environmental chamber is turned on and set to the test condition desired. During the testing, the chamber door is kept closed in order to avoid dramatic changes in the temperature and humidity level in the chamber. After the chamber is turned on, the chilled mirror dew-point hygrometer and current source used to energize the temperature sensors are turned on. This also includes turning on the sample module and adjusting it to the appropriate flow rate (i.e. 0.25 to 1.25 LPM) as well as making certain the power supply for the pressure transmitter is plugged in. An automatic cleaning of the chilled mirror is done daily and the chilled mirror is also cleaned manually on a weekly basis to ensure accurate results. The automatic cleaning performed is a GE patented contamination

compensation scheme called a PACER (Program Automatic Error Reduction) cycle. Once the chilled mirror dew-point hygrometer completes the automatic cleaning process, the data is logged. These steps are repeated for every test.

Chapter 5 – Wicking Height

In this chapter, the results of the experimental wicking height tests are presented. The motivation for this testing was to obtain an empirical relationship for the wicking height as a function of the predicted evaporative mass flow rate to improve the model of the wet-bulb aspirator apparatus. As is shown in the following discussion, the experimental results suggest a nearly linear relationship exists between wicking height and the predicted evaporative mass flow rate. This relationship forms the basis of the conduction/makeup water parasitic model, presented in Chapter 3, and is used to predict the wicking height at each psychrometric condition; thereby, allowing a more robust and accurate prediction of the conduction parasitic to the temperature sensor over an entire range of psychrometric conditions.

5.1 Wicking Height Measurement Apparatus

Minor modifications to the wet-bulb aspirator apparatus presented in Chapter 4 have been made in order to accommodate the wicking experiments. One modification is the addition of a 20.3 cm (8 in) PVC coupling to the inlet end of the acrylic pipe. The coupling allowed both the wet-bulb temperature sensor and velocity transducer to be re-installed at the entrance of the test section. The temperature sensor is moved so that it can be easily accessed for wicking height measurements and the velocity transducer is moved in order to obtain an accurate velocity measurement at the test site. Also, Omega PT100 RTD temperature sensors are used for the wicking height measurements rather than the Fluke Model 5640 thermistor probes that are utilized in the aspirated wet-bulb temperature

measurement apparatus. The purpose of using the RTDs in place of the thermistors is to simply avoid any unnecessary handling of the more expensive, high accuracy temperature probes that are vital to the primary goal of the research project (i.e., the accurate determination of the wet-bulb temperature). Lastly, a LakeShore Model 120 adjustable current source is used to provide the RTDs with a 1 milliWatt current supply. A photo of the test facility modified for the wicking experiments is shown in Figure 5-1.

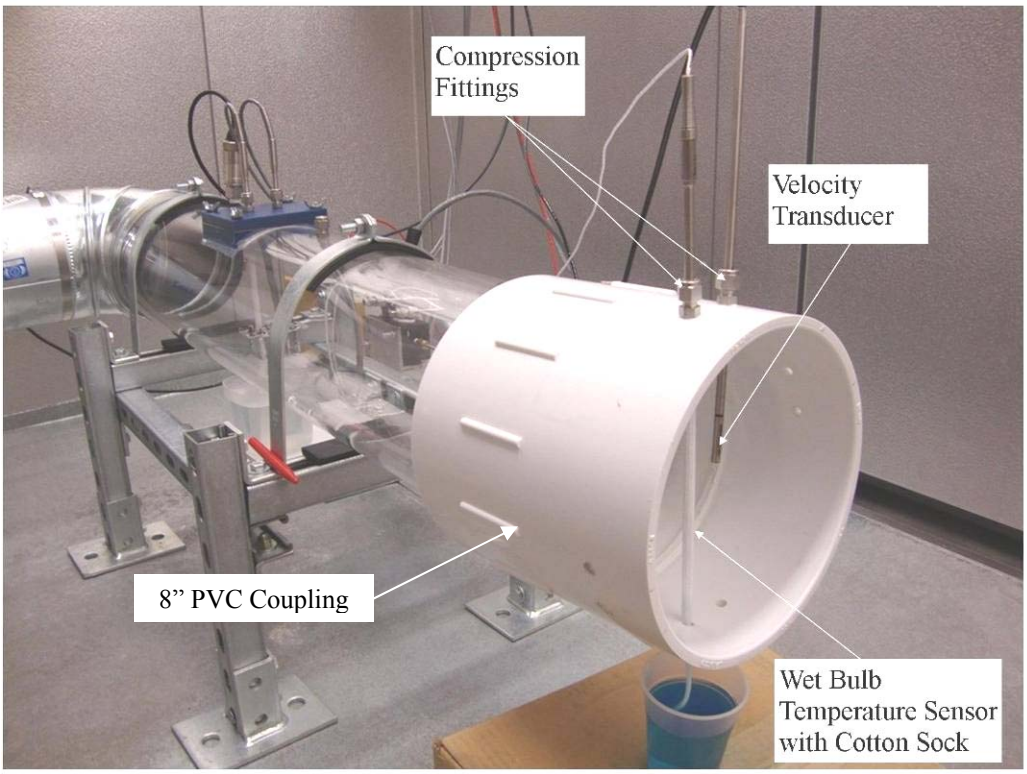

Figure 5-1: Experimental apparatus with modifications.

Although not visible in Figure 5-1, the inside surface of the coupling is lined with several layers of foam tape in order to ensure a snug fit between the PVC coupling and the acrylic duct, allowing for quick and easy installation and removal of the PVC coupling. Two 3.2 mm (0.3175 in) NPT holes have been tapped into the end of the PVC coupling in order to

allow for the installation of stainless steel Swagelok compression fittings (SS-400-1-2BT). The compression fittings permit the wet-bulb temperature sensor and the velocity transducer to slide easily into their position at the center of the pipe where they are locked in place. At the bottom of the coupling opposite of the compression fittings, two holes of equal diameter have been drilled to allow the cotton sock to pass through the pipe and into the reservoir. The second hole was drilled so that side-by-side comparison tests can be done using wicks that are exposed to different pre-treatments as well as tests with wicks made of different materials.

5.2 Wicking Height Measurement Procedure

The following steps are taken to measure the wicking height of the cotton sock at different environmental conditions using the experimental apparatus described in Section 5.1.

1. Attach the PVC coupling to the end of the acrylic pipe.
2. Turn on the environmental chamber and set to the desired temperature and humidity test condition.
3. Allow the chamber to reach the desired test condition (which requires between 30-60 minutes) before collecting data.
4. While the chamber is approaching the test condition, turn on the chilled mirror hygrometer, Lakeshore Model 120 current source, Campbell Scientific CR23X Micrologger and variable autotransformer.
5. Place the velocity transducer in one of the compression fittings at the end of the coupling pipe. Position the transducer so that it measures the air velocity next to the

wet-bulb temperature sensor in which the wicking height measurement is taking place.

6. Adjust the variable autotransformer to obtain the target air velocity for the test under consideration.
7. Begin individual experiments.

The wicking height is measured at several environmental conditions (temperature and humidity) for air velocities of 2, 6, and 10 m/s at each condition.

Once the environmental chamber has reached the desired test condition, the wet-bulb temperature sensor is inserted into the proper compression fitting. A cotton sock is placed on the temperature sensor and the sensor is lowered to the bottom of the duct. The sock passes through the hole at the bottom of the duct and into a reservoir of colored, distilled water. The water is colored so that the wicking height can be measured by visual observation. To color the water one drop of food coloring was used per cup of water. Separate experiments were carried out in order to verify that the addition of this amount of food coloring to the water does not affect the wicking characteristic of the cotton sock. The socks used for these experiments were all boiled in distilled water for ten minutes to avoid particulate contamination prior to their use. A new boiled sock is used before each individual test.

After the sock has been immersed in the reservoir, the wicking height is measured every 15 minutes until the liquid reaches a height that does not change over a period of at least 30 minutes. This steady state height is determined to be the “wicking height” at the given

conditions. The wicking height is measured, using a measuring tape (Figure 5-2), from the surface of the water reservoir to the highest point at which the colored water can be detected on the sock.

Figure 5-2: Wicking height measurement.

The air velocity, dew-point temperature, dry-bulb temperature, wet-bulb temperature, and pressure are measured and recorded throughout the tests in order to accurately determine the experiment conditions associated with each test.

5.3 Wicking Height Measurement Experimental Results

Using the procedure described above, the wicking height was measured at six different environmental conditions. Five values of the air velocity were used at the first two conditions and three values were used for the final four conditions. The data recorded by the

micrologger was then analyzed using EES to determine the actual dry-bulb temperature, wet-bulb temperature, dew-point temperature, air velocity, and pressure during each test.

5.3.1 Effects of Free Stream Velocity and Relative Humidity on Wicking Height

The experimental measurements show that the wicking height of the cotton sock is a function of the dry-bulb temperature, relative humidity and local air velocity of the surroundings in which the measurements are being taken. Figure 5-3 shows that there is a nearly linear relationship between the wicking height of the cotton sock and the velocity of the air at each environmental condition.

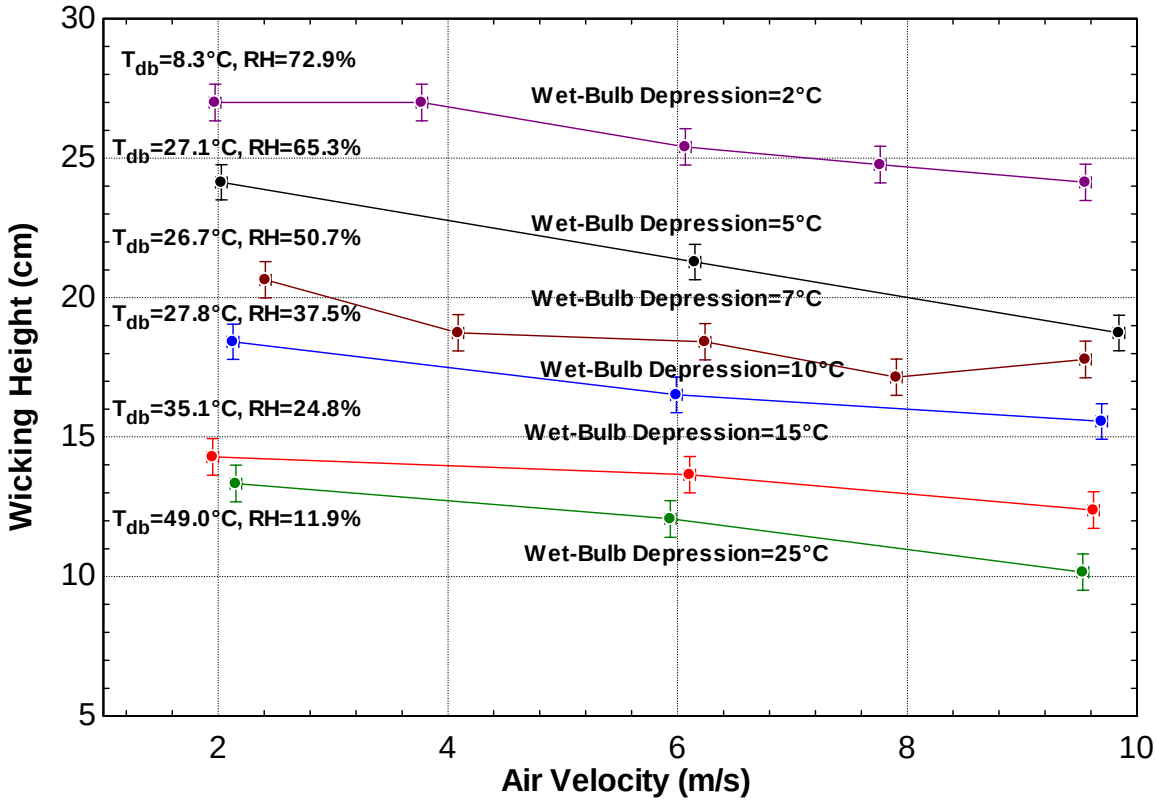

Figure 5-3: Wicking height as a function of air velocity for six different environmental set-points. Each environmental condition is labeled with the dry-bulb temperature, relative humidity and wet-bulb depression.

As the air velocity increases, the wicking height decreases almost linearly for each test condition. Figure 5-3 also indicates the strong relationship between the environmental condition and the wicking height, particularly the relative humidity and the wet-bulb temperature depression. At higher relative humidity conditions, the evaporative mass flow rate from the wet cotton sock is reduced and the water is able to wick higher up the sock. The opposite is true at lower relative humidity. Equation (5.3.1) provides a relationship for the water evaporation mass flow rate as a function of the average mass transfer coefficient, wick geometry, and concentration difference between the wick and free stream.

$$\dot{m} = \bar{h}_D \; \pi \; D_{sensor} \; L_{wick} \left(c_{v,sat} - c_{v,\infty} \right) \tag{5.3.1}$$

where $\dot{m}$ is the evaporative mass flow rate from the sensor, $\bar{h}_D$ is the average mass transfer coefficient, and D_{sensor} is the diameter of the cotton sock (which in this case is the same as the diameter of the sensor), L_{wick} is the wicking height, and $c_{v,sat}$ and $c_{v,\infty}$ are the concentration of saturated water vapor at the wet-bulb temperature and the concentration of water vapor in the free stream air, respectively. Equation (5.3.1) explains the experimental data shown in Figure 5-3. The evaporative mass flow rate is limited by the capillary action of the cotton sock. As the concentration gradient is increased, the evaporation rate will increase and, as a result, the wicking height will necessarily decrease because the mass flow rate is limited by the capillary action. The same is true, but to a lesser extent for an increase in air velocity. An increase in air velocity increases the mass transfer coefficient leading to an increase in the mass flow rate, but again the mass flow rate is limited by the capillary action of the sock and the wicking height is reduced. The capillary limit, as predicted by the empirical model

discussed below, is 7378 mg/hr. This is the evaporative mass flow rate corresponding to zero wicking height.

5 3.2 Effects of Evaporation Mass Flow Rate on Wicking Height

The main objective of the wicking height experiment is to develop an empirical model that is capable of predicting the wicking height at a given set of psychrometric conditions and air velocity. Figure 5-4 shows the wicking height as a function of the evaporation mass flow rate predicted by Eq. (5.3.1).

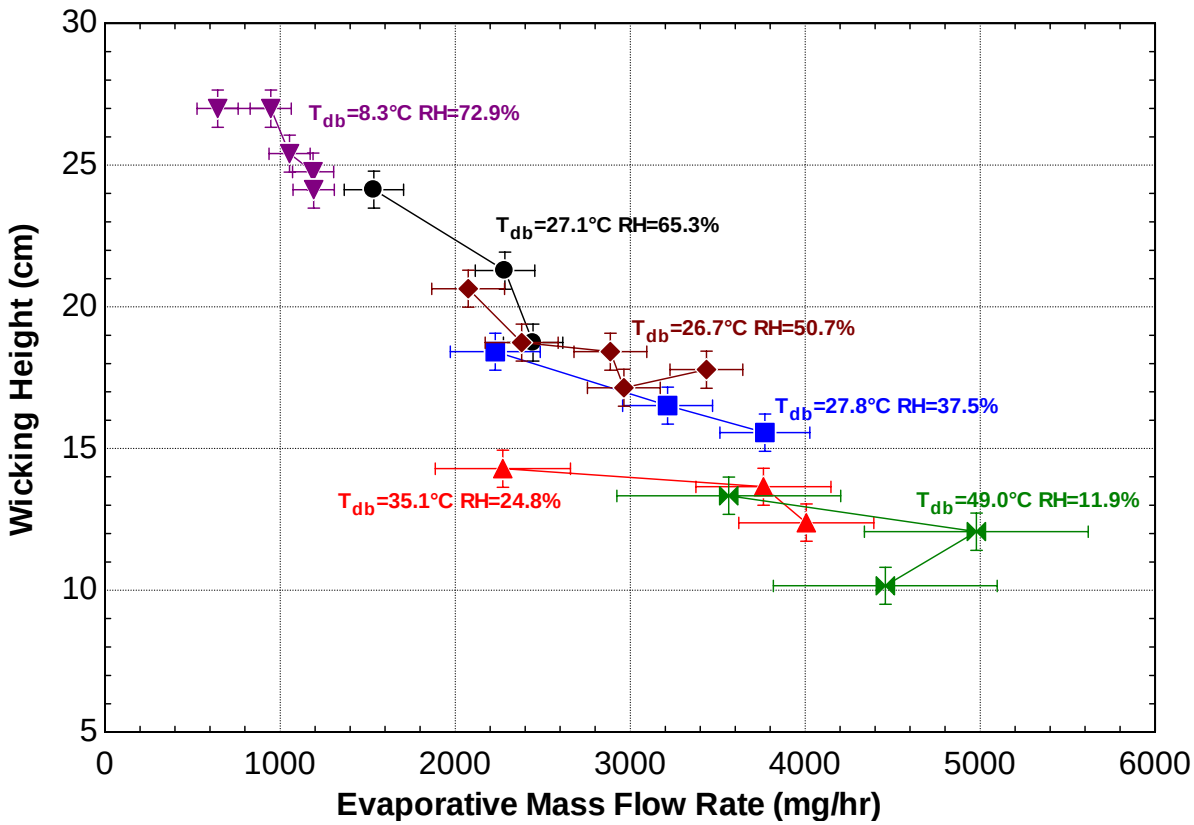

Figure 5-4: Wicking height as a function of evaporation mass flow rate for six different environmental set-points. Each environmental condition is labeled with the dry-bulb temperature and relative humidity.

Figure 5-4 indicates an approximately linear relationship between the wicking height and the evaporation mass flow rate. A linear curve fit to the experimental data displayed in Figure 5-4 can be described by Eq. (5.3.2).

$$L_{wick} = 28.90(cm) - 3.917\text{x}10^{-3}\left(\frac{cm-hr}{mg}\right)\dot{m} \tag{5.3.2}$$

where $\dot{m}$ is again the evaporative mass flow rate (mg/hr) and L_{wick} is the predicted wicking height (cm). The linear curve fit to the experimental data, Eq. (5.3.2), can be used in conjunction with Eq. (5.3.1) to predict the wicking height over the entire range of experimental test conditions. Figure 5-5 shows the wicking height predicted by the model as a function of the measured wicking height and demonstrates the agreement of the experimental data with the model prediction for all of the tests done

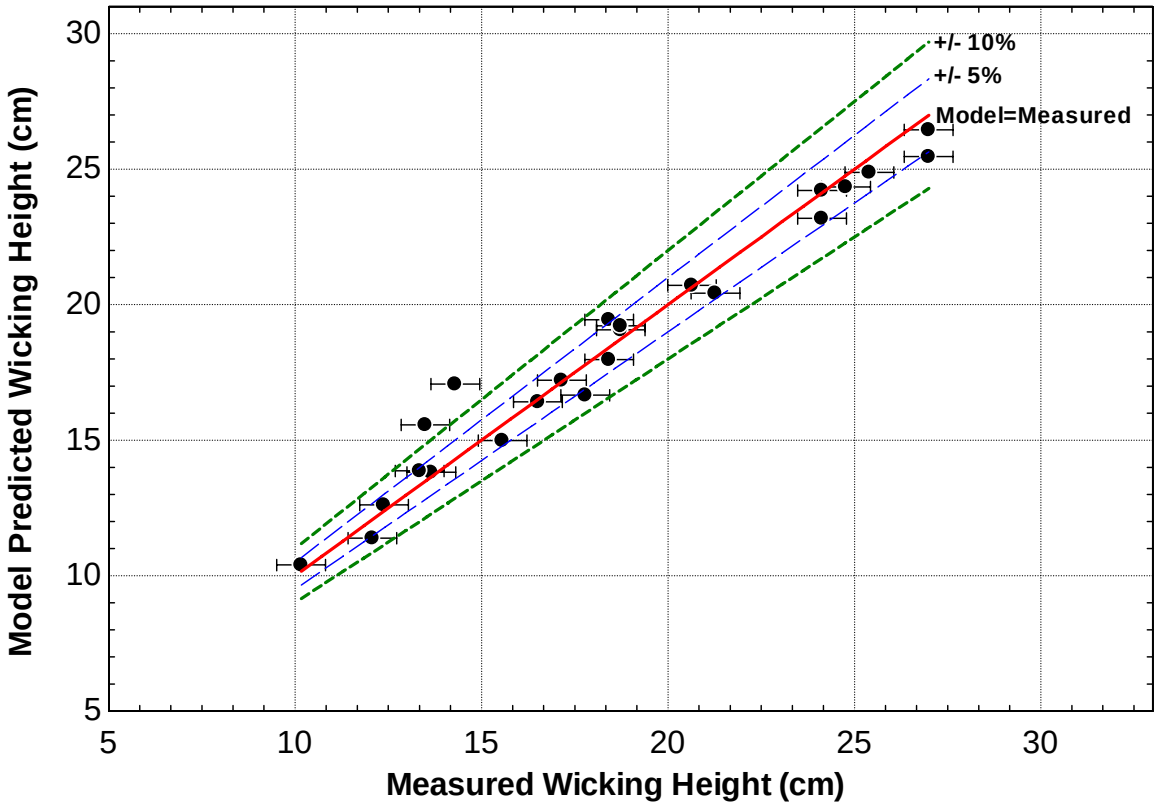

Figure 5-5: Wicking height predicted by the model vs. measured wicking height with curves for ± 5% and ±10% error.

The model predicted wicking height within 10% of the experimentally measured wicking height for all but two of the tests considered. It is important to remember, however, that the empirical relationship between the wicking height and the mass flow rate, as described by Eq. (5.3.2), is only characteristic of the boiled cotton sock used in the tests. Different sock material and pretreatments may alter the wicking height at various conditions, and may shift the observed linear relationship.

5.4 Wicking Height Measurement Uncertainty

The variables that are of particular interest in relation to the wicking height measurement tests are the dry-bulb temperature, air velocity, relative humidity, wicking height, and

evaporation mass flow rate. The calculation of the uncertainty for each of these quantities has been presented in previous progress reports. This section of the report will define the uncertainty in each of these quantities for the wicking height tests.

5.4.1 Dry-Bulb Temperature Measurement Uncertainty

The uncertainty in the dry-bulb temperature measured by the Omega PT100 RTD is calculated in a similar manner to the Fluke Model 5640 thermistor probe, which was presented in the Section 4.2.1. The PT100 has a nominal resistance of 100 Ω at 0°C and a rated uncertainty of ±0.15°C. The Campbell Scientific CR23X Micrologger has a calibrated voltage uncertainty of ±10 μV over a ±200 mV range, and the LakeShore Model 120 Current Source has an uncertainty of ± 0.1% at 1mA. Combining the uncertainty in each of these devices yields an uncertainty in the dry-bulb temperature measurement of ±0.3°C for the entire range of temperatures considered.

5.4.2 Air Velocity Measurement Uncertainty

The air velocity is measured with the same TSI Model 8455 velocity transducer that is used to specify the velocity for the wet-bulb temperature measurement. The uncertainty in this device, as described in Section 4.2.5, is ±0.05 m/s over the entire air velocity range.

5.4.3 Relative Humidity Measurement Uncertainty

The contributing factors to the uncertainty in the measurement of relative humidity during the wicking height tests are dry-bulb temperature, dew-point temperature and local pressure. The uncertainty in dry-bulb temperature, as calculated above, is ±0.3°C. The uncertainties in

the dew-point temperature measurement and local pressure measurement are ±0.04°C and ±180 Pa, respectively. These calculations and the respective uncertainty values can be found in Section 4.2.2 and 4.2.3, respectively. EES is then used to propagate these uncertainty values into an uncertainty estimate for relative humidity. The uncertainty in the various relative humidity values in which tests were conducted are show in Table 5-1.

Relative Humidity (%)	Dry-Bulb Temp (°C)	RH Uncertainty (%)
11.9	49.0	±0.2
24.8	35.1	±0.4
37.5	27.8	±0.7
50.7	26.7	±0.9
65.3	27.1	±1.4
72.9	8.3	±1.6

Table 5-1: Uncertainty in the relative humidity measurement.

5.4.4 Wicking Height Measurement Uncertainty

The uncertainty involved with measuring wicking height is estimated based on the precision of the measuring tape used and the variation in the wicking height around the circumference of the wick. Taking these factors into consideration, the wicking height is measured with an uncertainty of ±6.35 mm (±0.25 in).

5.4.5 Evaporation Mass Flow Rate Uncertainty

The uncertainty in the calculation of the evaporation mass flow rate is based on the uncertainties in measuring dry-bulb temperature, dew-point temperature, local pressure, free stream air velocity, and wicking height. The uncertainty values are listed in Sections 5.4.1-5.4.4. EES is used to propagate the uncertainty in each individual measurement into an

uncertainty associated with the calculated evaporative mass flow rate. The uncertainty in evaporation mass flow rate for each psychrometric state can be found in Table 5-2.

Relative Humidity (%)	Dry-Bulb Temp (°C)	2 m/s Air Velocity- Mass Flow Rate Uncertainty (mg/hr)	6 m/s Air Velocity- Mass Flow Rate Uncertainty (mg/hr)	10 m/s Air Velocity- Mass Flow Rate Uncertainty (mg/hr)
11.9	49.0	±302	±501	±640
24.8	35.1	±174	±306	±386
37.5	27.8	±124	±202	±257
50.7	26.7	±110	±170	±208
65.3	27.1	±95	±147	±170
72.9	8.3	±60	±99	±118

Table 5-2: The uncertainty in the mass flow rate prediction. As is shown, the uncertainty in the predicted evaporative mass flow rate increases with increasing air velocity and with decreasing relative humidity.

The main contributor to the uncertainty in the evaporative mass flow rate is the uncertainty in the dry-bulb temperature and wicking height measurements.

5.5 Wicking Height Measurement Repeatability

The repeatability of the wicking height measurement procedure was tested by completing four experiments, each at two different environmental set points and comparing the results. The air velocity was held constant for each test. The tests that were carried out at a dry-bulb temperature of 27.1°C and a relative humidity of 65.3% provided measurements with a repeatability of ±0.95 cm. Tests carried out at a dry-bulb temperature of 49.0°C and a relative humidity of 11.9% yielded measurements with a repeatability of ±0.3 cm, which is

less than the theoretical uncertainty in the wicking height measurement. The results from the repeatability tests are shown in Table 5-3.

Measured Wicking Height (cm)	
T_{db}=27.1ºC, RH=65.3%	**T_{db}=49.0ºC, RH=11.9%**
21.3	12.1
20.0	11.8
20.6	12.2
19.4	12.4

Table 5-3: Measured wicking heights at two specified conditions with the tests repeated four times for each test condition.

Possible sources of measurement variance are the replacement of the cotton sock for each test and possibly slight deviation of experimental conditions within the test facility.

5.6 Impact of Wick Orientation

With an empirical relationship between the wicking height and the predicted evaporative mass flow rate now determined, the impact of the orientation of the cotton sock could be further analyzed. The orientation that is referred to corresponds to the section of the cotton wick that extends from the bottom of the temperature probe to the top of the water reservoir. Figure 5-6 gives a clearer indication of the portion of the wick that is the subject of this analysis.

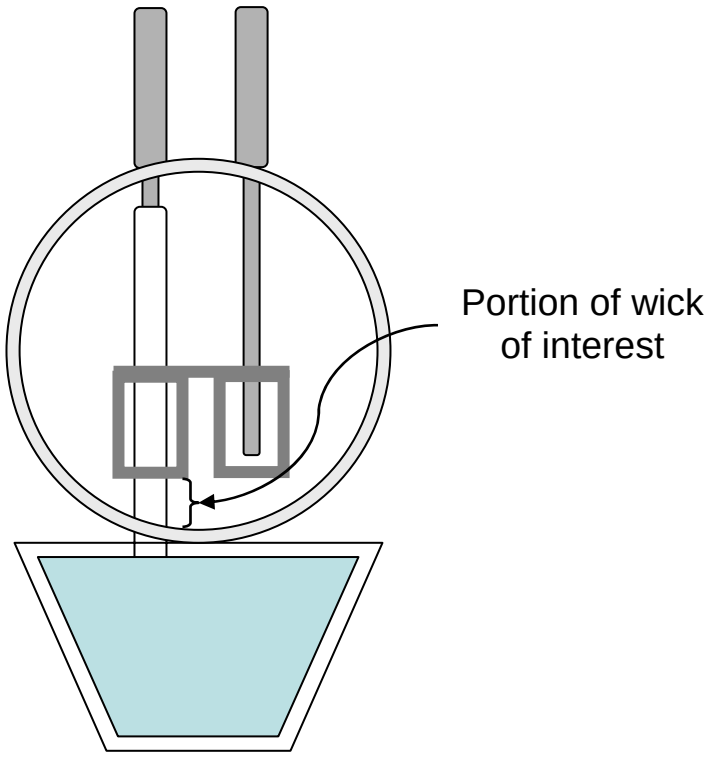

Figure 5-6: Schematic showing the portion of the cotton sock between the bottom of the temperature sensor and the top of the water reservoir.

It was previously determined that a 1.3 cm (0.5 in) length of wet cotton sock should be exposed to the air stream beneath the temperature probe in order to ensure that the wick comes to the wet-bulb temperature at the temperature probe; this reduces the conduction parasitic associated with the makeup water which is at the dry-bulb temperature to a negligible level. The previous analysis also indicated that the orientation of this section of cotton sock did not impact the length required to ensure that the sock came to the wet-bulb temperature. That is, the exposed portion of the cotton sock could be cylindrical, flattened with the flat portion of the wick oriented parallel to the flow, or flattened with the flat portion of the wick oriented perpendicular to the flow; in any of these orientations, a 1.3 cm (0.5 in)

length is sufficient to eliminate the entire makeup water parasitic. A photograph of the wick orientations is shown in Figure 5-7.

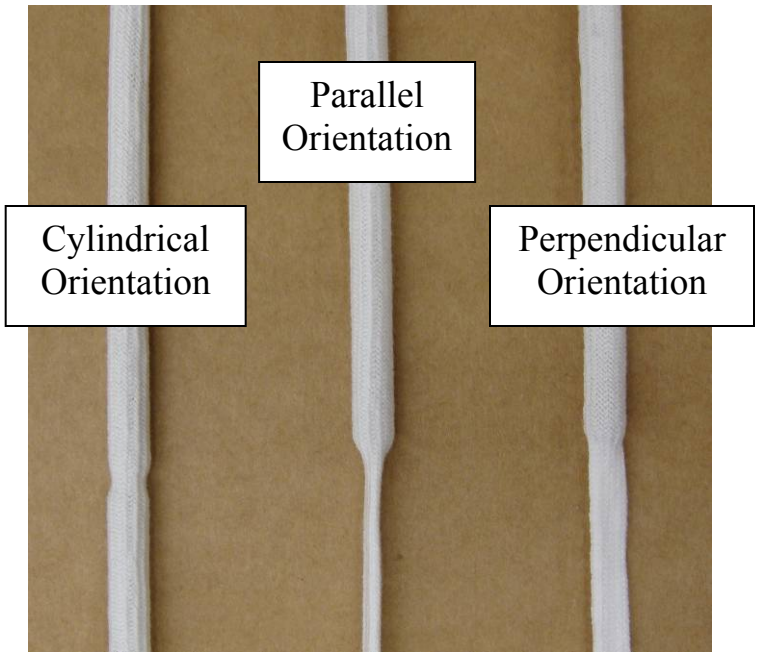

Figure 5-7: Three different sock orientations. The sock on the left is oriented in a cylindrical shape. The sock in the middle is oriented with the flat portion of the wick parallel to the flow (air flow direction is into the page) and the one on the right is oriented with the flat portion perpendicular to the flow.

The previous analysis neglected the impact of the orientation of the wick on the overall wicking height; the overall wicking height ultimately dictates the length of wetted sock above the sensor which is directly related to the conduction parasitic along the sheath of the sensor. A more complete analysis is now possible due to the empirical model of the wicking height discussed in Section 5.3.

The first step in determining the wicking height associated with the various orientations is to separate the analysis into two parts, one for the upper portion of the cotton sock and one for the lower portion. The “upper portion” is that portion of the cotton sock surrounding the

temperature sensor and the sheath. By virtue of its location on the temperature sensor sheath, the upper portion of the cotton sock will have a fixed (i.e., cylindrical) shape. The lower portion refers to the portion of the cotton sock extending from the bottom of the temperature probe to the top of the water reservoir, as depicted in Figure 5-6, and may be oriented differently as shown in Figure 5-7. The analysis that will be presented here is for a cotton sock with a parallel orientation.

The evaporative mass flow rate from the **top portion of the wick** can be described by:

$$\dot{m}_{top,par} = \overline{h}_{D,cyl} \pi D_{sensor} L_{wick,top,par} \left(c_{v,sat} - c_{v,\infty} \right) \tag{5.6.1}$$

where $\overline{h}_{D,cyl}$ is the mass transfer coefficient over a cylinder (Churchill and Bernstein, 1977), D_{sensor} is the diameter of the sock, which in this case is equal to the diameter of the sensor, and $L_{wick,top,par}$ is the height that the water wicks up in the top portion of the cotton sock. The concentration of saturated water vapor at the wet-bulb temperature and the concentration in the free stream are $c_{v,sat}$ and $c_{v,\infty}$, respectively, and $\dot{m}_{top,par}$ is the evaporative mass flow rate from the top portion of the cotton sock. Remembering that the top portion of the sock is the section of sock between the flattened section of the wick and the point in which the wick dries out. In both the mass flow rate and wicking height term, the subscript *par* is used to indicate that the values are for a test in which the bottom portion of the cotton sock is in the parallel orientation.

The evaporative mass flow rate from the bottom portion of the cotton sock is described by Eq. (5.6.2).

$$\dot{m}_{bottom,par} = \overline{h}_{D,par} \pi D_{sensor} L_{wick,bottom} \left(c_{v,sat} - c_{v,\infty} \right) \tag{5.6.2}$$

where $\overline{h}_{D,par}$ is the mass transfer coefficient experienced by the bottom portion of the cotton sock in a parallel flow orientation (Churchill and Ozoe, 1973), $L_{wick,bottom}$ is the wicking length for the bottom portion of the cotton sock (i.e., 1.3 cm), and $\dot{m}_{bottom,par}$ is the evaporative mass flow rate from the bottom portion of the cotton sock in a parallel flow orientation. All other terms are the same as previously described.

The sum of the evaporative mass flow rate from the top and bottom portion of the cotton sock can be used to predict the wicking height. The evaporative mass flow rate from the bottom portion of the sock can be found directly for each orientation by knowing only the psychrometric conditions at which the measurement is occurring and the air velocity in which the test is being run. The wicking height up the top portion of the sock will vary for each test based on the overall wicking height.

The empirical model discussed in Section 5.3 is used to predict a wicking height based on evaporative mass flow rate. The mass flow rate is the total mass flow rate which corresponds to the sum of the evaporative mass flow rates from the bottom and top portion of the wick.

$$\dot{m}_{total,par} = \dot{m}_{top,par} + \dot{m}_{bottom,par} \tag{5.6.3}$$

where $\dot{m}_{top,par}$ and $\dot{m}_{bottom,par}$ are the evaporative mass flow rates from the top and bottom portion of the wick, respectively, while the bottom portion of the wick is in the parallel orientation. The total mass flow rate from the entire wick with the bottom portion of the wick in the parallel flow orientation is represented by $\dot{m}_{total,par}$. The total wicking height is:

$$L_{wick,total,par} = L_{wick,top,par} + L_{wick,bottom} \tag{5.6.4}$$

where $L_{wick,top,par}$ is the wicking height up the top portion, $L_{wick,bottom}$ is the wicking height up the bottom portion of the sock (i.e., 1.3 cm), and $L_{wick,total,par}$ is the total wicking height from the top of the reservoir while the bottom portion of the cotton sock is in the parallel orientation. The final equation required is the empirically determined relationship between the total wicking height and the total evaporative mass flow rate.

$$L_{wick,total,par} = 28.90(cm) - 3.917\text{x}10^{-3}\left(\frac{cm-hr}{mg}\right)\dot{m}_{total,par} \tag{5.6.5}$$

With the appropriate unit conversions, Eqs. (5.6.2) to (5.6.5) can be used to determine the wicking height at any psychrometric condition with the bottom portion of the wick having a parallel orientation.

An analysis for the two other orientations is completed in the same manner as described above. The only difference is that a different correlation is used to determine the mass transfer coefficient. For the cylindrical orientation, a correlation for external flow over cylinder (Churchill and Bernstein, 1977) is used and for the perpendicular orientation a

correlation for external flow over a vertical plate (Jakob 1949) is used. The different mass transfer coefficients lead to different evaporative mass flow rates and different wicking heights under the same set of psychrometric conditions.

The wicking height is shown as a function of the wet-bulb depression in Figure 5-8.

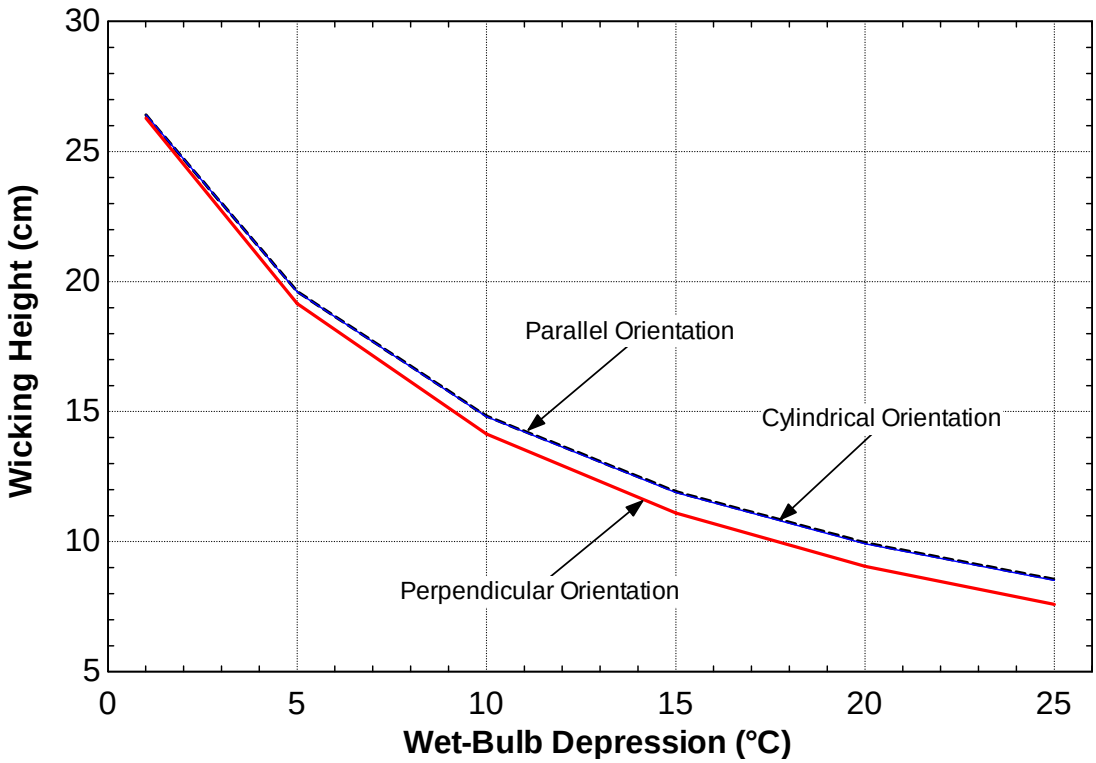

Figure 5-8: Predicted wicking height from the top of the water reservoir for the three different sock orientations. The data plotted is for a constant dew-point temperature of 2°C. Model predicted wicking heights deviate minimally with dew-point temperature (i.e., < 1 mm).

Figure 5-8 shows that both the parallel and the cylindrical orientations are preferable to the perpendicular orientation, as the wicking height associated with either of these orientations may be as much as 1 cm higher than the perpendicular orientation at a wet-bulb depression of 25°C. With a wet-bulb depression of 25°C the wicking height is low, and therefore a 1 cm

(0.39 in) reduction in wicking height can lead to a significant increase in the measurement error. The conduction parasitic model, discussed in the Section 3.3, predicts an increase in the wet-bulb temperature measurement **error of 0.4°C or more with a 1 cm reduction in the wicking height** under high wet-bulb depression conditions. This large increase in error highlights the importance of keeping the wick in a cylindrical or parallel orientation rather than a perpendicular orientation.

At wet-bulb depressions less than 10°C, however, the orientation of the wick is not important. The reason for this is that the wicking height deviation between the various orientations is small and the wicking heights are relatively high, as shown in Figure 5-8. High wicking heights provide an effective guard against conduction parasitic and therefore the slight deviations in wicking heights are unnoticed. To remain consistent between measurements and to maintain the wicking height as high as possible for all conditions, it is suggested that wick have a parallel orientation. The cylindrical orientation is as favorable as the parallel orientation; however, the cylindrical orientation is more complicated to implement due to the potential parasitic conduction associated with the structure required to maintain the wick in a cylindrical geometry.

Chapter 6 – Results

6.1 Test Matrix Results (1)

Chapter 4 presented details of the experimental equipment and apparatus used to measure the wet-bulb temperature, estimates of measurement uncertainty, and measurement procedures. Using the testing procedure documented in the Chapter 4, the wet-bulb temperature was measured at each of the thirty test points that make up the entire test matrix. The measured wet-bulb temperature is compared to the results obtained from a separate instrument with a known accuracy (a chilled mirror dew-point hygrometer) in order to determine the accuracy of each of the measurements. Figure 6-1 shows the difference between the measured wet-bulb temperature and the adiabatic saturation temperature (measured with the chilled mirror hygrometer) at each of the conditions in the test matrix.

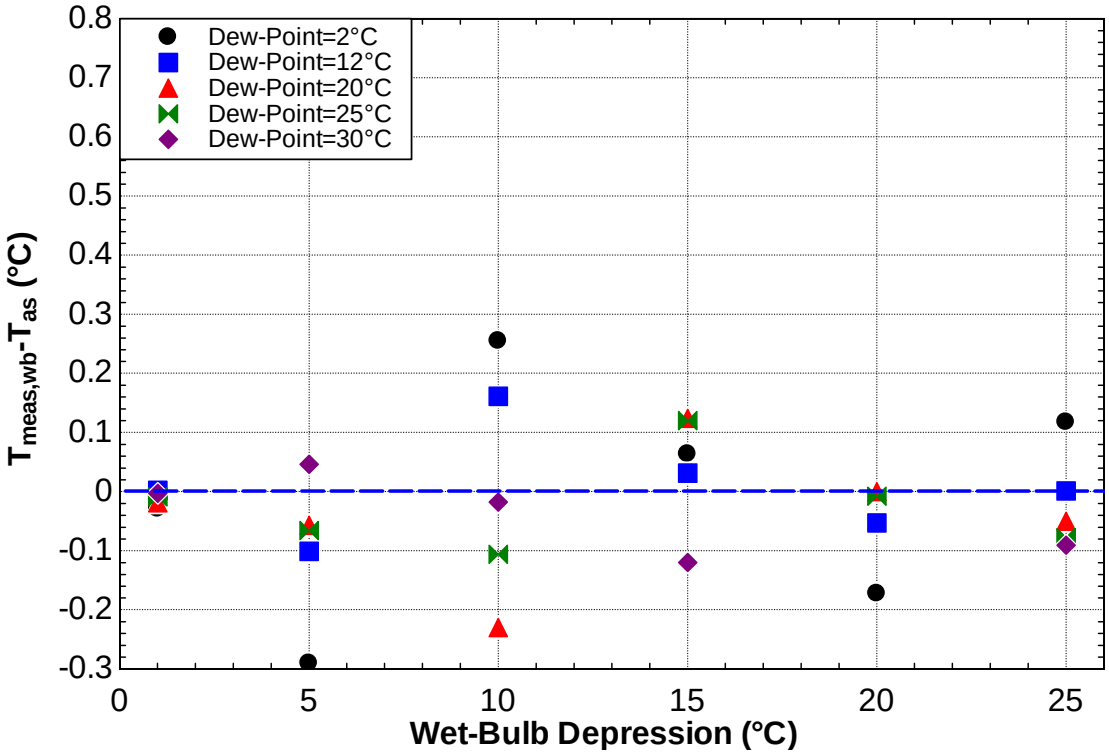

Figure 6-1: The difference between the measured wet-bulb temperature and the adiabatic saturation temperature for each of the thirty conditions in the test matrix. Each symbol indicates a constant dew-point temperature.

The difference between the measured wet-bulb and adiabatic saturation temperatures is plotted against the wet-bulb temperature depression in order to identify whether a clear trend might be revealed; notice that the test matrix varies the wet-bulb depression from 1°C to 25°C for each of five constant dew-point temperatures. From Figure 6-1, it is clear that the wet-bulb temperature measured is very close to the adiabatic saturation temperature (i.e. within ±0.05°C) at a 1°C wet-bulb temperature depression. The error increases, however, as the wet-bulb depression is increased above 1°C. With the exception of a few outlying points corresponding to very low dew point conditions, the experimental results indicate that the measured wet-bulb temperature can be used to predict the adiabatic saturation temperature within ±0.15°C over the entire range of conditions within the test matrix.

In Figure 6-2, the difference between the measured wet-bulb temperature and the true wet-bulb temperature is plotted as a function of the wet-bulb temperature depression. The true wet-bulb temperature is the wet-bulb temperature that the device should measure (based on the conditions measured using the chilled mirror) in the absence of any parasitic heat transfer to the wet bulb temperature sensor.

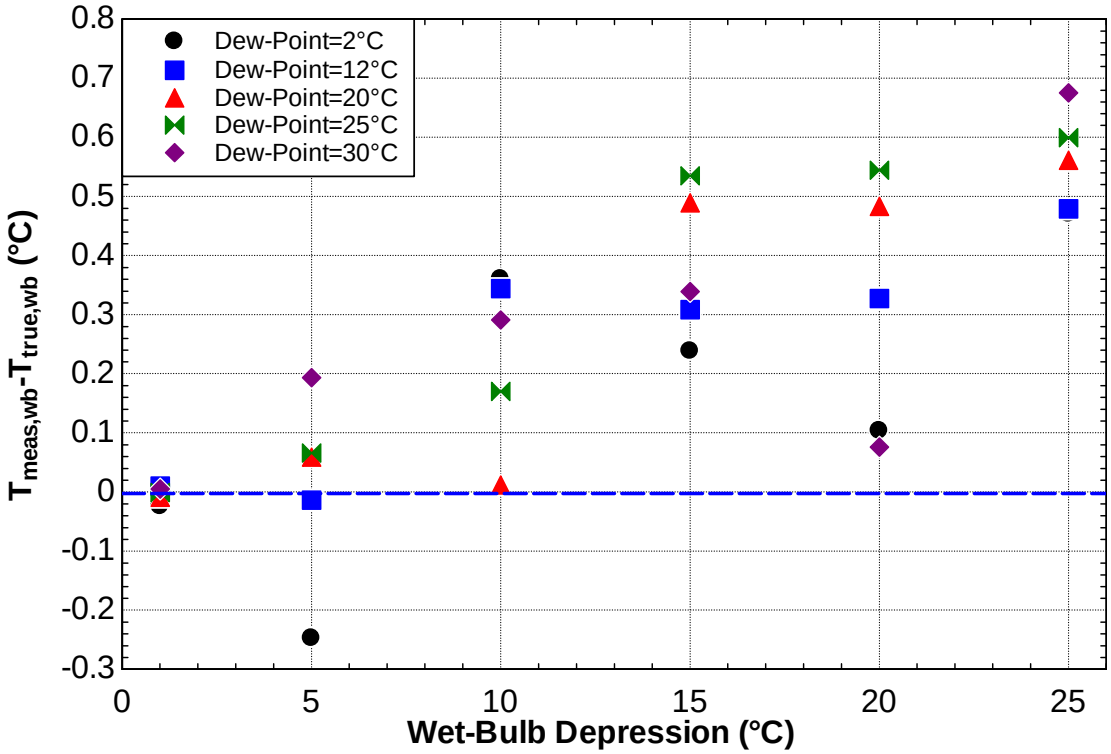

Figure 6-2: The difference between the measured wet-bulb temperature and the true wet-bulb temperature for each of the thirty conditions in the test matrix. Each symbol indicates a constant dew-point temperature.

Again, the measured wet-bulb temperature very closely approximates the true wet-bulb temperature (i.e. within ±0.05°C) at a wet-bulb depression of 1°C. However, there is a clear trend of increasing difference between the measured wet-bulb temperature and the true wet-bulb temperature as the wet-bulb temperature depression is increased. This is expected

because, as the wet-bulb temperature depression increases, the parasitic heat gain to the wet-bulb sensor will increase. As the depression is increased, radiation obviously increases. Also, the in-situ conduction parasitic increases even more substantially because the driving temperature difference increases and the wicking capability of the cotton sock is diminishing (as shown in Figure 5-3). Note that the increase in the parasitic heat transfer rate with increasing wet-bulb temperature depression is not evident in Figure 6-1 where the measured wet bulb temperature is compared to the adiabatic saturation (rather than the true wet bulb temperature). This is because the difference between the adiabatic saturation temperature and the true wet-bulb temperature also increases as the wet-bulb temperature depression increases. The increasing parasitic heat transfer to the wet-bulb sensor that occurs at increasing temperature depressions is compensated for (at least somewhat) by the increasing difference between the adiabatic saturation temperature and the true wet-bulb temperature. Figure 6-3 shows the difference between the adiabatic saturation temperature and the true wet-bulb temperature for various values of dew-point temperature as a function of the wet-bulb temperature depression. Note that Figure 6-3 has nothing to do with the data collected by the experiment; it is entirely related to the definition of the two quantities: true wet-bulb temperature and adiabatic saturation temperature.

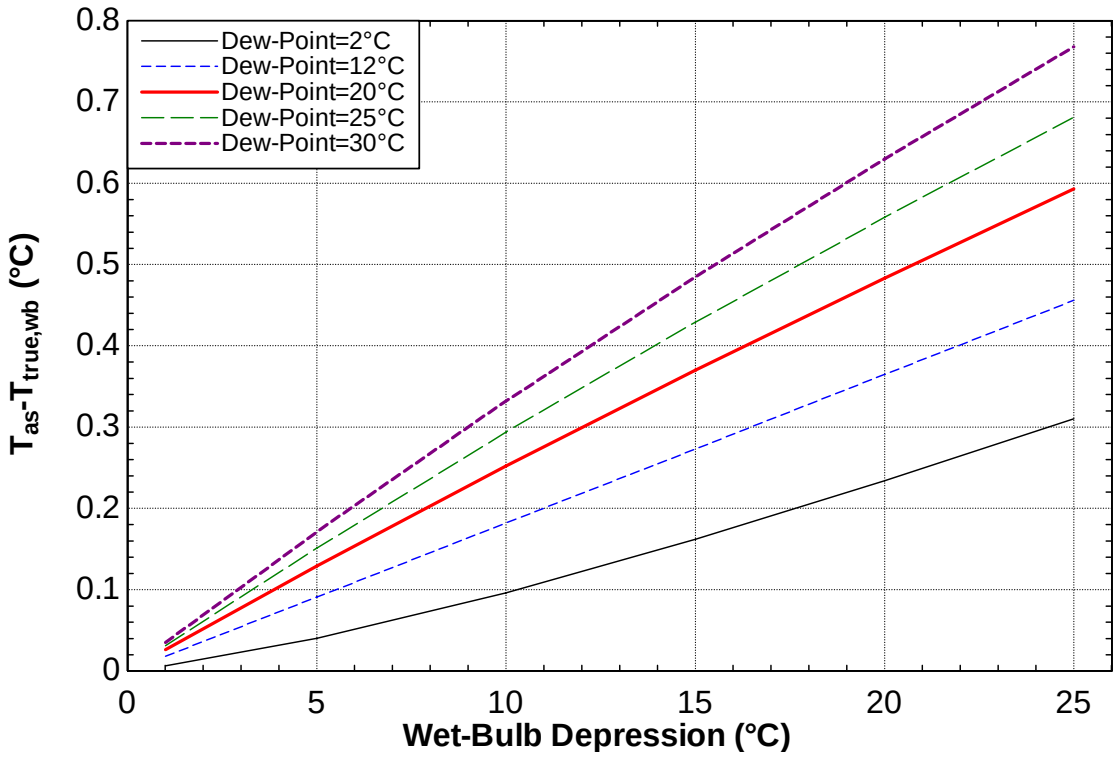

Figure 6-3: The difference between the adiabatic saturation temperature and the true wet-bulb temperature as a function of wet-bulb temperature depression for various values of constant dew-point temperature.

Figure 6-3 indicates that the adiabatic saturation temperature can be quite different from the true wet-bulb temperature, depending on the conditions. For example, at a wet-bulb depression of 25°C and a dew-point temperature of 30°C, the adiabatic saturation temperature is more than 0.75°C higher than the true wet-bulb temperature. Thus a "perfect" wet-bulb temperature sensor (with no parasitic heat gain) would measure a temperature that is 0.75°C lower than the adiabatic saturation temperature. The impact of the parasitic heat transfer to the actual device is to increase the measured wet-bulb temperature such that is more consistent with the adiabatic saturation temperature.

6.2 Repeatability Test Results

Figure 6-3 helps to explain the general trends observed in Figure 6-1 and Figure 6-2. However, the variability observed in the data collected during the first data collection period lacks consistency at each of the specified wet-bulb depressions. This behavior suggested that there may be an issue associated with the repeatability of the apparatus. To examine the repeatability of the test facility more closely, two test conditions were selected and the wet-bulb temperature was measured five separate times at each of the respective test conditions. The test conditions selected for repeatability testing both had a constant dew-point temperature of 12°C; one condition had a wet-bulb depression of 10°C and the second condition had a wet-bulb depression of 15°C. For all of the repeatability tests, the chilled mirror dew-point hygrometer was cleaned manually on a weekly basis. This was done in order to minimize the likelihood of errors associated with the mirror being unbalanced.

6.2.1 Sock & Radiation Shield Replaced Daily

The first sets of tests were performed using the following procedure. The cotton sock covering the wet-bulb temperature sensor was replaced daily with a clean boiled sock. Because the sock was replaced daily, the radiation shield had to be removed and reinstalled. Figure 6-4 indicates the results of this set of repeatability tests where the number adjacent to each data point represents the order of the measurement within the sequence. Results indicated by the same data marker (e.g., a triangle) were taken on the same day.

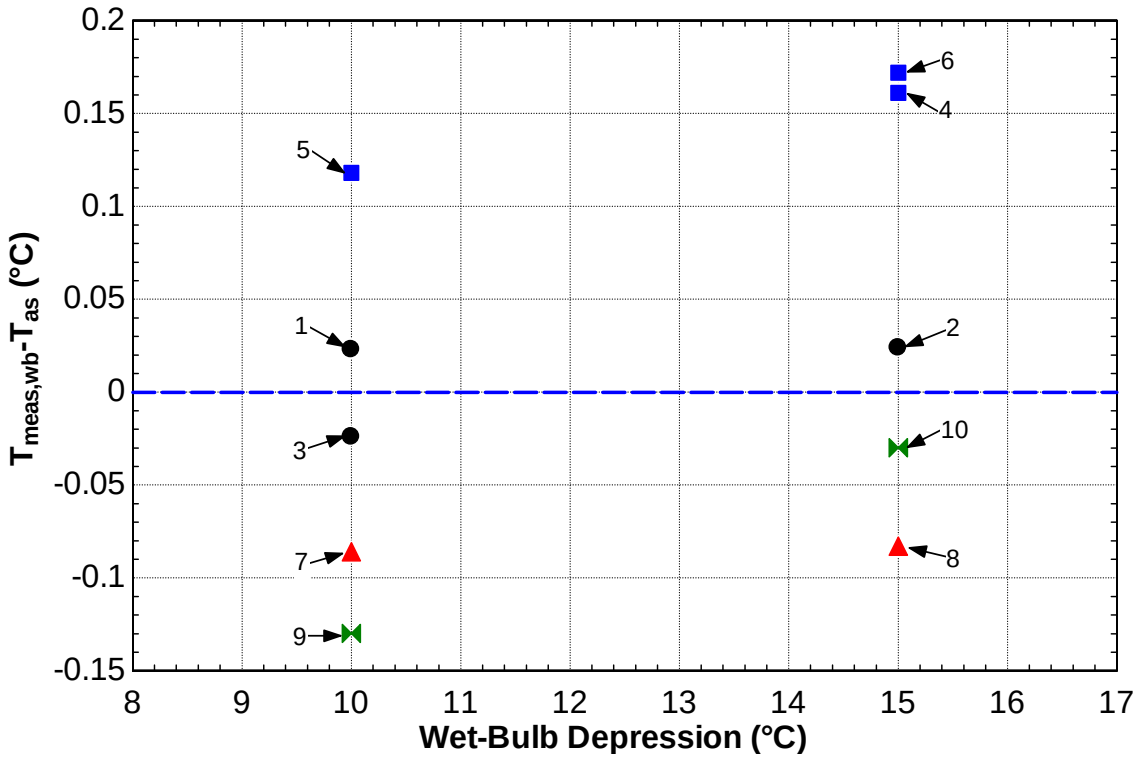

Figure 6-4: Repeatability results for the two conditions corresponding to a 12°C dew-point temperature and a 10°C and 15°C wet-bulb depression. The radiation shield was in place for each of the tests and the cotton sock was replaced daily. Results specified by the same data marker were obtained from tests occurring on the same day.

The repeatability of the measurement, as indicated in Figure 6-4, is less than desirable (i.e., the uncertainty associated with repeatability is approximately ±0.125°C). Interestingly, repeatability test runs conducted on the same day appear to have much lower uncertainty, which suggests that the accuracy of the wet-bulb measurement may be adversely affected by the removal and refastening the radiation shield each day and/or changing the cotton sock daily.

6.2.2 Sock Replaced Daily, Radiation Shield Removed

To test the hypothesis that larger wet bulb measurement uncertainty is being created by the daily removal and refastening of the radiation shield, additional tests were conducted at the same conditions but without the radiation shield attached. The cotton sock is still replaced daily in these tests, however. Figure 6-5 shows the results of this set of tests.

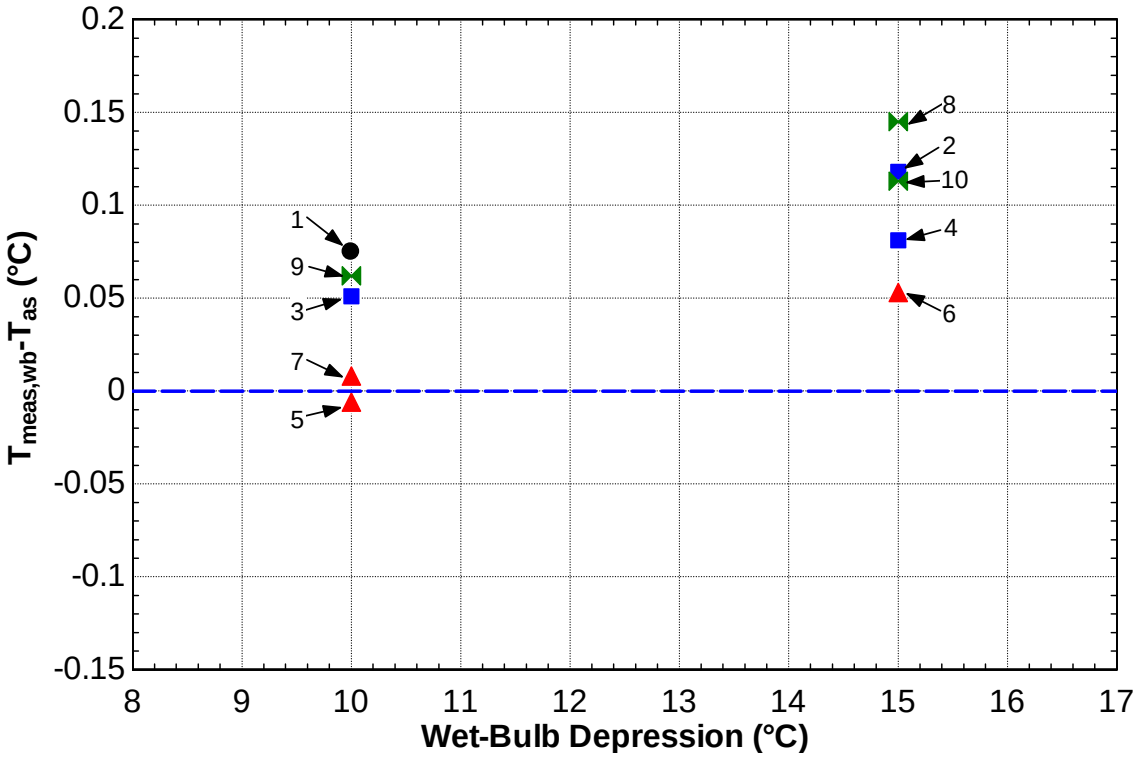

Figure 6-5: Repeatability results for the two conditions corresponding to a 12°C dew-point temperature and a 10°C and 15°C wet-bulb depression. The radiation shield was completely removed for each of the tests and the cotton sock was replaced daily. Results specified by the same data marker were obtained from tests occurring on the same day.

It was clear from these tests that the repeatability of the measurements improves considerably when the radiation shield is completely removed from the sensor, even though the sock continues to be replaced daily. Figure 6-5 indicates that the repeatability of this set of tests is

approximately ±0.05°C for both conditions. Again the daily repeatability in this measurement set is better than the total repeatability of the measurement.

6.2.3 Sock & Radiation Shield Remain For All Tests

The next repeatability test was done with the radiation shield in place (i.e., never removed and replaced) while continuing to use the same sock for the entire set of test runs. This set of data is shown in Figure 6-6.

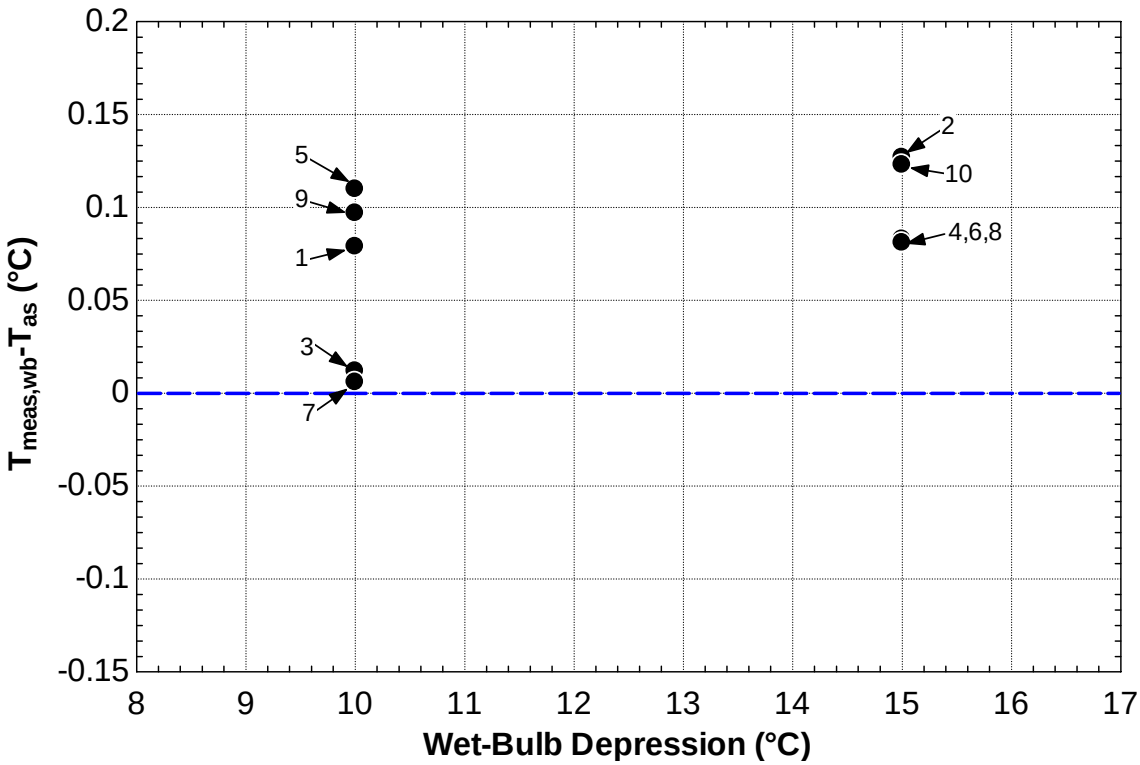

Figure 6-6: Repeatability results for the two conditions corresponding to a 12°C dew-point temperature and a 10°C and 15°C wet-bulb depression. The radiation shield and the same cotton sock remained in place for the entire set of test runs.

The repeatability results, again, show improvement relative to the scenario in which the radiation shield is removed and refastened and the cotton sock is replaced daily. At the 10°C

wet-bulb depression, the repeatability is approximately ±0.05°C and at the 15°C wet-bulb depression, the repeatability is even better, approximately ±0.025°C.

6.2.4 Sock & Radiation Shield Replaced Daily, Parallel Sock Orientation

After analyzing the results of the calculations shown in Section 5.6 of this report and consulting with the Project Monitoring Subcommittee sponsoring this research, one final set of wet-bulb temperature measurement repeatability testing was performed. For this set of tests the water level in the makeup water reservoir used to wet the cotton wick was held constant over the duration of the test and the lower section of the wick was maintained in the parallel orientation, as described in Section 5.6. The previous repeatability tests, as described in Section 6.2.1-6.2.3, were done before the analysis on the impact of the wick orientation was performed (see Section 5.6). As a result, each of these repeatability tests was done with the cotton sock in the perpendicular orientation rather than the parallel orientation.

To maintain an approximately constant water level, the smaller reservoir used to keep the cotton sock wet is connected to a larger reservoir with a much larger surface area. The two reservoirs are connected by a small tube which keeps their water levels at the same height, as shown in Figure 6-7.

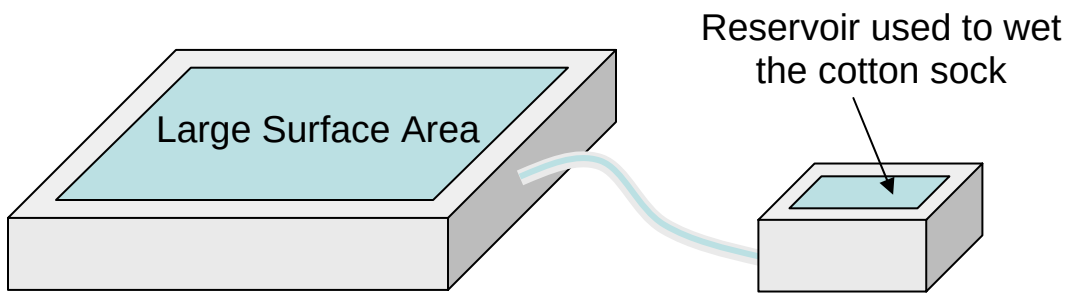

Figure 6-7: Schematic showing the larger water reservoir connected to the smaller water reservoir that is used to wet the cotton sock. The large water reservoir with the larger surface area keeps the water level approximately constant throughout a test.

Since the larger reservoir has a much larger surface area than the smaller reservoir, the height change in the two reservoirs is negligible over the course of one test.

The results from this set of repeatability tests are shown in Figure 6-8.

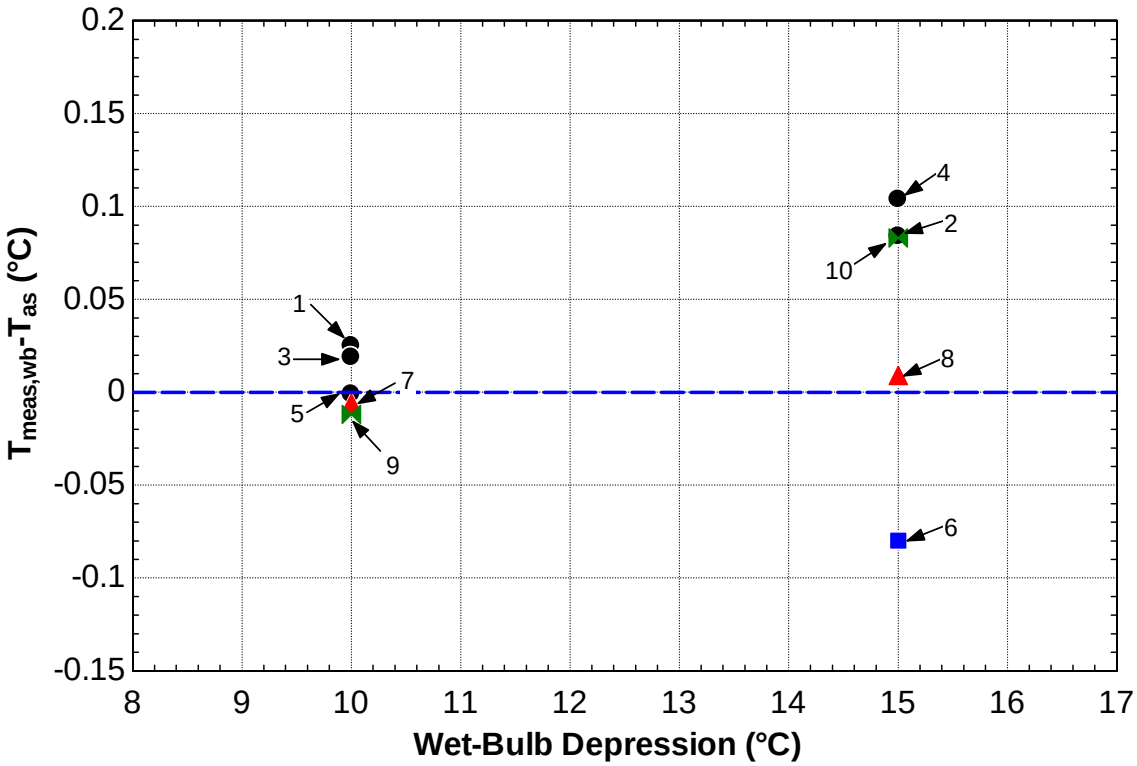

Figure 6-8: Repeatability results for the two conditions corresponding to a 12°C dew-point temperature and a 10°C and 15°C wet-bulb depression. The radiation shield was in place for all tests. All tests were done with the water level remaining constant throughout the test and the flat portion of the wick extending below the temperature sensor oriented parallel to the flow stream. Results specified by the same data marker were obtained from tests occurring with the same wick.

The results indicate that by maintaining a constant water level in the water reservoir and orienting the flat portion of the wick parallel to the flow stream (parallel orientation), the wet-bulb temperature measurement can be made with a repeatability of ±0.05°C at a dew-point of 12°C and a wet-bulb depression of 10°C. The repeatability is slightly worse (i.e., ±0.10°C) at a dew-point of 12°C and a wet-bulb depression of 15°C.

6.2.5 Summary of Repeatability Test Results

The four sets of repeatability data indicate that the measurement of the wet-bulb temperature can be made very repeatably (i.e. within ±0.05°C) but only if the tests are done very carefully

and consistently. The repeatability tests also indicate that simply removing and refastening the radiation shield and replacing the cotton sock can significantly and adversely affect the day-to-day repeatability of the measurement (i.e. from ±0.05°C to ±0.125°C). This variability in measurement is significant and cause for concern.

It is not entirely clear why replacing the cotton sock and removing and refastening the shield daily leads to such large variations in the wet-bulb temperature measurement. One possible reason is that when the radiation shield is removed and refastened to the wet-bulb temperature sensor, the set screws that are used to attach the shield to the sensor may be tightened differently. The variation in the tightness of the screws may alter the wicking height which will have an impact on the parasitic heat gain to the sensor.

The analytical models developed show that the measured wet bulb temperature is very sensitive to wick height at conditions of high wet bulb depression; these are also the conditions where the repeatability of the measurement is highest. As an example, the model suggests that at a wet-bulb depression of 25°C, the increased parasitic associated with reduced the wicking height by as little as 1 cm (0.39 in) can lead to an error of 0.4°C. Alterations in the shield attachment can also have an impact on the conduction parasitic through the set screws themselves. The tightness of the set screws will undoubtedly impact the length and area through which conduction will occur for the Teflon tipped set screws. The analytical model developed suggests that these alterations can vary the parasitic associated with the set screws by as much as 6 mW. This variation in parasitic corresponds to an estimated wet-bulb temperature measurement error of 0.042°C. Finally, replacing the

sock daily may affect the contact of the sock with the sheath of the wet-bulb temperature sensor. Every effort was made to keep the sock in good contact with the sensor sheath (i.e. not "bunched" up), but the variability of the sock contact with the sensor may also lead to repeatability issues.

After evaluating individual sources of parasitic gains predicted by the analytical models, it appears that the best way to reduce the error and improve the repeatability of the wet-bulb temperature measurement is a three-fold approach that will:

1. physically isolate the radiation shield from the temperature sensor,
2. maintain the lower portion of the cotton sock in the parallel orientation, and
3. control the water level in the water reservoir to be constant.

Physically isolating the shield from the sensor will eliminate all possible parasitic associated with the set screws. In addition, wicking action will not be impaired by the radiation shield's set screws. The revised design in which the radiation shield is isolated from the wet-bulb temperature sensor is shown in Figure 6-9.

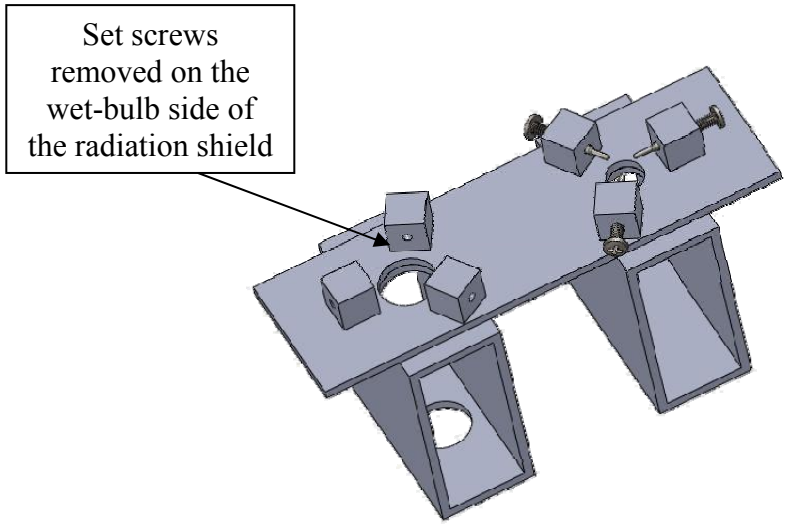

Figure 6-9: Radiation shield with the set screws removed on the wet-bulb temperature sensor side.

As shown in Figure 6-9, the radiation shield is only attached to the dry-bulb sensor and the set screws that were previously used to attach the shield to the wet-bulb sensor are removed. This arrangement ensures that the radiation shield is completely isolated from the wet-bulb sensor.

The purpose of orienting the parallel sock in the direction of air flow (see Figure 5-7) and maintaining a full water reservoir is to ensure that the water is able to wick up the sock as high as possible and maintain this configuration in a way that is as repeatable as possible.

6.3 Test Matrix Results (2)

Using the knowledge gained from the repeatability testing described in the previous sections, the wet-bulb temperature was again measured at each of the conditions composing the test matrix. Specifically, in this set of tests the radiation shield was physically isolated from the wet-bulb temperature senor, the wick was oriented parallel to the airflow for all tests, and the

water level in the water reservoir was held constant. The difference between the measured wet-bulb temperature and the adiabatic saturation temperature for each of the conditions compiling the test matrix is shown in Figure 6-10.

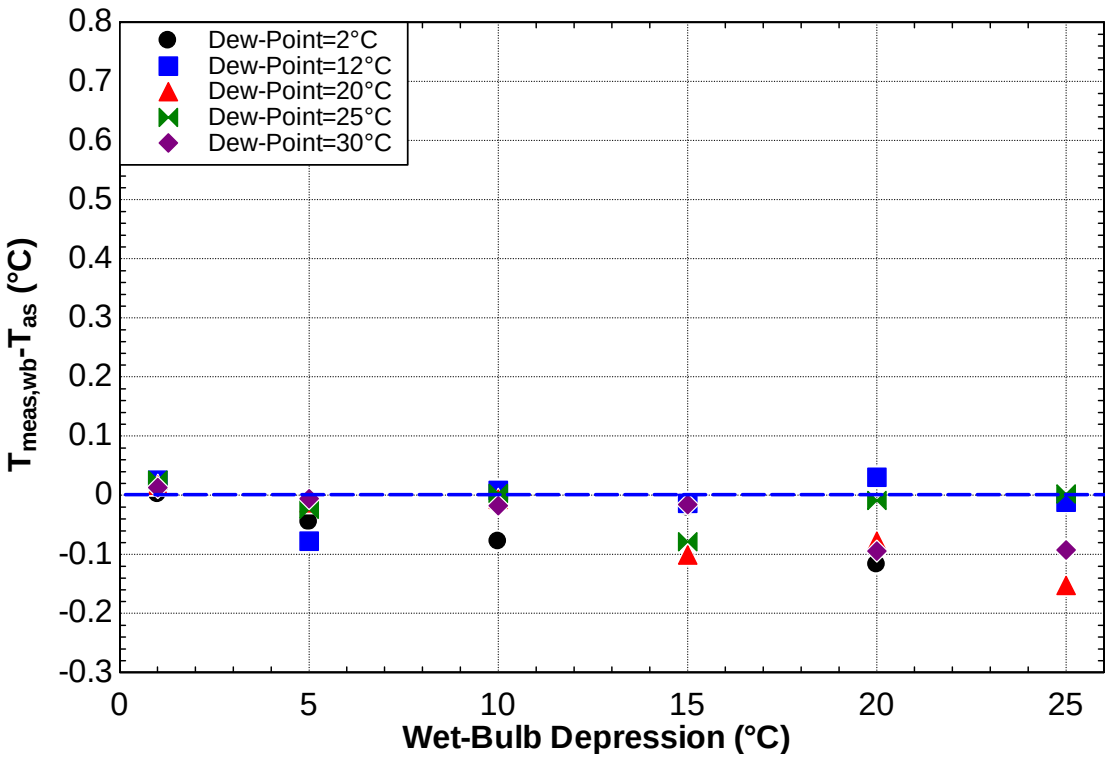

Figure 6-10: A plot of the difference between the measured wet-bulb temperature and the adiabatic saturation temperature for each of the thirty conditions in the test matrix. Each symbol indicates a constant dew-point temperature.

Figure 6-10 indicates that the measured wet-bulb temperature can be used to predict the adiabatic saturation temperature to within a bias error of -0.10°C for all test conditions with the exception of a few conditions at high wet-bulb depressions. At very low wet-bulb depressions the prediction is even better, within ±0.05°C. Overall the data shows a significant improvement in comparison to the initial data obtained and presented in Figure 6-1 on the same scale.

A comparison of the measured wet-bulb temperature to the true wet-bulb temperature is shown in Figure 6-11.

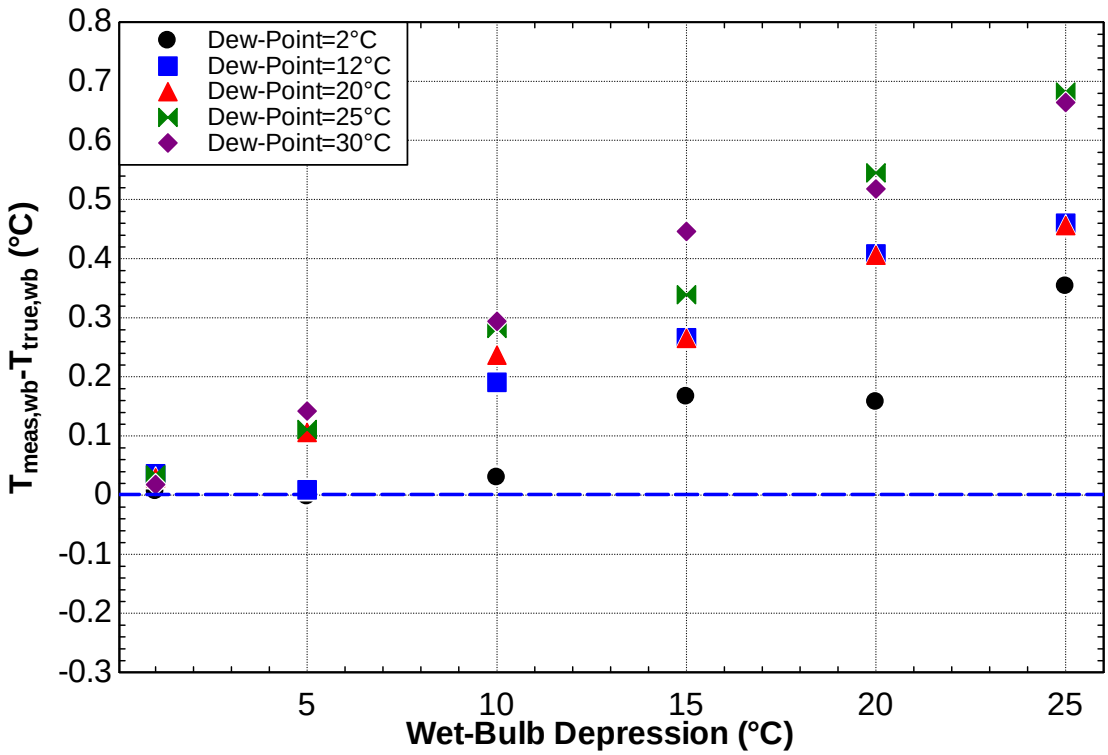

Figure 6-11: A plot of the difference between the measured wet-bulb temperature and the true wet-bulb temperature for each of the thirty conditions in the test matrix. Each symbol indicates a constant dew-point temperature.

For reasons similar to those discussed in Section 6.2, an increasing deviation between the measured wet-bulb temperature and the true wet-bulb temperature with an increasing wet-bulb depression is shown in Figure 6-11. Another encouraging sign from the second test matrix data compared to the first is the apparent trend in the measurement error with varying dew-point temperature at a constant wet-bulb depression. For each wet-bulb depression, the error increased with increasing dew-point temperature. This trend was not apparent from the

first test matrix data, and suggests that the repeatability of the measurements is significantly improved in the second test matrix data.

6.4 Model Prediction

The second round of testing produced consistent and repeatable results over the entire range of test conditions, meaning that it would now be applicable to compare these results to the model prediction. In Figure 6-12 the model prediction of the error in the wet-bulb temperature measurement is compared to the experimental test results presented in Figure 6-11.

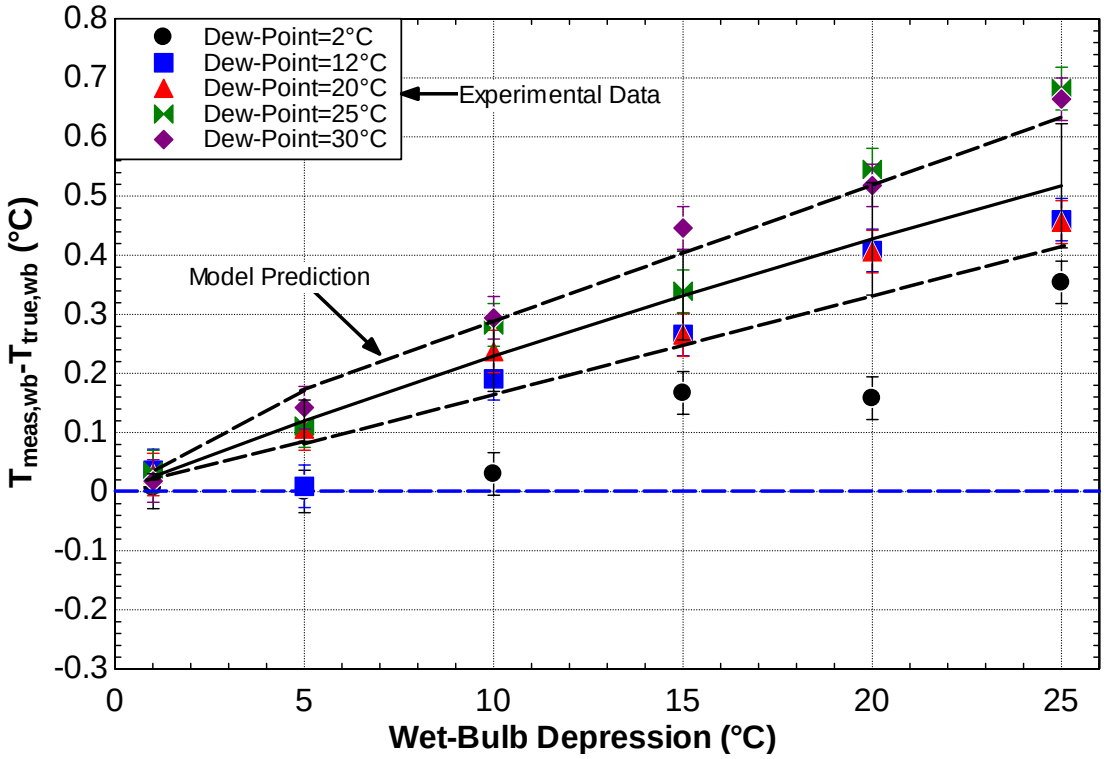

Figure 6-12: Model predicted error in the measurement of the true wet-bulb temperature. The error bars on each data marker indicate the uncertainty in the measurement result (±0.036°C). The model prediction range specified by the dashed lines accounts for the model uncertainty associated with uncertainty in the inputs.

Note that the model assumes that the radiation shield and the cotton sock surrounding the temperature sensor have an emissivity of 0.4 and 0.9, respectively. Although these values are slightly higher than the values initially used in the model, it appears these emittance values are more accurate. The model prediction of the error in the wet-bulb temperature measurement is in much better agreement with the experimental results when these higher emittance values are used.

As is shown in Figure 6-12, the model predicts the error in the measurement within ±0.10°C at wet-bulb depression up to 15°C and it predicts the error to within ±0.15°C at wet-bulb depressions of 20°C and 25°C. Although there is the deviation between the model prediction and the experimental results at the 2°C dew-point temperature conditions, the model is consistent enough with the experimental data to be able to be used to predict general trends in the measurement error with variations in various experimental parameters.

The model showed that the slight bias error in Figure 6-10 can be eliminated by following either one of two methods. Method one is to reduce the air velocity over the temperature sensor from 4 m/s to 3.5 m/s. In reducing the air velocity the parasitic "budget" of the temperature sensor is reduced and as a result the measured wet-bulb temperature deviates farther from the true wet-bulb temperature, but lies closer to the adiabatic saturation temperature for all test conditions. The other way in which to center the data is to keep the air velocity at 4 m/s, but remove the radiation shield. In removing the radiation shield the parasitic to the temperature sensor is increased and again the measured wet-bulb temperature will lie farther from the true wet-bulb temperature, but closer to the adiabatic saturation

temperature. When removing the shield, however, it is important to make sure that the wet-bulb temperature sensor only sees surroundings at the dry-bulb temperature. The reason the sensor should only see surroundings at the dry-bulb temperature is because this ensures that the sensor receives just enough radiation parasitic to cause the measured wet-bulb temperature to accurately predict the adiabatic saturation temperature. If either one of the two previously described techniques is followed the measured wet-bulb temperature will be able to predict the adiabatic saturation temperature within the target accuracy value of ±0.05°C.

6.5 Other Parameters Impacting Wet-Bulb Temperature Measurement

In this section of the report, three remaining parameters and their impact on the measurement of the wet-bulb temperature are discussed. These parameters include the duct size, the presence of upstream obstructions in the duct that might create non-uniform velocity flow, and the sensor diameter. The impact of these parameters is evaluated both experimentally and by using the model that is experimentally verified in Section 6.4. Results of these tests are described in detail in the subsequent sections.

6.5.1 Duct Size

As built, the experimental apparatus used to measure the wet-bulb temperature had an inner duct diameter of 19 cm (7.5 in). An experimental apparatus with a smaller duct diameter would be desirable if the accuracy of the measurement could be retained because the smaller diameter duct would provide increased application flexibility. To evaluate the impact of duct diameter on measurement results, a series of tests were conducted under two conditions.

First, an experiment that decreased the air flow over the guard portion of the wick was performed in order to simulate the reduced level evaporation that would occur when the guard portion of the sensor must be located outside of a small duct. The modification covered the entire portion of the temperature sensor that would otherwise be exposed to the airstream. The modified installation is shown in Figure 6-13. The upper portion of the probe and the wet cotton wick covering it are enclosed in a plastic sheath that isolates it from the air stream.

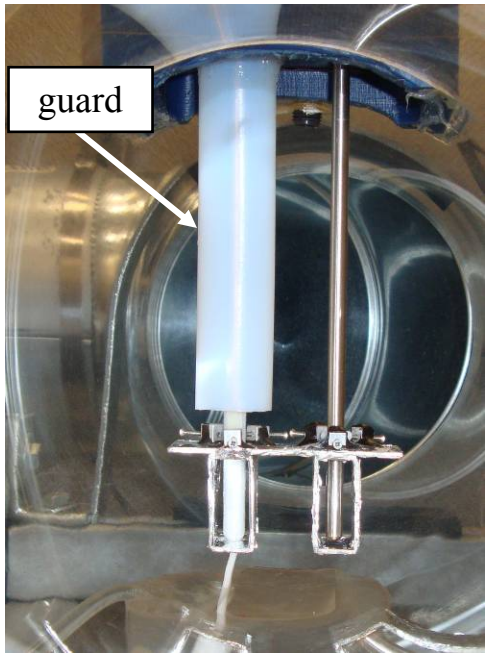

Figure 6-13: Guard used to isolate the guard portion of the sensor from the flow of air in order to simulate the removal of this portion of the sensor from a duct that is too small to accommodate the guard region.

Tests were run at the two nominal test conditions used throughout this project 8.3°C dry-bulb temperature with a 6.1°C wet-bulb temperature, and a 26.7°C dry-bulb temperature with a 19.4°C wet-bulb temperature. The results of these tests are presented in Table 6-1.

	Limited Aspiration	**Fully Aspirated**
Condition	$T_{meas,wb}$-T_{as} (°C)	$T_{meas,wb}$-T_{as} (°C)
8.3°C/6.1°C	0.012	0.016
26.7°C/19.4C	-0.017	-0.014
53.6°C/28.6°C	-0.120	-0.149

Table 6-1: Experimental test results. Limited aspiration refers to the apparatus shown in Figure 6-13. Fully aspirated is when the entire wick is exposed to the flow of air.

The tests indicate that with the upper portion of the wick guarded from the airflow, the aspirated psychrometer is still able to predict the adiabatic saturation temperature to within ±0.05°C at the nominal test conditions. Since both of the nominal test conditions are at

relatively low wet-bulb depressions, an additional test was carried out at a much higher depression (25°C). Tests run at a dry-bulb temperature of 53.6°C with a wet-bulb temperature of 28.6°C produced an error in the prediction of the adiabatic saturation temperature of -0.12°C. These results are not within the ±0.05°C target accuracy, but are consistent with the experimental results obtained at the same condition when the device was fully aspirated.

A second test condition was investigated in which the wick only covered the temperature sensor portion of the probe. In this set of tests, the wick is terminated at the top of the radiation shield. This arrangement is intended to represent the results achieved from a wet-bulb aspirator placed in a much smaller duct that cannot accommodate a guard section; in this case, no guard section is present at all (i.e., there is no isolated wicked section located outside of the duct). This setup is slightly different than the previously discussed setup in that the wick does not cover the upper portion of the temperature sensor probe, and can in no way guard against any possible conduction parasitic associated with the sheath and lead wires. Figure 6-14 shows a photo of the sensor setup for these tests.

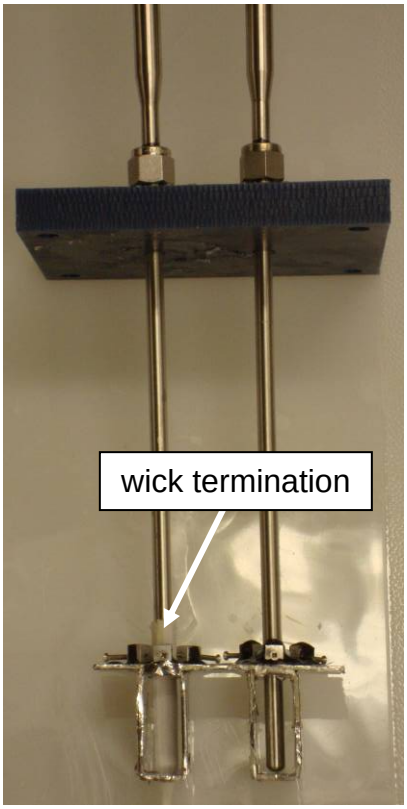

Figure 6-14: Cotton wick terminated at the top of the radiation shield.

The results of this set of tests are presented in Table 6-2.

	Aspirated Sensor Only	**Fully Aspirated**
Condition	$T_{meas,wb}$-T_{as} (°C)	$T_{meas,wb}$-T_{as} (°C)
8.3°C/6.1°C	0.008	0.016
26.7°C/19.4C	0.014	-0.014
53.6°C/28.6°C	0.080	-0.149

Table 6-2: Experimental test results. Aspirated sensor only data refers to the data taken with the sensor being wetted in the manner described by Figure 6-14. Fully aspirated is when the entire wick is exposed to the flow of air.

The results indicate that, at the two nominal test conditions, the additional wick guard over the upper portion of the sensor sheath is not necessary to accurately predict the adiabatic saturation temperature. Similar to before, a test was also performed at a wet-bulb

temperature depression of 25°C using this sensor arrangement. The objective of this test is to determine whether it is necessary for the wick to surround the portion of the temperature probe above the temperature sensor in order to accurately predict the adiabatic saturation temperature at large depression. The results of this test showed an error in the prediction of the adiabatic saturation temperature of 0.08°C. The prediction of the adiabatic saturation temperature is actually better when measured in this way, but it is no longer consistent with the experimental results for a fully aspirated sensor. Eliminating the portion of the wick above the temperature sensor increases the conduction parasitic and results in a slight over-prediction of the adiabatic saturation temperature, rather than the slight under-prediction at high depressions that otherwise is observed.

From the tests, it is clear that duct size can impact the measurement of the wet-bulb temperature. The impact can be eliminated, however, by installing the cotton sock over the entire length of the temperature probe, even if it extends outside of the air stream. This installation allows water to wick up the sock as high as possible under the given set of test conditions and helps guard against conduction parasitic since the water will be cool from evaporation in the active portion of the apparatus' air stream. Wet-bulb temperature measurements made in this manner have been shown to produce results consistent with those depicted in Figure 6-10. The benefit of having consistent measurements over a range of duct sizes is that a general correction can be applied to the data giving accurate results (i.e. within ±0.05°C) over the entire test matrix range.

6.5.2 Upstream Obstructions- Non-Uniform Velocity Distribution

Throughout the course of the experimental testing, there were no upstream obstructions placed in the duct that altered the velocity distribution in any way. The apparatus design and sensor locations allowed developed flow in the duct to reach the point of the temperature measurement.

To determine the impact of a non-uniform velocity distribution on the measurement of the wet-bulb temperature, a 90° bend was added to the upstream end of the duct. This is shown in Figure 6-15.

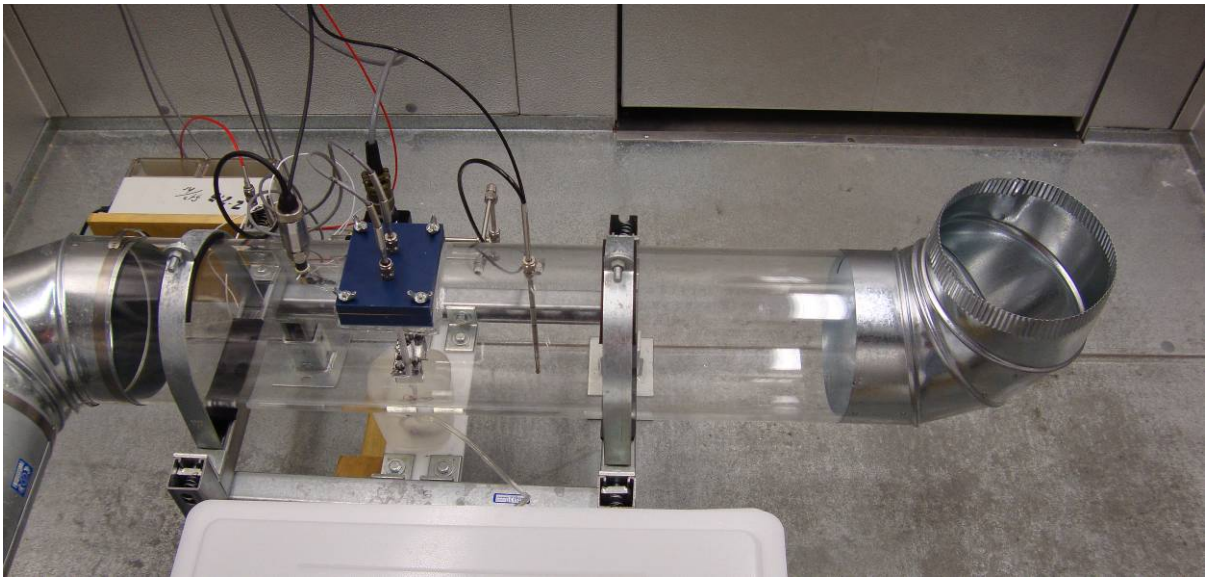

Figure 6-15: Experimental test setup with upstream bend added.

The elbow added to the end of the duct is approximately three duct diameters upstream of the sensor location. The measured velocity distribution generated while the elbow is pointed vertical (as shown in Figure 6-15) is shown in Figure 6-16.

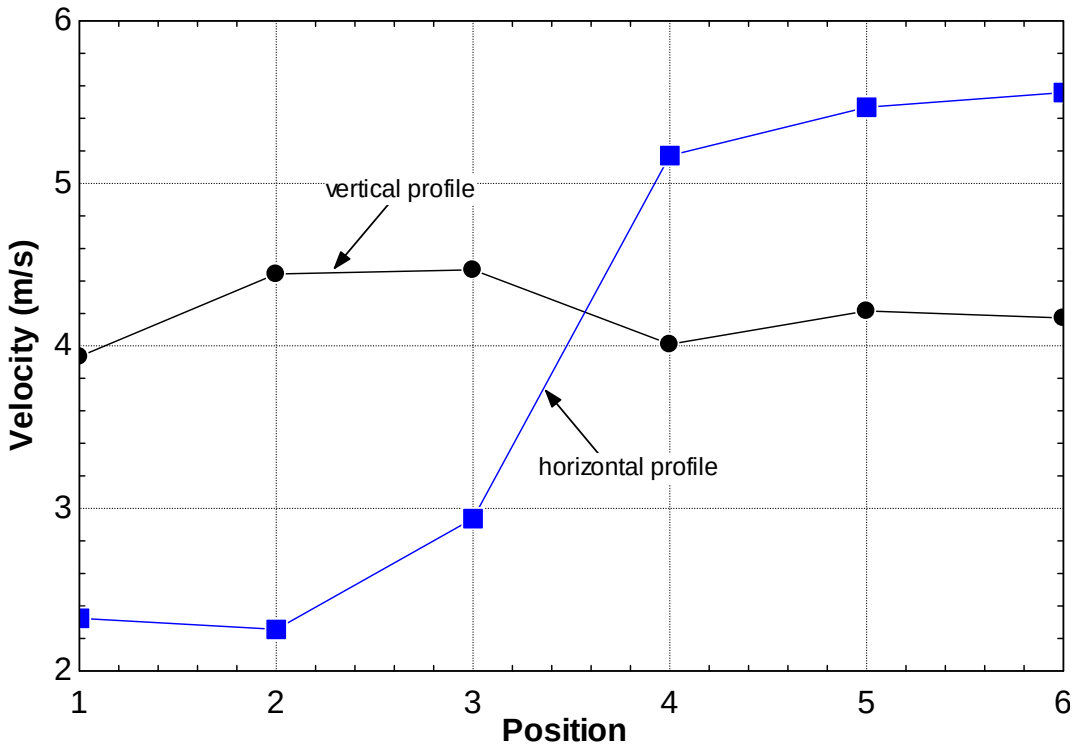

Figure 6-16: Velocity distribution in the duct with the elbow turned upright.

It is clear from Figure 6-16 that the addition of the upstream elbow creates a non-uniform flow through the duct. There is no longer a symmetrical velocity distribution about the center of the duct.

The measurement locations used to generate Figure 6-16 correspond to those specified in ASHRAE Standard 111-1988, for the accurate measurement of the flow rate of air through a cylindrical duct. These locations are shown in Figure 6-17 as they were located in the duct relative to the sensor; the vertical profile corresponds to positions 1 through 6 located on the vertical axis whereas the horizontal profile corresponds to positions 1 through 6 located on the horizontal axis.

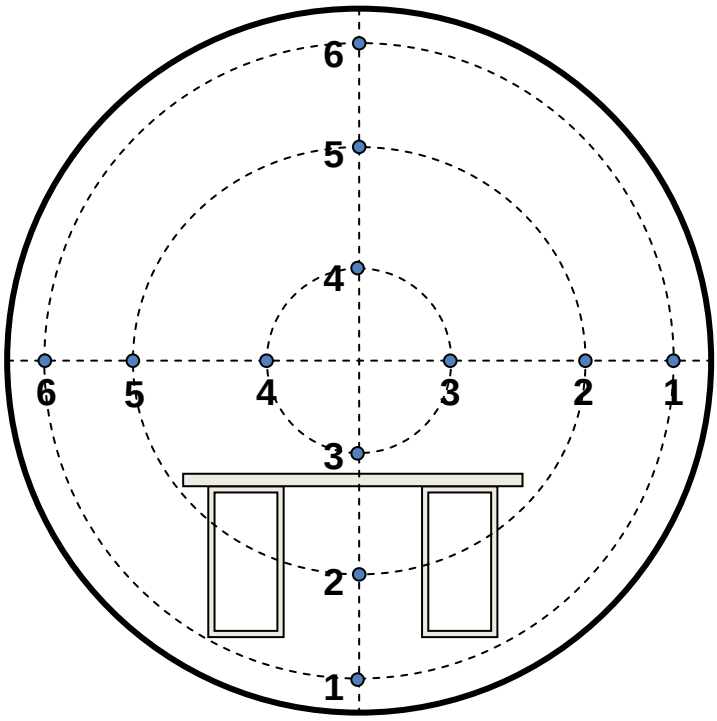

Figure 6-17: Velocity measurement locations. The locations are the following distances from the wall: location 1- 0.032*D, location 2-0.135*D, location 3-0.321*D, location 4-0.679*D, location 5-0.865*D, and location 6-0.968*D. D is the inner duct diameter, which in this case is 7.5 inches.

Wet-bulb temperature measurements were taken with the flow set so that a 4 m/s air velocity is measured at the temperature sensor location. The nominal test condition is used: a 26.7°C dry-bulb temperature and a 19.4°C wet-bulb temperature. The measurements taken at this condition, with the non-uniform velocity distribution, had an error in the measurement of the true wet-bulb temperature of 0.21°C and an error in the prediction of the adiabatic saturation temperature of 0.06°C. Although the error in the prediction of the adiabatic saturation temperature is very close to the target accuracy goal of ±0.05°C, it is noticeably higher than the error obtained with a uniform velocity distribution present (i.e. -0.02°C). Similar

differences were also obtained when the elbow on the upstream end of the duct was turned horizontally instead of vertically.

The results from this set of tests indicate that slightly different measurement results will be obtained if there is a non-uniform velocity distribution instead of a uniform distribution, even if the average velocity at the location of the sensor is maintained at its nominal value. Discrepancies in the results are likely due to fluctuating velocities experienced by the temperature sensor. Upstream obstructions can create turbulence in the flow and expose the sensor to erratic and unpredictable air velocities, creating slightly erratic and unpredictable results. These measurement results highlight the importance of having a developed flow over the temperature sensors to ensure accurate and consistent measurement results.

6.5.3 Sensor Diameter

The temperature sensor used throughout the modeling process and experimental testing had a 6.35 mm (0.25 in) diameter sheath. A 6.35 mm (0.25 in) diameter sheath probe was used, in large part, because of its common use in laboratory HVAC installations. In this section, other sensor sheath diameter sizes are analyzed using the model discussed in Chapter 3 and verified in Section 6.4 in order to determine the impact of the sheath diameter on measurement accuracy.

In Figure 6-18 the model prediction of the error in the measurement of the true wet-bulb temperature is shown for three different temperature sensor diameters: 3.2 mm (0.125 in), 4.8 mm (0.1875 in), and 6.35 mm (0.25 in).

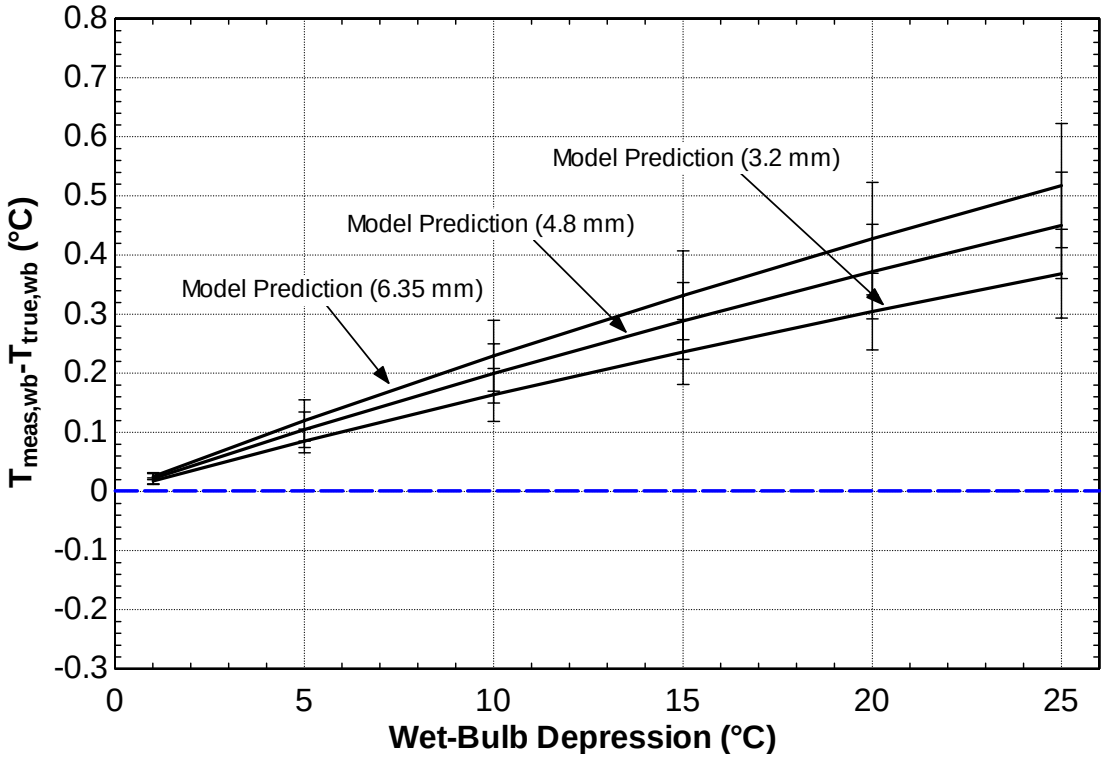

Figure 6-18: Model prediction of the error in the measurement of the true wet-bulb temperature for sensor diameters of 6.35, 4.8, and 3.2 mm in diameter and an air velocity of 4 m/s.

Figure 6-18 clearly indicates that with decreasing sensor diameter, the error in the measurement of the wet-bulb temperature decreases. As the temperature sensor diameter decreases, the radiation parasitic to the sensor and the parasitic budget both decrease. The radiation parasitic decreases much more drastically, however, and as a result the smaller diameter temperature sensor can do a better job of measuring the true wet-bulb temperature.

At first glance the results of Figure 6-18 suggest that smaller diameter temperature sensors are preferable to larger diameter temperature sensors. However, this is not necessarily the case. It is important to remember that early on in this project it was determined that the measurement of the true wet-bulb temperature to within ±0.05°C was not possible within the

means of the project scope. The use of the measurement of the wet-bulb temperature as a prediction of the adiabatic saturation temperature to within ±0.05°C, however is possible. Referring back to the experimental results in Figure 6-10, it is clear that the smaller wet-bulb temperature error associated with the smaller temperature sensor diameter, will only lead to a larger deviation between the measured wet-bulb temperature and the adiabatic saturation temperature.

The results of the analytical model indicate that a 6.35 mm (0.25 in) diameter probe is preferable at the 4 m/s air velocity. Smaller diameter probes will be able to produce comparable results, but only if the air velocity over the sensor is reduced so that the impact of the reduced parasitic is a larger temperature change. Model predictions indicate that in order to obtain the same wet-bulb temperature error with a 4.8 mm (0.1875 in) diameter probe, the air velocity over the sensor should be reduced to 3 m/s. If a 3.2 mm (0.125 in) diameter probe is used then the model suggests that an air velocity of 2 m/s should be used.

Chapter 7 – Conclusion

Analytical models were developed to predict the practical accuracy in the measurement of the wet-bulb temperature using a wet-bulb aspirator apparatus. Based on the analytical models, an optimized apparatus was built and tested over a range of experimental test conditions. The experimental test conditions in which the apparatus was tested ranged in dew-point temperatures from 2°C to 30°C with wet-bulb depressions ranging from 1°C to 25°C.

The analytical models and experimental results highlighted the difficulty in accurately measuring the true wet-bulb temperature. Both model predictions and experimental results indicated an error in the measurement of the true wet-bulb temperature of as much as 0.7°C at a wet-bulb depression of 25°C. The large error in the measurement of the true wet-bulb temperature is attributable to various forms of parasitic heat transfers to the temperature sensor. The three methods of parasitic heat transfer listed from most important to least important were: radiation parasitic, conduction parasitic (sheath and lead wires), and makeup water parasitic. The analysis of these parasitic heat transfer mechanisms provided the basis of an analytical model that is used to predict the wet-bulb temperature measurement error.

Although it was shown both analytically and experimentally that the true wet-bulb temperature cannot be measured to within the target goal of ±0.05°C, it was shown that the measured wet-bulb temperature can be a very good prediction of the adiabatic saturation temperature. The experimental apparatus described and tested was able to predict the

adiabatic saturation temperature to within ±0.10°C over the entire range of psychrometric conditions tested. With either a minor reduction in the air velocity across the temperature sensor (i.e. from 4 m/s to 3.5 m/s) or the removal of the radiation shield, the model shows that the measured wet-bulb temperature can be used to predict the adiabatic saturation temperature to approximately the target accuracy goal of ±0.05°C.

There are a few areas for future work related to this project:

1) Additional time could be spent building a more sophisticated radiation shield to eliminate radiation parasitic. The idea of actively cooling the radiation shield or adding upstream and downstream screens or louvers was suggested early on, but was not explored further. A more sophisticated radiation shield could reduce the radiation parasitic, making the measured wet-bulb temperature more closely reflect the true wet-bulb temperature.
2) The idea of using a material other than cotton as the sock surrounding the temperature sensor. Cotton sock consistent with ASHRAE Standard 41.6-1994 (RA 2006) was used throughout the course of the project. Other "high performance" fabrics may be beneficial in that they would be able to produce a higher wicking height creating a better guard against conduction parasitic. This would likely only provide a substantial benefit at very high wet-bulb depressions.
3) The impact of sensor diameter on the wet-bulb temperature measurement accuracy should be explored more completely. The sensors used in the experimental testing were 6.35 mm (0.25 in) in diameter. Other sensor diameters were modeled analytically, but the analytical results could not be verified experimentally.

References

ANSI/ASHRAE Standard 41.1-1986 (RA 1991), *Standard Method for Temperature Measurement,* ISSN 1041-2336 (1991).

ANSI/ASHRAE Standard 41.6-1994 (RA 2006), *Standard Method for Measurement of Moist Air Properties,* ISSN 1041-2336 (2006).

ANSI/ASHRAE Standard 111-1988, *Practices for Measurement, Testing, Adjusting, and Balancing of Heating, Ventilation, Air-Conditioning, and Refrigeration Systems,* (1988).

Auerkari, Pertti, "Mechanical and physical properties of engineering alumina ceramics," ***Technical Research Center of Finland***, pp. 7-8, (1996).

Churchill, S.W., and Bernstein, M., A Correlating Equation for Forced Convection from Gases and Liquids to a Circular Cylinder in Cross Flow, ***J. Heat Transfer,*** 99, 300-306, (1977); in Bejan, Adrian; Kraus, Allan D. ***Heat Transfer Handbook.*** John Wiley & Sons.

Churchill, S.W., and Ozoe, H, ***J. Heat Transfer,*** 95, 78, (1973); in Incropera, F.P. and DeWitt, D.P., ***Introduction to Heat Transfer***, 4th Ed., Wiley, (2002).

Cole-Parmer, ***Technical Library- Emissivity of Specific Materials***; accessible online at http://www.coleparmer.com/techinfo/techinfo.asp?htmlfile=Emissivity.htm&ID= 254

Howell, J. ***A catalog of radiation configuration factors***. New York: McGraw Hill, p. 154, (1982).

Hyland and Wexler, "Formulations for the Thermodynamic Properties of the Saturated Phases of H2O from 173.15 K to 473.15 K", ***ASHRAE Transactions***, Part 2A, Paper 2793 (RP-216), (1983).

Jakob M., ***Heat Transfer***, John Wiley & Sons, New York, (1949).

Klein, S.A., ***Engineering Equation Solver, EES,*** F-Chart Software, www.fchart.com, (2010).

Nellis, G.F., and S.A. Klein, ***Heat Transfer***, Cambridge University Press, New York, (2009).

Omega.com, ***Transactions in Measurement and Control***, vol. 1, 2nd edition, Putman Publishing Company and OMEGA Press LLC., (1998); accessible online at http://www.omega.com/literature/transactions/Transactions_Vol_I.pdf

Poling, Bruce E., Prausnitz, John M., O'Connell, John P., ***The Properties of Gases and Liquids,*** 5th edition, McGraw-Hill, (2000).

Rea, Samuel N., "Rapid method for determining concentric cylinder radiation view factors," ***AIAA J.***, vol. 13, no. 8, pp. 1122-1123, (1975).

Shukla, K.N. and Ghosh, D., "Radiation configuration factors for concentric cylinder bodies in enclosure," ***Indian J. Technology***, vol. 23, pp. 244-246, (1985).

Siegel, R. and Howell, J.R., ***Thermal Radiation Heat Transfer,*** 4th edition, Taylor and Francis, (2002).

White, Frank M., ***Fluid Mechanics***, McGraw-Hill, (2003).

Wiebelt, J. A. & Ruo, S. Y. Radiant-interchange configuration factors for finite right circular cylinder to rectangular planes, ***Int. J. Heat Mass Transfer***, vol. 6, no. 2, pp. 143-146, (1963).

Wiederhold, Pieter R., ***Water Vapor Measurement: Methods and Instrumentation***, Marcel Dekker, Inc., New York, (1997).

Appendix

Thermistor Calibration Certificates

GE Sensing

967 Windfall Road
St. Marys, PA 15857
USA

T 814 834-9140
F 814 834-5535

REPORT OF CALIBRATION FOR S10 4-WIRE THERMISTOR STANDARD

SERIAL NO.: 3259

The above designated thermistor standard was calibrated on November 10, 2009 using the test currents shown below.

The following calibration values were obtained and are traceable to the National Institute of Standards and Technology.

Temperature (1)	°C	0.01	15.00	25.00	30.00	32.00
Resistance (2)	Ω	12171.65	6285.33	4174.85	3432.51	3178.92
Current	uA	5	10	10	10	10

Temperature (1)	°C	37.00	50.00	60.00	N/A	N/A
Resistance (2)	Ω	2633.78	1654.32	1182.52	N/A	N/A
Current	uA	10	10	10	N/A	N/A

(1) All temperature observations were made by comparison with a standard platinum resistance thermometer Hart Scientific Model 5683, Serial No. 4024
Calibration of the platinum standard at the triple point of water was performed prior to and after calibration of the standard.
The drift in the platinum standard was found to be less than 0.0002°C.
The uncertainty in the temperature measurement was less than 0.001°C from 0°C to 60°C.

(2) All resistance obserations were made using a Hart Scientific Super Thermometer (serial # A68349 calibrated 09/15/09, due 12/16/09) whose readings were corrected against a ratio bridge, using comparison techniques. The ratio bridge used has an accuracy of 0.0002%. Ratio measurements were made against temperature controlled standard resistors having an accuracy of 0.001%. The total corrected resistance uncertainty was less than 0.0025%.

CALIBRATION TRACEABLE TO ITS-90

Cal. By: Tom Olewnick

Date: 12/8/09

Approved: [illegible]

Date: 12/9/09

GE Sensing

967 Windfall Road
St. Marys, PA 15857
USA

T 814 834-9140
F 814 834-5535

REPORT OF CALIBRATION FOR S10 4-WIRE THERMISTOR STANDARD

SERIAL NO.: 3208

The above designated thermistor standard was calibrated on November 10, 2009 using the test currents shown below.

The following calibration values were obtained and are traceable to the National Institute of Standards and Technology.

Temperature (1)	°C	0.01	15.00	25.00	30.00	32.00
Resistance (2)	Ω	12322.76	6356.67	4219.40	3468.03	3211.41
Current	uA	5	10	10	10	10

Temperature (1)	°C	37.00	50.00	60.00	N/A	N/A
Resistance (2)	Ω	2659.93	1669.48	1192.73	N/A	N/A
Current	uA	10	10	10	N/A	N/A

(1) All temperature observations were made by comparison with a standard platinum resistance thermometer Hart Scientific Model 5683, Serial No. 4024
Calibration of the platinum standard at the triple point of water was performed prior to and after calibration of the standard.
The drift in the platinum standard was found to be less than 0.0002°C.
The uncertainty in the temperature measurement was less than 0.001°C from 0°C to 60°C.

(2) All resistance obserations were made using a Hart Scientific Super Thermometer (serial # A68349 calibrated 09/15/09, due 12/16/09) whose readings were corrected against a ratio bridge, using comparison techniques. The ratio bridge used has an accuracy of 0.0002%. Ratio measurements were made against temperature controlled standard resistors having an accuracy of 0.001%. The total corrected resistance uncertainty was less than 0.0025%.

CALIBRATION TRACEABLE TO ITS-90

Cal. By: _____

Date: 12/8/09

Approved: _____

Date: 12/9/09

Velocity Transducer Calibration Certificate

TSI

CERTIFICATE OF CALIBRATION AND TESTING

TSI Model 8455-12 Serial No. 03030247

Description AIR VEL TRANSDUCER

Calibration Standard WIND TUNNEL CALIBRATION SYSTEM, SERIAL NO. 114

CALIBRATION VERIFICATION RESULTS

Calibration Standard Std ft/min (Std m/s)	Instrument Output Std ft/min (Std m/s)	Error Percent		Error Compared to Tolerance (Tolerance Limit- 0 Tolerance Limit+)
With range = 0- 200 Std ft/min:				
0.0 (0.000)	0.0 (0.000)		PASS	
24.9 (0.127)	25.0 (0.127)	0.6	PASS	
38.0 (0.193)	38.0 (0.193)	0.2	PASS	
52.9 (0.269)	53.1 (0.270)	0.4	PASS	
72.0 (0.366)	71.6 (0.364)	-0.6	PASS	
113.1 (0.574)	113.0 (0.574)	-0.1	PASS	
170.0 (0.863)	169.6 (0.862)	-0.2	PASS	
With range = 0- 1000 Std ft/min:				
255.6 (1.299)	259.0 (1.316)	1.3	PASS	
378.7 (1.924)	379.5 (1.928)	0.2	PASS	
533.4 (2.710)	531.2 (2.698)	-0.4	PASS	
721.1 (3.663)	721.8 (3.667)	0.1	PASS	
With range = 0-10000 Std ft/min:				
1135.8 (5.770)	1135.1 (5.767)	-0.1	PASS	
1706.4 (8.669)	1697.0 (8.621)	-0.6	PASS	
2546.2 (12.935)	2546.3 (12.936)	0.0	PASS	
3854.2 (19.579)	3869.9 (19.659)	0.4	PASS	
5314.9 (27.000)	5304.0 (26.945)	-0.2	PASS	
7195.0 (36.551)	7232.1 (36.739)	0.5	PASS	
9050.3 (45.976)	9033.4 (45.890)	-0.2	PASS	

Tolerance Limits:
± 2.0% of reading
± 0.5% of full scale of selected range

The indicated velocities were determined using the 0-5 Volt output.

Velocity Calibration Conditions: *Ambient Temp: 24.4°C* *Barometric Pressure: 736.4 mmHg*

Velocity Corrected to Std Conditions of: *Ambient Temp: 21.1°C* *Barometric Pressure: 760.0 mmHg*

TSI does hereby certify that all materials, components, and workmanship used in the manufacture of this equipment are in strict accordance with the applicable specifications agreed upon by TSI and the customer and with all published specifications. All performance and acceptance tests required under this contract were successfully conducted according to required specifications. Furthermore, all test and calibration data supplied by TSI has been obtained using standards whose accuracies are traceable to the National Institute of Standards and Technology (NIST) or has been verified with respect to instrumentation whose accuracy is traceable to NIST, or is derived from accepted values of physical constants. Our Quality Management System complies with ISO 9001 requirements and calibration procedures for this instrument adhere to ISO 10012. The accuracy of the velocity calibration facilities is at least a ratio of 1:1 with respect to the accuracy specifications of the instrument being calibrated.

Applicable Test Report	Report Number	Date Last Verified	Date Due
DC voltage	E001548	01-05-09	01-05-10
Barometric Pressure	E001154	04-13-09	04-13-10
Temperature (0°C)	E000822	07-08-08	07-08-10
Temperature (19-35°C)	E002857	07-08-08	07-08-10
Temperature (60°C)	E001806	07-08-08	07-08-10
Pressure	E001415	06-19-09	12-19-09
Pressure	E001290	06-19-09	12-19-09
Velocity	E003327	09-19-07	09-19-10
Dewpoint	E001266	12-29-08	12-29-09

Calibrated by

☐ Final Function Check

Oct 20, 2009
Calibration Date

TSI Incorporated
Environmental Measurements and Controls Division

Mailing Address: P.O. Box 64394 St. Paul, MN 55164 USA
Shipping Address: 500 Cardigan Road Shoreview, MN 55126 USA
Phone: (800) 777-8356 or (651) 490-2711 **Fax:** (651) 490-2874

Chilled Mirror Calibration Certificate

GE Sensing

Chilled Mirror Calibration Report

Report Number: CM3212

Model:	1111H	Analyzer SN:	N/A	Sensor SN:	0410709
Cal Date:	8/11/2009	Cal Due:	8/11/2010	Run ID:	CMHIGH0946
Lab Temp:	23.52 °C	Lab %RH:	20-30% RH	Voltage:	110 VAC
T100 SN:	0410709	PT 30/300 SN:	N/A	Flow Rate:	1-2 SCFH
Option:	SR	Comments			None

GE Standard Dew Point/RH	Customer Unit Dew Point/RH	Difference	Specification of Unit (+/-)	Analog Outs	
				Vout (Volts)	Iout (mA)
-9.02°C *	-9.09°C *	-0.07	0.20°C		
-4.77°C *	-4.64°C *	0.13	0.20°C		
0.50°C	0.59°C	0.09	0.20°C		
10.19°C	10.21°C	0.02	0.20°C		
19.62°C	19.76°C	0.14	0.20°C		13.570

GE Standard Air Temp.	Customer Unit Air Temp.	Difference	Specification of Unit (+/-)	Analog Outs	
				Vout (Volts)	Iout (mA)
23.52 °C	23.56 °C	-0.04	0.15°C		7.774

GE Standard Pressure (PSIA)	Customer Unit Pressure (PSIA)	Difference	Specification of Unit (+/-)	Analog Outs	
				Vout (Volts)	Iout (mA)

Manufacturer	Model Type	Serial#	Cal Due Date

Manufacturer	Model Type	Serial#	Cal Due Date
GE - General Eastern Instruments	Optica/1311DR SN 0280705	0280705	12/17/2009

Manufacturer	Model Type	Serial#	Cal Due Date
GE - General Eastern Instruments	T100	0280705	12/17/2009

Manufacturer	Model Type	Serial#	Cal Due Date

Manufacturer	Model Type	Serial#	Cal Due Date

Analog Out Scaling

Reading	Type	Range	Scale
Dew Point	Current	4-20 mA	-40 to 60°C
Dew Point	Voltage	0-5 V	-40 to 60°C
Temperature	Current	4-20 mA	0 to 100 °C
Temperature	Voltage	0-5 V	0 to 100 °C

*Below 0°C water can exist on smooth plane surfaces in liquid form rather than ice crystals, this phenomenon is known as supercooled water. The equations below yield saturation vapor pressure over water and ice respectively from the corresponding dew or frost point.

$$\lambda_{WS} = (1.007 + 3.46 \times 10^{-6} P) * 6.1121 e^{\frac{17.502T}{(240.97+T)}}$$

$$\lambda_{ie} = (1.003 + 4.18 \times 10^{-6} P) * 6.1115 e^{\frac{22.452T}{(272.55+T)}}$$

Where:

P = Total Pressure

λ_{WS} = Saturation Vapor Pressure over water

λ_{ie} = Saturation Vapor Pressure over ice

T = Dew point

CALIBRATION STATEMENT

GE Sensing certifies this instrument to meet or exceed published measurement specifications (unless other wise noted) and has been calibrated using standards traceable to the National Institute of Standards and technology (NIST) and CETIAT. Calibration records for inspection, measuring, and test equipment are maintained. The quality system at this facility complies with ANSI/ASQC Q9001-1994 (ISO 90001). GE Sensing's calibration service meets the requirements of ANSI/NCSL Z540-1-1994. This report shall not be reproduced, except in full, without the written approval of the laboratory.

UNCERTAINTY STATEMENT

The National Institute of Standards and Technology has a stated dew/frost point uncertainty with 95% confidence of ± 0.04°C from -10°C to +20°C, ±0.07°C from -40°C to -10°C, ±0.12°C from -55°C to -40°C and 0.15°C from -70°C to -55°C. GE Sensing's dew/frost transfer calibration standard has an uncertainty with 95% confidence of ±0.056°C from -35°C to -25°C and ±0.1°C for frost points from -70°C to -36°C. For Air Temperature GE Sensing's dew/frost transfer calibration standard has an uncertainty with 95% confidence of ±0.025°C.

Tested By: Paramjit Saini

Signature:

1100 Technology Park Dr., Billerica 01821, USA, Phone 800-833-9438